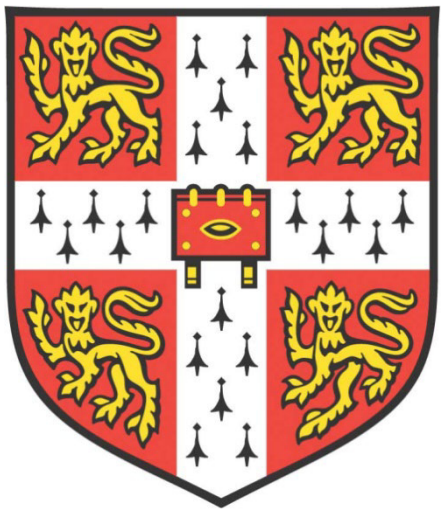
Preclinical Evaluation of 3D Printed Biomaterials for Repairing Critical-Size Bone Defects



Sara Ahmed Hassouna Elsayed

Newnham College

Department of Veterinary Medicine

University of Cambridge

This dissertation is submitted for the degree of Doctor of Philosophy

December 2022

Declaration

This thesis is submitted for the degree of Doctor of Philosophy (in Veterinary Medicine).

This thesis is the result of my own work and includes nothing which is the outcome of work done in collaboration except as declared in the preface and specified in the text.

I further state that no substantial part of my dissertation has already been submitted or is being concurrently submitted for any such degree, diploma or other qualification at the University of Cambridge or any other University or similar institution.

It does not exceed the prescribed word limit for the Clinical Medicine and Clinical Veterinary Medicine Degree Committee (60,000 words excluding figures, photographs, tables, appendices and bibliography).

I have also:

• Resided in Cambridge for at least three terms

• Undertaken the minimum requirement of research terms

I will also keep my contact details up to date using my self-service pages throughout the examination process.

Full name: Sara Ahmed Hassouna Elsayed

Signature: [Redacted]

Date: 20 December 2022

Thesis summary

Full name: **Sara Ahmed Hassouna Elsayed**

Thesis title: **Preclinical Evaluation of 3D Printed Biomaterials for Repairing Critical-Size Bone Defects**

Problem and study aim:

Millions of patients each year suffer from non-healing bone defects secondary to trauma, cancer, osteomyelitis, or congenital anomalies. The standard of care for managing these cases necessitates bone reconstruction surgery. Although using autologous bone (autograft) or banked cadaveric bone (allograft) has been considered the standard of care for decades, both come with significant attendant risks and limitations. Commercially available bone substitute materials overcome some of these challenges but do not necessarily meet the challenging anatomical and mechanical requirements of patients undergoing complex bone reconstruction surgeries. For this reason, **there is a clear, unmet need** for biomaterials that can support bone healing and act as bone graft substitutes for patients with challenging and non-healing bone defects.

The ultimate goal of my work is to offer a solution to non-healing bone defects with a particular focus on developing and characterising an osteoinductive, biocompatible and mechanically robust biomaterial that can act as a bone graft substitute to support bone healing for critical size (non-healing) bone defects and can be customised to patients' specific needs.

Research Methodology:

The work in this thesis extends across five fundamental sections:

1- Isolation and characterisation of adipose-derived mesenchymal stem cells (Ad-MSCs) as a source of osteogenic precursor cells.

2- Investigating the potential use of extracorporeal shockwave therapy (ESWT) to stimulate bone healing.

3- Development of a novel 3D printable biomaterial, based on decellularised bone matrix (DCBM), for potential use as bone graft substitute and *in-vitro* characterisation of the scaffolds to ensure complete decellularisation, evaluate mineral content, cytocompatibility, osteoinductivity, microstructure and biomechanical properties.

4- *In-vivo* testing of the local biological effect of candidate biomaterials following subcutaneous implantation in rats.
5- *In-vivo* evaluation of the biomaterials' ability to support bone healing in a critical-size bone defect (15 mm rabbit's radius segmental defect).

Results and conclusion:

Our results show that Ad-MSCs were capable of differentiating towards the osteogenic lineage, as indicated by the expression of markers of both early matrix maturation markers (such as (alkaline phosphatase, RUNX2, collagen type I, osteopontin osteonectin) and late matrix mineralisation markers (such as osteocalcin, Alizarin red staining), as well as exhibiting osteoblastic morphology upon scanning electron microscopy.

While ESWT didn't promote Ad-MSCs proliferation, the results showed that focused ESWT enhances Ad-MSCs osteogenic differentiation ability *in-vitro*.

The 3D-printed DCBM scaffold was shown to be cytocompatible and osteoinductive. And to have microstructure, mechanical and material properties that support clinical use as a bone graft substitute.

In-vivo testing in the rat subcutaneous model established the biocompatibility of the material, and data from the segmental bone defect study in rabbits confirmed that the scaffolds could integrate with native bone and support osteoinduction and osteoconduction by week 12 post-implantation.

Table of Contents

Declaration.....I

Thesis summary..... II

Table of Contents IV

List of Figures.....IX

List of Tables XIV

List of abbreviations XVI

1-Introduction 1

1.1-Study background: 1

1.2- Study aims and research questions: 3

1.3- Study hypothesises: 4

1.4- Study importance, relevance, and contribution to the scientific community: 5

1.5- Thesis outlines 6

2- Literature Review 8

2.1- Bone structure, fracture healing and bone formation: 8

2.1.1- Bone structure: 8

2.1.2- Fracture healing: 10

2.1.3- Bone formation (osteogenesis) at different anatomical locations: 13

2.2-Fracture non-union and critical-sized bone defects: 15

2.2.1- Fracture non-union: 15

2.2.2- Critical-size bone defect: 20

2.3- Bone grafts: 22

2.4- Bone graft substitutes: 27

2.4.1- Clinical use of bone graft substitutes: 32

2.5- The role of tissue engineering in solving the problem of non-healing bone defects: 38

2.5.1- Mesenchymal stem cells: 39

2.5.2- Scaffolds: 41

2.5.3- Biochemical signalling molecules and growth factors 43

2.5.4- Physical and mechanical stimuli: 45
2.6- Pre-clinical animal models: 49
2.6.1- Animal models for biomaterial safety testing: 49
2.6.2- Animal models for studying critical size bone defects: 53
2.7- Additive manufacturing for customisable orthopaedic implants: 56
3- Methodology 62
3.1- Adipose derived mesenchymal stem cells (Ad-MSCs) isolation and characterisation: 62
3.1.a- Ad-MSCs isolation 63
3.1.b- Ad-MScs characterisation: 64
3.1.c- Ad-MSCs osteogenic differentiation 74
3.2-The effect of extracorporeal shockwaves (ESW) on MSCs 78
3.2.1-The effect of focused versus radial ESW on Ad-MSCs (direct ESW application) 78
3.2.2- The effect of focused ESWT on Ad-MSCs (designed water bath *in vitro* testing apparatus): 80
3.3- Bone graft substitute biomaterials (scaffolds) fabrication and characterisation: 83
3.3.1: Material preparation and 3D printing: 84
3.3.2: *In vitro* characterisation: 87
3.4- Testing the local biological effect of the selected biomaterials (scaffolds) after implantation (biocompatibility testing): a rat preclinical subcutaneous implantation model: 93
3.4.1- Ethics approval and experimental design: 93
3.4.2- Anaesthesia and preoperative preparation 93
3.4.3- Surgical procedure and post-operative care 94
3.4.4-In-life animals' outcomes: 94
3.4.5- Euthanasia and post-mortem outcomes 95
3.5- Evaluation of the ability to support bone healing in a critical size segmental long bone defect: 102
3.5.1- Implant design for rabbit bone defects: 102
3.5.2- Ethics approval and experimental design: 106
3.5.3- Anaesthesia and preoperative preparation: 108

3.5.4- Surgical procedure and post-operative care. 112
3.5.5- In-Life animal outcomes: 118
3.5.6-Euthanasia and post-mortem outcomes: 119
4-Results 125
4.1- Adipose derived mesenchymal stem cells characterisation: 125
4.1.1- Cell morphology: 125
4.1.2: Behaviour in tissue culture 128
4.1.3: Trilineage differentiation 132
4.1.4: Immunophenotypic characterisation (Flowcytometry): 132
4.1.5- Ad-MSCs differentiation towards osteogenic lineage 137
4.2-The effect of extracorporeal shockwaves (ESW) on MSCs 142
4.2.1-The effect of focused vs radial ESW on Ad-MSCs (direct application) 142
4.2.2- The effect of focused ESW on Ad-MSCs (designed water bath *in vitro* testing apparatus): 145
4.3- Bone graft substitute biomaterials (scaffolds) fabrication and *in vitro* characterisation: 148
4.3.1-Confirmation of donor cells elimination in decellularised bone cores: 148
4.3.2- Mineralisation status in decellularised bone cores: 149
4.3.3-Cytocompatibility in 3D printing scaffolds: 149
4.3.4 – Osteoinductivity in 3D printing scaffolds: 150
4.3.5- Microstructure: 152
4.3.6- Biomechanical properties: 153
4.4- Testing the local biological effect of the selected biomaterials (scaffolds) after implantation (biocompatibility testing): a rat subcutaneous implantation preclinical model: 154
4.4.1-General health 154
4.4.2-Gross pathology 154
4.4.3-Histopathology 155
4.5- Evaluation of the ability to support bone healing in a critical size segmental long bone defect. 164

4.5.1. In-Life animals' outcomes: 164

4.5.2: Post-mortem evaluation 175

5- Discussion 193

5.1- Adipose derived mesenchymal stem cells (Ad-MSCs) characterisation: 194

5.1.I-Ad-MSCs defining criteria: 194

5.1.II- Ad-MSCs Differentiation towards osteogenic lineage: 195

5.2-The effect of extracorporeal shockwaves (ESW) on MSCs proliferation and differentiation 196

5.2.1-The effect of focused vs radial ESW on Ad-MSCs (direct application) 196

5.2.2- The effect of focused ESW on Ad-MSCs (designed water bath *in vitro* testing apparatus): 196

5.3- Bone graft substitute biomaterials (scaffolds) fabrication and *in vitro* characterisation: 197

5.3.1-Confirmation of donor cells elimination: 197

5.3.2- Mineralisation status 198

5.3.3-Cytocompatibility: 198

5.3.4 - Osteoinductivity: 198

5.3.5- Microstructure: 199

5.3.6- Biomechanical properties: 200

5.4- Testing the local biological effect of the selected biomaterials (scaffolds) after implantation (rat subcutaneous implantation preclinical model): 201

5.5- Evaluation of the ability to support bone healing in a critical size segmental long bone defect: 202

5.5.1-In-Life animal outcomes: 203

5.5.2-Post-mortem outcomes: 203

6- Conclusion: 207

6.1-Adipose derived Mesenchymal Stem cells (Ad-MSCs) isolation and characterisation. 207

6.2- The effect of extracorporeal shockwaves (ESW) on MSCs proliferation and differentiation 207

6.3- Scaffolds fabrication (3D printing) and *in vitro* characterisation.....207

6.4 – *In vivo* biocompatibility testing: rat subcutaneous implantation model 208

6.5- *In vivo* bone defect repair: rabbit radius segmental bone defect study.....208

6.6-Decision on hypotheses testing: 209

6.7- Summary Statement: 210

7-References 212

Acknowledgment.....274

Appendices 277

List of Figures

Figure 1: Thesis experimental themes 7
Figure 2: Bone Tissue Composition 10
Figure 3: Stages of fracture healing. 15
Figure 4: Classification of fracture non-union 18
Figure 5: The tissue engineering triad 39
Figure 6: Outlines the minimal criteria for defining multipotent mesenchymal stem (stromal) cells, as per the International Society for Cellular Therapy (ISCT) position statement [445]. 40
Figure 7: General functional and design characteristics of tissue engineering bioreactors..... 46
Figure 8: Adipose derived mesenchymal stem cell isolation steps. 62
Figure 9: Plate setup for MTT assay post ESW treatment (direct shocks application). The setup was replicated for day 1,3 and 7 post-treatment. 79
Figure 10: Plate set up for alizarin red S staining post ESW treatment (direct shocks application). 80
Figure 11: *In vitro* experimental setting to test the effect of ESW on Ad-MSCs proliferation and osteogenic differentiation. 81
Figure 12: Plate setup for MTT assay post ESW treatment (water bath setup). The setup was replicated for day 1,3 and 7 post-treatment 82
Figure 13: Plate set up for alizarin red staining post ESW treatment (water bath setup)..... 83
Figure 14: Decellularised bone matrix preparation, bio-ink synthesis and 3D printing. DCM (A), TCP (B), PCL (C). 86
Figure 15: Typical load-displacement curve (mechanical properties) for (A)DCBM scaffolds, (B) TCP scaffolds, and (C) PCL scaffolds. 92
Figure 16: Typical stress strain curve (material properties) for (A) DCBM scaffolds, (B) TCP scaffolds, (C) PCL scaffolds..... 92
Figure 17: *In vivo* biocompatibility experimental design outline..... 97
Figure 18: Surgical implantation of test biomaterials (scaffolds) subcutaneously in rat. 97
Figure 19: Histological processing of tissue specimens 98
Figure 20: 3D slicer software interface showing the colour coded segmented bone 3D model. 103
Figure 21: Flow diagram demonstrates the steps for rabbit bone model segmentation out of CT scan. 104
Figure 22: Autodesk Mesh mixer software interface 105
Figure 23: Virtual osteotomy in preparation for implant/scaffold design. 105
Figure 24: Rabbit study outline. 107

Figure 25: Surgical prep-room procedures. 109
Figure 26: Operating room layout 112
Figure 27: Surgical instruments for the rabbit radial defect surgery. 115
Figure 28: Rabbit radius 15 mm bone defect A) empty defect B) defect after scaffold implantation. C) the osteotomised bone segment side to side to the 3D printed scaffold 116
Figure 29: Cadaveric practice surgery demonstrates the osteotomy guide (jig) positioning. 116
Figure 30: Rat Ad-MSCs growing on tissue culture plastic, imaged using inverted light microscope (4x original magnification; scale as indicated). 126
Figure 31: Inverted light microscope image of haematoxylin-stained ovine Ad-MSCs. 126
Figure 32: Immunofluorescent staining of Ad-MSCs. Beta-actin in the cytoskeleton was labelled with Alexa Fluor® 488/ FITC (green) and the nucleus counterstained with DAPI (blue). 127
Figure 33: Ad-MSCs populating the surface of glass coverslips and imaged using SEM. 128
Figure 34: Crystal violet stained Ad-MSCs colonies. 129
Figure 35: Ad-MSCs proliferation over time as determined by MTT assay. 129
Figure 36: Fold-increase in MTT absorbance over time for ovine, rabbit and rat MSCs. 130
Figure 37: Wound healing assay to evaluate Ad-MSCs migration ability. 131
Figure 38: Trilineage differentiation of ovine Ad-MSCs as demonstrated by positive special staining and stains quantification. 133
Figure 39: Trilineage differentiation of rabbit Ad-MSCs as demonstrated by positive special staining and stains quantification. 134
Figure 40: Trilineage differentiation of rat Ad-MSCs as demonstrated by positive special staining and stains quantification. 135
Figure 41: Immunophenotypic characteristics of ovine, rabbit and rat Ad-MSCs comparing the expression of CD90, CD105, CD44, CD45 and CD73 surface markers. 136
Figure 42: Changes in ALP activity at different time points for (ovine, rabbit and rat) Ad-MSCs grown at growth media (GM-red line) vs osteogenic differentiation media (DM- blue line), at day 3, 7, 14 and day 21 138
Figure 43: Changes in alizarin red stain concentration at different time points for (ovine, rabbit and rat) Ad-MSCs grown in growth media (GM) vs osteogenic differentiation media (DM), at week 1, 2 and 3. 139
Figure 44: Expression of osteogenesis marker genes in ovine Ad-MSCs cultured for 7, 14 and 21 days in differentiation media (DM). 140
Figure 45: Expression of osteogenesis marker genes in rabbit Ad-MSCs cultured for 7, 14 and 21 days in differentiation media (DM). 141

Figure 46: Expression of osteogenesis marker genes in rat Ad-MSCs cultured for 7, 14 and 21 days in differentiation media (DM). 141
Figure 47: SEM images (x1391), highlighting the morphological difference between undifferentiated MSC Vs MSC differentiating towards osteogenic lineage (osteoblast-like cell). 142
Figure 48: The effect of focused and radial shockwave treatment on ovine Ad-MSCs proliferation at day 1 (A), day 3 (B), day 7 (C) post-treatment 144
Figure 49: Quantification of Alizarin red stain in control and shock wave treated ovine Ad-MSCs. 145
Figure 50: Effect of ESW treatment using in vitro water bath treatment setting on ovine Ad-MSCs proliferation. 146
Figure 51: Effect of ESW treatment using *in vitro* water bath treatment setting on ovine Ad-MSCs osteogenic differentiation as indicated by alizarin red stain quantification. 147
Figure 52: DNA quantification of unprocessed bone vs DCBM using a Pico green assay. .. 148
Figure 53: H&E (A,B) and DAPI staining (C,D) of unprocessed bone (A and C) vs Decellularised bone matrix DCBM (B and D) confirming absence of bone marrow (*) and cellular elements (osteocytes-black arrow) following decellularisation. 149
Figure 54: Cytocompatibility of cell seeded scaffolds. 150
Figure 55: Effects of scaffold material composition on the expression of osteogenic marker genes. 151
Figure 56: Alizarin red staining and quantification of the 3 scaffolds groups. 151
Figure 57: SEM images of the 3 scaffolds groups. 152
Figure 58: Representative photographs of the gross pathology findings. 159
Figure 59: Local biological effect 8 weeks post-implantation of DCBM based scaffolds. Original magnifications x4 (A), x10 (B and C), and x40 (D). 160
Figure 60: Local biological effect 8 weeks post-implantation of TCP based scaffolds. Original magnifications x4 (A), x10 (B), x20 (C) and x40 (D). 161
Figure 61: Local biological effect 8 weeks post-implantation of PCL scaffolds. 162
Figure 62: Local biological effect 8 weeks post-implantation of polyethylene (PE) control implants. Original magnifications x4 (A), x10 (B), x20 (C) and x40 (D). 163
Figure 63: Radiographs showing implant displacement 2 weeks post-operatively (ARI-321075-DCBM) A) Anterio-Posterior (AP) view, and B) Medio-lateral (ML) view. 166
Figure 64: Skin complication (skin necrosis and sloughing) necessitated culling of one animal (rabbit M00714530 (3864)-DCBM), A) on 15/2/2022, and B) on 28/2/2022 (the date of culling). 166

Figure 65: Ulcer on the sole of the foot that quickly complicated into gangrenous lesion (rabbit M00714492 (3870)-PCL.....167
Figure 66: Radiographs showing implant displacement 12 weeks post-operatively (rabbit M00714493 (3744)-DCBM) A) Anterio-Posterior (AP) view, and B) Medio-lateral (ML) view. 167
Figure 67: Implant displacement 12 weeks post-operatively (M00714483 (3854)-Cambridge-PCL). 168
Figure 68: An example radiographs series taken every 2 weeks from day 0 to week 12 of a rabbit received a DCBM scaffold (rabbit ID: Cambridge M00714484 (3755) DCBM).....169
Figure 69: Implant displacement in 2 of the animals received DCBM scaffolds (A to C: Cambridge M00754120 (K47261) and D to F: ARI 321073). 170
Figure 70: An example radiographs series taken every 2 weeks from day 0 to week 12 of a rabbit received a TCP scaffold (rabbit ID: ARI_ 321074_TCP).....172
Figure 71: Accidental partial osteotomy of the ulna at the level of the distal osteotomy cut directly after surgery (A) that healed by the time for the 2 weeks follow-up radiographs (B). Rabbit ID (ARI_321072_TCP). 173
Figure 72: Osteointegration at the level of the proximal and distal osteotomy cuts 4 weeks post-operatively (Cambridge, M00754118 (K67332)-TCP). 173
Figure 73: An example radiographs series taken every 2 weeks from day 0 to week 12 of a rabbit received a PCL scaffold (rabbit ID: Cambridge- M00714487 (3877)-PCL). 174
Figure 74: Osteointegration within PCL scaffold following the scaffold's unique porosity pattern. A) day 0 B) week 12 post operatively. (Rabbit ID: ARI-321077-PCL). 175
Figure 75: Bone fluorochrome labelling acquired using Nikon AxR (iT2 eclipse) inverted confocal Microscope and processed using Nikon-NIS element AR 5.41.01 software.....177
Figure 76: Undecalcified bone section with DCBM implant. 181
Figure 77: Undecalcified bone section with TCP implant. 182
Figure 78: Undecalcified bone section with PCL implant. 183
Figure 79: H&E stained decalcified bone section corresponding to specimen ID: Cambridge M00714493 (3744) - DCBM (culled at week 12 postoperatively due to implant displacement). 185
Figure 80: H&E stained decalcified bone section corresponding to specimen ID: ARI-321075 - DCBM (culled at 1 week postoperatively due to implant displacement). 186
Figure 81: H&E stained decalcified bone section from corresponding to Specimen ID: Cambridge- M00714530 (3864) - TCP (culled at 6 weeks postoperatively due wound complications). 186

Figure 82: H&E stained decalcified bone section corresponding to specimen ID: Cambridge-M00714483 (3854) -PCL (culled at 12 weeks postoperatively due implant displacement). .187
Figure 83: Representative reconstructed 3D models out of μ-CT scans of rabbit's antebrachium from the DCBM group (week 12 after surgery)- rabbit ID Cambridge-M00714491(3703)-DCBM). 188
Figure 84: Representative reconstructed 3D models out of μ-CT scans from of rabbit's antebrachia from TCP group (week 12 after surgery)- post-mortem (week 12 after surgery)- rabbit ID (Cambridge – M00714485 (38537)-TCP). 189
Figure 85: Representative reconstructed 3D models out of μ-CT scans from of rabbit's antebrachia from the PCL group, post-mortem (week 12 after surgery)- rabbit ID (Cambridge-M00714490 (3849)-PCL). 190
Figure 86: Axial plane micro-CT slices (rabbit ID-Cambridge- M00714531(3833)-DCBM group) showing: A) osteointegration at the level of proximal osteotomy (asterisk). B) soft tissue-like ingrowth within the scaffold's pores (most likely, fibrous tissue). 191
Figure 87: Axial plane micro-CT slices (rabbit ID-Cambridge- M00714532 (3743)-TCP group) showing: A) osteointegration at the level of proximal osteotomy (asterisk). B) bone ingrowth within the scaffold's pores. 191
Figure 88: Axial plane micro-CT slices (rabbit ID-Cambridge- M00714490 (3849)-PCL group) showing: A) osteointegration at the level of proximal osteotomy (asterisk). B) bone ingrowth within the scaffold's pores. 192

List of Tables

Table 1: Classification of factors leading to fracture non-union. 17
Table 2: Advantages and disadvantages of the different forms of bone graft 26
Table 3: Essential definitions related to bone healing. 27
Table 4: Evolution of biomaterials 35
Table 5: Comparison between TCP, HA and BCP 37
Table 6: The applications, advantages, and disadvantages of different post decellularisation processing 38
Table 7: Traceable evidences of MSCs osteogenic differentiation: 42
Table 8: Approved products for clinical use with osteogenic enhancing growth factors 44
Table 9: Types of bioreactors used for bone tissue engineering. 47
Table 10: ISO 10993-1 list of evaluation tests to be performed based on the area of contact between the medical device and the patient. 51
Table 11: Pros and cons of preclinical animal models in orthopaedic research: 55
Table 12: 3D printing technologies for medical applications 60
Table 13: Beta-Actin immunofluorescence staining for Ad-MSCs: 65
Table 14: Stains used to investigate trilineage differentiation of Ad-MSCs. 68
Table 15: Antibodies used for immunophenotypic characterisation of ovine Ad-MSCs. 70
Table 16: Antibodies used for immunophenotypic characterisation of rabbit Ad-MSCs. 71
Table 17: Antibodies used for immunophenotypic characterisation of rat Ad-MSCs. 72
Table 18: Staining plan for immunophenotypic analysis of ovine MSCs 72
Table 19: Staining plan for immunophenotypic analysis of rabbit MSCs. 73
Table 20: Staining plan for immunophenotypic analysis of rat MSCs 73
Table 21: Primers design for ovine Ad-MSCs qPCR. 77
Table 22: Primers design for rabbit Ad-MSCs qPCR. 77
Table 23: Primers design for rat Ad-MSCs qPCR. 78
Table 24: Shockwave treatment frequencies used in the study. 79
Table 25: Shockwave treatment groups (water bath *in vitro* testing apparatus). 82
Table 26: Bovine cancellous bone decellularisation steps. 85
Table 27: Primers design for qRT-PCR to evaluate scaffolds osteoinductivity. 90
Table 28: Local biological effect after implantation scoring system 99
Table 29: Material's bio-absorption scoring system 100
Table 30: Bio-irritancy and biodegradability score calculation and results interpretation. 101
Table 31: List of anaesthetic and analgesic drugs used for the rabbit study, its doses and commercial brand names. 110

Table 32: Rabbits post-operative scoring system. 118
Table 33: Fluorochrome labels injection time points and doses. 119
Table 34: Filters setting for the bone fluorochromes labels imaging. 122
Table 35: histopathology scoring system for undecalcified bone sections. 124
Table 36: Ad-MSCs quantified proliferation (absorbance at 570 nm) over time 130
Table 37: Scratch wound assay area measurements. 130
Table 38: The expression pattern of cell surface markers for Ad-MSCs isolated from sheep (ovine), rabbit and rat. 132
Table 39: Fold increase in the level of osteogenic markers genes at different time points for Ad-MSCs cultured in osteogenic differentiation media. 140
Table 40: The results from the Kolmogorov Smirnov test of normality for ESW treated cultures. 143
Table 41: Scaffolds microstructure morphometric parameters as indicated by micro-CT analysis. 153
Table 42: Comparison of the mechanical and material properties of the tested scaffolds. 154
Table 43: Local biological effect after implantation and biodegradation for DCBM Scaffolds. 156
Table 44: Local biological effect after implantation and biodegradation for TCP scaffolds:. 157
Table 45: Local biological effect after implantation and biodegradation for PCL Scaffolds. 158
Table 46: Collective histological scoring of the local biological effect after implantation and biodegradation for the 3 materials. 159
Table 47: Unplanned culling in the rabbit bone defect study. 165
Table 48: Fluorochrome labels quantitative analysis. 178
Table 49: Summary of the microscopic morphological changes in the 3 tested bio-materials groups at week 12 after implantation in rabbits' 15 mm radius defect. 179
Table 50: Histological findings from the decalcified bone sections. 184

List of abbreviations

ΔCt= Delta cycle threshold

µ-CT= Micro Computed Tomography

3D = Three dimensional

AAALAC = Association for Assessment and Accreditation of Laboratory Animal Care

Ad-MSCs = Adipose derived Mesenchymal Stem Cells

ALP = Alkaline phosphatase

AMP= Amino-methyl-1-propanol

AO= Arbeitsgemeinschaft für osteosynthesefragen

AP =Anterio-posterior

ARI = AO Research Institute

ARS= Alizarin red S Stain

ASTM = American Society for Testing and Materials

BCP= Biphasic calcium phosphate

BMP= Bone Morphogenic Protein

BSA= Bovine serum albumin

CAD =Computer-aided design

Cat. No.= Catalogue Number

CE = Conformité Européene

COL I= Collagen type I

CPC= Calcium Phosphate Ceramics

CPT= Current Procedural Terminology

CT =Computed tomography

DAPI = 4′,6-diamidino-2-phenylindole

DCBM = Decellularised bone matrix

DICOM = Digital Imaging and Communications in Medicine

DMBM= Demineralised bone matrix

DMEM = Dulbecco's Modified Eagle Medium

DMLS = Direct metal laser sintering

DMSO= Dimethyl sulfoxide

DNA= Deoxyribonucleic acid

DW = Distilled water

EBM = Electron beam melting

ECM = Extra Cellular Matrix

EDTA = Ethylenediaminetetraacetic acid

ESW =Extracorporeal Shockwaves

ESWT= Extracorporeal Shockwaves Therapy

FBS = Foetal Bovine Serum

FDA= Food and Drug Administration

FDM = Fused Deposition Modelling

FGF= Fibroblasts Growth Factor

FPS = Frame Per Second

FRI= Fracture related infection

GAPDH = Glyceraldehyde-3-phosphate dehydrogenase

GF = Growth Factor

H&E = Haematoxylin and eosin

H0= Null hypothesis

HA = Hydroxyapatite

Ha= Alternative Hypothesis

HMDS = Hexamethyldisilane

IM = Intramuscular

IMN= Intramedullary nailing

ISCT = International Society for Cellular Therapy

ISO= International Organization for Standardization

IV = Intravenous

IVC =Individually Ventilated Cages

Kg = Kilogram

KV = Kilovolt

LTD =Limited liability

mA = Milliampere

mAs = Milliampere second

MEKP = Methyl Ethyl Ketone Peroxide

mg= Micro-gram

mJ = micro joules

ML = Medio-Lateral

mM= milli mole

mm= millimetre

MPa= Megapascals

MRI = Magnetic Resonance Imaging

MSCs = Mesenchymal Stem Cells

MTT = 3-(4,5-dimethylthiazol-2-yl)-2,5-diphenyl-2H-tetrazolium bromide

N= Newton (1N = 0.10197 kg)

ng = Nano-gram

nM= Nano mole

NPP= Nitrophenyl phosphate

Ns= Newton second

OC= Osteocalcin

ON=Osteonectin

OPN = Osteopontin

PBS = Phosphate Buffer saline

PCL= Polycaprolactone

PCR= Polymerase chain reaction

PDGF= Platelet derived growth factors

PEEK = Poly ether ether ketone ketone

Pen-Strep =Penicillin/Streptomycin

PGA = Polyglycolide

PJI= Periprosthetic joint infection

PLA = Polylactic acid

PMMA= Polymethyl methacrylate

PRP = Platelet-rich plasma

PU= Polyurethan

qPCR= Quantitative polymerase chain reaction

RBCs = Red Blood Cells

RNA= Ribonucleic acid

RUNX= Runt-related transcription factor

SC or S/C = Subcutaneous

SEM = Scanning electron Microscopy

SLA = Stereolithography

SLM = Selective laser melting

SLS = Selective laser sintering

STL= Standard Tessellation Language

SVF = Stromal vascular fraction

TCP = Tricalcium Phosphate

TE= Tissue engineering

TGFβ = Transforming growth factors beta

UK = United Kingdom

Chapter 1: Introduction

1-Introduction

1.1-Study background:

Millions of patients suffer from challenging and non-healing bone defects each year. As a result, there is a growing, unmet need for biomaterials that can support bone regeneration and act as a substitute for bone grafts. Although autologous bone grafts ("autografts") are considered the standard of care for replacing bone, they have several significant limitations including donor site morbidity, risk of iatrogenic fractures, a physical limit to the bone volume that can be harvested and poor quality bone grafts in elderly patients, heavy smokers and patients undergoing long-term corticosteroids treatment [1-4]. Although allogeneic bone grafts overcome some of the limitations associated with autografts, they pose their own limitations, such as high cost, poor osteointegration, host immunogenic response and potential disease transmission [5-8].

Emerging from the unmet needs of patients with non-healing bone defects and the limitations associated with the current bone grafting procedures, the demand for synthetic bone graft substitutes has significantly increased over the past few decades. For dental and maxillofacial applications alone, the global bone graft substitutes market size was estimated at $719.1 million in 2021 and is expected to reach $1.3716 billion by 2028 [9, 10]. When the demand for bone graft substitutes in general orthopaedics, foot and ankle and spine surgery fields is factored in, the substitutes market size was valued at $ 2.91 billion in 2021 and is expected to reach $4.94 billion by 2030 [11]. However, these commercially available, off-the-shelf bone graft substitutes assume that one size fits all, which is not the case when dealing with complex bone reconstruction surgeries (post-trauma, post-cancer resection or congenital anomalies), where the surgeons are facing individually unique bone defects (anatomically, mechanically and functionally). In addition, most available bone substitutes do not offer stability and predictability as they only solve the bone defect problem. Yet, they do not address the primary aetiology that led to the non-healing bone defect in the first place. There is an urgent need for a cost-efficient, customisable solution for repairing these bone defects in both humans and animals.

Additive manufacturing technologies (3D printing and bio-printing) are revolutionising medicine and the manufacturing of anatomical models, surgical instruments, guides, and custom (“patient-specific”) implants. A number of research groups are actively exploring

ways to leverage the technical flexibility of 3D printing to allow for the fabrication of anatomically precise and mechanically optimised novel implants using either synthetic materials (e.g. polymers), natural materials (e.g. bio-ceramics and bone matrix derivatives) or combinations of synthetic and natural materials [12-14].

Fracture healing has been described as a race between bone union and implant failure; in the context of non-healing bone defects, the goal is to provide an implant that is mechanically robust, patient-specific (customisable) that provides an optimised environment for new bone formation by endogenous or exogenous cell sources [15]. Ideally, this scaffold will integrate with the native bone (osteointegration), support bridging of the defect gap (osteoconductive) and induce new bone formation (osteoinductive). If the material is resorbable, it should resorb at a rate that is well matched to the rate of new bone formation so that there is no risk of implant (or graft) failure before union occurs [16-18].

Bone graft substitute biomaterials (scaffolds) derived from animal sources, particularly food chain animals such as cows and pigs, have a track record of success in dental and orthopaedic applications. Its unique extracellular matrix and residual growth factors render it a good fit for the purpose of guided tissue healing. Additionally, tissues from food animals are abundantly available as a by-product of food production and are easily (and inexpensively) sourced from abattoirs. When processed correctly, they are safe, non-immunogenic and eliminates the risk of human disease transmission associated with allogenic grafts [11, 12, 19]. A number of these xenograft products are already on the market (such as Bio-Oss® and Nova Bone®), but they are most often supplied as blocks, putty, paste or granules for dental applications; none of these formulations match the geometric or mechanical complexities needed for patients undergoing bone reconstructive surgeries after trauma, cancer resection surgeries or as part of a corrective procedure (e.g. angular limb correction, bone lengthening procedures).

Combining the biological advantages of using animal-derived biomaterial as a base and the technological advantages of using 3D printing, we have developed a 3D printed bovine decellularised bone matrix (DCBM) based scaffolds aiming to provide a biocompatible, mechanically robust bone graft substitute that can be customised to patients' specific needs. Several other research groups have experimented with providing DCBM in a 3D printable form [13, 20, 21]; however, to the best of our knowledge, the highest successfully printed percentage of DCBM is 70 % of the final total volume of the scaffolds [21]. We have successfully printed scaffolds with 85 % DCBM content using 15 % polycaprolactone (PCL as the polymeric matrix to facilitate the preparation of 3D printable bio-ink. The combination of DCBM with polycaprolactone (PCL), a material with a solid track record as a biologically

compatible resorbable polymer, offers real potential as a solution for patients with significant bone loss.

The majority of the work included in this thesis focuses on the development and characterisation of a novel 3D printed bovine decellularised bone matrix (DBM) based scaffolds. Individual sections focus on a detailed description of the manufacturing methodology we used to produce our scaffolds, alongside the systemic approach we followed to understand the structure, the biomechanical properties and the osteoinductivity of these novel scaffolds and above all to ensure the material's biosafety in both the *in vitro* and the *in vivo* settings (cytocompatibility and rat biocompatibility study respectively)- before moving forward towards testing these scaffolds as bone graft substitutes in a long bone critical size bone defect preclinical model (in our case, a 15 mm segmental defect in rabbit radius).

We used plain PCL as negative control and tricalcium phosphate (TCP) based scaffolds as positive control for all the *in vitro* assays and the rabbit bone defect *in vivo* study. TCP has a well-established record as a bio-ceramic in the field of bone tissue engineering [22-24], and our collaborator from the University of Rochester has an established research record successfully working with TCP (particularly α-TCP) for multiple potential orthopaedic applications, including bone tissue engineering [15, 25-27]. Hence, the choice to use it as a positive control. For the rat study to evaluate the materials' *in vivo* biocompatibility, we have used commercially provided medical implant-grade polyethylene discs (provided by BioMedtrix) as a bio-inert control for comparison.

This new composite and the fact that it is 3D printable offers a tremendous potential solution for patients (and surgeons) undergoing complex bone reconstruction surgeries tailored to each patient's specific needs.

1.2- Study aims and research questions:

The goal of my work was to develop and characterise a 3D printed osteoinductive, biocompatible and mechanically robust biomaterial that can support bone healing for critical size bone defects and can be customised to individual patient's needs.

My overarching research question, namely whether a 3D printed decellularised bovine extracellular matrix-based scaffolds can be used to treat critical size bone defects, will be addressed by answering 5 fundamental research questions:

1. Can a composite of resorbable polymer and decellularised bone matrix (DCBM) be fabricated into a flowable formulation that is suitable for 3D printing? If so, what is the

maximum % of DCBM that can be used to achieve the maximum biological benefit while maintaining printability?

2. Are 3D-printed scaffolds made from this composite able to support the growth and osteogenic differentiation of mesenchymal stem cells *in vitro?*

3. What is the relationship between material composition, mechanical performance, and biological properties?

4. Do scaffolds fabricated from these materials evoke any adverse tissue response when implanted *in vivo*?

5. Will scaffolds fabricated from these materials support bone healing/ regeneration when implanted *in vivo*?

In addition to the core work focusing on the bone graft substitute aspect, I also performed an introductory discovery work focusing on the adipose derived mesenchymal stem cells (Ad-MSCS) isolation, characterisation and how they differentiate towards osteogenic lineage to better understand its potential use for bone tissue engineering applications. Alongside with a preliminary study to determine whether the proliferation and osteogenic differentiation of Ad-MSCs could be boosted by using clinically relevant doses of extracorporeal shock wave therapy (ESWT).

1.3- Study hypothesises:

The work in this thesis tests two core hypotheses:

- The alternative Hypothesis (Ha) are:

Ha #1: 3D-printed bovine DCBM-based scaffolds are biocompatible and capable of supporting bone repair through enhanced osteoconduction and / or osteoinduction.

Ha #2: The *in vitro and in vivo* performance of DCBM-based scaffolds is equivalent or superior to that of a control material (TCP or PCL).

- Hence, the null hypotheses (H0) are:

H0 #1: 3D-printed bovine DCBM-based scaffolds are non-biocompatible and incapable of supporting bone repair through enhanced osteoconduction and/or osteoinduction.

H0 #2: The *in vitro* and *in vivo* performance of DCBM-based scaffolds is inferior to that of a control material (TCP or PCL).

Additional secondary hypotheses

Ha #3: Mesenchymal stem cells isolated from adipose tissue (Ad-MSCs) are capable of differentiation towards the osteogenic lineage.

Ha #4: Extracorporeal shock wave therapy (ESWT) enhances bone healing through encouraging stem cell differentiation to osteoblast-like cells.

- Hence the null hypotheses are:

H0 #3: Mesenchymal stem cells isolated from adipose tissue (Ad-MSCs) are incapable of differentiating towards the osteogenic lineage.

H0 #4: Extracorporeal shock wave therapy (ESWT) does not enhance bone healing.

1.4- Study importance, relevance, and contribution to the scientific community:

The impact of my study resonates at 3 different yet interconnected levels.

The immediate/ short term - (Research):

My study offers a detailed methodology, establishing and validating several *in vitro* assays as well as (and most importantly) 2 preclinical (*in vivo*) animal models that benefit those who work in the field of orthopaedics research in general and those who are looking at developing and testing novel implantable biomaterials in particular. The first is a rat preclinical model to test biomaterials biocompatibility. The second is a rabbit preclinical model to test biomaterials performance in the context of critical size bone defects.

The development of standardised, cost-effective small animal models with measurable outcomes dramatically accelerates the pace of research and leads to significant breakthroughs in the field of orthopaedic research. We shared our findings by presenting the data at international meetings and conferences (ORS 2020 [28] and 2022 [29], EORS 2020 [30] and 2021 [31], ICORS 2022 congress [32]), a peer reviewed abstract was published in the Bone & Joint Journal in 2020 [30] and full peer reviewed manuscripts of the experimental results are in progress.

Hence, I am confident that my work will be a valuable reference that offers clear guidelines to be followed by researchers, scientists, and clinicians.

The medium term (Marketing):

In my project we optimised the 3D printing parameter for a novel DCBM based biomaterial as well as the TCP positive control and the PCL negative control. In addition to characterising the behaviour of these materials *in vitro* and *in vivo*, I believe that I will have the resources and expert opinions to move along the path of FDA approval, with the help of my established

collaboration with the AO Research Institute in Davos, Switzerland as well as the Preclinical Surgical Research Laboratory at Colorado State University and their good track record of helping to prepare medical devices for regulatory submission to the FDA, and other experts and industrial collaborators. I am hopeful, that this will offer a valuable addition to the growing market of bone graft substitutes.

My scaffolds / biomaterials can be modified in the future to deliver growth factors, antibiotics, antimicrobial and /or anticancer drugs locally to the bone defect site, which will broaden the horizon of its use, clinical applicability and further augment the concept of customisability (tailoring) to patients' specific needs. My established collaboration with the musculoskeletal tissue engineering (Awad) Lab at University of Rochester medical centre-NY, USA that allowed me to optimise the 3D printing parameters in the first place, as well as several potential industrial collaborators will provide me with the necessary expertise in bioengineering and material sciences that will help me to modify and improve my biomaterial performance.

The long term (Clinic/Patients):

The ultimate goal of my work is to offer patients undergoing complex bone reconstructive surgeries (and their surgeons) a customisable solution that can be tailored to each patient's specific needs. I believe that my work (even if not necessarily in its exact current format) can be of impact, through improving the clinical outcomes for patients with clinical presentations that are otherwise associated with a high risk of delayed or non-union, prolonged morbidity, and often the need for repeat surgery or even amputation. Ultimately, it will lead to improvement of patients' (humans and in animals) standard of care and quality of life.
Potential fields of applications include craniomaxillofacial, orthopaedic, and spine surgery.

1.5- Thesis outlines

The work included in this thesis is divided into four interconnected experimental themes that feed into the primary purpose of my work (developing and characterising / testing a bone graft substitute biomaterial), namely: **Adipose-derived Mesenchymal Stem cells** (Ad-MSCs) isolation and characterisation, **scaffolds** fabrication and *in vitro* characterisation, ***in vivo*** **biocompatibility testing** (a rat study) and ***in vivo*** **bone critical size defect healing study** (a rabbit study). See **Figure 1**.

The work included in this thesis is organised into seven chapters. The Introduction (Chapter 1) is followed by the literature review (Chapter 2), which frames the thesis plan in the context of what is already known and that defines the gap in knowledge that this thesis seeks to address. Methodology (Chapter 3) details the materials and methods used in each experimental theme outlined in Figure 1. The results (Chapter 4) details the key experimental findings from this work, leading to a systematic discussion (Chapter 5) of what has been learned. Chapter 6 presents a high-level summary of the conclusions from the work, as well as addressing some unanswered questions for future work. The last chapter of the thesis (Chapter 7) presents a consolidated list of references cited within the thesis.

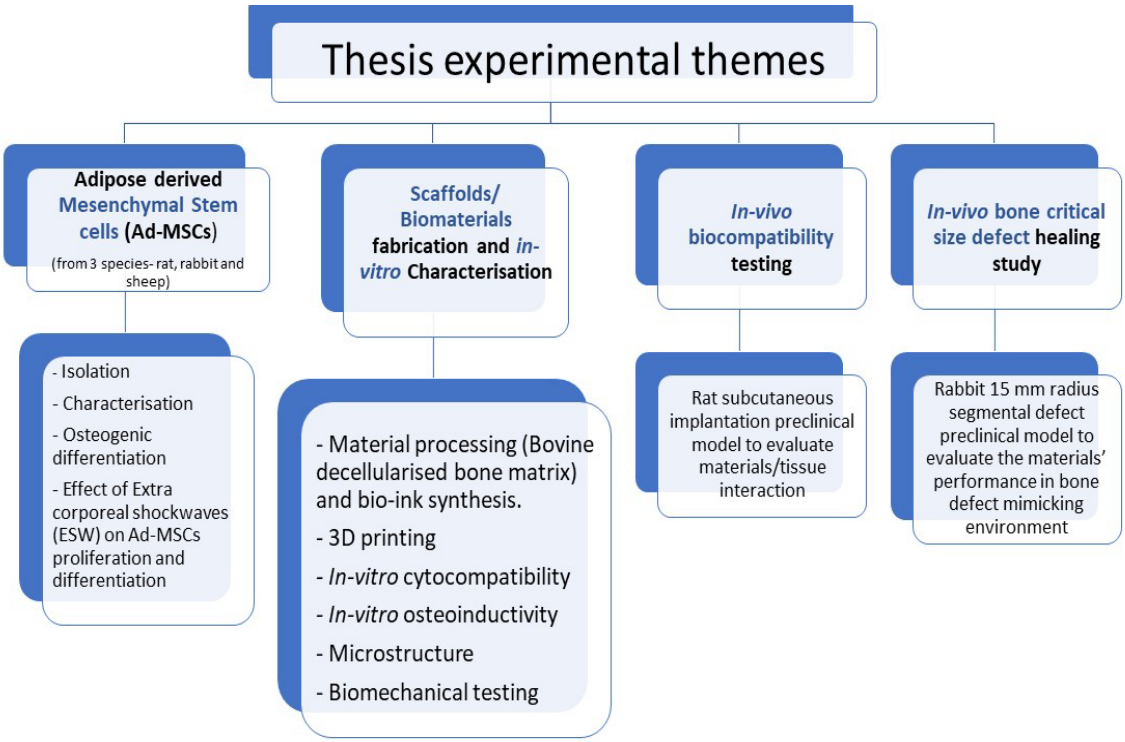


Figure 1: Thesis experimental themes

Chapter 2: Literature Review

2- Literature Review

Under ideal circumstances, bone has an enormous innate self-healing ability. Hence, after being injured (fractured), the bone can regenerate with new vascularised tissue that is almost indistinguishable from the original bone microscopically and macroscopically. However, for millions of patients, this innate healing ability is challenged in the face of extensive trauma, cancer resection surgery, post osteomyelitis debridement, congenital anomalies or due to compromised biology associated with metabolic disorders (e.g., diabetes), long-term medication (e.g., long-term steroids use), heavy smoking and alcohol consumption leading to fracture non-union or bone defects that will not heal spontaneously without additional intervention within the lifetime of the patient (or within the duration of the experiment). In an experimental setting, these non-healing defects are known as critical-size bone defects [33, 34]. Bone grafting (particularly autologous bone grafts) has long been the gold standard of care for managing fracture non-union and bone defects; however, both autografts and allografts are associated with several drawbacks and limitations, that stimulated research investigating the development of bone graft substitutes and tissue engineering themed solutions to promote/facilitate bone healing in such challenging defects.

In this chapter, I will lay the foundation for my work by reviewing the literature on topics of fracture healing, fracture non-union, critical size bone defects, bone grafts and bone graft substitutes, how tissue engineering research addresses critical size bone defects, including the potential use of physical stimuli such as extracorporeal shockwaves therapy to enhance bone healing, what preclinical animal models are most relevant and finally advances in biomaterials and medical implants manufacturing that allows for the development of customisable, patient-specific implants.

2.1- Bone structure, fracture healing and bone formation:

2.1.1- Bone structure:

At the tissue level, bone is composed of **65% mineral** (predominantly carbonated apatite), **25% organic components** (22.5% collagen (predominately collagen type I with a small amount of Collagen type III and V), 2.5 % non-collagenous proteins (bone cells and extracellular matrix proteins) and **10% water** [35] (See **Figure 2)**. At the cellular level, there are three main types of bone cells: osteoclasts, osteoblasts and osteocytes. Osteoclasts are the primary cells responsible for bone resorption, and they originate from the hematopoietic precursor cell lineage and compromise 1 to 3 % of total bone cells [36, 37]. Osteoblasts are

the primary cells responsible for bone formation, and they originate from the mesenchymal progenitor cells lineage comprising 4 to 6 % of the total resident bone cells [36, 38]. Osteocytes are former osteoblasts entrapped within the mineralised bone matrix during the bone deposition process. They form a network that senses mechanical and hormonal environmental cues and orchestrate the function of osteoblasts and osteoclasts. Osteocytes make up between 90 to 95 % of the cellular component in skeletally mature adult bone tissue [39, 40].

Throughout life, bone undergoes continuous modelling and remodelling (also known as bone turnover) which is dependent on the ability of bone cells to resorb and form bone in the right places and at the right time in order to strike the balance between bone resorption and deposition [39, 41, 42]. Normal bone remodelling is necessary for fracture healing, skeletal mechanical adaptation and bone structural integrity, as well as for calcium homeostasis [43, 44].

The organisation of bone structure varies between cortical (compact) and cancellous (spongy) bone. Briefly, cortical bone consists of tightly packed osteons (the Haversian system) which are cylindrical structures composed of concentric layers of bone tissue called lamellae that surround a central canal (Haversian canal). The spaces between the lamellae are called lacunae and are where osteocytes reside [45]. Cancellous bone consists of trabeculae which form a lattice-like structure containing irregularly arranged lamellae forming interconnected cavities filled with red bone marrow [46]. Cancellous bone trabeculae are organised to provide maximum strength; in fact the orientation of the trabeculae follow the lines of stress on the bone, which is known as Wolff's law (law of remodelling) that states that the internal trabecular bone adapts to external loadings, reorienting with the principal stress trajectories to maximise mechanical efficiency and creating a naturally optimum structure [47, 48].

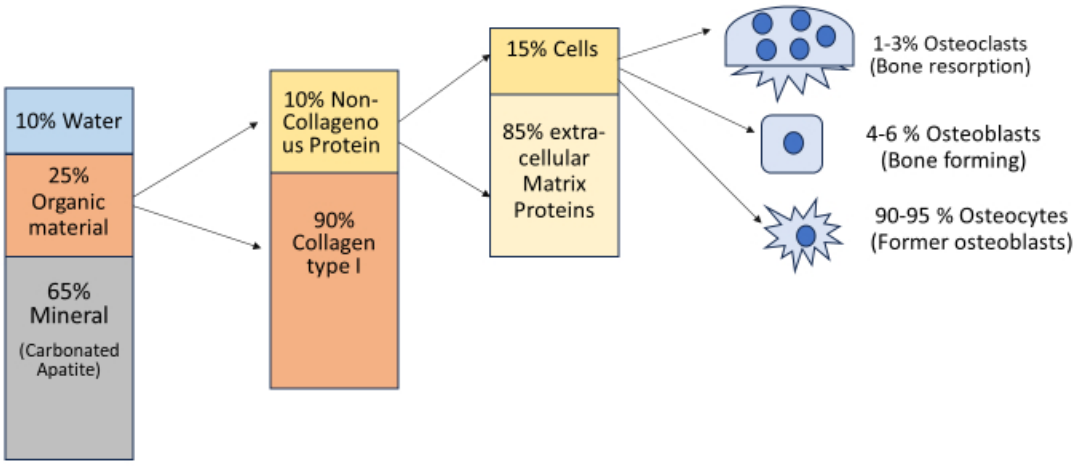


Figure 2: Bone Tissue Composition

Bone is composed of 65% inorganic (minerals mostly carbonated apatite), 25% organic matrix (collagen type I and non-collagenous proteins) and 10% water.

2.1.2- Fracture healing:

The way fractures heal depends on the mechanical environment at the fracture site and can be classified into two main healing pathways. **Primary (also known as direct or intramembranous) bone healing** is achieved when there is absolute stability (minimal interfragmentary motion and no interfragmentary gap), as found in case of anatomical reduction and rigid internal fixation where the strain between the fracture fragments is less than 2%. **Secondary (also known as indirect or endochondral) bone healing** occurs when there is controlled movement between the bone fragments (mainly axial micromotion) and controlled interfragmentary space (less than 2 mm), as is the case with closed fracture reduction and non-rigid bone fixation by intramedullary nailing, external fixators and external non-surgical bone fixation using a splint or cast where the strain between the fracture fragments is ideally maintained between 2 – 10 % [49-54].

Primary fracture healing involves a direct attempt by the cortex to re-establish continuity between the bone fragments via intramembranous ossification, a process during which the osteoblast progenitor cells lining the periosteum (the periosteal mesenchymal stem cells) differentiate into osteoblasts that lay down osteoid on the exposed bone surfaces and directly synthesise new bone matrix on the bone surface without first forming cartilage. New Haversian systems will then be reestablished through intracortical remodelling [51, 55]. In other words, primary fracture healing is achieved mainly through the direct conversion of mesenchymal stem cells into woven bone, followed by bone remodelling.

Secondary fracture healing is considered as a series of four sequential yet overlapping stages that involve a response of the periosteum and the surrounding soft tissues at the fracture site. These stage are: Inflammation (haematoma formation), soft callus (fibrocartilage) formation, hard callus formation and finally bone remodelling [44, 51] (See **Figure 3**). However, it's important to understand that the progression through these four stages is not always linear, and there can be an overlap. The specific timeframes and outcomes vary based on factors such as the type of fracture, the individual's age, overall health, and the fracture fixation method and robustness. Additionally, in real-life (clinical) scenarios, the distinction between primary and secondary fracture healing is not always clear-cut. There is plenty of overlap, and the healing process can involve a combination of both mechanisms [54].

Stage 1- Inflammation (Haematoma formation):

The traumatic injury of the bone leading to bone fracture results in disruption of the blood vessels at the fracture site leading to bleeding followed by haematoma formation. The newly formed haematoma is rich in progenitor cells, helps with temporary fracture stabilisation, provides a framework (scaffold) for subsequent tissue healing, and initiates the inflammatory response. Degranulated platelets, macrophages, and other inflammatory cells (granulocytes, lymphocytes, and monocytes) infiltrate the hematoma and release growth factors and cytokines (such as tumour necrosis factor-alpha, bone morphogenetic proteins, platelet-derived growth factors, transforming growth factor-beta, vascular endothelial growth factor and interleukins) into the fracture site [44, 54]. These factors facilitate the recruitment of additional inflammatory cells and the migration of mesenchymal stem cells (MSCs) from the periosteum, bone marrow, the circulation and surrounding soft tissues. [44, 51, 56].

Stage 2- Soft callus (fibrocartilage) formation:

Within a few days, newly formed blood vessels, together with mononuclear cells and fibroblasts, initiate the transformation of the haematoma into granulation tissue [53].

The MSCs recruited to the fracture site start to gradually differentiate into chondrocytes and synthesise cartilaginous matrix. The low oxygen tension at the fracture site favours chondrogenic differentiation. Where cartilage production is deficient, fibroblasts replace the region with fibrous tissue under the influence of growth factors (such as fibroblast growth factor-1, insulin-like growth factor and members of the bone morphogenic protein family) and the chondrocytes secrete collagen (type II) rich extracellular matrix. Eventually all the granulation tissue is replaced by fibrocartilage [44, 57].

The periosteum surrounding the fracture site thickens prior to undergoing chondrogenic transformation, producing an external callus vascularised by extraosseous blood vessels. The internal or medullary callus develops from the endosteal cell layer and is confined to the medullary canal and receives its blood supply from the medullary blood vessels. The presence of a fibrocartilage layer within the medullary canal temporarily interrupts the medullary blood flow across the fracture gap. Both the external and the internal calluses constitute the **bridging callus** [55, 58-60]. This soft callus acts as a scaffold for new bone tissue formation [51].

Stage 3- Hard callus formation (endochondral ossification):

This stage involves gradual removal of the soft callus fibrocartilage and its systematic replacement with woven bone [44, 61]. As the chondrocytes in the soft callus proliferate, they become hypertrophic, and they initiate the formation of mineralised clusters. Although the exact mechanism of this calcification remains unclear, it is thought that mitochondria in the fracture gap behave as they do in growth plates [55].

Chondroclasts migrate to the fracture site and gradually resorb the calcified cartilaginous matrix. Simultaneously, fibroblasts differentiate into osteoblasts guided by various bone morphogenic proteins and fibroblast growth factors at the fracture site. New blood vessels penetrate the tissue and recruit the perivascular MSCs that differentiate into bone-forming osteoblasts that begin to produce osteoid [61]. Sub-periosteal woven bone continues to be laid down [54, 62]. At the end of this phase, a hard, calcified callus of immature (woven) bone forms. In rat preclinical models, the peak of hard callus formation usually occurs around 14 days post-fracture, as indicated by callus volume as well as osteoblast markers, such as type I collagen, alkaline phosphatase (ALP), and osteocalcin [51, 63] .

Stage 4- Bone remodelling

Although the hard callus is a rigid structure providing biomechanical stability, it does not fully restore the biomechanical properties of normal bone. In order to achieve this, the fracture healing cascade initiates a second resorptive phase (also known as secondary bone formation), this time to remodel the hard callus from woven into a lamellar bone structure with a central medullary cavity [64]. The remodelling process is driven by a coupled process of orderly bone resorption followed by the formation of lamellar bone, which is orchestrated by the osteoclasts/osteoblasts' consecutive activities. The osteoclasts are the key cell types involved with the resorption of woven bone. To initiate remodelling, osteoclasts become

polarised and adhere to a mineralised surface. They form a ruffled border, which is sealed off and acid and proteinases are pumped into the resorption domain. The acid environment demineralises the matrix, while proteinases degrade the organic components, such as collagen. The degradation products are removed through a vesicular pathway from the ruffled border to the functional secretory domain, and the osteoclasts either undergo apoptosis or return to the non-resorbing form. Bone resorption by osteoclasts creates erosive pits on the bone surface known as "Howship's lacunae". Once completed, osteoblasts lay down new bone on the eroded surface [44, 65, 66]. Bassett et al. suggest that bone remodelling results from the production of electrical polarity created when pressure is applied in a crystalline environment. This is achieved when axial loading of long bones occurs, creating one electropositive convex surface and one electronegative concave surface, activating osteoclastic and osteoblastic activity, respectively. By these actions, the external callus is gradually replaced by a lamellar bone structure, whereas the internal callus remodelling re-establishes a medullar cavity characteristic of a diaphyseal bone [67].

A similar process happens during **osteointegration,** which is defined as the direct structural and functional connection between the living bone and surface of a load-bearing implant [68]. Osteointegration involves a cascade of cellular and extracellular biological events that take place at the bone-implant interface that are similar to those occurring during bone healing [69, 70]. The surgical implantation of bone implants opens blood vessels, leading to an initial inflammatory response and **blood clot (haematoma) formation**. That in turn attracts inflammatory cells (such as monocytes and macrophages) and releases cytokines and growth factors from degranulated blood platelets. The fibrin-rich matrix (the haematoma) is osteoconductive, as it acts as a scaffold for the recruited osteogenic progenitor cells (MSCs). The growth factors and cytokines are osteoinductive as they promote the mesenchymal stem cells osteogenic differentiation [69, 71]. Like primary bone healing, MSCs differentiate into osteoblasts that lay down osteoid forming woven bone at the implant/bone interface. The woven bone eventually remodels into lamellar bone in direct contact with most of the implant surface [69, 71, 72].

2.1.3- Bone formation (osteogenesis) at different anatomical locations:

From an embryo development perspective, there are three distinct lineages that generate the skeleton. The somites generate the axial skeleton, the lateral plate mesoderm generates the limb skeleton, and the cranial neural crest gives rise to the branchial arch and craniofacial bones and cartilage [73]. As explained above (section 2.1.2- Fracture healing), there are two

main pathways of bone formation (osteogenesis), and both involve the transformation of a preexisting mesenchymal tissue into bone tissue. The direct conversion of mesenchymal tissue into bone is called intramembranous ossification. In other cases, the mesenchymal cells differentiate into cartilage, and this cartilage is later replaced by bone. The process by which a cartilage intermediate is formed and replaced by bone cells is called endochondral ossification. This process occurs in the skeletal components of the vertebral column, the pelvis, and the limbs [73, 74].

Intramembranous ossification is the main type of bone formation in flat bones of the skull (calvarial bones and mandibles) and parts of the clavicles and scapulae, while endochondral ossification is the mechanism responsible for bone formation of all long bones of the axial skeleton (vertebrae and ribs) and the appendicular skeleton (limbs) [75, 76].

Several mechano-regulation theories have been developed to understand the impact of mechanical stimuli on bone healing / bone formation. According to these theories, the magnitude of mechanical stimuli such as mechanical stress (force per unit area) and strain (deformation in the material's shape resulting from the applied force) determines the bone formation pathway (either intramembranous ossification or endochondral ossification) [77-79]. These studies suggested that, under low mechanical stimulus magnitude, the MSCs differentiate directly into osteoblasts through the process of intramembranous ossification. Under moderate magnitude of mechanical stimuli (e.g. weight bearing and controlled interfragmentary movement), MSCs differentiate into chondrocytes through an endochondral ossification process [63, 80].

This correlates to the nature of mechanical loading at different anatomical locations, hence the bone formation (bone healing) pathway that is most likely to take place.

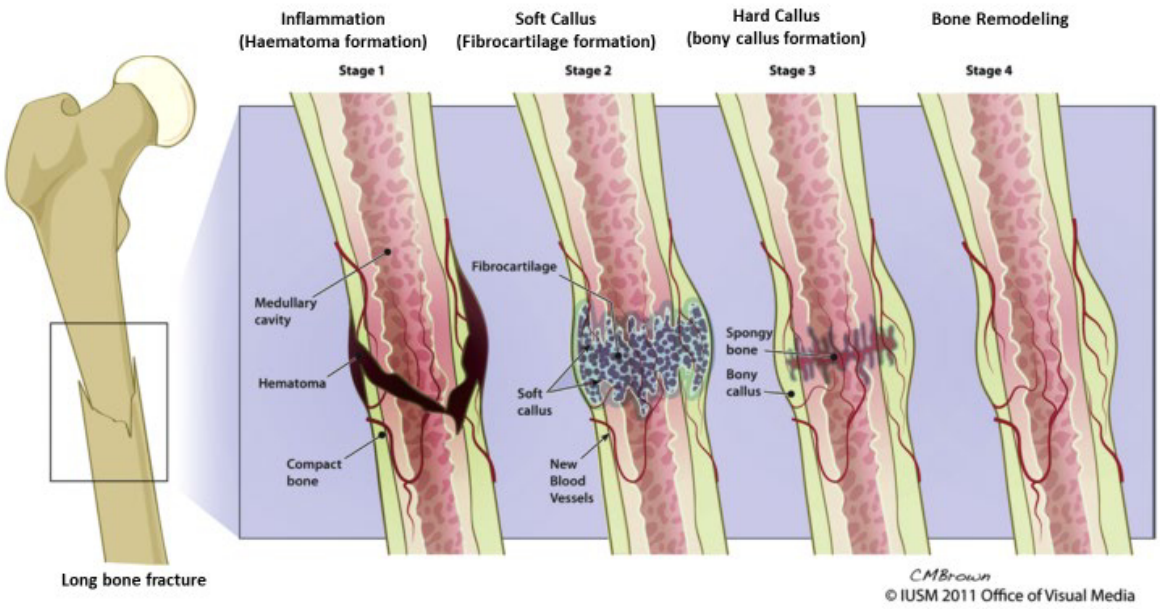


Figure 3: Stages of fracture healing.

Stage 1: following fracture or osteotomy bleeding occurs followed by haematoma formation.

Stage 2: Mesenchymal stem cells recruited to the fracture site start to gradually differentiate into chondrocytes and synthesise cartilaginous matrix (soft callus formation).

Stage 3: Hard callus formation via gradual removal of the soft callus fibrocartilage and its systematic replacement with woven bone.

Stage 4: Bone remodelling through the orchestrated activity of the osteoclasts/osteoblasts. Osteoclasts and osteoblasts facilitate the conversion of woven bone into lamellar bone eventually restoring the appropriate anatomical shape.

This illustrative diagram is courtesy of Li et al. (2019) [51].

2.2-Fracture non-union and critical-sized bone defects:

A fracture (or a bone gap) fails to heal when the healing phases (section 2.1.2) do not proceed efficiently due to the size and complexity of the defect and/or patient related risk factors.

2.2.1- Fracture non-union:

The number of fracture cases in the UK has been estimated to be 850,000 new fractures seen per annum [81]. 5 – 10 % of these fractures do not heal spontaneously and develop non-union, despite the best efforts of the healthcare team. The statistics are unavailable for animals; however, fracture non-union is a common problem in veterinary orthopaedics. A few published studies indicate that the incidence rate of fracture non-union in dogs is 4.6% [82] and 0.85% in cats [83].

Unlike delayed union (ununited fracture that shows progress in healing yet at a slower rate) [84, 85] and mal-union (a fracture that has healed but in a non-anatomical position) [84], where the fracture is anticipated to heal eventually, in case of non-union the bone will not heal without additional intervention [86]. There is actually no universally accepted definition of non-union in the orthopaedic literature [87]. According to the United States Food and Drug Administration (FDA), non-union has been defined as a fracture that occurred a minimum of nine months previously and has not shown radiographic signs of progression toward healing for three consecutive months [88, 89]. Other definitions indicate that the nine months since injury criterion cannot be used for every fracture and recommend that fracture non-union of long bones be recognised after a minimum of six months without any improvement toward union [17, 90].

Fracture non-union is one of the most disabling medical conditions affecting patient quality of life, physically and mentally, besides having a large economic impact on healthcare systems and society[91-94]. The cost to the National Health Service of treating non-union has been estimated to range between £7,000 and £79,000 per person [81, 95, 96]. The estimated cost for treating tibia non-union was £16,330, for the humerus £15,660 and for the femur £17,200 [97]. In the USA, the cost of treating a tibial shaft non-union was estimated to be 25,566 USD [98]. In Australia, one study reported a median inpatient hospital cost of 14,957 AUD per patient for fracture and fracture-related complications treatment [91].

Some bones are more likely to develop non-union due to biological, anatomical, or mechanical factors. For instance, the **tibia** is particularly prone to non-union, especially in cases of high-energy fractures, due to its weight-bearing nature and poor blood supply at the tibial subcutaneous border [99]; publications suggest that the tibia has the highest rate of non-union (5% and 15%) [100-102]. Furthermore, the occurrence of tibial shaft non-union in Europe is responsible for more than 80% of overall costs caused by tibial fractures [92]. The prevalence of tibial shaft delayed union or non-union reported in some of the literature reaches up to 54 % depending on type and grade of soft tissue injury and type of surgical intervention [103, 104].

Femur fracture non-union comes second in risk to tibia (1 - 11 %) due to its high susceptibility to complicated fractures with significant comminution and injury to the surrounding soft tissue [101, 105-107]. Followed by the humerus (0.3 – 10 % non-union rate) due to the difficulty in achieving fracture absolute stabilisation [108, 109]. Non-union occurs in 2 – 10 % of all **forearm** fractures [110]. Other examples of bone fractures with a high risk of developing non-union are navicular bone and proximal pole **scaphoid bone** fractures due

to poor blood supply to these areas [111, 112]. Yet non-union can occur in any other bone in the body. The statistics are not readily available for veterinary patients; however, published studies suggest that out of the reported fracture non-union cases in dogs, 60 % occur in the radius and ulna, and 25 % occur in the tibia [113, 114].

Causes leading to fracture non-union can be classified into mechanical, biological and patient related factors (**see Table 1**).Weber and Cech classified fracture non-union according to radiographic appearance and bone viability into viable (biologically active) non-unions and non-viable (biologically inactive) non-unions [115]. Viable non-union is primarily attributed to the mechanical instability of the fracture, while the callus and bone maintain good vascularisation, and it sub-classified into hypertrophic (elephant foot), slightly hypertrophic (horse hoof) and oligo trophic (see **Figure 4**). Non-viable non-union is primarily attributed to a poor fracture biological environment (particularly poor vascularisation), closed medullary canal (hence deficient bone marrow) or if the defect is too severe that it exceeds the body's innate healing ability. Non-viable non-union is subclassified into dystrophic (torsion wedge), necrotic, atrophic and defect type non-viable non-union [86, 115, 116] (**see Figure 4**).

Table 1: Classification of factors leading to fracture non-union.

Factors	**Explanation**
Mechanical	• Inadequate immobilisation or failure to maintain immobilisation for a sufficient length of time. [86, 144] • Inadequate fracture reduction.[145]
Biological, defect related	• Loss of blood supply [146] • Severe soft tissue trauma [147] • Excessive stripping or injury to the periosteum [148] • Severe comminution that requires extensive surgical intervention [149] • Infection [150, 151]
Patient related	• Smoking [152, 153] • Age [154, 155] • Gender [156, 157] • Alcohol [147, 158] • Diabetes [159, 160] • Steroid use [161, 162] • NSAID use[163, 164] • Compliance [165] • Species / breed (in veterinary orthopaedics) [166, 167]

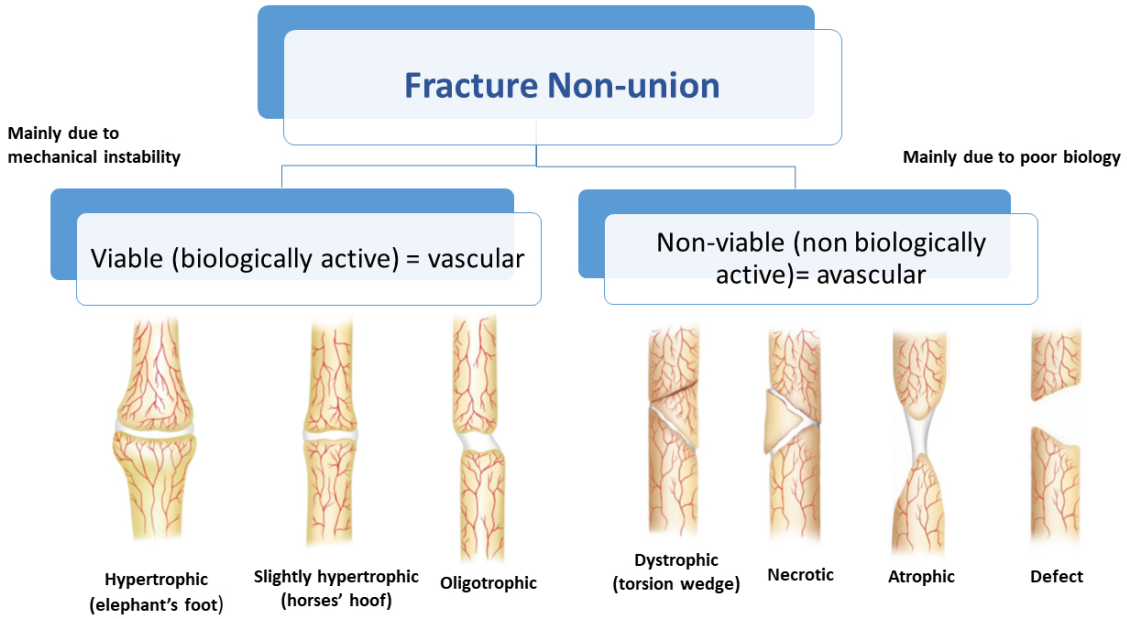


Figure 4: Classification of fracture non-union

This illustrative drawings are courtesy of Kocaoglu et al. (2016) [116].

Role of infection in non-union:

Infected non-unions pose significant challenges for complete resolution and functional restoration [117]. The clinical presentation of infection can be either acute with classical clinical signs (such as fever, local swelling, redness, pain, purulent drainage and wound dehiscence), laboratory markers (such as elevated C-reactive protein, erythrocytes sedimentation rate and/or white blood cells count); or it can be a low-grade (chronic) infection that lacks the classical clinical and laboratory indicators. The former is easy to diagnose yet difficult to treat, while the latter is difficult to diagnose and to treat [118, 119]. Published data in the context of orthopaedic infection is extensive on periprosthetic joint infection (PJI), but published consensus guidelines on diagnosis and treatment of fracture-related infection (FRI) are still lacking [118]. Although both are implant-related 'biofilm' infections, management strategies for PJI cannot be completely applied to patients with FRI. The main difference in the management of FRI is the fact that fracture fixation devices can be removed without loss of function after bone healing [120, 121]. Biofilm formation on the surface of a foreign material (such as a fixation device or bone implant) is crucial in the pathogenesis of FRI [122]. A biofilm is defined as a heterogenous, multicellular, complex three-dimensional bacterial community enclosed by exopolysaccharides-rich extracellular matrix [123]. The bacteria in the biofilm are in a stationary phase of growth and are metabolically less active. Due to this dormant state, these bacteria are more resistant to host immune defence and to

antibiotics [124, 125]. For this reason, the successful management of FRI requires a combination of surgical and antimicrobial treatment [122, 126].

The infection is introduced to the fracture site either during the trauma (for example, in open fractures), during surgery while inserting the fixation device or postoperatively in the hospital (nosocomial infection) or after patient discharge secondary to surgical wound complications [122, 127, 128]. Polymicrobial infections are frequent; however, *Staphylococcus* aureus and coagulase-negative *Staphylococci* are the most frequently isolated microorganisms [118, 122].

It is important to understand how infection impacts bone healing and lead to fracture non-union. Multiple interconnected factors lead to non-healing and critical size bone defects secondary to infection. These factors can be summarised into metabolic imbalance, failed osteointegration (implant loosening) and post-surgical debridement bone defects.

Imbalanced bone metabolism secondary to infection contributes towards delayed healing or lack of healing (non-union). Inflammatory cell infiltrations, toxic metabolites (such as phenol soluble modulins and delta toxin) and inflammatory cytokines release (such as interleukin (IL)–1β and tumour necrosis factor (TNF)-α) trigger a cascade of biochemical reactions leading to the activation of necrosis or apoptosis in osteoblasts [129]. Additionally, enhanced osteoclastogenesis leads to disruption of the bone remodelling balance with increased resorption rates without adequate bone formation [130]. Infection compromises the blood supply to the fracture site, which not only compromises healing but may also lead to bone necrosis at the fracture site [117, 118, 120].

The concept of “the race for the surface” has been around for a few decades; Anthony Gristina in 1987 coined the phrase the “race for the surface,” suggesting that tissue cell integration and bacterial adhesion compete for real estate on the implant’s surface [131]. Unfortunately, the implants designed to encourage osteointegration and bone ingrowth offer a favourable surface for bacterial colonisation and biofilm formation, leading to failure of osteointegration and subsequent **implant loosening** [132, 133]. The post-infection implant loosening leads to failure to maintain immobilisation for sufficient time for the healing to take place, which subsequently leads to fracture non-union [134, 135].

Treating fracture site infection or periprosthetic infection necessitates a combination of systemic treatment, surgical intervention (to remove the infected implant, necrotic tissue debridement, local application of antimicrobials at the site of infection and re-stabilise the bone segments) and soft tissue management [129, 136]. **Extensive tissue debridement,** which is essential in the treatment of FRI, results in a bone gap (a dead space). The extensive volume of the removed necrotic bone, in addition to the compromised general health status of

the patient secondary to infection, renders most of the post-debridement bone gaps **a critical sized bone defect**. The most common clinical approach is to fill the post-debridement bone defect with antibiotic-loaded bone cement [137]. PMMA cement is considered the standard material on which antibiotics were impregnated for many years [138, 139]. However, the non-biodegradable PMMA acts purely as a spacer and a vehicle for local antibiotic delivery that lacks any osteoinductive or osteoconductive properties. Hence, it requires an additional intervention to remove the spacer to allow subsequent bone grafting. Currently, bioabsorbable materials are increasingly being used for local antibiotic delivery, with no inferiority in comparison to PMMA cement beads [138]. On the contrary some of these biomaterials (such as calcium sulphate [140-142] and calcium phosphate [27, 143] have additional osteoconductive properties.

2.2.2- Critical-size bone defect:

The work outlined in this thesis focuses on finding a solution for extensive bone loss beyond the body's innate healing ability: in the context of bone tissue engineering research this is referred to as a critical-size bone defect, which is defined as a bone defect that will not heal spontaneously within the patient's lifetime [168, 169]. More recently there has been consensus in defining a critical size bone defect as a bone defect that will not heal despite surgical stabilisation or shows less 10% bridging within the lifetime of the patient (or the animal) and requires further surgical intervention [33, 170, 171]. The main difference between a critical-size bone defect and a fracture non-union is the fact that a non-union often has no appreciable bone gap, while the critical size defect is predicated by having a substantial bone void [34, 115]. The literature suggests some guidelines regarding the size or volume of bone loss that is considered critical sized. For instance, if the defect length is greater than 1 – 2 cm and greater than 50% loss of the bone circumference [170, 172, 173]. Others suggest that critical size defects depend on the specific bone involved and occur when the length of the defect is 2 – 3 times the bone diameter [174]. In veterinary orthopaedics, Key's hypothesis is a well-known guideline for an animal model to investigate augmented bone healing techniques. It states that a segmental long bone defect 1.5 times the diaphyseal diameter exceeds the regenerative capacity of bone in skeletally mature dogs and results in non-union [175]. However, age has a huge influence on bone regenerative capacity; skeletally immature (young) animals frequently defy this rule and bone healing still occurs at or beyond the 1.5 time the diameter limit [176]. In addition to the size of the created bone defect, there are other methods to intentionally establish a non-healing bone defect model, such as placement of an autogenous soft tissue

(such as fat) graft between the osteotomy segment [177], periosteal stripping [150, 178, 179], suturing the periosteum over the ends of the bone [176, 180] or heat induced periosteal and/or bone necrosis [181, 182] .

In clinical scenarios, critical size bone defects are seen secondary to severe trauma, severe infection, after tumour resection and skeletal congenital anomalies [183].

- **Management of critical size bone defect**

Bone grafting (either autologous or allogenic) has been considered the standard of care for treating critical size bone defects for decades. Yet, the scale of bone loss often determines the best way to manage the bone defect. According to Greed et al [184], Rockwood et al. [185] and Gage et al. [186] defects less than 4-6 cm are considered small scale defects and bone grafting (autologous or allogenic) is the standard of care, while defects larger than 6 cm are considered large scale defects and either an induced membrane technique or bone transport are the primary treatment options.

A well-known clinical approach to managing long bone defects relies on applying the principles of distraction osteogenesis pioneered by Ilizarov [187], that formed the foundation of modern reconstructive surgery for limb lengthening and bone transport [188]. The Ilizarov technique works on the principle of distraction osteogenesis, which is defined as a technique of applying controlled traction across the site of surgically produced bone disruption while it is healing. The mechanical forces are directed predominantly away from the site, and the technique takes advantage of the regenerative capacity of bone by creating and maintaining an active area of bone formation in the surgically created gap. The bone is lengthened along with its envelope [189]. Ilizarov showed that osteogenesis can be induced if bone is expanded (distracted) along its long axis at the rate of 1 mm per day, leading to new bone formation along the vector of pull without requiring the use of a bone graft [190]. However, it requires keeping an external fixator in place for a long time as the expected healing rate is 1 cm per month in paediatric patients and 1 cm each three to four months in adult patients [191]. The external fixator is associated with pin tract infections, soft tissue scarring and limited range of motion [192, 193]. That led to the development of intramedullary nail (IMN) lengthening systems to overcome some of Ilizarov's device-related risks. Yet, the intramedullary nail lengthening systems have reported limitations such as mechanical instability and difficulty in controlling bone lengthening [194, 195]. Driven by the desire to optimise a technique that overcomes these limitations and achieves a positive and reproducible clinical outcome, led to

the development of magnetic intramedullary nails. The magnetic IMN system offered the unique benefit of accurate deformity correction and distraction osteogenesis without the need for external fixation with its inherent challenges [196]. It also adds, the new concept of bone lengthening with an external remote controller (ERC). There are several magnetic IMN systems that have been used and proven to be clinically successful. The first mechanical, motor-driven intramedullary lengthening nail was the Fitbone, developed by Rainer Baumgart in Germany [197]. It has been used successfully all over the world for over a decade [198]; the Phenix M-Bone intramedullary device demonstrated by Konofaos et al. [199]. The PRECICE intramedullary lengthening nails are the latest development and have been reported to achieve accurate and precise limb lengthening [200, 201]. Finally, plate-assisted bone segment transport (PABST) is principally used in bone transport [202-204].

Bone transport osteogenesis is an adaptation of distraction osteogenesis used to preserve limb function after resection of large segmental bone defects via creating an osteotomy on the proximal bone segment to create a distraction focus, and resulting in a small portion of healthy bone which acts as the transport segment. Bone grafting can be considered when the transport segment is approximately less than 0.5 cm from contact with the docking site [205, 206]. Distraction osteogenesis is considered one of the most reliable methods available for long bone segmental defect reconstruction and limb lengthening [204, 207, 208].

Masquelet's induced membrane technique for reconstruction of bone defects has proved its effectiveness and is now widely accepted. It is a two-stage reconstruction technique (6-10 weeks apart); it implies using cement spacer in combination with internal or external fixation that allows formation of a periosteum-like membrane around the cement spacer, followed by removal of the cement spacer and filling the defect with autologous bone graft [209-212]. In human patients, the Masquelet method is a reasonable option for upper limb bone defects but it is not a suitable option for long bones in the lower limb due to reported high complication rate such as non-union and deep infection [213, 214].

2.3- Bone grafts:

The current global statistics indicate that approximately 2.2 million bone grafting procedures are performed each year, with an anticipated 13% annual growth rate [215, 216]. It has been considered the gold standard of care for over 10 decades; in fact, bone is the second most transplanted tissue after blood [217, 218], with a history of the first recorded bone grafting procedure dated back to 1682, where a cranial defect was successfully restored using a cranial bone graft from a deceased dog [216, 219].

Bone grafts are typically classified according to the origin of the graft tissue. According to the donating individual, grafts can be autologous bone grafts (autografts)- when the bone is harvested from the same individual that they are to be used in (it is considered the gold standard); allogeneic grafts (allografts), where the bone is harvested from a different individual of the same species; and, xenogeneic grafts (xenografts), where graft material is harvested from one species and used in an individual of a different species [218, 220]. See **Table 2** for the definition, advantages, and limitations of each bone graft type.

Autografts can be harvested from cancellous bone, cortical bone, a combination of the two (cortico-cancellous graft), or from the bone/cartilage interphase (osteochondral) [21]. Autografts are advantageous because of their lack of immunogenicity, histocompatibility and superior osteoinduction and osteogenesis [17, 18]. However, they pose several limitations such as donor site morbidity, bleeding, infection, chronic pain, poor graft quality in heavy smokers, alcoholics and patients with underlying conditions. Additionally, there is a limit to the volume of bone that can be harvested from the same individual, particularly in paediatric patients [18, 221]. Some studies have also reported pulmonary emboli and other cardiovascular complications [222, 223].

Similar to autografts, **allografts** can come in several different forms, such as cortical, cancellous, and corticocancellous [224]. The bone can be used fresh or fresh frozen, but these types of grafts tend to be less popular due to the risks of immunogenicity and/or disease transmission. Most contemporary allografts undergo some form of processing before implantation into the host; this can include freeze-drying, ethanol treatment, ethylene oxide treatment or gamma irradiation for sterilisation [224, 225]. Demineralised bone matrix (DMBM) is a form of processed allograft that involves harvesting cadaveric cortical bones that are subsequently sterilised and demineralised to be used as graft substrate [226, 227]. Allografts overcome some of the limitations associated with autografts, particularly the donor site morbidity. Yet, it has its own share of disadvantages, to name a few, the high cost, risk of disease transmission, and high risk of immunogenic rejection (it has been reported that even after freezing, allogeneic bone containing no living cells caused complications in 25 to 35 % of patients) [228, 229]. Additionally, processed bone commonly exhibits compromised biological and structural integrity secondary to chemical treatment and/or irradiation [221].

Cancellous bone grafts are the most commonly used bone autografts; they can be harvested from the iliac crest, femoral greater trochanter, proximal ulna, distal radius, or proximal/ distal tibia [230, 231]. Cancellous bone provides a substrate for osteoinduction, osteoconduction

and osteogenesis (see **Table 3** for definitions). The trabecular nature of cancellous bone offers a larger surface area, hence rapid remodelling, faster graft incorporation, quicker revascularisation and osteointegration. It does not provide instant structural-mechanical integrity, yet it has been established that after 6 - 12 months post-implantation, structural-mechanical integrity is achieved upon complete graft turn-over [232-234]. The cancellous bone graft incorporates into the host bone through bone remodelling, a process characterised by bone resorption and substitution [17, 230]. The theory behind how cancellous bone grafts support new bone formation is attributed to osteoblastic activity; during the first 48 hours post-transplantation, neovascularisation is established [230, 235, 236], simultaneously a local haematoma rich with inflammatory mediators and chemotactic factors forms at the graft site, and the low oxygen tension at the defect site contributes towards Mesenchymal Stem Cells (MSCs) recruitment to the defect site these MSCs have the potential to differentiate into functional osteoblasts [18, 233]. Prior to neovascularisation, part of the transplanted cancellous bone does not survive the initial ischemic events; hence, macrophages are attracted to the graft site to remove nonviable (necrotic) trabeculae. The osteoblasts inhabiting the cancellous bone graft and the MSCs establish a base for new bone formation through osteoblastic differentiation and osteoid deposition. New bone formation is usually observed within a few weeks, and remodelling takes place by 8 weeks. Complete bone turnover occurs after 6 - 12 months [233, 234]. This process of concurrent osteoblast deposition of new osteoid and osteoclast resorption of necrotic donor trabeculae is known as creeping substitution [230, 234, 237].

The highly organised and highly dense nature of cortical bone grafts is a double-edged sword. It provides instant structural and mechanical stability, as well as supporting osteoconduction. However, it comes at the cost of limited access to osteoblasts, osteocytes, and other cellular progenitors, hence limited osteoinductive and osteogenic properties [17, 238, 239]. Non-vascularised cortical grafts are most commonly harvested from the iliac crest; other harvesting locations include the fibula, ribs, and ulna [240, 241]. Vascularised cortical grafts are taken from areas such as free vascularised fibular bone graft [242, 243]. The incorporation with host bone follows the same concept of creeping substitution as cancellous graft, yet at a much slower rate; depending on the graft size and both local and systemic healing environments, cortical graft incorporation can take many years [17]. It is predominantly a result of osteoclastic activity: beginning at the graft-host junction, moving along the axis of the cortical graft with slow, near-complete resorption of the graft and simultaneous deposition of new, viable bone [18, 221].

Cortico-cancellous bone grafts offer the best of both worlds, combining early mechanical stability and osteoconductivity while maintaining osteoinductivity and osteogenicity. The most frequent donor site is the iliac crest, which can provide unicortical, bicortical or tricortical graft material [230, 234].

Osteochondral bone grafts are mainly used to treat articular lesions secondary to trauma, osteonecrosis and developmental orthopaedic diseases such as osteochondritis dissecans [244, 245]. Osteochondral autografts are usually harvested from a non-weight bearing area of the knee joint, for example, slightly anterior to the sulcus terminalis at the junction of the lateral trochlea and lateral femoral condyle, superior and lateral to the intercondylar notch [246].

Xenograft bone is typically obtained from food chain animals such as cows (bovine) [247-249] and pigs (porcine) [250-252] due to its abundance, cheap price and ease of sourcing, but some studies report using horse (equine) bones as a modified xenograft as well [253-256]. Due to the immunogenic nature of xenografts, they must undergo further processing prior to use to eliminate the immunogenic donor cells, surface antigens and any pathogens while preserving biochemical composition and microstructure [257, 258]. There are several processing methods have been established over the years, aiming to achieve decellularisation, deproteinisation and delipidation, most commonly via physical (i.e., heat, freeze/thawing or freeze drying), chemical and/or mechanical treatments [258-265]. The process of decellularisation will inevitably affect the extracellular matrix composition and cause a degree of ultrastructure disruption. Hence, it is important to optimise which method or combination of methods to use [266]. See **Table 2** for more details. A particular focus on decellularised bone matrix will be discussed in an upcoming section under bone graft substitutes.

Table 2: Advantages and disadvantages of the different forms of bone graft

	Autologous bone graft	**Allogeneic bone grafts**	**Xenogeneic bone grafts**
Definition	A bone graft that is harvested from the same individual in which it is ultimately used	A bone graft that is harvested from a different individual of the same species	A bone graft that is harvested from one species and used in a different species
Types	• Cortical (non-vascularised or vascularised) • Cancellous • Cortico-cancellous • Osteochondral	Similar to autograft. They can be used: • Fresh • Fresh frozen • Freeze-dried • Ethanol treated • Gamma irradiated decellularised bone matrix	Bovine and porcine xenografts are the most common. The bone is usually deproteinised through chemical or physical treatments. It comes in the form of granules, putty, gel, sponges or block [257]
Pros	• Histocompatibility/lack of immunogenicity • Superior osteoinduction and osteogenesis • No risk of disease transmission • No financial cost	• Available in a variety of forms • Abundant supply • Overcomes donor site morbidity	• Abundant supply • Reasonably priced • Can be modified to enhance osteoinduction through adding growth factors and other bio-enhancements • Rigorous testing is required to ensure freedom from zoonotic diseases • Available in a variety of forms
Cons	• Donor site morbidity • Chronic pain • Infection • Blood loss • Poor graft quality in patients with underlying conditions. • Limitation to the volume of bone that can be harvested	• Risk of disease transmission • Risk of immunogenic reaction • Cost • Compromised biological and structural integrity secondary to graft treatment and sterilisation	• Processing compromises biological and structural integrity of the graft • Risk of zoonotic disease transmission if not rigorously tested

Table 3: Essential definitions related to bone healing.

Term	Definition
Osteoinduction	The process implies recruitment, proliferation, and differentiation of host immature cells (MSCs) into chondrocytes and osteoblasts as precursor for new bone formation [267, 268] usually influenced by growth factors and other biochemical/biomechanical stimuli [17].
Osteogenesis	The synthesis of new bone by donor cells derived from either the host or graft donor [216, 268].
Osteoconduction	The process during which bone grows on a surface of an implant. Where the implanted material acts as a bioactive scaffold over which host cells can grow [216, 267, 269].
Osteointegration	The ability of the host bone to interdigitate with the implant material. This is what creates a stable anchorage of an implant through direct bone-to-implant contact [17, 267].

2.4- Bone graft substitutes:

Driven by the limitations of bone grafts and the pressing demand for a substitute that can support bone healing, the market for synthetic bone graft substitutes has flourished in the past few decades and continues to follow an upward trend. For dental and maxillofacial applications alone, the global bone graft substitutes market size was estimated at $719.1 million in 2021 and is expected to reach $1371.6 million by 2028 [9-11]. Upon adding on the demand for bone graft substitutes in the orthopaedics, foot and ankle and spine surgery fields, the bone substitutes market size was valued at $2.91 billion in 2021 and is expected to reach $4.94 billion by 2030 [11].

An ideal bone graft substitute biomaterial should be able to provide mechanical support and stimulate bone regeneration through promoting the four fundamental biological elements of bone repair: osseointegration, osteogenesis, osteoconduction, and osteoinduction [270, 271]. **The evolution of modern biomaterials has passed through three generations**, the first generation biomaterials are bioinert, second generation biomaterials are bioactive and biodegradable and third generation biomaterials are customisable biomaterials and materials designed to trigger cellular and molecular responses of interest) [272, 273]. The third generation biomaterials do not substitute the materials from previous generations, but modify the biomaterials either to serve a specific purpose for a patient/ disease and/or to enhance the performance of the biomaterials. Classifying the evolution of biomaterials into three

generations is more of a conceptual than a chronological perspective [272] (see **Table 4** for more details).

Clinically used **bone graft substitute biomaterials come in multiple forms,** such as solid blocks, powders, pellets, mouldable sheets, injectable pastes and 3D-printed implants. The mouldable and pellet forms of grafts are advantageous in emergency surgeries such as trauma cases or when no pre-surgical planning is involved. Injectable forms are very useful in minimally invasive surgeries [274-276]. At the same time, 3D-printed implants are better suited to situations where pre-surgical planning can be used to develop tailored implants designed to fit the specific needs of the patient [276, 277].

The work described in this thesis is centred around 3 main biomaterials: a polymer (polycaprolactone, **PCL**), a bio-ceramic (tricalcium phosphate (**TCP)** / Hydroxyapatite (HA) 80:20 mix), and a modified xenograft (**bovine decellularised bone matrix**, **DCBM).** Since our particular focus was on determining the suitability of these materials for use in clinical cases of extensive bone loss, we focused on using **3D printing** as a method of manufacturing scaffolds /implants that would be customisable according to patients' specific needs.

The polymeric implantable biomaterials particularly the bioresorbable polymers (belonging to the second generation biomaterials) was introduced in the 1960s by Kulkarni et al. [278, 279]; since then biodegradable polymers such as polyglycolide (PGA), polylactide (PLA), polycaprolactone (PCL) and many others have been extensively studied [280]. In the context of orthopaedics, these materials have been used in multiple applications such as bioresorbable bone fixation devices (screws, plates, and pins) [281], but have also been used in research. Polymers have a well-established record as bone and cartilage substitute biomaterials either solely or in combination with other polymers, bio-ceramics, or biological materials [282-286].

Polycaprolactone (PCL) it is an FDA approved **biodegradable polymer** for use in implantable biomaterials and injectable implants [287-289]. It is widely used in musculoskeletal regeneration and bone tissue engineering research either as plain PCL scaffolds [290, 291] or in combination with other materials, predominantly bio-ceramics, for the purpose of bone tissue engineering [13, 287, 292-294] due to its biosafety, slow biodegradation [294, 295] and exceptional mechanical properties. It has an average bulk tensile strength of 16 MPa, compressive strength of 38.7 MPa, elongation at break 350 %, elasticity modulus of 430 MPa, and compressive modulus of 300 MPa (these values are for non-porous PCL and vary according to porosity %), which makes PCL extremely flexible yet tough [296, 297]. In addition, it is very versatile in the way it can be fabricated into a scaffold

via different methods such as solvent casting, electrospinning and 3D printing. PCL melts around 60°C and has a glass transition temperature of -60°C [297]. The low melting temperature in comparison to other polymers, make PCL a widely used 3D printable polymer that has been printed using different 3D printing methods such as fused deposition modelling (FDM), selective laser sintering (SLS) or bioprinting [93].

The use of **bio-ceramics as a bone substitute** is dating back to the 1970s [272, 298, 299]. Calcium phosphate ceramics include tricalcium phosphate (α-TCP or β-TCP; Ca3(PO4)2), hydroxyapatite (HA- (Ca10(PO4)6(OH)2)), and biphasic calcium phosphate (BCP, a mixture of HA + TCP at varying ratios) (**See Table 5** for comparison between TCP, HA and BCP). These are the most commonly used ceramics as bone substitute due to similarity to bone composition and desirable biocompatibility and bioactivity (macroporosity, microporosity, dissolution and osteoconductivity) [272, 300, 301]. They are available in different forms such as granules, putty, blocks or wedges [276]. In the context of bone tissue engineering research, calcium phosphate porous scaffolds can be fabricated using traditional techniques such as foaming, mould-casting, or powder compaction [302], or newer methods such as 3D printing, and the use of sacrificial porogens which allow better control over pores size, fraction and interconnectivity of both macropores and micropores [303-305].

The main disadvantage of bio-ceramics is their poor mechanical properties particularly under compression [6, 276]. Another limitation of calcium phosphate bioceramics is the uncontrolled biodegradation rate and concern about potential effusion of the material into surrounding tissues leading to soft tissue damage [216, 271]. Aiming to overcome these limitation, investigators have explored mixing bioceramics with each other (e.g. TCP + HA [306-308]) or with other materials such as polymers [15, 26, 309], chitosan [310] or hyaluronic acid [311-313] in an attempt to optimise particles distribution, control biodegradation, improve handleability and/or improve biomechanical properties while maintaining the advantageous biocompatibility , osteoinductivity and osteoconductivity. To sum-up, calcium phosphates are the gold standard when it comes to bone substitute biomaterial but, they do have their own limitations.

While bioceramics have a composition similar to the inorganic component of bone, **decellularised bone matrix (DCBM)** has preserved the organic component of bone yet without the immunogenic cells. Depending on mineralisation status, it can also preserve some or all the inorganic bone components (decellularised (DCBM) vs. demineralised bone matrix

(DMBM)) [20]. DCBM is a naturally derived scaffold formed by removing cellular components from the native bone matrix and preserving the specific microarchitecture and composition of the bone extracellular matrix (ECM) including collagen, minerals and bioactive molecules such as growth factors and cytokines [266]. This offers a naturally occurring three-dimensional scaffold with tissue-specific structural and molecular cues that are not easily created synthetically in the laboratory, leading to superior osteoinduction rather than relying solely on osteoconduction [314]. Cancellous bones from food chain animals mainly bovine and porcine are the most popularly used to prepare DCBM scaffolds due to ease of access , low cost, quality control (for food production purposes) and abundant availability [19, 20, 266, 315]. There are a few commercially available bovine decellularised and deproteinised bone matrix (falls under the category of modified xenografts) products such as BioOss ® OsteoGraf ® and Cerabone ®; these products are particularly popular in the field of dentistry. They have proven to be biocompatible, non-immunogenic and to promote bone healing. Yet, these materials offer very little mechanical support as they are extremely brittle, hence not suitable for load-bearing bone defects or in complex traumas. So far these products (most famously used Bio-Oss®) [316] are used for non-load bearing bone augmentation such as sinus, socket preservation and peri-dental implant defects [216, 317, 318].

Several studies (including my own) aiming to further evaluate the efficiency of DCBM as a bone graft substitute are trying to overcome the mechanical and anatomical shortcomings of the commercially available products that are designed on the notion of one size fits all, which is not necessarily applicable to patients undergoing complex bone reconstruction surgeries.

From a material fabrication / manufacturing perspective, there are 2 crucial elements to be take into consideration when designing a study involving DCBM. First, the bone decellularisation method that ensures elimination of the immunogenic cellular components while preserving the integrity of the ECM [266, 319]. Second, post-decellularisation processing, that includes the scaffold fabrication method and final format [14].

Decellularisation is achieved through chemical, enzymatic and/or physical treatments of the collected bone samples; two or more methods are usually combined to achieve proper decellularisation [14, 266]. It is inevitable that the process of decellularisation will affect the ECM composition and cause a certain degree of ultrastructure disruption, hence it is important to optimise which method or combination of methods to use [266].

Chemical processing involves using detergents, acids or alkaline solutions. Chemicals decellularise tissues through delipidation (lipids removal), cell membrane permeabilisation (hence cell lysis) and tissue clearing [315, 320]. Proteases such as trypsin and nucleases

(RNase and DNase) are the most commonly used enzymes in the process of enzymatic decellularisation. These enzymes work by hydrolysing the phosphodiester bonds (in the case of nucleases) or peptide bonds (in the case of proteases). To reduce (or even prevent) the disruption of ECM proteins such as elastin and collagen, these enzymes are frequently used in conjunction with chelating agents, such as ethylenediaminetetraacetic acid (EDTA), to aid in detaching cells from the ECM proteins by sequestering metallic ions such as calcium [321, 322]. Finally, the physical decellularisation methods rely on cell membrane destruction, leading to cell rupture. Methods of physical decellularisation include freezing-thawing [323], direct pressure [324], sonication [325], agitation, osmotic lysis (hypotonic [326] or hypertonic[327]), electroporation and/or vacuum-assisted decellularisation [328].

The evaluation of the efficiency of the decellularisation process follows 3 main streamlines. **First is to confirm the elimination of cellular components** through a) DNA quantification and b) histological evaluation. Measuring the amount of DNA in DCBM is the current gold standard for evaluating the success degree of decellularisation through comparing the amount of DNA in tissue samples before and after decellularisation using quantitative assays such as the PicoGreen assay [322, 329]. A fully decellularised tissue has a residual DNA content ≤ 50 ng/mg, and any remaining DNA fragments should be smaller than 200 base pairs [321, 330]. Upon histological examination, the tissue should not contain any visible nuclear material when stained with DAPI or H&E [321].

Second is to evaluate the effect of decellularisation on tissue **mechanical and material properties**; the uniaxial compression test is the most commonly used, where results are plotted as stress versus strain curve [320, 331].

Lastly, microstructure evaluation using imaging tools such as SEM and μ-CT to evaluate trabecular thickness, porosity, the interconnectivity of the pores, and distribution of pore size [316, 320, 332, 333]. Mechanical properties and microstructure evaluation are particularly important if the decellularised tissue is going to be used without further modification (such as milling in preparation for moulding or 3D printing). One fact to bear in mind when intending to use un-modified DCBM is that the biomechanical priorities and the microstructure vary according to the site where the bone was harvested from, even within the same bone from the same donor.

In order to ensure a more uniform scaffolds' biomechanical properties and to achieve customisability, post-decellularisation processing must be considered. Example post-decellularisation processing include homogenisation, milling to powder, hydrogel synthesis,

mixing with polymers, or dissolving into a bio-ink **Table 6** summarises the applications, advantages, and disadvantages of different post decellularisation processing.

2.4.1- Clinical use of bone graft substitutes:

Bone substitutes should be used selectively based on the intended clinical application. The literature suggests that bone substitute biomaterials behave differently in different bone reconstruction procedures to reconstruct (i.e. long bone vs. maxillofacial vs. spine) bone defects [334].

2.4.1.a- Long bone defects and fracture non-union

The literature indicates that calcium phosphate ceramics (CPC) can provide similar to and better mechanical support than autologous iliac bone grafts in the treatment of defects in unstable fractures [335]. Hydroxyapatite (HA) and beta Tricalcium Phosphate (β-TCP) ceramics have been used for many decades in long bone fractures, such as tibial plateau fractures [336, 337]. However, their use in distal radial fractures showed no significant benefits in terms of extra stability compared to solely using internal fixation and the complications rate didn't reduce in a statistically significant manner [338]. In a review reporting 70 cases, when β-TCP ceramics were used as wedges in an open-wedge tibial osteotomy (OWTO) there were more than 96 % osteointegration and 98.5 % of the cases achieved bone healing. However, HA is assumed to be too fragile to be implanted in bones that are under mechanical stress or weight bearing conditions, such as in the case of OWTO [143, 339-341]. Decellularised Bone Matrix (DCBM) became a popular bone substitute for grafting non-healing bone defects [17, 342]. It has been compared to autologous bone and had superior results in terms of fracture healing and a decrease in adverse effects such as donor site morbidity. However, using commercial DCBM was reported to make the procedure more expensive (an average difference of 190 USD per case) [342].

2.4.1.b- Craniomaxillofacial (CMF) applications

- **Oral/periodontal procedures**

Periodontal disease which comprises gingivitis and periodontitis is a common oral infection that affects the tissues that surround and support teeth [343]. The condition often presents as gingivitis, characterised by bleeding, swollen gums, and pain. If left untreated, it progresses to periodontitis, which involves the loss of periodontal attachment and supporting bone [344]. When treating periodontal defects, the use of bone grafts seems to promote better healing compared to open flap debridement alone [345]. However, even if bone replacement grafts

offer clinically satisfying results in terms of bone fill, histologic evidence of periodontal regeneration has only been reported for autologous bone grafts and demineralised bone matrix (DBM). DBM has also proven to be suitable for use in buccal bone defect filling after dental implant placement [334, 346].

- **Sinus Augmentation**

For sinus augmentation, the available evidence neither supports nor refutes the superiority of autologous bone over other graft materials when considereing implant survival and/or complications at the recipient site [347]. DBM [348, 349] and bioglasses [350, 351] show particularly positive results in sinus augmentation procedures.

- **Cranioplasty**

Cranioplasty is a procedure performed after traumatic injuries, tumour removal, or decompressive craniectomies in order to protect the brain and achieve a natural appearance [352]. The ideal bone graft substitute for cranioplasty should be easy to shape (customisable), resistant to infections, biocompatible, firm, and stable. Polymethyl methacrylate (PMMA) is the most extensively used material for cranioplasty [352-354]. Other materials such as titanium, various bioceramics, HA and DBM are safely used for cranioplasties [355-357]. Synthetic polymers (such as PCL) are successfully used for cranioplasty, and the fact that they are easily 3D printed makes them a cost-efficient and customisable option [358]. Similarly, reconstruction of zygomatic and mandibular defects using 3D-printed PCL or PCL/bioceramics composite implants have been reported, usually combined with soft tissue and/or bone flaps [359, 360].

2.4.1.c- Spine applications

- **Spine Fusion**

Autografts and allografts are used mainly to promote spine fusion [361]. DBM mixed with marrow aspirate or with autologous bone graft showed good results in spine fusion. However, DBM did not prove to be suitable as a standalone material for spinal fusion [17, 362, 363], as it showed a higher rate of graft collapse and pseudarthrosis when compared to autograft [364]. Beta-TCP demonstrated efficacy for use as a bone graft extender in posterolateral spinal fusion [361]. However, that was not the case for HA, attributed to the fact that the host bleeding bone surface in this area is minimal. Knowing that HA needs adequate bleeding to bond to the bone surface, HA was not suitable for spinal fusion [365], neither was calcium sulphate [366].

- **Vertebroplasty and kyphoplasty**

Vertebroplasty is a procedure that involves injection of bone cement into vertebral body to stabilise a vertebral body compression fracture and to alleviate pain in patients with various other conditions (such as haemangioma, spine tumour, or osteoporosis) [367, 368]. Kyphoplasty is a variation of vertebroplasty that usually involves the use of a balloon to create a cavity within the vertebrae cancellous bone, the cavity is then filled with bone cement to reinforce the vertebral body [367, 369]. PMMA bone cement is the most common clinically used biomaterial for that purpose, but it is associated with some disadvantages such as heat generation during exothermic polymerisation, nonbiodegradability, and a lack of biologic potential to remodel or integrate into the surrounding bone Other alternative materials have been reported in the literature such as CPC, that is easily moulded and injected into the defect area. It offers the potential for resorption and replacement with new bone and does not generate heat. However, it is less mechanically strong compared to PMMA [367, 369, 370]. Calcium sulfate has a relatively higher mechanical strength than CPC, but its fast degradation rate does not support spinal alignment while it is remodeling [367, 371].

Table 4: Evolution of biomaterials

	First Generation Biomaterial	Second Generation Biomaterial		Third Generation Biomaterials
		A) Bioactive	**B) Biodegradable**	
Main criteria	Bioinert, causing minimal immune response	The material interacts with the host's tissue and produces a controlled desirable response. In the context of orthopaedics, these desirable responses are osteoconduction and osteoinduction [372].	The materials of choice undergoes a controlled breakdown inside the body at a clinically relevant rate, so by the time the material is resorbed, it will be completely replaced by neo-regenerated tissue up to a point where it is indistinguishable from the healthy tissue [373, 374].	Biomaterials that have been designed to stimulate desirable cellular responses at molecular and/or gene levels [272, 273]. These responses are achieved via one or more of the following: - combination of bioactivity and biodegradability properties. - 3D structure, porosity and surface roughness criteria that are favourable for cell proliferation and differentiation. - seeding scaffolds with progenitor cells with or without desirable signalling factors (i.e. BMP-2, FGF, TGF and VEGF). - scaffolds are designed to controllably release osteogenic stimulating factors [375].
Aim behind development	Providing mechanical stability without triggering rejection (immune) response by the body.	Supporting tissue healing through guided tissue regeneration and favourable material/tissue interaction, rather than solely filling a dead space.		-As an advanced application of tissue engineering approaches. - Mimicking normal tissue architecture and creating a tailored niche that augments the target tissue self-healing capacity. - Combining more than one desirable feature in one implantable construct.
Examples	**Metallic:** Stainless-steel, titanium and its alloys, cobalt chrome alloys **Ceramics:** Alumina, zirconia Calcium carbonate **Polymers**: Medical grade silicone, polyethylene, acrylic resins, polyurethanes, polypropylene and polymethylmethacrylate. **Carbon fibres**	**Bioactive ceramics** such as: Hydroxyapatite, and bioactive glass, which can be used in the form of powder, porous implants, and implant coatings or as a composite in combination with other materials [273, 376-379]. **Carbon based scaffolds** such as**:** Graphene oxide [380-383] **Organic materials such** as:	**Resorbable polymers** such as: Poly lactic acid (PLA), polyglycolic acid (PGA) and polycaprolactone (PCL) are the most common biodegradable polymers used in implantable medical devices[273], **Resorbable ceramics**: such as resorbable calcium sulphate and calcium phosphate (TCP)	**3D printed, biodegradable and bioactive scaffolds – plain or seeded with progenitor cells:** 3D-Printed PCL Scaffolds combined with bioactive ceramics (i.e. TCP, HA) or with DCBM [12]. 3D printed poly(lactic-co-glycolic acid) (PLGA) scaffold with Nano hydroxyl apatite scaffold[391] **Scaffold supplied with signalling molecules, e.g.** 3D printed scaffolds loaded with BMP-2 [392]·[393]. **Micro and Nano porous foam scaffolds to**

		collagen and chitosan that could be used either solely or loaded with other ceramics and/or bioactive materials, they show excellent biocompatibility but mechanically they were not the best choice to support load bearing bone healing [384-388]	which have well reported use as bone graft substitutes as well as in-situ controlled antibiotic release to control surgical site related infection [389, 390].	**mimic the cancellous bone structure.** Bioglass (BG) and ceramic foam scaffold, circular photonic, Metallic foam scaffold (i.e. Ti foam), biodegradable composite foam scaffold [394-397] **In situ tissue regeneration:** Where biomaterials are delivered in the form of powder, hydrogel, solution, micro particles or even biodegradable molecularly tailored polymers, with controlled release of growth factor into the affected site via diffusion or network breakdown which act as a chemotactic/ activation factors for cells contributing into the healing process [398-401].
Advantages	1- Used for many decades in fracture fixation and joint replacement devices. 2- Proven its mechanical stability. 3- Surgeons became very familiar with these materials.	1- Osteoinductive and osteoconductive. 2- Promotes neovascularisation 3- Superior osteointegration	1-Biodegradability attuned to the bone healing rate, eliminates the need for a second surgery (such as in case of biodegradable bone spacers for single stage revision surgery) [402, 403]. 2- Osteoconduction and to some extent osteoinduction [404, 405].	1-Combination of more than on desirable criteria (hence more than biomaterial) in one implant leading to superior biocompatibility, mechanical suitability, osteointegration, osteoinduction, osteoconduction and osteogenesis). 2-Allow novel and innovative implants fabrication. 3-Customisability to patients' specific needs.
Disadvantages	1-Deposition of an unspecific proteins over the implant surface, which acts as a nidus for bacterial biofilm formation [406, 407]. 2-Fibrous tissue layer formation leading to total implant encapsulation [408-410].	1-Lack of the osteogenic properties. 2- Inferior mechanical properties. 2- Lack of biodegradability of some of these materials leads to a noticeable morphological and structural differences at the material-tissue interface that may impact the quality of the bond at material tissue junction as well as the mechanical properties of the grafted site [411].	1-Lack of the osteogenic properties. 2- The performance of these materials is mostly dependant on their manufacturing method and microstructure (i.e. porosity and surface roughness) [412, 413].	Most third generation biomaterials are still in the experimental phase and need further approvals before they will become available for the surgeons to offer their patients as a treatment option.

Table 5: Comparison between TCP, HA and BCP

	Tricalcium Phosphate (TCP)	**Hydroxyapatite (HA)**	**Biphasic Calcium Phosphate (BCP)**
Definition	TCP is a calcium salt of phosphoric acid ($Ca_3(PO_4)_2$). It exists as three crystalline polymorphs α, α′, and β.	HA is a naturally occurring mineral form of calcium apatite ($Ca_{10}(PO_4)_6(OH)_2$)	Mixture of hydroxyapatite and tricalcium phosphate (most commonly β-TCP) at varying HA: TCP ratios [300]
Resorption time	Resorbed in 13–20 weeks after implantation [276, 414, 415]	Very slow resorption, it remains in the body for up to 3 years after implantation [276, 340, 416]. Nanocrystalline hydroxyapatite has been developed with a higher surface to volume ratio to allow faster resorption [417, 418].	Differs according to the HA: TCP ratio.
Advantages	1-TCP is the most similar in chemical composition to human bone [6] 2- Biocompatible [276] 3-Osteoconductive [6, 216] 4- Osteoinductive [419] 5- Radiopaque hence easy to follow-up after implantation [216]. 6- Bioresorbable	1-Up to 50% by volume and 70% by weight of human bone is a modified form of HA [420] 2- Biocompatible 3- Macro-porous structure 4-Osteoconductive 5- Osteoinductive[216, 276, 418] 6- Promotes neovascularisation [216] 7- Higher compression and tensile strength than TCP[6]	1-Osteoconduction 2-Osteoinduction 3-Adjustable resorbability 4-Comparatively greater mechanical strengths than either TCP or HA alone [276, 421]
Limitation	1- Poor mechanical properties particularly compressive tensile strength [6, 216, 422] 2- Unpredictable biodegradation [276]	1-Very slow resorption means it is incorporated into remodelled bone, compromising the bone's mechanical properties. 2- Low mechanical strength in comparison to bone.	Material properties vary according to the HA: TCP ratio.
Example commercial products	Cerasorb® OSferion® Orthograft®	Ostim® Endobon®	MASTERGRAFT®

Table 6: The applications, advantages, and disadvantages of different post decellularisation processing

Application	Processing method	Advantages	Disadvantages
Scaffold is used as a whole tissue [320, 332, 423]	No further processing- DCBM to be stored until further use.	-Ease of fabrication - Superior mechanical priorities	-More challenging to decellularise. -Limited control over scaffold's geometry (usually as block, wedge, or cylinder)
Moulding [251, 424, 425]	Homogenised into powder followed by freeze drying (more common for cartilage ECM)	More control over scaffold geometry	-Poor mechanical properties compared to whole tissue scaffold. -Loss of unique native bone architecture and microstructure
Hydrogel [426-428]	DCBM is milled into powder, then digested in pepsin or extracted with urea	Thermosensitive gelation at physiological temperature	Loss of t unique native bone architecture and microstructure.
3D printing and electrospinning [13, 20, 21]	DCBM is milled into powder and mixed with polymers to be extruded or electro-spun	- Control over scaffold design, geometry and mechanical properties that it can be tailored to patients' specific needs. - Ability to mix multiple materials	- Loss of the bone unique native architecture and microstructure. - Challenging to optimise the printing protocol.
Bioink [429-431]	DCBM is digested in pepsin in acidic buffer, then the pH is adjusted using NaOH to form a pre-gel solution used as bioink	- Control over scaffold design, geometry and mechanical properties that it can be tailored to patients' specific needs. - Ability to mix multiple materials	- Loss of the unique native bone architecture and microstructure. - Challenging to optimise the printing protocol and the bio-ink formula.
Cell seeding [20, 322, 432-435]	Cells (usually MSCs) are seeded over the scaffolds either statically or dynamically	Enhanced osteoinduction and ability to used patients own cells to repopulate the scaffold	-Additional time is needed for cell isolation, proliferation and seeding. -Higher risk of infection

2.5- The role of tissue engineering in solving the problem of non-healing bone defects:

Tissue engineering (TE) and regenerative medicine-related research has thrived within the past three decades, as bio-medical sciences and engineering have merged to offer solutions for musculoskeletal injuries, including bone defect repair [436]. These TE solutions rely on three main pillars (see **Figure 5**): the basal structural support (scaffolds) that mimics extracellular matrix, the correct type of cells, and biochemical/physical stimuli suitable for the targeted tissue type and function [437-439].

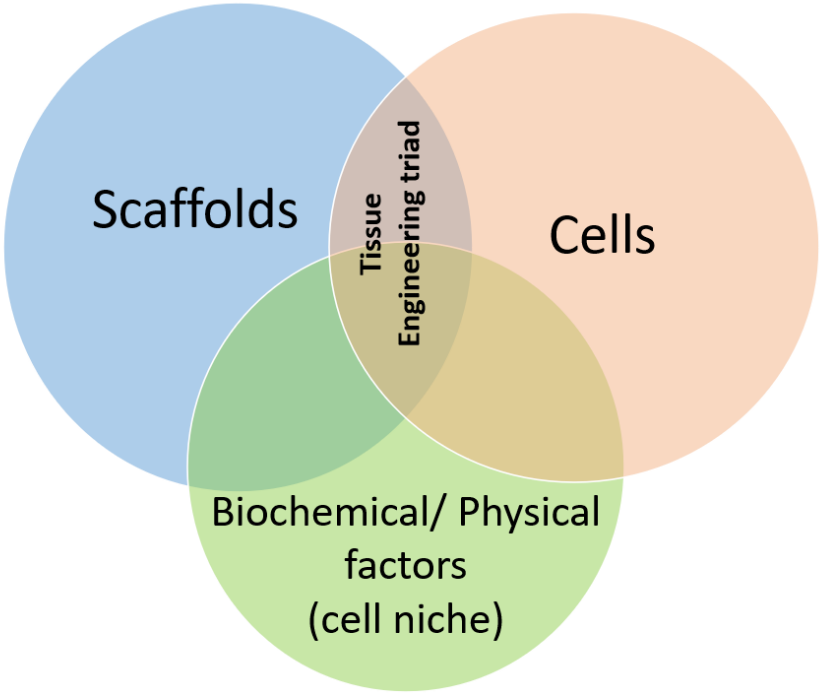


Figure 5: The tissue engineering triad

The scaffolds/ biomaterials in the context of bone TE and bone graft substitutes have been discussed in the previous section (2.4). When it comes to cells in tissue engineering, self-renewing, undifferentiated, yet multi-potent stem cells are the cells of choice [440]. There are several types of stem cells based on the tissue of origin; yet, the mesodermal origin of mesenchymal stem (stromal) cells (MSCs) and the fact that these cells are the precursors of the osteoblast and its role in regulating normal skeletal homeostasis and fracture repair, all render MSCs an ideal candidate for bone regeneration applications [441].

2.5.1- Mesenchymal stem cells:

Mesenchymal stem (stromal) cells (MSCs) are a heterogeneous population of stem cells that represent an attractive cell population to work within the context of tissue engineering and regenerative medicine due to their multipotentiality (ability to differentiate to several cell lineages even beyond their mesodermal origin) *in vitro* and *in vivo*, self-renewal-ability, the relative ease of isolating MSCs from an adult's body and expansion in tissue culture [442-444]. In order to be considered multipotent MSCs, cells have to meet certain criteria, according to the International Society for Cellular Therapy (ISCT) position statement [445]; these criteria can be categorised into morphology, behaviour in tissue culture, proliferation ability, evidence of multipotentiality and immuno-phenotype related criteria [445-449] as summarised in **Figure 6**. Some variation in immunophenotypic characteristics has been

reported between different species and tissues from which the MSCs have been isolated [450, 451].

In the adult body, most tissues have their own reservoir of progenitor cells that participate in these tissues self-healing and renewal; some tissues are richer in progenitor cells than others. Luckily, in the past few decades, multiple tissues have been identified and proven as sources for the isolation of MSCs, that are usually found to be associated with the perivascular niche [452, 453]. The earliest identified source of MSCs was the bone marrow [454, 455]; despite its reliability, the invasive nature of bone marrow biopsy and donor site morbidity initiated the search for other, less traumatic sources of such a valuable, highly demanded cell population [456]. That started the search for other possible sources of MSCs, such as umbilical cord blood [457], placenta [458], exfoliated deciduous teeth apical papilla, periodontal ligament [459], peripheral blood stem cells [460] and adipose tissue-derived MSCs [461]. One significant advantage of these alternative MSCs sources is based on the fact that they have previously been considered as surgical/medical wastes, which turned out to have a massively underestimated value.

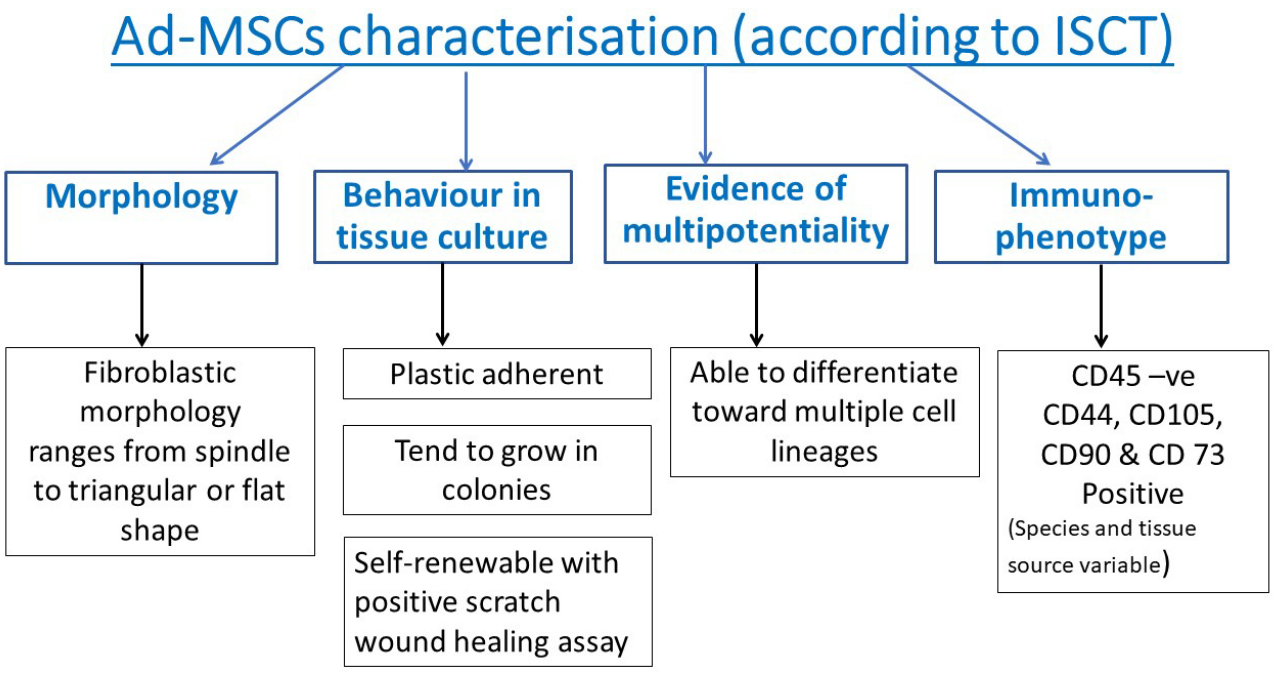


Figure 6: Outlines the minimal criteria for defining multipotent mesenchymal stem (stromal) cells, as per the International Society for Cellular Therapy (ISCT) position statement [445].

Adipose-derived mesenchymal stem cells (Ad-MSCs):

Adipose tissue has proven its reliability as a source of MSCs. This reliability is based on its abundance across the body, ease of harvest with minimal donor site morbidity and the relatively high MSCs yield, which can be isolated from the stromal vascular fraction (SVF). It has been estimated that each gram of fat can give approximately 0.5×10^4 to 2×10^5 cells/ g [449, 462]. Additionally, stem cells in the adipose tissue SVF account for 3% of the total cell population, which is 2500 fold more than stem cells in bone marrow, where they are only 0.002% of the cell population [463, 464].

In addition to the advantage of high cellular yield, recent studies have shown that Ad-MSCs have higher *in vitro* multiplication and stronger osteogenic differentiation abilities than bone marrow derived MSCs (BMMSCs) [465, 466].

MSCs osteogenic differentiation:

The mesodermal origin of MSCs makes them an ideal option to be used in musculoskeletal regeneration. MSCs have a proven capability to differentiate toward the osteogenic lineage once the appropriate medium is provided. *In vitro* when the MSCs culture medium is enriched with ascorbic acid (50 μg/ml), β-glycerophosphate (10 mM) and dexamethasone (100 nM), that successfully drove the MSCs toward osteogenic differentiation [448, 467, 468]. During the process of osteogenic differentiation, cells go through three main stages: cell proliferation, matrix maturation (early osteogenesis) and matrix mineralisation (late osteogenesis) [469, 470]. Relative traceable evidences of differentiation at early and late stages of osteogenesis and their quantification methods are explained in **Table 7.**

2.5.2- Scaffolds:

The scaffold provides the extracellular microenvironment for supporting and stimulating stem cell-driven tissue regeneration, serving as a supportive platform for transplanted cells or recruiting and retaining endogenous cells together with appropriate biochemical signalling molecules and mechanical stimuli [436]. A detailed review of scaffolds and biomaterials as bone substitutes has been addressed in section 2.4 above.

Table 7: Traceable evidences of MSCs osteogenic differentiation:

Stage	Marker	Role	Quantification method (s)
Early osteogenesis (Matrix maturation)	Alkaline phosphatase (ALP)	Membrane-bound enzyme, that provides free calcium and phosphate essential for mineral deposition [471, 472].	ALP enzyme activity measurement, ALP staining. ALP gene expression level (qPCR)
	Collagen I	Main component of bone organic ECM [473]	Collagen I gene expression level (qPCR)
	RUNX2	The first transcription factor required for determination of the osteoblast lineage, it induces the differentiation of MSCs cells into immature osteoblast [474]	RUNX2 gene expression level (qPCR)
	Osteonectin	A collagen binding protein that has a role in linking mineral to the collagen matrix and functions as a regulator of the osteoblast proliferation [475].	Osteonectin gene expression level (qPCR)
Late osteogenesis (Matrix mineralisation)	Osteocalcin	Bone matrix maturation and ossification [471-473]	Osteocalcin gene expression level (qPCR)
	Osteopontin		Osteopontin gene expression level (qPCR)
	Mineral Deposition		Alizarin red staining (binds to calcium) Von Kossa staining (binds to phosphorus).

2.5.3- Biochemical signalling molecules and growth factors

As a consequence of bone injury, the levels of certain growth factors and cytokines become elevated at the injury site, suggesting that they play an active role in promoting bone repair by regulating cellular chemotaxis, proliferation, and differentiation [57]. The five main families of growth factors involved in bone healing are fibroblast growth factors (FGF-1 and 2), platelet derived growth factors (PDGF AA, AB and AB), transforming growth factors beta (TGFβ-1 and 2), bone morphogenic protein (BMP-2,3,4 and 7) and insulin-like growth factors (IGF-1 and 2) [476-478]. Inspired by the body's natural healing mechanism, adding these growth factors to the tissue engineered construct (scaffold + cells) enhances its osteoinductive and osteogenic properties. The two main methods of growth factor delivery to the injury site are either by controlled release from the scaffold or by induced over-expression by the cells seeded in the scaffold (genetic modification) [465, 479-482].

The application of osteogenesis-enhancing growth factors is not limited to experimental use only; some products have been approved by the US Food and Drug Administration (FDA) and are already available for clinical use (details **in Table 8).**

Despite promising outcomes, cost efficiency and several other concerns are related to the use of these growth factors. Deciding the right concentration and release rate of growth factor is still a point of investigation, as the lack of an appropriate delivery system results in rapid clearing from the system. Dose-wise, a sub-therapeutic dose leads to failure of osteogenesis, and an overdose leads to either poor quality bone formation with multiple adipose tissue filled bone cysts, as seen with BMP [483], or even inhibition of bone formation as reported in the case of FGF [484]. In addition, there are clinically reported side effects related to the use of BMP, such as postoperative oedema, dysphagia, ectopic bone formation and osteolysis when used in spinal fusion surgeries [485-488], heterotopic bone formation has been reported related to the use of BMP for fracture healing [489] and some studies reported a carcinogenic effect of BMP [490-494].

Table 8: Approved products for clinical use with osteogenic enhancing growth factors

Product	Supplier	Discerption	FDA approved use
INFUSE® Bone along with LT-CAGE® device	Medtronic	BMP-2 supplied within a bovine collagen sponge carrier. LT-CAGE® is a small, hollow metal cylinder, or cage, that holds the biologic material and restores the degenerated disc space to its original height.	2002 - lumbar spine fusion 2004- open tibial fracture with intramedullary nail fixation. 2007- sinus and localised ridge augmentation
OP-1® implant OP-1® putty	Stryker	rhBMP-7 supplied as 1 gram powder in Type I bovine collagen carrier mixed with sterile saline solution to form a paste. + Carboxymethylcellulose (CMC) in case of OP-1 Putty	OP-1 implant as bone graft substitute and in fracture healing. OP-1 putty for spinal fusion.
GEM 21S®	Lynch Biologics LLC	PDGF-BB on β-TCP base	Dentistry (used for periodontal tissues regeneration)
AUGMENT® bone graft and AUGMENT® injectable	Wright Medical group	PDGF-BB + β-TCP PDGF-BB + Collagen matrix	Ankle and foot arthrodesis

Platelet-rich plasma and platelets concentrates for bone healing:

When growth factors are being discussed in the context of musculoskeletal regeneration, the topic of platelet rich plasma (PRP) presents itself. PRP is defined as a small volume of plasma prepared by centrifugation of peripheral blood that has a platelet concentration 3-5 folds above the baseline platelet number in whole blood [495, 496], bearing in mind the average platelet counts in blood is 200,000/µl (range 150,000 to 350,000/µl) [497]. Platelets are a rich natural source of growth factors, cytokines and other molecular elements that improve tissue healing [495]. The principle behind using PRP is that it acts as a vehicle to deliver critical growth factors and cytokines from platelet granules (α-granules) to the targeted tissues, aiming to induce or improve their healing [498]. For the PRP to be effective, platelet activation must undergo 2 key steps: platelet degranulation to release growth factors and fibrinogen cleavage (or clotting) to initiate matrix formation [499]. This activation step can

happen spontaneously inside the body after injection after exposure to tissues' native collagen [500] or prior PRP administration by freezing and thawing [501] or, most commonly, by adding thrombin or calcium chloride [499, 502]. Cost-wise, PRP and platelet concentrates are more affordable than cell therapy [503]. PRP can be prepared from the patient's blood (autologous) shortly before or during the treatment session or surgical procedure (intraoperatively), which renders it non-immunogenic and more practical to use as a regenerative therapy option [498, 504]. The effect of PRP on bone healing has a well-established publication record. Where PRP can be delivered to the bone defect site as an injectable solution [505], hydrogel [506-508] or sponge [509]. Yet, most commonly (and most successfully), PRP is being used mixed with autologous bone grafts [510-512], allografts [513-515] or in combination with synthetic osteoinductive scaffolds and bone graft substitutes [516-521]. A review article published by Roffi et al. (2017) that included 45 preclinical *in vivo* studies and 19 clinical studies highlighted that 91.1 % of the preclinical studies support the benefit of PRP use for bone healing; however, upon more in-depth analysis a lower success rate (84.4 % in terms of histological analysis, and 72.7 % when biomechanical evaluation was included) was revealed. Similar statistics were concluded from the clinical literature, where the real benefit of using PRP to treat fractures and non-unions needs further investigation to be better predicted and understood [522]. Some studies indicated that using PRP led to non-union [523] and hindered bone repair due to fibroproliferative properties that consequently inhibited bone matrix deposition [523].

2.5.4- Physical and mechanical stimuli:

The cells inside our bodies exist in a dynamic environment, which influences gene expression, cell signalling, homing, arrangement, proliferation, differentiation and even morphology. The dynamics of the *in vivo* environment are not replicated in standard static tissue culture conditions, and this limits the translational relevance of many of the *in vitro* models used preclinically. In the context of bone tissue engineering, the ultimate goal is to be able to generate a system where the end product is an *in vitro* engineered bone graft ready to be implanted into the patient. In traditional static cell culture systems, cells grow well in monolayer because they depend on diffusion to get nutrition, but when a complex three-dimensional structure is required (i.e. a multi-centimetre 3D scaffold seeded with cells), the static culture system fails to maintain the viability of cells in the core of the scaffold and a necrotic centre develops due to lack of nutrition; additionally seeding scaffolds with cells in a static system will not achieve an adequate cell distribution over the scaffold's surface. Even if the scaffold is completely immersed in culture media, a nutrient diffusion gradient develops

that drives the cells to migrate toward the periphery, where the nutrients are more abundant [524]. On top of that, physical stimuli are critical for functional regeneration, particularly for bone cells, which are known to be very sensitive to mechanical stimuli that provoke intra and inter-cellular signals involved in bone remodelling as well as healing in case of injury [525, 526].

Introducing biochemical stimuli for the purpose of bone healing can be either done ***in vitro*** (i.e. pre-implantation) or ***in vivo*** (i.e. patient/ animal treatment) through development of tailored dynamic *in vitro* tissue culture systems (also known as bioreactors) [527-529] or through treating the cells and/or the scaffolds (*in vitro*) or the patient (*in vivo*) with other reported means of physical/mechanical stimuli such as focused ultrasound [530-533] shear stress and dynamic compression [534, 535], magnetic field stimulation [536-538] and extracorporeal shockwaves [539-541]. Functional and design characteristics for tissue engineering bioreactors are demonstrated in **Figure 7.** The types of bioreactors used for bone tissue engineering and the basic principles behind them are explained in **Table 9.**

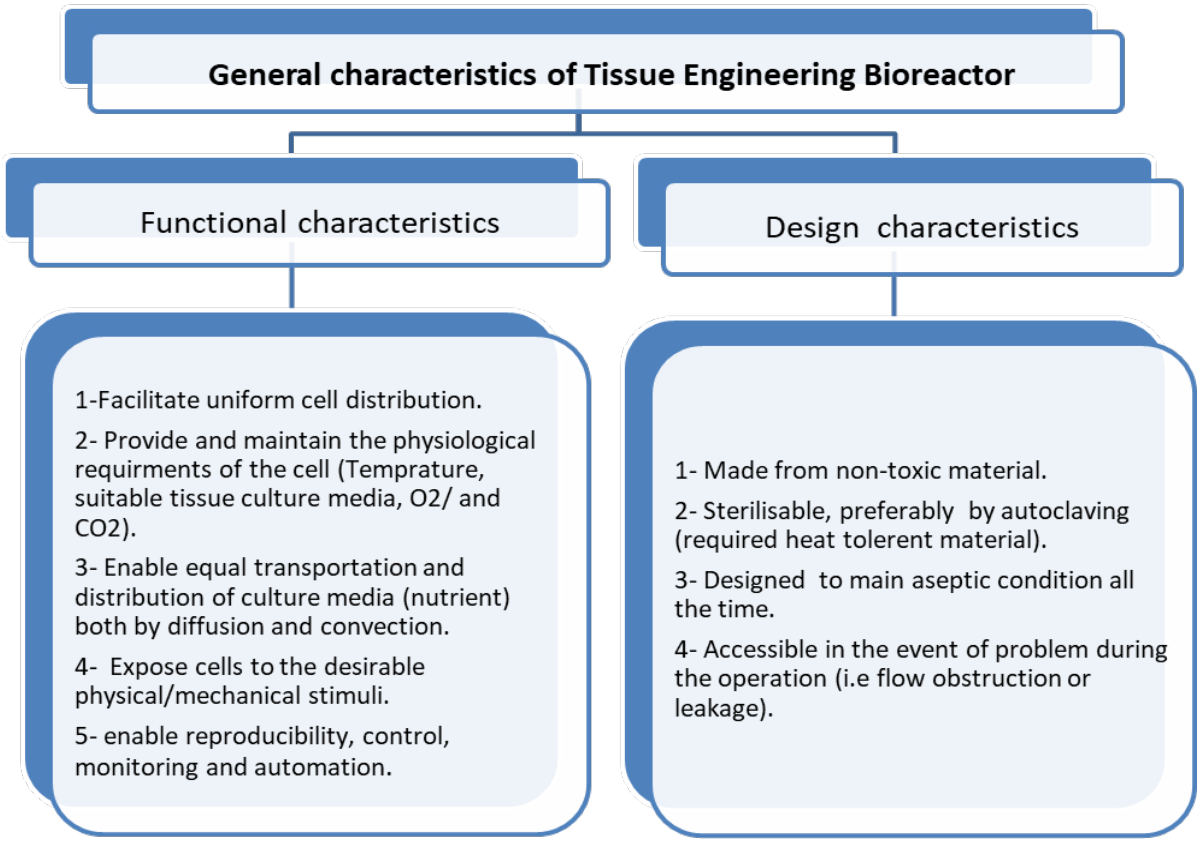


Figure 7: General functional and design characteristics of tissue engineering bioreactors.

Table 9: Types of bioreactors used for bone tissue engineering.

Bioreactor type	General principle
Rotating wall vessels	Originally designed to test the effect of space's microgravity condition on tissues [542]. It is basically a concentric rotating horizontal cylindrical tissue culture vessel filled with culture medium, where media oxygenation is provided via a coaxial tubular silicon membrane. When the velocity of the rotating fluid evens out the sedimentation rate of the cell/scaffold constructs, they maintain a "free-fall" state and are subjected to dynamic laminar flow [543].
Spinner flasks	Traditionally used to support large biomass growth and recently used as tissue engineering bio reactors [544]. A glass or plastic vessel in which cell/scaffold constructs are attached to vertical needles hanging from the top of the vessel and immersed in the culture medium. The gas exchange system is provided from the top of the vessel, while a stir plate at the bottom of the vessel is used for media mixing, the force generated during stirring produces turbulences that enhance media transport toward the center of the construct [545].
Perfusion bioreactors	They are culture systems composed of one or more perfusion chambers where the cell/scaffold constructs are placed, a medium reservoir, a tubing circuit and a pump enabling mass transport of nutrients and oxygen throughout the perfusion chamber. Perfusion bioreactors are broadly classified into indirect or direct systems, depending on whether the culture medium is perfused around or throughout the cell/scaffold constructs [529, 546, 547].
Compression systems	These bioreactors are the closest system that mimics bone physiological environment *in vitro*. It achieves a repeated mechanical stimulation via system providing linear motion and a compression chamber in which one or more pistons apply static or dynamic compressive loads directly to the cell/scaffold constructs [529, 548].
Combination of different types	Combinations of more than one types of bioreactors in order to better mimic the bone physiological environment *in vitro* (i.e. compression bioreactors with added perfusion) [549].

- **Extracorporeal shockwave therapy (ESWT)**:

Shockwaves are high-energy sonic waves with peak pressure 1000 times higher than ultrasounds [550]. The first reported medical use of ESWT was for the purpose of kidney stones treatment [551]. Extracorporeal shockwave therapy has proven to be effective in translational (*in vitro*), pre-clinical and clinical studies related to multiple musculoskeletal disorders. *In vitro*, ESWT shows a positive effect on the mesenchymal stem cells (MSCs) proliferation [539, 552], MSCs surface markers expression [541], and preservation of MSCs multipotentiality, although some researchers reported no significant effect on differentiation toward the osteogenic lineage [539].

Different *in vitro* setups were developed aiming to study the effect of shock waves on stem cells [553]; including direct treatment of cell suspensions in tubes [554-556], adherent cells in tissue culture flasks or plates [557], or cell pellets [558, 559]. In these setups, the shock waves travel through air then through cell culture medium before reaching the cells. The issue with air/ culture medium shockwave transition is that the difference between the acoustic impedance of cell culture medium and air is very high (1,440,000 Ns/m^3 for culture medium vs 420 Ns/m^3 for air); thus, more than 99% of the shock waves are reflected, and phase shift of shock waves also occurs. Phase shift turns the positive pressure pulse into a tensile wave that might destroy the cells [560].

To overcome this issue, researchers designed an *in vitro* system that involve submerging cell culture containers full of medium in a water bath to avoid air-to-water transition [560-562]. Others embedded the cells in agarose gel [563-565] or even used pork skin [566], trying to mimic natural tissue consistency.

ESWT has been successfully used clinically and in *in vivo* studies to treat fracture non-union [567-570], chronic tendonitis and tendinopathy [571-573], peripheral nerve lesions [574], ischemic lesions [575, 576], chronic wounds and ulcers healing [577-580]. The mechanism of action of shockwaves is still poorly understood. There is a strong suggestion that it exerts its effect through the principle of mechano-transduction, which means the conversion of mechanical stimuli into a biochemical signal. Mechanically, the pressure created by the ESW generates energy that gets concentrated at the target point where treatment is provided. This initiates an inflammatory response in the target tissue, which in turn results in increased blood supply, neovascularisation and inflammatory mediators release, which is believed to have a chemotactic effect leading to MSCs attraction from the surrounding tissues to the site of shockwave application and initiates growth factors release as well as transcription factors cascade [581-585]. The National Institute for Health and Care Excellence (NICE) published

guidelines on the use of Extracorporeal shockwave therapy for refractory plantar fasciitis, refractory Achilles tendinopathy and refractory tennis elbow [586-588]. However, the published literature on the treatment of musculoskeletal disorders using ESWT still needs further validation.

2.6- Pre-clinical animal models:

2.6.1- Animal models for biomaterial safety testing:

The ISO10993 (Biological Evaluation of Medical Devices) is considered the gold standard when designing a study to determine the bio-safety of implantable biomaterials [589, 590]. The ISO standard is recognised by most major national regulatory bodies, including the FDA and CE (Conformité Européene) [591]. To select the biological tests necessary for assessing the safety of a medical device, part 1 of ISO 10993 (Part 1: Evaluation and testing within a risk management process)[592] has listed the tests to be performed based on the area of contact between the medical device and the patient and its duration of contact as shown in **Table 10.**

When selecting the animal model species, the guidelines point out that small laboratory animals such as mice, rats, hamsters or rabbits are preferred. However, the use of larger animals may be justified based upon special scientific considerations of the particular biomaterial under study and taking into consideration the size of the implant test materials, the number of implants per animal, the intended duration of the test in relation to the expected lifespan of the animals, as well as potential species' differences regarding biological response. Generally speaking, study duration vary with short-term responses are normally assessed from 1 - 4 weeks and long-term responses in tests exceeding 12 weeks [589].

The listed implantation sites are subcutaneous, muscles, bone and brain. The rule of thumb is that test samples shall be implanted into the tissues most relevant to the intended clinical use of the material. If other implantation sites are chosen, the general scientific principles behind the test methods described for the selected implantation site shall still be adhered to, and justification provided. Test materials are to be compared to a control material that is clinically acceptable and has an established biocompatibility profile. Preferably, the control and the test materials are implanted in the same animal under the same circumstances [589]. At least three animals and sufficient implantation sites to yield a total of 10 test samples for each material and implantation period have been established as sufficient to reach a conclusion regarding the material's bio-safety [589, 593]. Another recognised guideline is the ASTM F981– 04, which instructs that rats (from acceptable strains), New Zealand white rabbits, and other small

laboratory animals may be used as test hosts for soft tissue implant responses, where there shall be a minimum of four animals at each sacrifice interval for a total of twelve animals per study. If larger animals are used, in which a greater number of implants may be placed, at least two animals shall be sacrificed at each time point [594].

Table 10: ISO 10993-1 list of evaluation tests to be performed based on the area of contact between the medical device and the patient.

Medical device category			**Biological evaluation test**									
Category	**Contact**	**A – limited** (≤24 h) **B – prolonged** (>24 h to 30 d) **C – Long term** (>30 d)	**Physical and/or chemical information**	**Cytotoxicity**	**Sensitisation**	**Irritation or intracutaneous reactivity**	**Material mediated pyrogenicity**	**Acute systemic toxicity**	**Sub acute toxicity**	**Sub chronic toxicity**	**Chronic toxicity**	**Implantation effects**
Surface medical device	Intact skin	A	X	X	X	X						
		B	X	X	X	X						
		C	X	X	X	X						
	Mucosal membrane	A	X	X	X	X						
		B	X	X	X	X		X	X			X
		C	X	X	X	X		X	X	X	X	X
	Breached or compromised surface	A	X	X	X	X	X	X				
		B	X	X	X	X	X	X	X			X
		C	X	X	X	X	X	X	X	X	X	X
Externally communicating medical device	Blood path, indirect	A	X	X	X	X	X	X				
		B	X	X	X	X	X	X	X			
		C	X	X	X	X	X	X	X	X	X	X
	Tissue/ bone/	A	X	X	X	X	X	X				
		B	X	X	X	X	X	X	X			X

	dentin	C	X	X	X	X	X	X	X	X	X	X
	Circulating blood	A	X	X	X	X	X	X				
		B	X	X	X	X	X	X	X			X
		C	X	X	X	X	X	X	X	X	X	X
Implant medical	Tissue/bone	A	X	X	X	X	X	X				
		B	X	X	X	X	X	X	X			X
		C	X	X	X	X	X	X	X	X	X	X
	Blood	A	X	X	X	X	X	X				X
		B	X	X	X	X	X	X	X			X
		C	X	X	X	X	X	X	X	X	X	X

Evaluation of the local biological effect (also known as: material/ tissue interaction) is performed macroscopically and microscopically by a comparison of the tissue response caused by a test specimen to that caused by a control material used in medical devices of which the clinical acceptability and biocompatibility characteristics have been established [595].

Bio-irritancy parameters include fibrosis, inflammatory cells infiltration, tissue degeneration, immune cell response in terms of numbers and distribution, necrosis, vascularisation, new tissue formation, and fatty infiltration. Material biodegradation parameters, include surface erosion, fragmentation, and phagocytosis [289, 591, 593, 596].

2.6.2- Animal models for studying critical size bone defects:

Despite the continuous efforts and advancements toward establishing *in vitro* models to test a therapeutic approach or to mimic the disease conditions of interest, not all the biological, physiological, chemical, and physical circumstances can be achieved on an *in vitro* basis. Hence, a clinically relevant animal model is an essential requirement to validate the obtained results translatability from bench to bed.

When choosing a suitable animal model, several factors should be considered, such as: species availability, cost, manageability, availability of housing facilities and social acceptability [597]. However, the anatomical, physiological and biomechanical properities relative to the scientific question of interest remain the key detrimining factors.

In the context of orthopaedic research and tissue engineering, a wide range of animal models have been developed over the years; generally, they can be classified into two major categories: large animal models (i.e. sheep, goat, dog and pig) and small animal models (i.e. rat, mouse and guinea pig), the rabbit model is somewhere in between large and small preclinical models [598, 599]. Rabbit and rodent models are not uncommonly used in orthopaedic research as they are more affordable and socially acceptable; additionally, they have proven their suitability for proof-of-concept studies and bone biology studies. However, the large animal models are the ones of choice for preclinical translational research [600]. According to ASTM F981– 04 guidelines, rats (from acceptable strains), New Zealand white rabbits, and other small laboratory animals may be used as test hosts for soft tissue implant response. It is suggested that the rats be age and sex matched. Rabbits or larger animals may be used as test hosts for bone implants. When larger animals such as dogs, goats, or sheep are used, the decision should be based upon special considerations of the particular implant

material or study [594]. Pros and cons of different preclinical animal models are listed in **Table 11**.

Choosing the most suitable animal model for critical size bone defects is also debatable. However, from the previously published research, it has been concluded that: small animal models such as mice, rats, and to some extent, rabbits have proven their suitability for non-load bearing critical size defects such as calvarial bone, ulnar and long bones epiphyseal and partial cortical defects [601-606], while the dog model was reported the most suitable pre-clinical model for mandibulo-maxillary defects due to the relative mechanical similarity to human [607, 608]. Meanwhile, small ruminants, particularly sheep, are the most translationally relevant for studying long bone segmental defects due to the advantages of availability, having comparable body weight and bone dimensions, mineral composition and bone remodelling rates that are all very similar to human [597, 609-611].

In my study, the rabbit radius segmental defect was my preclinical model of choice. Radial defects are one of the rabbit's most used load-bearing bone defect preclinical model. Due to the lack of need to use fixation devices (e.g. pins or plates) that is attributed to the support offered by the adjacent ulna. This makes it relatively straightforward, less expensive, less risky and more refined from an animal experience perspective in comparison to femoral defect for instance [599, 612, 613]. In addition to the radial defect, other rabbit models have been used to test new bone substitute biomaterials in the past few decades, including tibial defects [614-616], distal femur defects [617-619], femoral diaphysis segmental defect [620-622], calvarial defects (which is another common use for rabbits as a preclinical model) [603, 623, 624] and peri-alveolar dental defects [617]. The ease of management, the manageable cost compared to large animal models, and the similarity to veterinary patients (small dogs, cats and pet rabbits) make rabbits an appealing preclinical model, particularly in proof-of-concept studies.

Table 11: Pros and cons of preclinical animal models in orthopaedic research:

	Large animal models	**Small animal models**	**Intermediate model**
Species	**Sheep, goat, dog and pig**	**Rat and mouse**	**Rabbit model**
Advantages	• Comparable bone anatomy to human which allows testing of human costumed implants [625]. • Bone growth, modelling and remodelling patterns close to human (it varies between species). • Allows the use of clinically relevant internal and external fixation devices [626]. • Allows development and validation of novel surgical planning strategies and surgical techniques [627, 628]. • Mechanically reliable for studying load bearing defects. • Allows more advanced and clinically relevant outcomes assessment methods such as: kinetic and kinematic gait analysis [629-631].	• Less expensive. • Easier to manage. • Allow studies that need to be carried out on a large number of animals (i.e., bone biology studies). • Their shorter life span also facilitates studies on the effects of aging on bone and tissue-engineered constructs[606]. • More socially acceptable to use for research purpose.	• Similarities in bone mineral density and the fracture toughness of mid-diaphyseal bone between rabbits and human bones [632], although debatable. • Easily available and less expensive to house/ manage than small ruminants, pigs and dogs. • Comparable body weight to some of veterinary patients (small breed dogs, cats and pet rabbits)
Disadvantages	• More expensive. • More difficult to manage and requires large housing facilities. Thus, limits the number of animals that can be included per study.	• Major physiological difference from human and veterinary patients which are represented chiefly by unstoppable bone growth and modelling throughout the animal's life and very different bone remodelling patterns [626, 633] . • Mechanically challenging and has several limitations on mechanical testing (i.e. rats long bone mechanical testing is usually limited to bending or torsion of long bones but not compression) besides the difficulty to accurately measure the mechanical properties of trabecular bone in rodents [606]. • Don't allow the use of internal and external fixation devices or need use of specially tailored ones. • Not the ideal model for studying defects involves load bearing. • Small size renders it unsuitable for studying orthopaedic implants [634].	• Small size renders it unsuitable to study joint replacement implants [634] • Faster skeletal change and bone turnover than human that makes it difficult to translate the results from rabbit studies to human clinical application [635].

2.7- Additive manufacturing for customisable orthopaedic implants:

Additive manufacturing is the process of creating an object by building it one layer at a time, represented by 3D printing; it is a rapidly growing technology with multiple successful applications in various medical fields, including orthopaedics. These applications resonate with three themes: education, planning and manufacturing. **Education**: 3D printed anatomical models and patient specific models from patients' CT scans are excellent training tools for medical students and trainees (residents and interns) and to help explain the diagnosis and surgical procedures to the patients during consults [636-639]. **Planning**: 3D *in silico* and 3D printed bone models are invaluable tools during pre-surgical planning, particularly in complex cases, by providing enhanced visualisation of anatomical models and allowing surgical procedures rehearsal [636]. The pre-operative planning and rehearsals facilitated by 3D printed models limit the time needed in the operating room (for instance, determining ideal fixation device location and configuration, and in turn minimise the time spent intra-operatively having to make these same decisions) and improve the surgical outcomes leading to a safer more refined patients experience [636, 640, 641]. **Manufacturing:** 3D printing and CAD (computer-aided designs) are revolutionising tools that allow the production of custom-made patient-specific surgical guides (e.g. cutting jigs, guides and templates) [642-645] as well as custom-made implants (e.g. joint replacement implants, bone fixation device and biocompatible prosthetics for bone reconstruction surgeries) [639, 646-650].

There are several steps in between, from the point where the patient gets admitted to the hospital to having a 3D-printed bone model and/or custom-made surgical guide or implant in hand. Briefly, it starts **with patient's** Computed Tomography **(CT)** or Magnetic Resonance Imaging **(MRI) scans** with output files in **DICOM** (Digital Imaging and Communications in Medicine) format, followed by creating ***in silico* 3D models** out of these scans using medical image processing software (such as 3D slicer, Mimics, OsiriX, 3D doctor, Magics and In Vesalius) to create a standard tessellation language (**STL**) or Geometric code (**G-code**) file that can be used as a template for virtual planning or to define regions for the 3D printer. **Mesh refinement** of these 3D models is advisable using software like Autodesk Meshmixer, Ansys or 3-matics. These 3D models are either used as templates for *in silico* surgical planning, including designing custom-made guides or implants using **CAD designing** software such as Fusion 360, Autodesk Meshmixer, 3-matics, AutoCAD or Sketch UP or go directly for **3D printing**. The different methods of 3D printing are summarised in the section below [639, 651, 652].

It is not obligatory, but it is preferred that the software program has Food and Drug Administration (FDA) clearance, which is a necessary first step to obtaining Current Procedural Terminology (CPT) codes required for insurance reimbursement according to USA healthcare policies. The FDA considers any software that is used to create "Diagnostic use" anatomical models a class II medical device [636, 653]. While 3D models are listed under Category III CPT codes by the American Medical Association as an "emerging technology, service, and procedure" [654].

The 3D printing technologies for medical applications are broadly based on four main principles: extrusion, powder polymerisation, sintering, or droplet spraying [639, 655] (see **Table 12** for further details).

3D printing with biological substrates, often referred to as **bioprinting**, is an innovative and interdisciplinary field that merges the principles of 3D printing technology with those of tissue engineering and regenerative medicine. Bioprinting is defined as depositing cells, extracellular matrices, and/or biologically relevant materials in user-defined patterns to build tissue constructs de novo or to build upon prefabricated scaffolds [656]. This technology is used for fabricating tissue constructs or even organs, along with generating microfluidic models of organs-on-a-chip [657]. These constructs have been successfully applied to *in vitro* drug testing and disease modelling. The ultimate goal of bioprinting is clinical engraftment. While a complete, functional organ has yet to be printed, the field is moving towards this eventual feasibility [658].

Similar to 3D printing, bioprinting can be inkjet-based, laser-based, or extrusion-based bioprinting (explained in table 12) [659]. Extrusion based bioprinting is the most commonly used type of 3D printing in tissue engineering applications including orthopaedic tissue engineering [660-662]. Most extrusion bioprinters contain multiple print heads for printing multiple materials within a single construct. This allows researchers to manufacture constructs with regional differences in biomaterials, cell types, cell densities, and signalling molecules [661]. Additionally, extrusion bioprinters can also operate at higher cell densities; however, the cells are exposed to shear stress during extrusion which decreases cell viability [663, 664].

Several materials, such as synthetic polymers and naturally derived biomaterials have been intensively explored to innovate 3D bioprinting and reproduce functional tissue structures [665]. The materials used for bioprinting can be either a plain biomaterial (or a combination of more than one biomaterial) used to 3D print acellular scaffolds that are intended to recruit

the patient's own cells to migrate into the scaffold [658] or printing with cells combined with hydrogel and/or any bioactive compounds, the materials in this instance are referred to as bioinks [666]. A bioink is a ‘formulation of material(s) and biological molecules and/or cells processed using bioprinting technologies [667]. Hydrogels are preliminary used when printing with cells due to their high-water content and ability to suspend cells. However, because of the high water content, it has become evident that it is challenging for hydrogel alone to hold shape upon deposition; on the other hand if the hydrogel viscosity is too high it cannot be extruded without damaging the cells due to high shear stress [658, 663]. Hence, most bioinks are not self-supporting without some secondary intervention. Most commonly, one or more forms of crosslinking (thermal, ionic or ultraviolet (UV) crosslinking) are used [668].

Biocompatible synthetic polymers, such as polycaprolactone (PCL), polylactic acid (PLA), and polyurethane (PU), are the most applicable biomaterials in 3D bioprinting owing to their biocompatibility, adjustable mechanical properties, controllable degradability, and great printability [669, 670]. Despite their lack of bioactivity, plain polymers are commonly used as framework materials that provide an intrinsic physical and mechanical support within the resulting tissue construct. Synthetic polymers are usually combined with biological materials and/or factors (such as tissue matrices, bio-ceramics, growth factors or cells) to attune the composite bioactivity according to the intended application [659, 671].

In recent years 3D printing with decellularised extracellular matrix (DECM) has proven to be promising in the field of tissue engineering. Pati et al. in 2014 were the first to demonstrate the feasibility of using decellularised ECM as a printable bioink [672]. Printing with extracellular matrix can replicate this tissue-specific structural and compositional complexity that are difficult to reproduce using synthetic biomaterials and support cellular migration and proliferation [673, 674]. However, concerns were raised concerning batch-to-batch variation, inconsistency of DECM compositions, low mechanical stability (unless mixed with polymeric biomaterial), and potential xeno-immune responses [659, 673, 675].

For musculoskeletal tissue engineering, 3D bioprinting-based bioprinting has opened new avenues in the production of 3D functional tissue substitutes that encourage the regeneration of impaired tissues such as bone [676, 677], cartilage [678, 679], tendon/ligament [680, 681], and their associated multi-tissue interface [682-684].

Most biomaterials (bioinks) used for bone tissue engineering applications incorporate bioceramics (such as HA and β- TCP) or DCBM to improve the scaffolds’ osteoinductivity and osteoconductivity (see section 2.4- bone graft substitutes).

Printed scaffold design plays an important role in its behaviour in the body upon implantation. With bone scaffolds, porosity, pore size and surface roughness influence the scaffolds osteointegration with native bone and osteoinductive properties [685, 686]. Scaffold porosity and pore size relate to the surface area available for the adhesion and growth of cells both in vitro as well as *in vivo* and so to the potential for host tissue ingrowth [687]. High porosity encourages osteointegration, neovascularisation, better nutrients and oxygen exchange [688, 689]. However, there is a trade-off between porosity and the scaffold's mechanical properties (moduli) [690, 691]. Pores smaller than 100 μm in diameter were found to restrict vascular penetration; interestingly, these results correlate with the diameter of the physiological Haversian systems in bone tissue that possess an approximate diameter of more than 100 μm [687, 692]. Pores and pore interconnections >300 μm in diameter were found to allow sufficient vascularisation [689]; a pore size of around 500–600 μm is ideal for osteointegration [693]. In addition to pore size, the shape of the pores also plays a role in determining the scaffold's properties; for example research has shown that circular pores of around 500 μm lead to superior cell adhesion [694]. Besides porosity, the scaffold's surface roughness also has a large impact on osteogenic response; it favours cell attachment, proliferation, and osteogenic differentiation [695, 696]. A rough scaffold surface not only provides a wider growth space to accommodate more cells but also allows the scaffold to absorb more water and expose more protein adsorption sites thus promoting cell attachment and proliferation [686].

Table 12: 3D printing technologies for medical applications.

Principle	Printing technology	How it works	Advantages	Disadvantages	References
Extrusion-based	Fused deposition modelling (FDM)	Filament extrusion through heated nozzle	- Wide range of FDM based 3D printers are available on the market for affordable prices. - Wide range of materials or combination of materials can be used (most commonly thermoplastics).	- Slow printing speed - Average resolution - Print failure due to various reasons is not uncommon - The printed models cannot be autoclaved	[697-699]
	Bio-plotting and direct ink writing 3D printing	Different fluids (inks) ± cross-linker are extruded through a nozzle (or a needle) in a continuous manner using pressure or mechanical forces driven by dispensing systems such as air, a piston, or screws.	- Allow usage of novel bio-inks including cell-laden inks. - Open door to innovative research including tissue engineering applications, organs on chip and 3D printed tissues or even organs. - For Bio-plotting, it allows using bioinks with high viscosity and high cell density. - Both FDM and bio-plotting, extrusion-based 3D printing allows multi-material deposition, high level of structural complexity and heterogeneity.	- Average printing speed - Average resolution - Expensive - Low mechanical strength	[659, 700-706]
Polymerisation	Stereolithography	Polymeric resins	- Higher resolution	- Mid-range cost	[707-709]

	(SLA)	photopolymerised by ultraviolet laser or visible light	- Faster print speed - Availability of autoclavable resins	- Expensive resins	
Sintering	- Selective laser sintering (SLS) - Selective laser melting (SLM) - Electron beam melting (EBM) - Direct metal laser sintering (DMLS)	Thermoplastic, ceramics or metallic powders are being heated by high-energy CO2 laser and deposited in required shape	- Allow different material combinations hence, it allows novel implant manufacturing - Allows custom made metallic implant manufacturing	- Expensive - Slow print speed - Printed objects needs post printing processing (such as machining and polishing)	[710-715]
Droplet-based	Inkjet printing	Polymeric and or biomolecules solution droplets are being sprayed onto a platform where they then cure into the desired shape. The inkjet printing heads are temporally deformed by thermal or piezoelectric approaches to eject droplets of varying sizes	- Allow usage of novel inks including ones loaded with bio-active molecules (such as hyaluronic acid, growth factors or even cells) - Fast printing speed - High resolution	- Limited mechanical strength - Expensive - Low cell density - Restricted range of ink viscosity - Difficulty in large volumetric constructs	[659, 716-720]

Chapter 3: Methodology

3- Methodology

In this chapter, I will describe in detail the materials and methods I used, followed and developed during the course of my PhD. There are five main subsections:

3.1- Stem cells (particularly Ad-MSCs) isolation, characterisation and differentiation towards the osteogenic lineage.

3.2- Investigating the potential use of extracorporeal shockwaves (ESW) and its effect on MSCs proliferation and osteogenic differentiation

3.3- Bone graft substitute biomaterials (scaffolds) fabrication and their *in vitro* characterisation

3.4- Testing the local biological effect of the selected biomaterials (scaffolds) after implantation (biocompatibility testing) in a preclinical rat subcutaneous implantation model.

3.5- Testing the ability of the selected biomaterials (scaffolds) to support bone healing in a critical size segmental long bone defect (15 mm long radial defect) rabbit model.

3.1- Adipose derived mesenchymal stem cells (Ad-MSCs) isolation and characterisation:

We isolated and characterised AD-MSCs cells from 3 different species (sheep, rabbit and rat); see **Figure 8** for the summarised Ad-MSCs isolation steps.

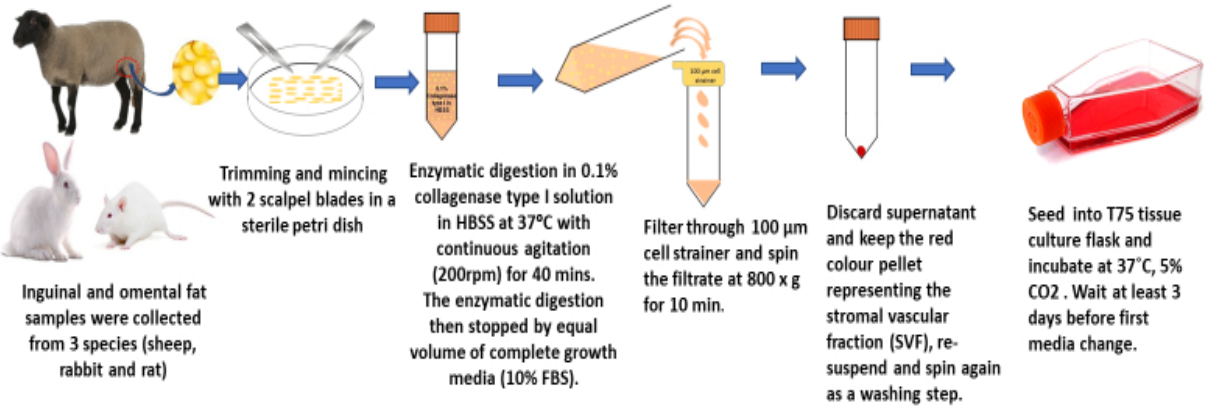


Figure 8: Adipose derived mesenchymal stem cell isolation steps.

3.1.a- Ad-MSCs isolation

Sample collection, preparation and cell isolation:

Adipose tissue sample collection: Omental and inguinal fat samples were collected aseptically immediately post-mortem from animals euthanised for reasons unrelated to this study. Approximately 20 g were collected from sheep (Welsh mountain ewes less than 3 years old and weighing between 60 and 80 kg); 5 g were harvested from rabbits (female New Zealand white rabbits, 12 weeks of age and weighing between 2.5 and 3.5 kg); and 2 g were collected from rats (male Sprague Dawley rats weighing 250 - 300 g). Fat samples were recovered into phosphate-buffered saline (1x PBS; Thermo Fisher, Gibco™- Cat. No. 70011044, Loughborough-UK) supplemented with 1 % (v/v) penicillin-streptomycin (Pen-Strep; Sigma Aldrich, Cat. No. P4333, Gillingham, Dorset, UK), then washed 3 times with 1 % Pen-Strep in PBS solution. All visible blood vessels and connective tissue were isolated and discarded using fine scissors and forceps.

Mechanical dissociation and enzymatic digestion: The trimmed fat specimen was minced into fine pieces using two scalpel blades in a sterile petri dish, then enzymatically digested using 0.1 % collagenase type I (Fisher Scientific, Gibco™-17018029, Loughborough, UK) in Hank's balanced salt solution (Fisher Scientific, Gibco™, Cat. No. 24020117, Loughborough, UK) ≃1 ml/g fat, for 30 - 40 min with continuous agitation (200 rpm) at 37 ºC. An equal volume of complete growth medium (GM) with 10 % fetal bovine serum was added to the reaction to stop the enzymatic digestion. Complete growth medium consisted of Dulbecco's modified Eagle's medium (DMEM, (Gibco™ low glucose), GlutaMAX™ Supplement, pyruvate (Fisher Scientific, Gibco™, Cat. No. 21885108), Loughborough, UK) with 10 % foetal bovine serum (FBS) (Fisher Scientific, Gibco™, Cat. No. 26140079, Loughborough, UK) and 1 % Pen-Strep (Sigma Aldrich, Cat. No. P4333, Gillingham, Dorset, UK).

Stromal vascular fraction isolation: The digested sample was subsequently filtered through a 100 µm cell strainer (Sigma Aldrich, Corning® cell strainer, Cat. No. CLS431752, Gillingham, Dorset, UK) and the filtrate was spun at 800 x ***g*** for 10 min. The supernatant was discarded and the red coloured pellet representing the stromal vascular fraction (SVF) was kept. The pellet was then re-suspended in complete growth medium and spun again (800 x ***g*** for 10 min) as a washing step.

Primary culture seeding: The washed SVF was seeded into a T75 tissue culture flask (Sigma Aldrich, Cat. No. C7231, Gillingham, Dorset, UK) at a density of $1x10^5$ cells/cm^2 and incubated at 37 ˚C, 5 % CO_2 . As an optional step, an ammonium chloride based RBC lysis step could be used before seeding cells. The primary cell culture was left for at least three

days without a medium change to allow cells to adhere to the tissue culture flask plastic. The cells were monitored for confluency; when 80 % confluency was reached, the first passage (split) commenced.

3.1.b- Ad-MScs characterisation:

3.1.b.I: Cell Morphology:

- **Inverted light microscopy:**

The EVOS™ XL Core Imaging System was used to check basic cell morphology, cell adherence and first colony formation, and to evaluate the cell confluency percentage.

The adherent cells were stained with haematoxylin for more detailed cell morphology imaging. $1x10^4$ cells/well were seeded in a 6-well tissue culture plate for 48 hours in growth medium. After 48 hours, the growth medium was removed, the cell monolayer was rinsed with PBS, and the cells were fixed with 70 % ethanol (3 ml/well) for 1 hour at room temperature. Then, filtered haematoxylin solution-Harris modified (Sigma Aldrich, Cat. No. HHS16, Gillingham, Dorset, UK) was added to the fixed cells (3 ml/well) for 4 min at room temperature, followed by rinsing the monolayer under running water for 2 min, then, rinsing with 70 % ethanol for 30 seconds. The stained monolayer was then examined and imaged using a EVOS™ XL Core inverted light microscope imaging system.

- **Immunofluorescence:**

For the ovine MSCs, beta-actin specific (13E5) rabbit monoclonal antibody (Cell Signalling Technology®, Cat. No. 4970; Leiden, NL) was used to bind to the MSC cytoskeletal β –actin, which was then labelled by goat anti-rabbit IgG H&L (Alexa Fluor® 488) secondary antibody (Abcam, Cat. No. ab150077, Cambridge, UK). For the rabbit and rat MSCs, anti-β-Actin–FITC, mouse monoclonal antibody (Sigma Aldrich, Cat. No. F3022, Gillingham, Dorset, UK) was used. Images were acquired using a Nikon Eclipse 80i upright fluorescent microscope and processed using Fiji (Image-J) image analysis software [721]. Details are explained in **Table 13.**

Table 13: Beta-Actin immunofluorescence staining for Ad-MSCs:

Step	Explanation
Cell culture	600 µl of $2x10^4$ cells/ml per well were seeded in a Nunc™ Lab-Tek II four-well chamber slide system (Fisher Scientific, Thermo Scientific™, Cat. No. 16240671, Loughborough, UK), then incubated overnight at 37 ˚C, 5 % CO_2 to allow cell adherence.
Cell fixation	Culture medium was removed and cells were washed with PBS (600 µl/well) and fixed using 4 % paraformaldehyde for 20 min at room temperature. Then the fixative was aspirated and cells were washed 3 times with PBS.
Methanol permeabilisation	Cells were covered with 100 % ice-cold methanol, and incubated at -20 ˚C for 10 min, then rinsed 5 times with PBS.
Blocking	Cells were incubated with blocking buffer consisting of 5 % goat serum, 0.3 % Triton™ X-100 (Sigma Aldrich, Cat. No. 93443, Gillingham, Dorset, UK) in PBS at room temperature for 1 hour.
Primary Antibody application	After removal of the blocking buffer, the slide was washed 3 times with PBS for 5 minutes each. Then the recommended dilution of the primary antibody (1:200) was added to each well and the slide was incubated for 2 h at room temperature or overnight at 4 ˚C.
Secondary Antibody application	The primary antibody was washed away by rinsing 3 times with PBS, and the diluted secondary antibody (1:200) added to each well and the slide incubated for 2 h at room temperature in the dark, then washed 3 times with PBS.
Mounting and slide examination	A drop of mounting medium VECTASHIELD® Antifade Mounting Medium with DAPI (2b Scientific-SKU: H-1200-10, Kirtlington, Kidlington, UK) was added over the coverslip then pressed against the slide to avoid air bubble accumulation. The slide was examined immediately using a Nikon Eclipse 80i upright fluorescent microscope at x40 magnification. Images were capture using an INFINITY-2 Microscopy Camera system.

- **Scanning electron microscope (SEM):**

The Ad-MSCs were seeded over 10 mm round glass coverslips in 24-well tissue culture plates (1 x 104 cells/well) in GM and incubated at 37 ˚C, 5 % CO2 for 48 hours. Then, the culture medium was removed, the coverslip was rinsed twice with PBS, and the cells were fixed using 3 % glutaraldehyde (Sigma Aldrich, Cat. No. G5882, Gillingham, Dorset, UK) for 3 hours at room temperature, followed by sample dehydration in ascending concentration series of ethanol (30 %, 40 %, 50 %, 60 %, 70 %, 80 %, 90 % and 2x 100 %), 15 min each. Drying was carried out using hexamethyldisilazane (HMDS, Sigma Aldrich, Cat. No. 440191, Gillingham, Dorset, UK) in a series of the following: HMDS:100% ethanol (ratio 1:2), HMDS:100% ethanol (ratio 2:1) and HMDS alone for 20 min each, then the specimen was left to dry overnight in a fume hood. All steps with HDMS were performed inside the fume hood. Finally, processed glass coverslips were sputter coated with gold and imaged with

under a scanning electron microscope (NOVA Nano SEM 450- FEI, supported by ThermoFisher, Loughborough, UK) using different magnifications.

3.1.b.II: Behaviour in tissue culture

- **Colony Forming Unit (CFU) assay:**

Isolated Ad-MSCs at early passage (p2 to p3) were seeded at a density of 100 cells/well in 6-well tissue culture plates and incubated at 37 ˚C in a humidified atmosphere containing 5 % CO_2 for 10 days. Then, the culture medium was removed, cells were washed with PBS, then fixed in 10 % neutral buffered formalin for 10 min at room temperature. To visualise the colonies, cells were stained with 0.5 % (w/v) crystal violet in 2 % (v/v) ethanol for 5 min at room temperature, followed by washing with distilled water (DW) several times until stain residues were cleared out. The wells were imaged, and stained colonies were examined using an inverted light microscope.

- **Cell proliferation and viability assay (MTT):**

A standard curve was plotted by seeding a known number of Ad-MSCs (ranging from $1x10^6$ to 0) cells/well in 24-well tissue culture plates in duplicate for 6 h to allow cell adhesion. This was followed by running an MTT assay as follows: 5 mg/ml MTT stock solution was prepared by dissolving 0.1 g MTT reagent (3-(4,5-dimethylthiazol-2-yl)-2,5 diphenyltetrazolium bromide) (Abcam, Cat. No, ab146345, Cambridge, UK) in 20 ml 1x PBS, followed by filter sterilisation. One hundred µl of the MTT stock solution (final 10 % volume) was added to each well containing 1 ml media and incubated at 37 ˚C for 2 hours. Unconverted MTT reagent was removed by aspirating the medium and then rinsing the cells with PBS. The formazan crystals in the cells (converted MTT product) were then solubilised by adding 500 µl of dimethyl sulfoxide (DMSO, Sigma Aldrich, Cat. No. D4540, Gillingham, Dorset, UK) to each well with continuous agitation on a plate shaker (200 rpm) for 5 min. Aliquots of the solubilised reaction product (violet in colour) were transferred to a 96-well plate and the absorbance was measured at 570 nm using a microtiter plate reader (Multiskan™ FC Microplate Photometer, Fisher Scientific, Thermo Scientific ™, Cat. No. 51119000, Loughborough, UK).

To quantify proliferation rate over time, the isolated Ad-MSCs were seeded at a density of $1x10^5$ cells per well in 24-well tissue culture plates. A MTT assay was conducted on days 1, 3, 7 and 10. The resultant absorbance at each time point was measured and plotted against the standard curve.

- **Cell migration assay (scratch wound healing assay):**

Ad-MSCs were seeded at a density of $5x10^5$ cells per well in a 6-well tissue culture plate, incubated at 37 ℃, 5 % CO_2 until reaching 80 % confluency. The cell monolayer was gently scratched across the surface of the well using a 1 ml pipette tip to create a gap in the monolayer, and rinsed with PBS to remove detached cells. Fresh medium was added, the plate was incubated at 37 ˚C, 5 % CO_2 and cells were monitored for migration to close the gap at 0 hours and 24 hours (n=3 wells/time point). I used Fiji (Image-J) image analysis software [721] to measure the scratch wound area over time. The wound closure percentage was calculated using the formula: Wound closure % $= \frac{0\text{ hr area} - 24\text{ hr are}}{24\text{ hr area}}\ x100.$

3.1.b.III: Tri-lineage differentiation

To investigate the Ad-MSCs multi-potentiality and ability to differentiate into multiple lineages, Ad-MSCs were conditioned to differentiate towards osteogenic, adipogenic and chondrogenic lineages. Briefly, for the osteogenic and the adipogenic differentiation assays, cells were seeded at a density of $1x\ 10^5$ cells per well in 24-well tissue culture plates in GM for 24 - 48 hours for cell adhesion and proliferation. Ready-made commercially available differentiation medium (DM) was added to half of the wells to induce cell differentiation, while the other half were kept in GM as controls for the differentiation detection assays. StemPro® Osteogenic and StemPro® Adipogenic differentiation media (Fisher Scientific, Gibco™, Cat. No. A1007201 and A1007001, respectively, Loughborough, UK) were used in the study.

For chondrogenic differentiation, a micromass culture was created by seeding a 5 µl droplet of cells at $1.5\ x\ 10^7$ cells/ml in the centre of each well; the micromass culture was incubated for 2 hours under high humidity at 37 ˚C, 5 % CO_2 to allow cell attachment, then chondrogenic medium (StemPro® Chondrogenic differentiation medium, Fisher Scientific, Gibco™, Cat. No. A1007101, Loughborough, UK) was added to half of the wells and re-incubated. For all plates, medium was changed every three days and special stains were used to confirm the differentiation status after 21 days in DM, as explained in **Table 14**. All differentiation assays were performed in quadruplicate.

Table 14: Stains used to investigate trilineage differentiation of Ad-MSCs.

Stain	**Alizarin red S stain** (Fisher scientific, Thermo Scientific™, Cat. No. 11329707)	**Oil red O stain** (Sigma Aldrich, Cat. No. O0625)	**Alcian blue stain** (Sigma Aldrich, Cat. No. A3157)
Used for	Staining of calcium deposition as an indicator of osteogenic differentiation	Staining of oil droplets in cells as an indicator of adipogenic differentiation	Staining of proteoglycans as an indicator of chondrogenic differentiation
Cell fixation	Ice cold 70 % ethanol for 1 hour	10 % formalin at RT for 1 hour	10 % formalin at RT for 10 min then replace it with fresh 10 % formalin for 1 hour.
Working Concentration	40 mM, pH 4.2	0.35 % weight/ volume	1 % Alcian blue solution in 0.1 N HCL
Staining protocol	Remove medium, rinse cells with PBS, fix with 70 % ice-cold ethanol, and rinse with PBS then stain for 10 min, rinse the cells again with PBS then add 1 ml/well alizarin red S stain for 15 min at RT, followed by rinsing 4 - 5 times with DW, followed by visual inspection and microscopic imaging	Remove medium, rinse cells with PBS, fix with 10 % formalin, and rinse with DW followed by rinsing in 60 % isopropanol for 2 min at RT. Let the cell monolayer dry completely then add 1ml/well Oil Red O working solution for 15 min at RT, followed by rinsing 4 -5 times with DW, followed by visual inspection and microscopic imaging. Haematoxylin can be used as a counter background stain to facilitate visualisation of the oil red O-stained fat droplets.	Remove medium, rinse cells with PBS, fix with 10 % formalin, discard fixative and rinse with DW then add 1ml/well staining solution, incubate for 1 h at room temperature protected from light. Then staining solution removed and cells rinsed 2 - 3 times with 0.1 N HCl (200 µl/well). Finally, visual inspection, and microscopic imaging.
Destaining and quantification	10 % cetylpyridinium chloride (Sigma Aldrich, Cat. No. C0732) was added to wells and the resulting eluted colour was quantified at 570 nm using microtiter a plate reader.	100 % isopropanol was added to wells and the resulting eluted colour quantified at 450 nm using a microtiter plate reader.	6 M guanidine HCl (Merck, Millipore, Cat. No. 369079) was added to wells and the resulting eluted colour quantified at 620 nm using a microtiter plate reader.

3.1.b.IV: Surface markers expression (Flowcytometry):

Immunophenotypic characterisation of the isolated Ad-MSCs was performed using flow cytometry (BD Accuri™ C6, BD Biosciences, Reading, UK). Sequential identification and refinement of the cell population of interest (gating) was performed in a double gate discrimination, relying on negative staining of isotype control and the negative expression of CD 45 surface marker as an inclusion criteria. The antibodies that were used are listed in **Table 15 (for the ovine MSCs), Table 16 (for rabbit MSCs) and Table 17 (for rat MSCs).**

Cell preparation for flow cytometry was performed as follows:

- Cells were harvested using 5 mM EDTA in calcium and magnesium-free Dulbecco's PBS (ThermoFisher, Gibco™, Cat. No. 14200059, Loughborough, UK), counted, washed with cell staining buffer (Biolegend®, Cat. No. 420201) and adjusted to a concentration of 10^7 cells/ml.
- 100 µl of the cell suspension were added to Eppendorf tubes (1.5 ml) to get 10^6 cells/ tube.
- Primary conjugated antibodies were then added according to the recommended dilution and incubated for 30 min in the dark at 4 ˚C.
- The cells were then washed twice by adding 400 µl of cell staining buffer and centrifuging at 300 ***g*** for 5 min.
- For biotinylated CD45 antibody, an extra step of incubation with PerCP Streptavidin for 30 minutes in the dark at 4˚C was conducted after washing off the primary antibody solution, followed by washing the Streptavidin containing solution.
- Cells were resuspended in 150 µl FACS buffer and kept on ice until flow cytometric analysis.
- UltraComp Beads™ (ThermoFisher, Invitrogen™, Cat. No. 01-3333-41, Loughborough, UK) were used to facilitate compensation as shown in **Table 18** for ovine MSCs, **Table 19** for rabbit MSCs, **Table 20** for rat MSCs.

Table 15: Antibodies used for immunophenotypic characterisation of ovine Ad-MSCs.

Marker	Conjugation	Antigen	Antibody Clone	Host	Reactivity	Supplier and Catalogue number	Dilution
CD90	PE	Thy-1 cell surface antigen	Polyclonal	Rabbit	Human, Mouse, Rat, Sheep	Bioss antibodies bs-0778R-PE	(1:20-100)
CD44	FITC	glycoprotein receptor for hyaluronic acid	25.32	Mouse	Sheep Bovine Goat Human	Bio-RAD MCA2219 F	Neat - 1:10
CD45	Biotin + PerCP Streptavidin	Lymphocyte Phosphatase-Associated protein	1.11.32	Mouse	Sheep Bovine Goat	Bio-RAd MCA2220 B	Neat - 1:10
						PerCP Streptavidin Biolegend 405213	≤0.125 µg/ 106 cells in 100 µl volume
CD105	APC	Endoglin	MJ7/18	Rat	Mouse	Biolegend 120413	≤0.25 µg/ 10^6 cells in 100 µl volume
CD73	PE	5'-nucleotidase	TY/23	Rat	Mouse	BD Bioscience s 550741	1:10
Isotype Control	PE	IgG Isotype Control Antibody		Rabbit		Bioss antibodies bs-0295P-PE	Concentrations comparable to those of the specific antibody of interest.
Isotype Control (for CD44)	FITC	IgG1, κ Isotype Control Antibody	MOPC-21	Mouse		Biolegend 400107	
Isotype Control (for CD45)	Biotin	IgG1, κ Isotype Control Antibody	MOPC-21	Mouse		Biolegend 400103	
Isotype Control (for CD105)	APC	IgG2a, κ Isotype Control Antibody	RTK2758	Rat		Biolegend 400511	
Isotype Control (for CD90 and CD73)	PE	IgG2a, κ Isotype Control Antibody	RTK2758	Rat		Biolegend 400507	

Table 16: Antibodies used for immunophenotypic characterisation of rabbit Ad-MSCs.

Marker	Conjugation	Antigen	Antibody Clone	Host	Reactivity	Supplier and Catalogue number	Dilution
CD90	Alexa Fluor® 647	Thy-1 cell surface antigen	OX-7	Mouse	Rat, Rabbit, Mouse, Guinea Pig	Biorad MCA47A647T	Neat-1:10
CD44	Unconjugated	glycoprotein receptor for hyaluronic acid	W4/86	Mouse	Rabbit	Biorad MCA806GA	1:25 – 1:200
Goat F(ab')2 Anti-Mouse IgG H&L (PE)		Secondary antibody for CD 44		Goat	Mouse	Abcam ab7002	1:100 – 1:250
CD45	Unconjugated	Lymphocyte Phosphatase-Associated protein	Poly clonal	Rabbit	Human, Mouse, Rabbit, Rat	ThermoFisher, Invitrogen PA5-85429	1:50-1:200
Goat Anti-Rabbit IgG H&L preadsorbed (FITC)		Secondary antibody for CD 45		Goat	Rabbit	Abcam ab7086	1:200-1:500
CD105	FITC	Endoglin	MEM-226	Mouse	Human	Abcam ab18278	Neat-1:10
CD73	PE	5'-nucleotidase	AD2	Mouse	Human	Abcam ab157335	Neat-1:10
Isotype Control for CD90	Alexa Fluor® 647	IgG1 kappa Isotype Control	MOPC-21	Mouse		Abcam ab239459	Concentrations comparable to those of the specific antibody of interest.
Isotype Control for CD73 and CD44	PE	IgG1	B11/6	Mouse		Abcam ab91357	
Isotype Control for CD105	FITC	IgG2a, kappa monoclonal	MOPC-173	Mouse		Abcam ab18455	
Isotype Control for CD45	FITC	IgG	Polyclonal	Rabbit		Abcam ab37406	

Table 17: Antibodies used for immunophenotypic characterisation of rat Ad-MSCs.

Marker	Conjugation	Antigen	Antibody Clone	Host	Reactivity	Supplier and Catalogue number	Dilution
CD90	Alexa Fluor® 647	Thy-1 cell surface antigen	OX-7	Mouse	Rat, Rabbit, Mouse, Guinea Pig	Biorad MCA47A647T	Neat-1:10
CD44	PE	glycoprotein receptor for hyaluronic acid	OX50	Mouse	Rat	Abcam ab23396	Neat-1:10
CD45	Unconjugated	Lymphocyte Phosphatase-Associated protein	Poly clonal	Rabbit	Human, Mouse, Rabbit, Rat	ThermoFisher, Invitrogen PA5-85429	1:50-1:200
Goat Anti-Rabbit IgG H&L preadsorbed (FITC)		Secondary antibody for CD 45		Goat	Rabbit	Abcam ab7086	1:200-1:500
CD105	FITC	Endoglin	MEM-226	Mouse	Human	Abcam ab18278	Neat-1:10
CD73	PE	5'-nucleotidase	AD2	Mouse	Human	Abcam ab157335	Neat-1:10
Isotype Control for CD90	Alexa Fluor® 647	IgG1 kappa	MOPC-21	Mouse		Abcam ab7086	Concentrations comparable to those of the specific antibody of interest.
Isotype Control for CD73 and CD44	PE	IgG1	B11/6	Mouse		Abcam ab239459	
Isotype Control for CD105	FITC	IgG2a, kappa	MOPC-173	Mouse		Abcam ab91357	
Isotype Control for CD45	FITC	IgG	Polyclonal	Rabbit		Abcam ab18455	

Table 18: Staining plan for immunophenotypic analysis of ovine MSCs

Tube #	Contents
1.	Unstained cells
2.	Cells + PE CD90
3.	Cells+ PE CD73
4.	Cells+ APC CD105
5.	Cells+ CD45 Biotin/PerCP Streptavidin
6.	Cells+ FITC CD44
7.	Cells+ PE CD90+ APC CD105+FITC CD44+CD45 Biotin/PerCP Streptavidin
8.	Cells+ CD45 Biotin/ PerCP Streptavidin+ isotypes master mix PE,APC, FITC
9.	Cells + isotype ctrl PE
10.	Cells + isotype ctrl FITC
11.	Cells + isotype ctrl APC
12.	Cells + isotype ctrl PerCP Streptavidin
13.	Beads + FITC-Rabbit IgG
14.	Beads+ PE CD90
15.	Beads+ APC CD105
16.	Beads + CD45 Biotin/PerCP Streptavidin

Table 19: Staining plan for immunophenotypic analysis of rabbit MSCs.

Tube #	Contents
1.	Unstained cells
2.	Cells + Alexa 647 CD90
3.	Cells+ PE CD73
4.	Cells+ FITC CD105
5.	Cells + isotype ctrl Alexa 647
6.	Cells+ CD45+ secondary FITC
7.	Cells+ CD44+ secondary PE
8.	Cells + isotype ctrl PE
9.	Cells + isotype ctrl FITC mouse IgG
10.	Cells + isotype ctrl FITC rabbit IgG
11.	Cells + isotype ctrl master mix 1 (Alexa 647+PE+FITC mouse IgG)
12.	Cells + Alexa 647 CD90 + PE CD73 + FITC CD105
13.	Cells + unconjugated mouse IgG1 + PE secondary AB
14.	Cells+ CD45/ 2ndry FITC + Alexa 647 isotype+ PE isotype
15.	Cells+ CD45/ 2ndry FITC + Alexa 647 CD90 + PE CD73
16.	Cells + CD44/PE secondary AB + Alexa 647 isotype + isotype ctrl FITC mouse IgG
17.	Cells + CD44/PE secondary AB + Alexa 647 CD90 + FITC CD105
18.	Beads + FITC-Rabbit IgG
19.	Beads+ PE Mouse IgG1 [B11/6]
20.	Beads+ Alexa Fluor® 647 Mouse IgG1 kappa [MOPC-21]

Table 20: Staining plan for immunophenotypic analysis of rat MSCs.

Tube #	Contents
1.	Unstained cells
2.	Cells + Alexa 647 CD90
3.	Cells+ PE CD73
4.	Cells+ PE CD 44
5.	Cells+ FITC 105
6.	Cells+ CD45+FITC 2ndry AB
7.	Cells + unconjugated CD45 + 2ndry FITC
8.	Cells+ FITC rabbit IgG Isotype CTRL for CD45
9.	Cells + isotype ctrl mater mix 1 (Alexa 647+PE+FITC mouse IgG)
10.	Cells + isotype ctrl mater mix 2 (Alexa 647+PE+FITC rabbit IgG)
11.	Cells+ CD45/ 2ndry FITC + Alexa 647 isotype+ PE isotype
12.	Cells + PE CD73 +FITC CD105
13.	Cells+ PE CD44 + Alexa 647 CD90
14.	Cells+ CD45/ 2ndry FITC + Alexa 647 CD90
15.	Beads unstained
16.	Beads+ Alexa 647 CD90
17.	Beads+ PE CD73
18.	Beads+ FITC CD105

3.1.c- Ad-MSCs osteogenic differentiation

3.1.c.I- ALP activity

Alkaline phosphatase activity is indicative of the matrix maturation stage. To measure ALP activity, Ad-MSCs were seeded at a density of $1x10^5$ cells/well in 24-well tissue culture plates. Only 12 wells were seeded in total, half of the wells (6 wells) were used as controls and grown in GM and the other half (6 wells) were switched to osteogenic DM 48 hours after seeding. This plate set-up was repeated for each time point (3 days, 7 days, 14 days and 21 days in osteogenic DM).

Alkaline Phosphatase activity detection is a four-stage assay: cell lysis, protein quantification, ALP quantification and result interpretation.

- Cell lysis:

At each time point, medium was removed, and cells were washed with ice-cold PBS, then 500 µl of cold RIPA cell lysis buffer (Fisher Scientific, Invitrogen™, Cat. No. FNN0011, Loughborough, UK) mixed with 5 µl of protease inhibitor compound (Fisher Scientific, Thermo Scientific™ Pierce™, Cat. No. A32955, Loughborough, UK) added. The plate was kept on ice for 5 min with occasional swirling. Cells were scraped from the well bottom using a one ml pipette tip then, cell lysate was transferred to microcentrifuge tubes. The tubes were shaken on a plate shaker at maximum speed for 10 min on ice, followed by centrifugation at 14000 x ***g*** for 15 min. The supernatant was transferred to new labelled microcentrifuge tubes, and the pellets were discarded.

- Protein quantification:

The protein content in the extracted cell lysate was quantified using the Micro BCA™ Protein Assay Kit (Fisher Scientific, Thermo Scientific™, Cat. No. 23235, Loughborough, UK) following the manufacturer's instructions. Briefly, it is a three-stage procedure that starts with the preparation of bovine serum albumin (BSA) dilutions (from 0 µg/ ml to 600 µg/ml) for a standard curve plotting, followed by working reagent (WR) preparation out of the provided reagents (A, B and C) based on the calculated required volume for both standards and unknown samples and the number of replicas, taking into account that 100 µl WR is needed per sample and the A:B:C solution ratio should be (25:24:1). Finally, the microplate was set up in 96-well plates: 100 µl of each standard and unknown sample, then an equal volume of the prepared working reagent was added to each well, then the plate was covered and incubated at 37 ˚C for 2 hours, and the absorbance was measured at 570 nm using the microtiter plate reader (Multiskan™ FC Microplate Photometer, Fisher Scientific, ThermoScientific™, Cat. No. 51119000, Loughborough, UK). The protein concentration in

the unknown samples was calculated by comparing the absorbance against the BSA standard curve, and results were expressed as µg protein/ml cell lysate.

- Alkaline phosphatase (ALP) activity quantification:

The ALP activity in the extracted cell lysate was quantified using 2-amino-methyl-1-propanol (AMP) substrate buffer. To prepare 100 ml of the AMP substrate buffer, 6.28 g of 2-amino-methyl-1-propanol (Sigma Aldrich, Cat. No. 08578, Gillingham, Dorset, UK) was dissolved in 80 ml of DW, then 0.019 g of magnesium chloride (Sigma Aldrich, Cat. No. M8266, Gillingham, Dorset, UK) was added to give a final concentration of 2 mM, followed by 0.237 g 4-nitrophenyl phosphate bis(tris) salt (pNPP) (Sigma Aldrich, Cat. No. S783064, Gillingham, Dorset-, UK) to give a final concentration of 9 mM. Finally, the pH was adjusted to 10.5, and the volume topped up to 100 ml with DW. A standard curve was plotted using different concentrations of 4-Nitrophenol stock (p-nitrophenol) solution 10 mM (Sigma Aldrich, Cat. No. N7660, Gillingham, Dorset, UK) diluted in the AMP substrate buffer (from 0 to 0.4 µmol/ml). Finally, the microplate setup in a 96-well plate, 100 µl of each unknown sample, and then an equal volume (100 µl) of the prepared AMP substrate buffer was added to each well. The plate was covered and incubated at 37 ˚C for 30 min. The absorbance was measured at 405 nm using the microtiter plate reader (Multiskan™ FC Microplate Photometer, Fisher Scientific, Thermo Scientific ™, Cat. No. 51119000, Loughborough, UK). The concentration of ALP in the unknown samples was calculated by comparing it against the pNPP standard curve.

- Interpretation of results:

ALP activity was normalised to protein concentration and reaction time, and was expressed as µmol p-nitrophenol per µg protein per minute.

3.1.c.II-Alizarin red S staining (ARS) and quantification:

Matrix mineralisation was detected and quantified using alizarin red S staining. The plate setup for ARS experiments was similar to that used for ALP assays, with $1x10^5$ Ad-MSCs per well in 24-well tissue culture plates. Alizarin red S staining was conducted as described in **Table 14** on days 3, 7, 14 and day 21. Briefly, cells were fixed in 70 % ice-cold ethanol for 1 hour, rinsed with PBS, and then stained with 40 mM ARS for 15 minutes at room temperature. The stained monolayers were then rinsed with DW, air dried and visualised/photographed. After imaging, the stain was eluted with 10 % (w/v) cetylpyridinium chloride and the optical density of the resulting solution was measured with a microplate reader at 570 nm.

3.1.c.III- Quantification of osteogenic marker gene expression by quantitative PCR (qPCR):

The expression of osteogenesis-related genes: runt-related transcription factor (Runx-2), osteonectin (ON), osteocalcin (OC), collagen type I (COL I) and osteopontin (OPN) were quantified by qPCR after culturing Ad-MSCs in osteogenic DM for 7 days, 14 days and 21 days. Ad-MSCs cultured in GM were used as control/calibrators to calculate the fold increase in gene expression. The expression of these genes of interest was normalised against two housekeeping genes (Glyceraldehyde-3-phosphate dehydrogenase, GAPDH, and β-actin).

The MSCs were seeded at a density of $1x10^5$ cells in T25 tissue culture flasks in duplicates for each medium type per time point.

- RNA extraction and reverse transcription to cDNA:

At each time point, cells were harvested and spun at 300 x ***g*** for 5 min to obtain a cell pellet. Then the RNA was extracted using RNeasy® Plus Mini kit (QIAGEN, Cat. No. 74034, Hilden, Germany) according to the manufacturer's instructions, followed by RNA quantification using NanoDrop® ND-1000 Spectrophotometer (Fisher Scientific, Thermo Scientific™, Loughborough, UK).

Finally, the isolated RNA was reverse transcribed to cDNA using a high-capacity cDNA reverse transcription kit (Fisher Scientific, Applied Biosystems™, Cat. No. 4368814, Loughborough, UK) and FlexCycler2 PCR thermocycler (Analytik Jena, Überlingen-Germany).

- Primer design:

Sheep, rabbit and rat specific oligonucleotides were designed after reviewing relevant literature and searching the for the gene sequence using the NIH, National Center for Biotechnology Information (NCBI) online gene database [722]. The gene sequences were used to design primers using the Primer3Plus online primer design tool [723] with the following criteria: 20 – 30 nucleotides in length, 60 °C, +/− 2 °C melting temperature, 50 -60 % GC content and at the 3′ end a C, G, CG or GC (**Tables 21, 22 and 23).** The designed primers were purchased from Sigma Aldrich (Gillingham, Dorset, UK) predesigned DNA Oligos and qPCR Probes online ordering system [724].

- qPCR**:**

The quantitative PCR was performed using a SYBR® green PCR kit (Rotor-Gene SYBR® Green PCR Kit, Qiagen, Cat. No. 204001, Hilden, Germany) and Rotor-Gene® Q2 plex Priority qPCR thermocycler with 72 Well Rotor (Qiagen, Product ID: 9001861, Hilden, Germany) in a 25 µl reaction volume (for ovine Ad-MSCs) or iTaq Universal SYBR Green Supermix (BioRad, product number 1725121, Watford, Hertfordshire, UK) and BioRad

CFX96 Real-Time PCR Machine C1000 or BioRad® qPCR thermo-cycler (BioRad, Watford, Hertfordshire, UK); 96-well plate and 20 µl reaction volume (for rabbit and rat Ad-MSCs).

Table 21: Primers design for ovine Ad-MSCs qPCR.

Gene	Sequence (5′-3′, F = forward, R = reverse)
Runx-2	F: AAGAAGAGCCAGGCAGGTGC
	R: CATACCGAGGGACATGCCTGAG
Osteonectin (ON)	F: AGCTGCGAGTGAAGAAGATCCACG
	R: TCGGTGTGAGACAGGTACCCG
Osteocalcin (OC)	F: CACAGCCTTCGTGTCCAAGC
	R: GCTCACACACCTCCCTCCTG
Collagen type I (Col I)	F: AGAACAGCGTGGCCTACATG
	R: TCCGGTGTGACTCGTGC
OPN	F: AGGGACAGAACTCGGCCGTG
	R: CCAGTGTATTGTGTTTGGCCCTC
β –actin (house keeping gene)	F: TCAGCAATGCCTCCTGCAC
	R: TCTGGGTGGCAGTGATGGC
GAPDH (house keeping gene)	F: TTCGAGCAAGAGATGGCCAC
	R: ACAGGACTCCATGCCCAG

Table 22: Primers design for rabbit Ad-MSCs qPCR.

Gene	Sequence (5′-3′, F = forward, R = reverse)
Runx-2	F: TCAGGCATGTCCCTCGGTAT
	R: TGGCAGGTAGGTATGGTAGTGG
Osteonectin (ON)	F:CTCCACCTGGACTACATCG
	R: GCTGGCCAAACTGCCAGTG
Osteocalcin (OC)	F: ACTCTTGTCGCCCTGCTG
	R: CTGCCCTCCCTCTTGGAC
Collagen type I (Col I)	F:GCGGTGGTTACGACTTTGGTT
	R: AGTGAGGAGGGTCTCAATCTG
OPN	F: GCAGAATCTCCTAACACCGCAG
	R: GGTCATCGTCCTCATCCTCATC
β –actin (housekeeping gene)	F: AGA TCA AGA TCA TCG CGC C
	R: TCC AAC GAC TGC TGT CAC CT
GAPDH (housekeeping gene)	F: GCCTGGAGAAAGCTGCTAAGT
	R: GAGTGGGTGGCACTGTTGAA

Table 23: Primers design for rat Ad-MSCs qPCR.

Gene	Sequence (5′-3′, F = forward, R = reverse)
Runx-2	F: AGCGGACGAGGCAAGAGTTT
	R: CTGTCTGTGCCTTCTTGGTTCC
Osteonectin (ON)	F: CTC CCT GGC CCC CCT GGT GCA CC
	R: CCC TGG ACC CCC TGG CAC TGC TGG TGC TC
Osteocalcin (OC)	F: GAG GAC CCT CTC TCT GCT CAC TCT GCT GG
	R: CCT CTC TCT GCC TCG AAA GTA TGG AC
Collagen type I (Col I)	F: CTC CCT GGC CCC CCT GGT GCA CC
	R: CCC TGG ACC CCC TGG CAC TGC TGG TGC TC
OPN	F:GTTGAGTCATTCCTGTGGGC
	R:GCCCTTTAAGCACGACACCC
β –actin (housekeeping gene)	F: TGATAAAGGCAACTGTTGGATTGA
	R: CCGCTGGGTGTCCTGATGT
GAPDH (housekeeping gene))	F: CCA CGA GAA ATA TGA CAA CTC CCT C
	R: GGT GGT GAA GCA GGC GGC CGA GGG

Result interpretation

Target gene expression was quantitatively analysed using the delta delta CT (ΔΔCT) method. ΔΔCT is the difference between the ΔCT of the gene of interest for an experimental sample (Ad-MSCs in osteogenic DM) and the ΔCT of that same gene for the calibrator sample (Ad-MSCs in GM). Calculated as the following:

ΔCT = CT (gene of interest) – CT (housekeeping gene)

ΔΔCT= ΔCT (Ad-MSCs in Osteogenic DM) – mean ΔCT (Ad MSCs in GM)

CT (cycle threshold) is defined as the number of cycles required for the fluorescent signal to exceed background levels. CT levels are inversely proportional to the amount of target nucleic acid in the sample (i.e. the lower the CT level the greater the amount of target nucleic acid in the sample).

3.1.c.IV- Scanning Electron Microscopy (SEM):

The Ad-MSCs were seeded over 10 mm round glass coverslips in a 24-well tissue culture plate (1 x 10^5 cells/well) in GM for 24 hours, followed by switching to osteogenic DM for two weeks with a regular medium change every three days. The sample was prepared and imaged as in section 3.1.b.I.

3.2-The effect of extracorporeal shockwaves (ESW) on MSCs

3.2.1-The effect of focused versus radial ESW on Ad-MSCs (direct ESW application)

The effect of focused and radial extracorporeal shockwave therapy (ESWT) on Ad-MSC proliferation and osteogenic differentiation was studied *in vitro* using 6 different settings (500 shocks each) in comparison with a control negative group that did not receive any ESWT.

The experiment was carried out in triplicates, using a DUOLITH® VET shockwave machine (Storz Medical, Tägerwilen, Switzerland).

3.2.1.a-Effect of shockwave treatment on Ad-MSC proliferation:

The effect of ESWT on Ad-MSC proliferation was assessed using an MTT assay on day 1, day 3 and day 7 post-treatment. The MTT assay was performed as described in the cell characterisation section (3.1.b.II).

A total of $7x10^6$ cells divided between seven 15 ml falcon tubes (1 x 10^6 cells per tube suspended in 15 ml complete growth media) received the ESWT, as summarised in **Table 24.** Ultrasound coupling gel was applied to the shockwave probe, and the shocks were applied directly to the falcon tube wall, moving gradually along its longitudinal axis to ensure exposure of the entire cell suspension. After the ESWT, the cells from each tube were seeded in three 24-well plates (one plate for each time point) at a density of $1x10^5$ cells/well in triplicates **(Figure 9).**

Table 24: Shockwave treatment frequencies used in the study.

Tube Number	Frequency	Type of shockwaves	Number of shocks
1	0 - Control	No shockwave	Zero
2	0.05 mJ/mm^2	Focused	500 shocks
3	0.12 mJ/mm^2	Focused	500 shocks
4	0.4 mJ/mm^2	Focused	500 shocks
5	1.2 bar	Radial	500 shocks
6	1.8 bar	Radial	500 shocks
7	2.4 bar	Radial	500 shocks

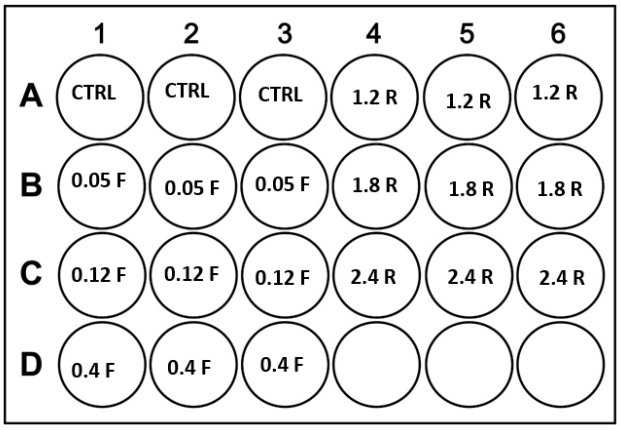


Figure 9: Plate setup for MTT assay post ESW treatment (direct shocks application). The setup was replicated for day 1,3 and 7 post-treatment.

3.2.1.b-Effect of shockwave treatment on Ad-MSCs osteogenic differentiation:

To evaluate the effect of ESWT on Ad-MSC osteogenic differentiation, a similar experimental set-up to the one used for the proliferation assay was used. Ad-MSCs from each treatment group were seeded at a density of 1x 10^5 cells per well in 24-well plates (n=6 wells/treatment group) in growth medium for 48 hours at 37 ˚C, 5 % CO_2. Then the medium was switched to the osteogenic DM (Stempro® osteogenesis differentiation kit) in half of the wells, leading to each treatment group having 3 wells of cells seeded in GM and 3 wells seeded in osteogenic DM (see **Figure 10).** The plates were incubated for 19 days with regular medium changes every 3 days. Alizarin red S staining and stain quantification was performed at day 21 post-treatment as previously described at the tri-lineage differentiation (osteogenic differentiation) section 3.1.b.III.

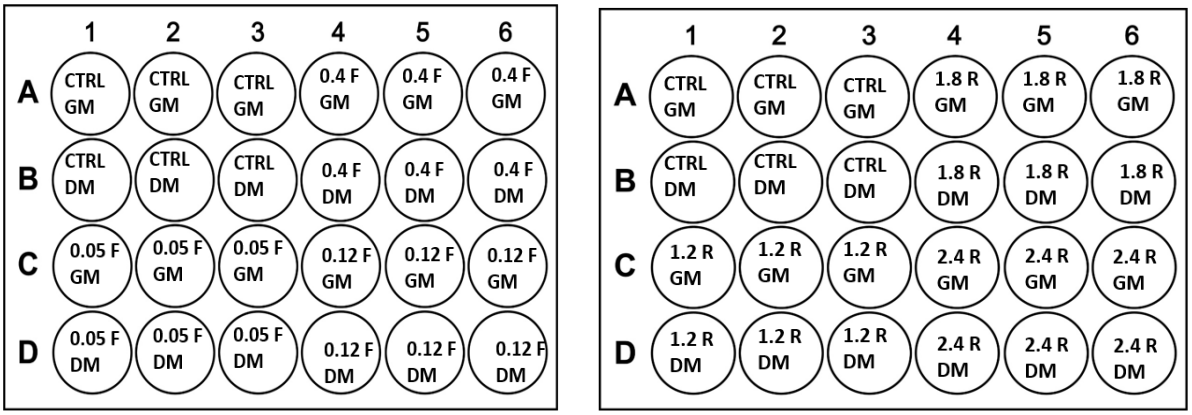


Figure 10: Plate set up for alizarin red S staining post ESW treatment (direct shocks application).

3.2.2- The effect of focused ESWT on Ad-MSCs (designed water bath *in vitro* testing apparatus):

3.2.2.a-*In vitro* apparatus design:

In the direct application ESWT method mentioned above, the shockwaves pass through 2 different media, water (in the tissue culture medium) and air. The difference in the acoustic impedance between the cell culture medium and the air is very high; leading to more than 99 % of the shock waves becoming reflected, and a phase shift of the shock waves occuring. The phase shift turns a positive pressure pulse into a tensile wave which might be destructive to the cells.

Hence, I designed an *in vitro* apparatus to allow ESW to travel through water around the treatment target (i.e. cell culture medium). It is a modified water bath inspired by Holfeld et.al (2014) [560] in a published video article (see **Figure 11** below for the design). The main frame of this apparatus is a plexiglass water bath (30 cm wide x 45 cm long x 26 cm deep)

with a silicon membrane (80 mm diameter aperture) fitted at its anterior aspect (treatment port) where the shock wave probe was placed to deliver the ESWT; ultrasound coupling gel was used during the application to avoid air gaps. A heater at the bottom and a digital thermometer to control water temperature at 37 °C to avoid cooling of cell cultures were fitted. A holder (Cole-Palmer burette clamp) was used to hold culture flasks or tubes to be treated. During treatment the cell culture container needed to be completely filled with culture medium as air bubbles compromise the shock wave efficiency. A wedge-shaped reflector was fitted at the back of the water bath opposite the treatment port to eliminate ESW reflection and possible deleterious effects on the cells.

3.2.2.b-Experimental setting:

A DUOLITH® VET (Storz Medical, Tägerwilen, Switzerland) shockwave machine was used. For the purpose of this experiment and to mimic what we use clinically in fracture non-union patients, I elected to use focused shockwaves for the MSC treatment. The number of cells needed for this experiment was $5x10^6$ cells divided between 5 falcon tubes (15 ml) each tube containing 1 x 10^6 cells suspended in 15 complete GM. The water bath was pre-heated to 37 °C and the tube distance was set to 2 cm away from the silicon membrane treatment port. Ultrasound coupling gel was applied to the shockwave probe and the shocks were delivered through the silicon membrane (treatment port). The shock wave treatment groups were as shown in **Table 25**. Cell proliferation and osteogenic differentiation were evaluated for each treatment.

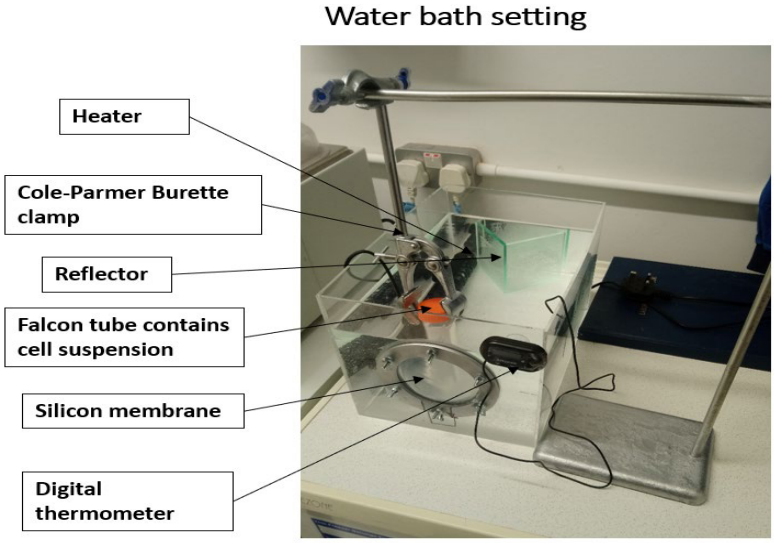


Figure 11: *In vitro* experimental setting to test the effect of ESW on Ad-MSCs proliferation and osteogenic differentiation.

Table 25: Shockwave treatment groups (water bath *in vitro* testing apparatus).

Tube Number	Frequency (mJ/mm^2)	Type of shockwaves	Number of shocks
1	Zero (control)	No shockwave	Zero
2	0.05	Focused	500 shocks
3	0.15	Focused	500 shocks
4	0.3	Focused	500 shocks
5	0.55	Focused	500 shocks

3.2.2.b.I-Cell Proliferation (MTT assay):

In 24-well cell culture plates, cells from the control group and each treatment group were seeded in growth medium at a density of 1x10^4 cells/well in quadruplets. Cell proliferation was quantified using an MTT assay on days 1, 3, and 7 post-treatment. The MTT assay was performed as previously described in the cell characterisation section (3.1.b.II).

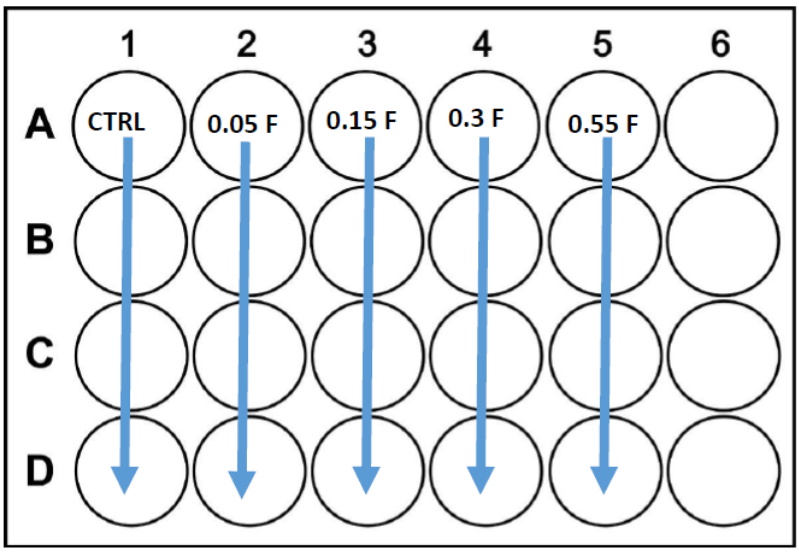


Figure 12: Plate setup for MTT assay post ESW treatment (water bath setup). The setup was replicated for day 1,3 and 7 post-treatment

3.2.2.b.II-Osteogenic differentiation:

Ad-MSCs from each treatment group were seeded at a density of 1x10^4 cells per well in 24-well plates (n=8 wells/treatment group) in GM for 48 hours. Then, the medium was changed to the osteogenic DM (Stempro® osteogenesis differentiation kit) in half of the wells, leading to each treatment group having 4 wells of cells seeded in GM and 4 wells seeded in DM. Alizarin red S staining and stain quantification were performed at day 21 post-treatment as described in the tri-lineage differentiation (osteogenic differentiation) section 3.1.b.III.

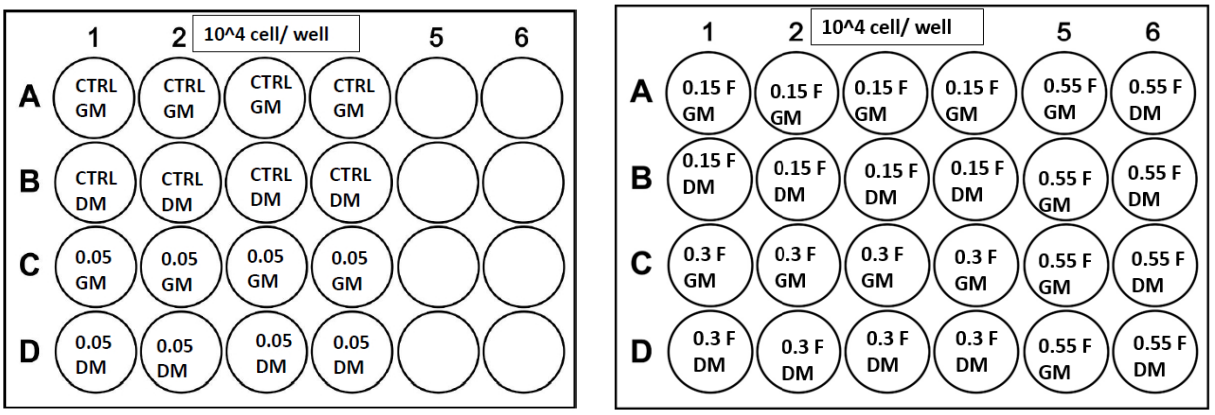


Figure 13: Plate set up for alizarin red staining post ESW treatment (water bath setup).

The setup was replicated for day 15 and day 21 post-treatment.

3.3- Bone graft substitute biomaterials (scaffolds) fabrication and characterisation:

The process through which I developed my scaffolds went through multiple stages of optimisation, testing and refinement. I knew from the beginning that I wanted to use 3D printing as the manufacturing method for my scaffolds due to the advantages mentioned in the study background section, particularly the fact that it allows implants to be manufactured that are customisable to a patient's specific anatomical and biomechanical needs. However, I did not know exactly which polymer or osteoinductive additive (eg. ceramic, bone matrix etc.) I was going to use, nor which 3D printing method was going to work at the start. During my preliminary trials, I started by using FDM (Fused Deposition Modelling) 3D printers, and I printed with different polymers (i.e. Polylactic acid, PLA, polycaprolactone, PCL, nylon, Polyetherether ketone ketone-PEEKK), then I tried mixing ceramics such as HA and TCP even a novel decellularised bone matrix (DCBM, details below) with polymer pellets (mainly PLA and PCL). I extruded the mixture as a filament (using Noztek Touch filament extruder, Nozetek Ltd, Shoreham-by-Sea-UK) and fed this hybrid filament into a 3D printer to print a scaffold of my design. However, these preliminary trials had several setbacks and did not show much promise in obtaining a homogeneous, reliable end product.

I eventually developed a protocol to successfully decellularise bovine cancellous bones by removing the immunogenic donor cells while maintaining the integrity of the bone extracellular matrix (DCBM). In collaboration with the musculoskeletal tissue engineering (Awad) lab at the University of Rochester Medical Centre, NY, USA, I optimised a protocol to synthesise a 3D printable bioink made of 85 % DCBM and 15 % polycaprolactone as my main bone graft substitute biomaterial (scaffold).

3.3.1: Material preparation and 3D printing:

The performance of the 3D-printed bovine DCBM-based scaffolds was compared to that of two control materials:

1- **TCP** based scaffolds as a **positive (osteoinductive) control**. The exact composition of these scaffolds is α-TCP (Innotere- Cat. No. 100AT3, Radebeul- Germany) and HA (Sigma Aldrich- Cat. No. 289396, St. Louis, MO-USA) at a TCP: HA ratio of 80:20.

2- **PCL** based scaffolds were used as a **negative (vehicle) control** (PCL M_n 80,000 Sigma Aldrich, Cat. No. 440744, St. Louis, MO, USA).

To characterise the *in vivo* biocompatibility, implant-grade polyethylene discs (from BioMedtrix, LLC, Whippany, NJ-USA) were used as my controls as an approved bio-inert implantable biomaterial.

- **Bovine DCBM preparation**

Bovine femora were collected from local abattoirs. After soft tissue removal, the distal epiphysis of each femur was separated from the shaft and split in the sagittal plane with a bone-cutting band saw. The two halves of the epiphysis were secured in a vice, and a hole saw (mounted to a vertical drill press) was used to remove cylinders of cancellous bone (bone cores) with an outer diameter of 20 mm and a length of 20-35 mm. **(see Figure 14).**

The cancellous bone cores were then transferred into sterile screw top glass bottles for washing and processing (see **Table 26** for details)

In the beginning, I investigated the possibility of using the DCBM bone cores directly as our scaffolds (prior to the cryo-milling step), but due to the variability of its mechanical properties (see discussion section and appendix 6), I decided that the best way to move forward was to further process it into a printable bioink.

Table 26: Bovine cancellous bone decellularisation steps.

Step	Details	Time needed	Temperature
Wash	Wash with 500 ml **nuclease free water,** 1 % (v/v) penicillin-streptomycin (P/S) with continuous agitation (200 rpm), with a water change every 12 h.	72 h	37 °C
Enzymatic treatment	Add 250 ml **0.05 % trypsin-EDTA** (Thermo Fisher, Gibco™-Cat. No. 25300054, Loughborough, UK) with continuous agitation at 200 rpm.	2 h	37 °C
	Add 250 ml **DMEM (high glucose,** Thermo Fisher, Gibco™, Cat. No. 11965092, Loughborough, UK)**+10 % FBS+1 % P/S and Amphotericin B** to deactivate the trypsin (agitation at 200 rpm)	24 h	37 °C
Rinse	Add 500 ml of **nuclease free water** with continuous agitation (200 rpm), with a water change every 12 h.	24 h	37 °C
Detergent treatment	Washing with detergent **10 mM trisaminomethane (Tris) + 0.5 % Sodium Dodecyl Sulfate (SDS) (**Merck, Roche-10812846001 and Sigma Aldrich, 11667289001, Gillingham, Dorset, UK), respectively.	24 h	RT
Rinse	Flush samples with 500 ml autoclaved **distilled water** (x5 cycles) with continuous agitation (200 rpm) to remove all remnants of detergents.	1-2 h each cycle	37 °C
Weak acid treatment	Add 500 ml **(1.5 % Peracetic acid + 2 % Triton X-100)** oxidising solution in DW (Bonnymans, Cat. No. FPERACID5, Beith, Scotland) and (Sigma Aldrich, Cat. No. 93443, Gillingham, Dorset, UK) respectively.	3 h	37 °C
Rinse	Flush samples with 500 ml **autoclaved DW** (x5 cycles) (200 rpm) to remove all remnants of peracetic acid.	1-2 h each cycle	37 °C
Neutralisation	Neutralisation solution consisted of **1.875 % sodium metabisulfate + 0.7 % sodium hydroxide in distilled water** (200 rpm) (Sigma Aldrich, Cat. No. S9000 and 415413; Gillingham, Dorset, UK).	3 hr	RT
Final wash	Flush samples with 500 ml autoclaved DW (x5 cycles) (200 rpm) to remove all remnants of peracetic acid.	1-2 h each cycle	RT
Drying	Freeze dry under vacuum	24 h	-80 °C
Storage	Transfer samples to conical tubes and **freeze at-80 °C**	Until use	-80 °C
Cryo-milling	Used Spexmill 6875 (Spex SamplePrep, Metuchen, NJ-USA). Cycles: 15 – Precool: 3 minutes-Run: 1 min 30 sec- cool: 2 minutes – rate 10 CPS.		In liquid nitrogen
Sieving	To obtain particle size ≤40 µm		

- **Bioink synthesis and 3D printing:**

To enable bioink formulation in preparation for 3D printing, the polycaprolactone (PCL, Mn=80,000, Sigma Aldrich, Cat. No. 440744, St. Louis, MO-USA) was dissolved into an inorganic double solution composed dichloromethane (75 %) with 2-butanone (25 %) (Sigma

Aldrich, Cat. No. 360473 and 270997, St. Louis, MO-USA) at concentrations of 20% w/v. The solution was then mixed with DCBM powder (particle size ≤40 µm) to create the printable bioink at a 7:1 ratio of (DCBM: PCL). The bioink was then 3D-printed at low temperature using a bio-printer (BioX from Cellink, SKU: D16110020717, Boston, MA, USA) with a 50 % infill-grid pattern, a 0.3 mm layer height, extrusion pressure of 120 kPa and a print speed of 10 mm/s. The same preparations and print settings were used for the TCP scaffolds (positive control). In contrast, the plain PCL (negative control) scaffolds were printed using a thermo-nozzle at 150 ºC (See **Figure 14**).

To evaluate the *in vitro* cytocompatibility, osteoinductivity, and microstructure as well as *in vivo* biocompatibility testing, the scaffolds were designed as discs (8 mm Ø x 2 mm H) with a 50 % infill grid pattern, while for the purpose of testing biomechanical properties, the scaffolds were printed as cylinders (8 mm Ø x 10 mm H) with a 50 % infill grid pattern. After printing, the scaffolds were placed in a vacuum chamber overnight to ensure complete evaporation of any residual solvents. Finally, scaffolds were sonicated in DW to remove any loose material, air-dried in a biosafety cabinet, and sterilised with ethylene oxide prior to use.

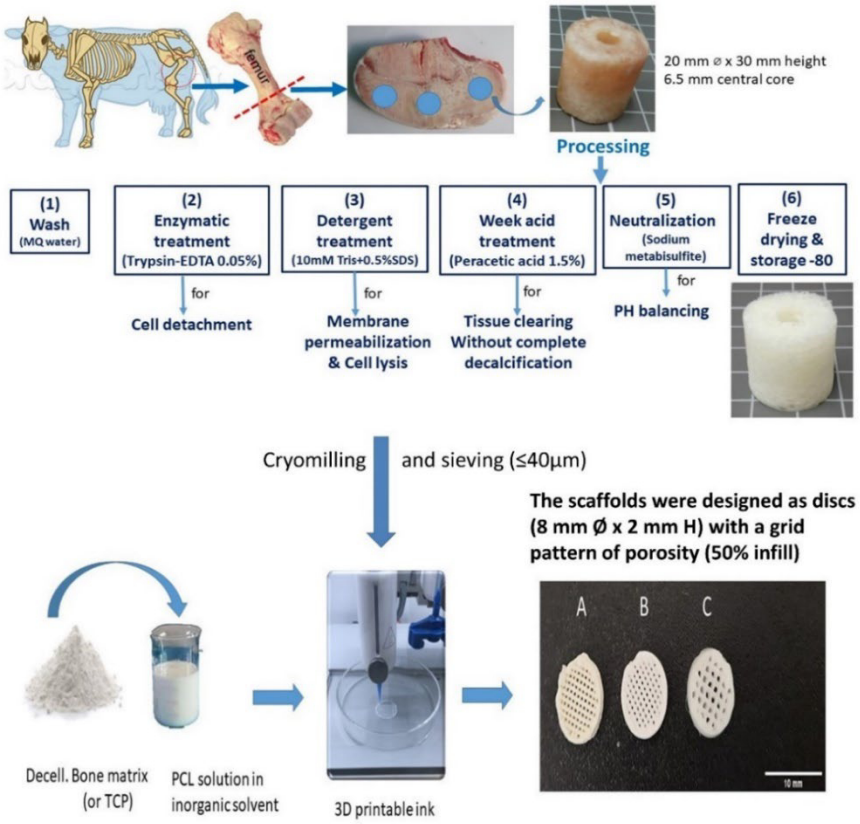


Figure 14: Decellularised bone matrix preparation, bio-ink synthesis and 3D printing. DCM (A), TCP (B), PCL (C).

3.3.2: *In vitro* characterisation:

The *in vitro* characterisation focused on confirming donor cells elimination from the DCBM end product and evaluating DCBM mineralisation status, as well as the cytocompatibility, osteoinductivity, microstructure and biomechanical properties of the 3D printed scaffolds.

3.3.2.1-Confirmation of donor cells elimination:

3.3.2.1.a- DNA quantification of the DCBM:

The DNA content in the DCBM was compared to that of the unprocessed bovine bone. DNA from both the DCBM and the unprocessed bone samples (n= 7 samples/group) was extracted using the DNeasy Blood & Tissue Kit (QIAGEN, Cat. No. 69504, Hilden, Germany) following the manufacturer's instruction except that at the tissue lysis and DNA elution steps, the samples were incubated overnight with ALT buffer at 56 °C for lysis and with AE buffer at RT for elution instead of 1 h. DNA quantification used the Quant-iT™ PicoGreen® dsDNA Kit (Thermo Fisher, Invitrogen™, Cat. No. P7589, Loughborough, UK) following the manufacturer's instructions. The plates were read using the CytoFluor® Series 4000-Fluorescence Multi-Well Plate Reader (Thermo/Applied Biosystems, Waltham, MA, USA) using the following parameters: excitation 480, emission 530 and gain 1000.

Fluorescence outputs were converted to DNA concentrations (in ng/ml) by reference to an internal standard curve. The percentage of DNA content reduction in the DCBM compared to the unprocessed bone was then calculated.

3.3.2.1.b- Histological confirmation:

Decalcified, paraffin-embedded sections of the decellularised and unprocessed bone cores were prepared and stained with H&E and DAPI. A qualitative review was performed to confirm the completeness of the removal of cellular elements from the processed sample and assess the preservation of the integrity of the extracellular matrix structure.

The bone cores were fixed in 70 % ethanol and sent to the histopathology service (Department of Veterinary Medicine, University of Cambridge) for histopathological evaluation.

The bones were decalcified for 5 h in hydrochloric acid (10 %)/sodium chloride (20 %) based decalcification solution (Decal II, rapid; atom scientific, Cat. No. RRDC1-G, Hyde, Cheshire, UK) at room temperature. The bone specimens were further processed overnight in a Epredia™ STP 120 tissue processor (Fisher Scientific, Epredia™ 813160, Cat. No. 12943705, Loughborough, UK) followed by embedding in paraffin wax blocks and sectioning into 4 µm thin transverse sections using a Finess E+ microtome (ThermoScientific ™- Series A77510300GB, Loughborough, UK). The wax-embedded tissue sections were floated in a

warm (40 °C) water bath and mounted onto slides. Dewaxing, dehydrating and H&E staining were done using an automated slide staining system (Leica ST5010 Autostainer XL, Leica Biosystems, Cat. No. 14 0456 35136, Nussloch, Germany). Cover slipping was done using an automated glass cover slipper (CV5030 Glass Coverslipper, Leica Biosystems, Cat. No. 140478 80101, Nussloch, Germany).

3.3.2.2- Mineralisation status

Calcium and phosphate contents of the DCBM were quantified using calcium and phosphate colourimetric detection kits (Abcam, Cat No. ab272527 and ab65622, respectively, Cambridge, UK) following the manufacturer's instructions. Concentrations, calculated by reference to a standard curve, were expressed in µg/ml for calcium and nmol/ml for phosphate).

3.3.2.3-Cytocompatibility:

Ethylene oxide sterilised scaffolds from each material (DCBM, TCP and PCL- n= 5/material group/time point) were preconditioned by incubation for 2 h in GM (DMEM, low glucose, GlutaMAX™ Supplement, pyruvate +10 % FBS +1 % P/S) at 37 °C in 24-well plates followed by seeding each scaffold with $2x10^4$ rabbit Ad-MSCs per well. Cell viability was assessed using a MTT assay at days 3, 5, and 7 post-cell seeding. The results were expressed as a percentage of PCL control.

3.3.2.4 - Osteoinductivity:

Temporal patterns of expression of the osteogenesis markers (RUNX2, osteocalcin, osteonectin, osteopontin, collagen I and ALP) were determined using qRT-PCR as well as Alizarin red S staining; to evaluate the scaffolds' osteoinductivity and ability to support osteogenic differentiation 21 days after seeding with rabbit Ad-MSCs. Two sets of 5 preconditioned scaffolds from each material (see cytocompatibility section) out of each material group were seeded with $2x10^4$ Ad-MSCs in 12-well plates in MSC complete GM at 37 °C, 5 % CO_2 for 21 days (medium change twice/week). One set of plates was used for qRT-PCR analysis, and the second was used for Alizarin red S staining (n= 5/scaffold type/assay).

3.3.2.4.a- qRT-PCR analysis for quantification of the level of expression of osteogenesis markers:

- RNA extraction from the scaffolds using TRIzol reagent:

The scaffolds were removed from the cell culture medium, washed 3 times with PBS, split into 4 pieces with a scalpel blade and transferred into 2 ml tissue homogeniser tubes with

beads (Precellys® evolution Tissue Homogenizer-Bertin instruments, Montigny-le-Bretonneux, France) containing 500 µl TRIzol Reagent (Thermo Fisher, Invitrogen™, Cat. No. 15596026, Loughborough, UK) for **homogenisation** (10,000 rpm, for 10 cycles 30 seconds each). Then, the homogenised samples were transferred to new labelled 2 ml tubes containing 500 µl TRIzol Reagent and incubated at room temperature for 5 min. **Phase separation** was achieved by adding 200 µl chloroform (Sigma Aldrich, Cat. No. C2432, Gillingham, Dorset, UK) for each 1 ml TRIzol, followed by vortexing for 15 seconds then incubation at RT for 3 min. For **RNA precipitation,** tubes were centrifugated at 11,600 x ***g*** for 15 min; the RNA-rich uppermost transparent aqueous phase was collected in a new tube containing 500 µl isopropanol with gentle pipetting then incubated at room temperature for 10 min, then spun at 11,600 x ***g*** for 10 min**.** All TRIzol and chloroform handling steps were done in the fume hood. The precipitated RNA formed a translucent gel-like pellet. The supernatant was discarded, and the **RNA pellet was washed** gently with 1 ml of 75 % ice-cold ethanol, then spun at 10,000 x ***g*** for 5 min. The supernatant was discarded, and the RNA pellet was left to dry by leaving the tube open in the fume hood for 15 - 20 min. Finally, the RNA pellets were **resuspended** in 50 µl nuclease-free water with gentle mixing by pipetting up and down, followed by incubation in a 60 °C water bath for 10 min up to 1 h, and finally mixing by flicking then spinning (11,600 x ***g*** for 1 min) to collect the supernatant. The resuspended RNA concentration (ng/µl) was measured on the NanoDrop™ 1000 Spectrophotometer (ThermoFisher Scientific™, Loughborough, UK).

- <u>RNA reverse transcription to cDNA.</u>

The extracted RNA from the samples was reverse transcribed into cDNA using the High-Capacity cDNA reverse transcription kit (Fisher Scientific, Applied Biosystems™, Cat. No. 4368814, Loughborough, UK) with incubations in a FlexCycler2 PCR thermocycler (Analytik Jena, Überlingen, Germany) following the manufacturer's instructions.

- <u>Primer design and qRT-PCR:</u>

Primer design for rabbit Ad-MSCs as shown in **Table 27**.

The quantitative PCR was performed using a SYBR® green PCR kit (Rotor-Gene SYBR® Green PCR Kit, Qiagen- Cat. No. 204001, Hilden, Germany) and Rotor-Gene® Q2 plex Priority qPCR thermocycler with 72 Well Rotor (Qiagen, Product ID: 9001861, Hilden, Germany) in a 25 µl reaction volume.

The fold increase in target gene expression was quantitatively analysed using the ΔΔCT method, where the PCL scaffolds were used as a calibrator (control). *ΔCT = CT (gene of interest) – CT (housekeeping gene). ΔΔCT= ΔCT (DCBM or TCP) – mean ΔCT (PCL).*

Table 27: Primers design for qRT-PCR to evaluate scaffolds osteoinductivity.

Gene	Sequence
GAPDH (housekeeping gene)	Forward: GCCTGGAGAAAGCTGCTAAGT Reverse: GAGTGGGTGGCACTGTTGAA
β-actin (housekeeping gene)	Forward: AGA TCA AGA TCA TCG CGC C Reverse: TCC AAC GAC TGC TGT CAC CT
Runx2	Forward: TCAGGCATGTCCCTCGGTAT Reverse: TGGCAGGTAGGTATGGTAGTGG
Osteocalcin	Forward: ACTCTTGTCGCCCTGCTG Reverse: CTGCCCTCCCTCTTGGAC
Osteonectin	Forward: CTCCACCTGGACTACATCG Reverse: GCTGGCCAAACTGCCAGTG
Osteopontin	Forward : GCAGAATCTCCTAACACCGCAG Reverse: GGTCATCGTCCTCATCCTCATC
Collagen-I forward	Forward: GCGGTGGTTACGACTTTGGTT Reverse: AGTGAGGAGGGTCTCAATCTG
Alkaline Phosphatase- ALP	Forward: ACTGTGGACTACCTCTTG Reverse: GGTCAGTGATGTTGTTCC

3.3.2.4.b- Alizarin red S staining:

Twenty-one days after seeding Ad-MSCs over the scaffolds, GM were removed, and the scaffolds were washed using three rounds of 500 µl 1x PBS/ well. Cells were fixed using 1 ml of ice-cold 70 % ethanol/well for 1 h, followed by staining with 40 mM Alizarin red S staining solution, pH adjusted to 4.2 (1 ml/well) for 15 min at room temperature. The staining solution was removed, and cell-seeded scaffolds were rinsed four times with DW, followed by visual inspection, de-staining and alizarin red quantification using 10 % cetylpyridinium chloride (500 µl/ well). The resulting eluted colour was quantified at 570 nm using a microtiter plate reader (Multiskan™ FC Microplate Photometer, Thermo Scientific ™, Cat. No. 51119000, Loughborough, UK).

3.3.2.5- Microstructure:

The microstructure of the scaffolds was assessed via scanning electron microscopy (SEM) and micro-computed tomography (µ-CT).

3.3.2.5.a-SEM:

Three scaffolds from each material group were seeded with $1x10^4$ rat Ad-MSCs/scaffold and cultured in a growth medium for 48 h (37 °C, 5 % CO_2). After 48 h, the culture medium was removed, the scaffolds were rinsed twice with PBS, and the cells were fixed using 3 %

glutaraldehyde (Sigma Aldrich) for 3 h at room temperature. Samples were then serially dehydrated in a graded ethanol series (30 %, 40 %, 50 %, 60 %, 70 %, 80 %, 90 % and twice in 100 %) with 15 min in each concentration, followed by air drying for 24 h in a chemical fume hood. Finally, scaffolds were sputter-coated with platinum and imaged in a SEM (NOVA Nano SEM 450, FEI, supported by Thermo Fisher, Loughborough, UK) using 20 KV accelerating voltage and different magnifications.

3.3.2.5.b- Micro-Computed Tomography (µ-CT):

Three scaffolds from each group were scanned using the Skyscan 1272 benchtop µ-CT scanner (Bruker (UK) Ltd, Coventry, UK) using the following scanning settings: 100 KV, 100 MA, exposure time 700 ms, pinning 2016 x 1344, 360-degree rotation and 13.4 µm pixel size. The output was TIFF files, which were then converted into BMP files using proprietary micro-CT software (NRecon version 1.6.10.4; Bruker CT). The microstructure of the reconstructed micro-CT image (including total volume, material volume, % porosity, trabecular thickness and trabecular separation) was then quantified in a second software package (CT-Analyser v. 1.13; Bruker CT).

3.3.2.6- Biomechanical *properties:*

Five scaffolds from each group were used for biomechanical testing. The mechanical performance of the scaffolds was determined by compression to failure (destructive) mechanical testing. Tests were performed using a screw-driven materials testing machine (Instron Model 5544; Instron Materials Testing Systems, Norwood, MA, USA) fitted with a 2000-N load cell. Loading was performed under displacement control, with a 1 mm/min displacement rate. Data (extension in millimetres and applied load in Newtons) were collected at a frequency of 1Hz using Instron Bluehill-3 proprietary software.

The extension values were corrected as the first recorded value was not zero; hence, all the extension values were subtracted from the first recorded extension value, followed by calculating the absolute values of the corrected extension values using the ABS function in Excel.

The absolute values of the recorded load were calculated using the (ABS) function in Excel, followed by peak load calculation using the (MAX) function in Excel.

The load-displacement curve was plotted for all specimens, representative examples are shown in **Figure 15**; the linear phase of the curve was determined visually, and material stiffness was calculated from the slope of the linear phase of the resulting load-displacement curve.

The stress was calculated by dividing the load (N) by the scaffold's (circular) surface area (mm^2), and the **strain** was calculated by dividing the extension (displacement) (mm) by the scaffold height (10 mm).

The stress-strain curve was plotted (see **Figure 16**), the linear phase of the curve was determined visually, and material stiffness (**Young's modulus)** was calculated from the slope of the linear phase of the stress-strain curve.

3.3.2.7- Statistical analysis for *in vitro* assay:

The Kolmogorov–Smirnov test was used to test for data normality. A P value ≥ 0.05 was taken to mean that the data were normally distributed, while P ≤ 0.05 meant the data were not normally distributed. Comparisons between parametric data from the three groups were made using a one-way ANOVA (using IBM SPSS Statistics for Windows, Version 28.0) [725] followed by a Bonferroni post hoc test to determine the significance of differences between the frequencies of categorical variables. For all tests, P values of ≤ 0.05 were considered to be significant.

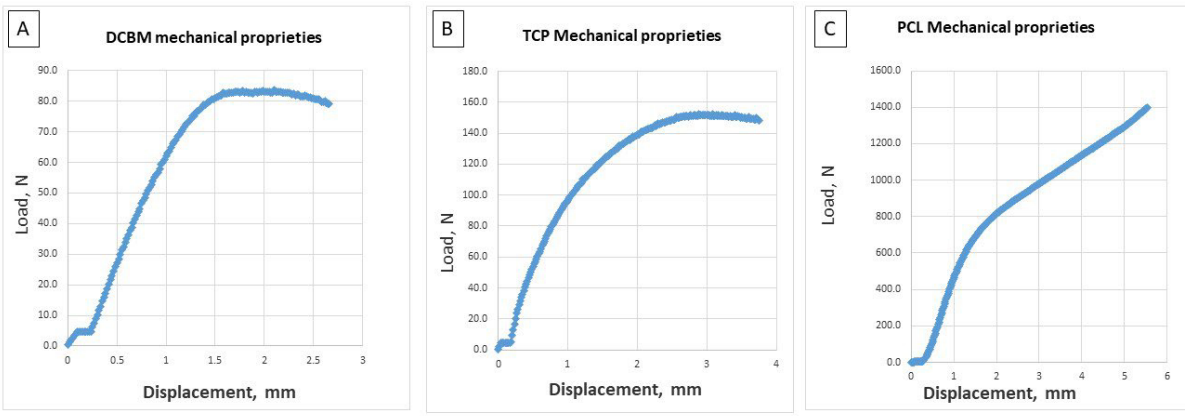


Figure 15: Typical load-displacement curve (mechanical properties) for (A)DCBM scaffolds, (B) TCP scaffolds, and (C) PCL scaffolds.

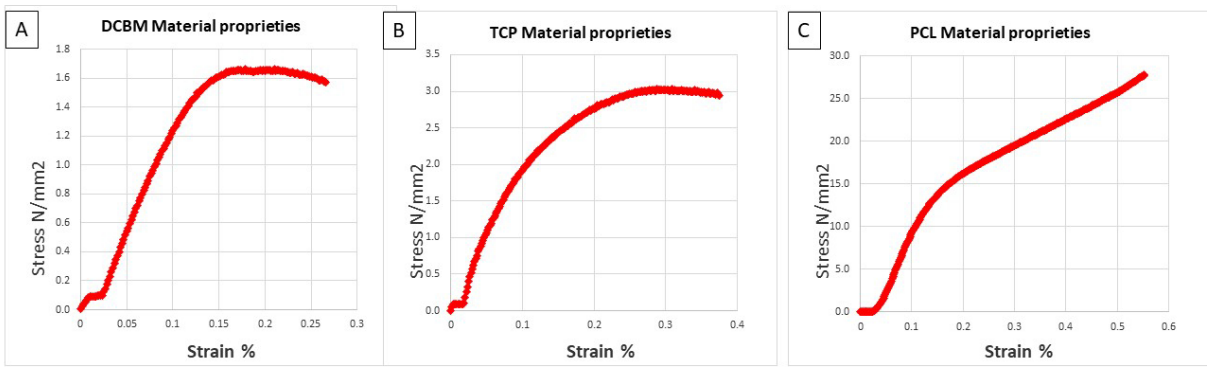


Figure 16: Typical stress strain curve (material properties) for (A) DCBM scaffolds, (B) TCP scaffolds, (C) PCL scaffolds

3.4- Testing the local biological effect of the selected biomaterials (scaffolds) after implantation (biocompatibility testing): a rat preclinical subcutaneous implantation model:

3.4.1- Ethics approval and experimental design:

Ethics approval: The experimental work involving live animals was reviewed and approved by the United Kingdom Home Office as required by the UK law under the Animals (Scientific Procedures) Act 1986, project licence number PP1153947. All the animal work was conducted at the University of Cambridge biomedical services research animal facilities.

Sample size calculation:

We designed the rat study in line with the ISO and ASTM regulatory standards, ISO 10993-6:2016 - Biological evaluation of medical devices-part 6: tests for local effects after implantation and ASTM F981 - 04 (2016) - Standard Practice for Assessment of Compatibility of Biomaterials for Surgical Implants with Respect to Effect of Materials on Muscle and Insertion into Bone. The guidelines recommend an average of 8 implants per time point. We implanted 3 implants per animal, with at least 3 rats (i.e., 9 implants) per time point for each material.

Experimental design outlines: Twenty-one (10 Males and 11 females) 8-week-old Sprague-Dawley rats (Charles River UK Limited, Kent, UK) were operated in total. All rats were housed in a group of 3-4 rats/ cage in individually ventilated cages (IVC); the rats were quarantined/acclimatised for 3 weeks prior to starting the study.

Seven rats were randomly allocated to each biomaterial/scaffold group (DCBM, TCP and PCL). For the purpose of biocompatibility testing, the 3D printed scaffolds (8 mm Ø x 2 mm H) were implanted subcutaneously in the rats' dorsum. Medical-implants grade polyethylene discs (provided by BioMedtrix, LLC, Whippany, NJ-USA) with similar dimensions were used as a bio-inert control for comparison. Each rat received 4 implants (1 polyethylene standard + 3 test implants of the same type) (see **Figure 17)**. Rats were euthanised at 4 weeks (n=3 rats/ group, hence n=9 tested scaffolds/group) and 8 weeks (n=4 rats/group, hence n=12 tested scaffolds/group) postoperatively for material/tissue interaction evaluation.

3.4.2- Anaesthesia and preoperative preparation

Anaesthesia: The rats were induced using 5 % isoflurane in oxygen (1 Litre/ minute), followed by maintenance of anaesthesia using 2.5 % isoflurane in oxygen (0.6 Litre/ minute). The rats' body temperature was monitored by a digital rectal thermometer providing a continuous reading on a monitor.

Surgical site preparation: Nail clipping and ear notching (as an identification method) were done while the rats were under anaesthesia in preparation for surgery. Then, each rat's dorsum was clipped and disinfected using 70% ethanol followed by chlorhexidine gluconate and isopropyl alcohol antiseptic applicator (ChloraPrep ™ 3 ml clear applicators, BD, Franklin Lakes, NJ, USA). The rats were positioned in sternal recumbency on a heated pad. Eye lubricant (Optixcare Eye Lube Plus, CLC Medica, London, UK) was applied to avoid corneal dryness, and the rat was draped using a sterile fenestrated disposable surgical drape (Buster Sterile Op Covers 30 x 45 cm: Vet Direct- Cat. No. BUSD3045, Newcastle upon Tyne, UK) to maintain the surgical field sterility.

3.4.3- Surgical procedure and post-operative care

Surgeries:

The four implants were inserted through a single 1.5 cm long midline surgical incision in the rat's dorsum, starting 3 cm distal to the scapulae (**see Figure 18**). Subcutaneous pockets were created in 4 directions in preparation for implants insertion using a curved mosquito forceps as a dissection tool. The standard polyethylene control discs were always implanted at the same location on the top left side pocket. After implantation, the skin was sutured using 4/0 Monocryl (Ethicon Monocryl® Plus Antibacterial Sutures (4/0 USP – reverse cut prone multi-pass needle (19 mm needle size), IMS Euro Ltd- Cat.No. MCP496H, Stockport, UK) in intradermal fashion and skin glue (3M VETBOND tissue adhesive, Vet Direct, Cat. No. VB3M, Newcastle upon Tyne, UK).

Postoperative care:

For analgesia, the rats were given Buprenorphine (Bupaq multidose 0.3mg/ml solution; Chanelle Pharma, Hungerford, Berkshire, UK) at a dose of 0. 5 mg/kg orally, every 8 hours in hazelnut-cocoa spread (Nutella; Ferrero, Alba-Italy) for 3 postoperative days. The number of days and/or the frequency of administration were increased if necessary.

3.4.4-In-life animals' outcomes:

The rats were monitored daily for their general health condition and any signs of swelling, inflammation, or adverse reaction around the implants' sites. Pain scoring for all rats was performed using the grimace scale for the first post-operative week; body weight was recorded on the day of surgery, then weekly thereafter.

3.4.5- Euthanasia and post-mortem outcomes

3.4.5.I-Euthanasia: Rats were euthanised by carbon dioxide overdose and death was confirmed by exsanguination. Nine rats (n=3/group) were euthanised at 4 weeks postoperatively, and 12 rats (n=4/group) were euthanised at 8 weeks postoperatively. Implants and a small region of surrounding subcutaneous tissue were dissected and fixed in 10% neutral buffered formalin solution for subsequent histopathological evaluation.

3.4.5.II-Post-mortem outcomes: The main evaluation method used was histopathological scoring following the ISO 10993-6 guideline that specifies test methods for assessing the local effects after implantation of biomaterials intended for use in medical devices. Specimens processing for Haematoxylin and Eosin (H&E) staining in preparation for scoring is summarised in **Figure 19**. The tri-calcium phosphate (TCP) and decellularised bone matrix (DCBM) specimens required surface decalcification prior to sectioning. Hydrochloric acid (10 %)/ sodium chloride (20 %) based decalcification solution (Decal II, rapid; atom scientific, Cat. No. RRDC1-G, Hyde, Cheshire, UK was applied to the surface of the paraffin wax block for 15 minutes on ice packs. Specimens processing, sectioning (in to 4 μm thin transverse sections) and staining were done as described in section 3.3.2.1.b- Histological confirmation.

Evaluation Criteria:

3.4.5.II.a- Local biological effect after implantation (material/tissue interaction): The local biological effect was quantified following the ISO 10993-6 guidelines [726, 727], via giving a score ranging from 0 to 4 (non-existent to severe) to the following features: **Inflammatory cells infiltration** (specifically, neutrophils and eosinophils (i.e. polymorphonuclear cells), mast cells, M1-like macrophages, M2-like macrophages, giant cells, lymphocyte and plasma cells, **necrosis, calcification, neovascularisation, fibrosis and fatty infiltration.** See **Table 28** for a detailed description of the scoring system**.**

3.4.5.II.b- Bio-absorption features: The bio-absorption features of the implanted materials were evaluated based on residual implant material, surface erosion, fragmentation, phagocytosis, and hydrolysis. See **Table 29** for a detailed description of the used scoring system.

Ten high power fields (x40) per slide were examined and scored, and the average score/criteria/sample was then calculated for both the test materials (DCBM, TCP and PCL) and polyethylene control.

The bio-irritancy (and biodegradability) scores were calculated by subtracting the average score of the local biological effect features of the three test materials implanted in each animal from the total score of the polyethylene control implanted in the same animal (*average test (-) control*). Under the conditions of this study, the test material was considered a:

- Non-irritant (score 0.0 up to 2.9)
- Slight irritant (score 3.0 up to 8.9)
- Moderate irritant (score 9.0 up to 15.0)
- Severe irritant (score > 15)

to the tissue as compared to the negative control sample. See **Tables 28**, **29 and 30** for more detail.

Statistical analysis:

As the results from the histopathology scoring were qualitative (i.e., slight, moderate, or severe), there was no need for running inter-group statistical tests. While for the intra-group data comparison, a Kolmogorov–Smirnov test was used to test for data normality, P value ≥ 0.05 meant the data were considered normally distributed, while P≤ 0.05 meant the data were not normally distributed. Comparisons between parametric data from the three groups were made using a one-way ANOVA (using IBM SPSS Statistics for Windows, Version 28.0) [725]. Followed by running a Bonferroni post hoc test to determine the significance of differences between the frequencies of categorical variables. For all tests, P values of ≤ 0.05 were considered to be significant.

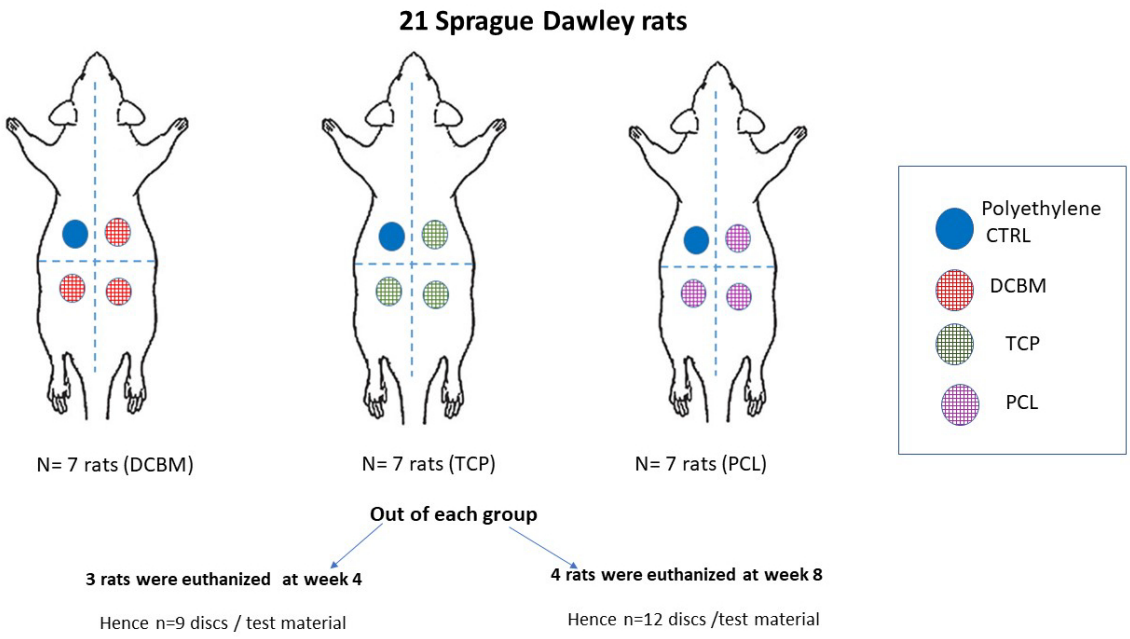


Figure 17: *In vivo* biocompatibility experimental design outline.

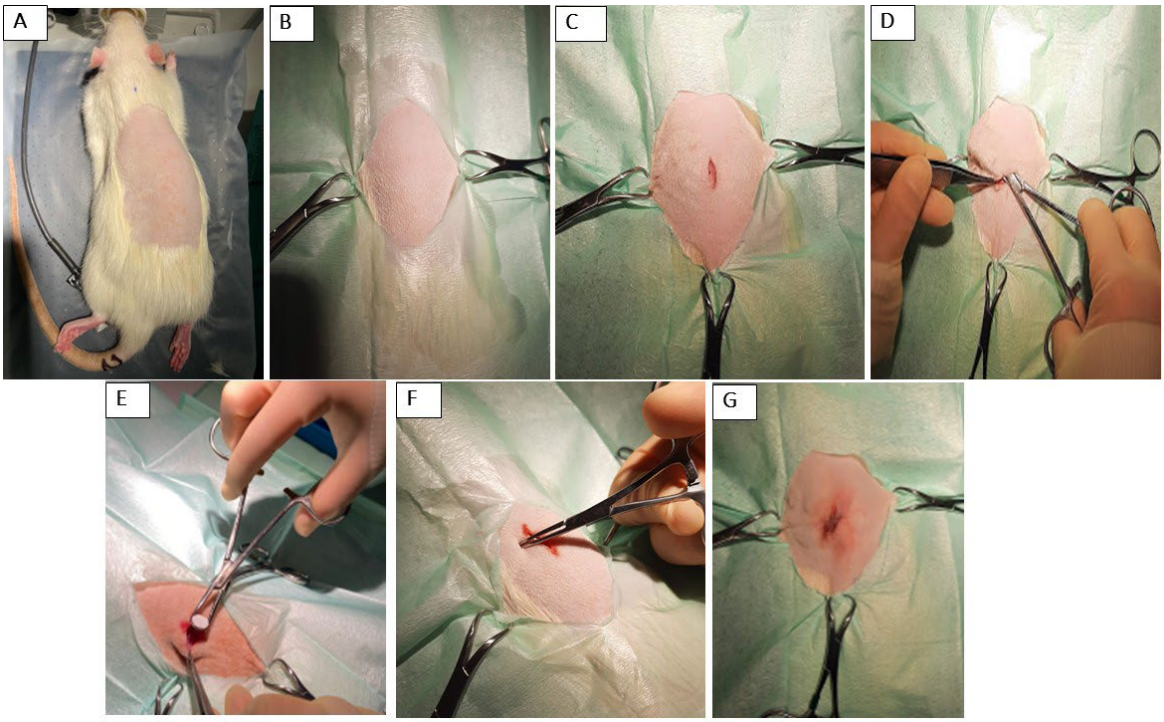


Figure 18: Surgical implantation of test biomaterials (scaffolds) subcutaneously in rat.

A) Rat was positioned in sternal recumbency, and the rat's dorsum was clipped in preparation for surgery.

B) Surgical draping using a fenestrated disposable drape.

C) 1.5 cm long midline surgical incision in the rat's dorsum, 3 cm distal to the scapulae.

D) Creating a subcutaneous pocket for the implants/scaffolds to be inserted at.

E) And F) Scaffold implantation

G) Sutured and glued wound after implanting the 4 scaffolds

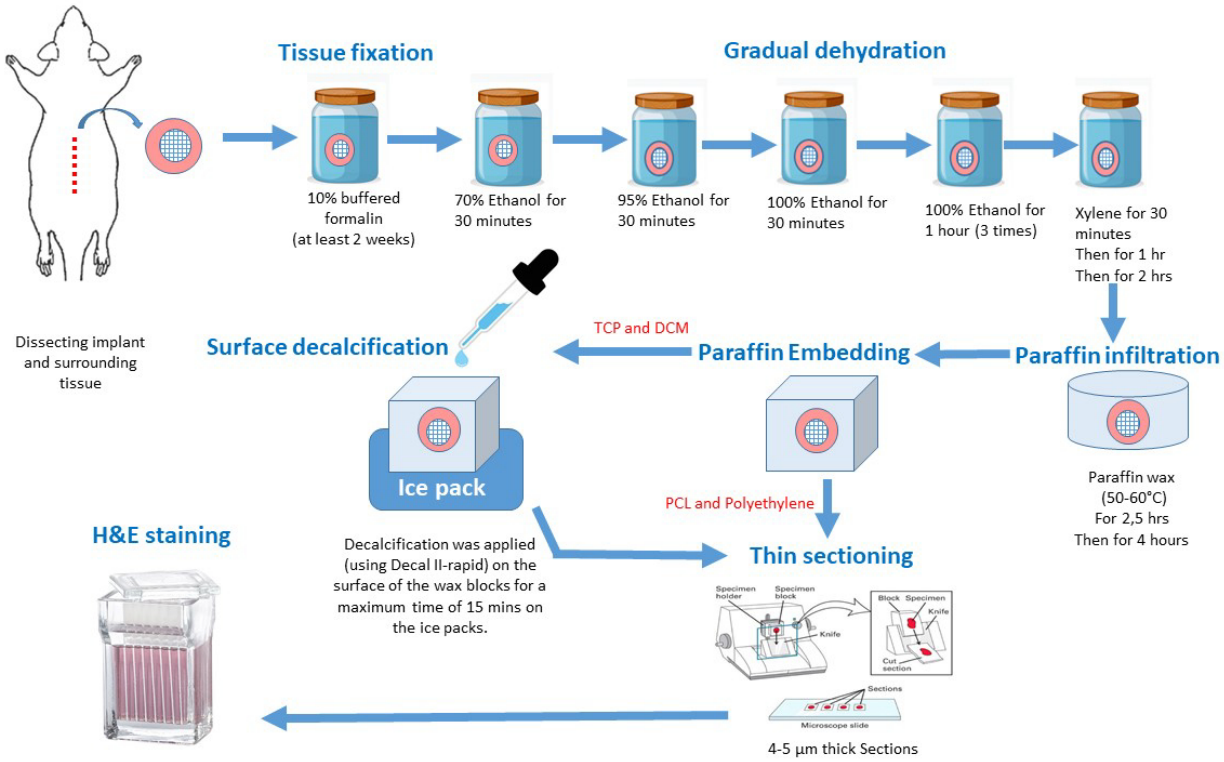


Figure 19: Histological processing of tissue specimens

Table 28: Local biological effect after implantation scoring system

Response	**Score**				
Inflammatory cells infiltration	**0**	**1**	**2**	**3**	**4**
Neutrophils (Polymorphonuclear cells)	None	Rare (1-5/ hpf*)	5-10/ hpf	Heavily infiltrated	Packed
Eosinophils (Polymorphonuclear cells)					
Mast cells					
M1-like Macrophages **					
M2-like Macrophages **					
Giant cells					
Lymphocyte					
Plasma cells					
Necrosis	None	Minimal	Mild	Moderate	Severe
Neovascularisation	None	Minimal capillary proliferation, focal, 1-3 buds	Groups of 4-7 capillaries with supporting fibroblastic structures	Broad band of capillaries with supporting structures	Extensive band of capillaries with supporting fibroblastic structures
Fibrosis	None	Narrow band	Moderately thick band	Thick band	Extensive band
Fatty infiltrate	None	Minimal amount of fat associated with fibrosis	Several layers of fat and fibrosis	Elongated and broad accumulation of fat cells about the implant site	Extensive fat completely surrounding the implant
Calcification	Expressed as 0= absent 1= present				

*hpf= high-power field

** M1 macrophages appeared large, rounded and flat with “fried egg morphology), while M2 macrophages were stretched and elongated cells [728, 729].

Table 29: Material's bio-absorption scoring system

Response	Score
Residual implant material	0= No implant absorption
	1=Minimal absorption <25%
	2= Mild absorption 25-50%
	3= Moderate absorption 50-90%
	4= Marked absorption >90%
Surface erosion	0= No visible pitting or scalloping (intact profile)
	1=Minimal pitting with little to no reduction in the overall bulk
	2= Mild pitting along the surface with slight decrease in the biomaterial bulk (~25%)
	3= More advanced erosion with reduction in the biomaterial bulk (up to 75%)
	4= Marked reduction in material bulk associated with fragmentation and scalloping of residual pieces (less than 25% remaining residual implant)
Fragmentation	0= No fragmentation or clefts
	1=Minimal clefts that does not completely divide the material
	2= Mild clefting into few fragments that remains tightly apposed
	3= Moderate fragmentation with separation of the material into multiple fragments typically showing altered profile and erosion
	4= Severe fragmentation into multiple small fragments with evident loss of material.
Phagocytosis	0= No phagocytosis
	1= Rare macrophages (1 - 2 layers) lining the material showing cytoplasmic vacuolation or intracellular micro-particles of digested biomaterial.
	2= Mild - more than 2 layers of macrophages
	3= Moderate- abundant macrophages forming a solid sheet around the biomaterial with evident biomaterial erosion
	4= Severe phagocytosis with a macrophage forming solid sheets around the biomaterial accompanied with severe fragmentation and erosion of the biomaterial.
Hydrolysis	0= No discolouration
	1=Barely detectable discolouration (acidophilic or basophilic) of the biomaterial
	2= Faint discolouration (acidophilic or basophilic) of the biomaterial
	3= Evident discolouration (acidophilic or basophilic) of the biomaterial
	4= Same as 3 accompanied with severe erosion of the biomaterial.

Table 30: Bio-irritancy and biodegradability score calculation and results interpretation.

	TEST SAMPLES (*X3 replicas*)				**CONTROL SAMPLE**	**Average test - control**
	Test 1	**Test 1'**	**Test 1"**		**Polyethylene control 1**	
ISO Irritancy Score				Average		
Neutrophils (Polymorphonuclear cells)						
Eosinophils (Polymorphonuclear cells)						
Mast cells						
M1-like Macrophages						
M2-like Macrophages						
Giant cells						
Lymphocyte						
Plasma cells						
Sub total				A	C	
Necrosis						
Calcification						
Neovascularisation						
Fibrosis						
Fatty infiltrate						
Sub total				B	D	
Total				**A+B= X**	**C+D=Y**	**X-Y**
Conclusion: Under the conditions of this study, the test sample was considered a – non-irritant (0.0 up to 2.9) – slight irritant (3.0 up to 8.9) – moderate irritant (9.0 up to 15.0) – severe irritant (> 15) to the tissue as compared to the negative control sample.						
Bio-absorption Features						
Residual implant material						
Surface erosion						
Hyaline hydrolysis						
Fragmentation						
Phagocytosis						
Total				**Z**	**W**	**Z-W**
Under the conditions of this study, the test sample was considered a – non-biodegradable (0.0 up to 2.9) – slightly degradable (3.0 up to 8.9) – moderately degradable (9.0 up to 15.0) – Highly degradable (> 15) to the tissue as compared to the negative control sample**.**						

3.5- Evaluation of the ability to support bone healing in a critical size segmental long bone defect:

The ability of the scaffold to support bone healing was evaluated in a critical size bone defect in rabbits. The selected pre-clinical model for this study was a 15 mm long full-thickness segmental bone defect in a rabbit's radius. The scaffolds (implants) were designed based on a pre-study rabbits cadaveric forelimbs CT scans (see details in the section below).

3.5.1- Implant design for rabbit bone defects:

For the purpose of implant design, I CT scanned cadaveric rabbits' forelimbs using a Toshiba Aquilion 16 CT Scanner, using the following scan settings: 120 KV, 75 mAs, 0.5 mm slice thickness, 1.5 second exposure time.

3.5.1.a- Creating a bone 3D model:

The CT scanning data (as DICOM* files) were imported to medical images processing software (3D Slicer 4.11.2) [730-732] to reconstruct the scans into 3D models using the segment editor module and the grow from seed machine learning function, see **Figure 20** for 3D slicer software interface showing the colour coded segmented bone 3D model and **Figure 21** for a flow diagram summarising the model reconstruction steps. The 3D models of each bone were exported as STL** files.

* DICOM stands for Digital Imaging and Communications in Medicine.

** STL stands for Standard Tessellation Language.

3.5.1.b- Mesh refinement and virtual osteotomy:

The exported STL files were then opened in Autodesk Meshmixer (a mesh refinement and virtual 3D planning software), see **Figure 22** for the software interface. The radius was selected, and virtual osteotomy cuts were created using the plane-cut function from the edit menu. I planned to create a 15 mm long bone defect in the radius mid-shaft; the bottom osteotomy cut was made 15 mm proximal to the radiocarpal joint (**see Figure 23).** The dimensions of the osteotomised bone segment were measured using the dimensions function from the analysis menu.

3.5.1.c- Implant/Scaffold design:

The measurements from the virtual osteotomy indicated that the excised bone segment had an elliptical cylindrical shape with a wider base than its top. Base dimensions = 5 mm major ø x 4 mm minor ø; Top dimensions = 4.44 mm ø x 3.5 mm ø; Height= 15 mm. I used Fusion 360 CAD design software to design a cylinder of these dimensions, which was then exported as an

STL file in preparation for 3D printing. Given the compressible nature of the scaffolds and to ensure press fit upon implantation, 1 mm was added to the scaffold design (hence 16 mm height). The print settings were as mentioned in section 3.3.1 (under bio-ink synthesis and 3D printing).

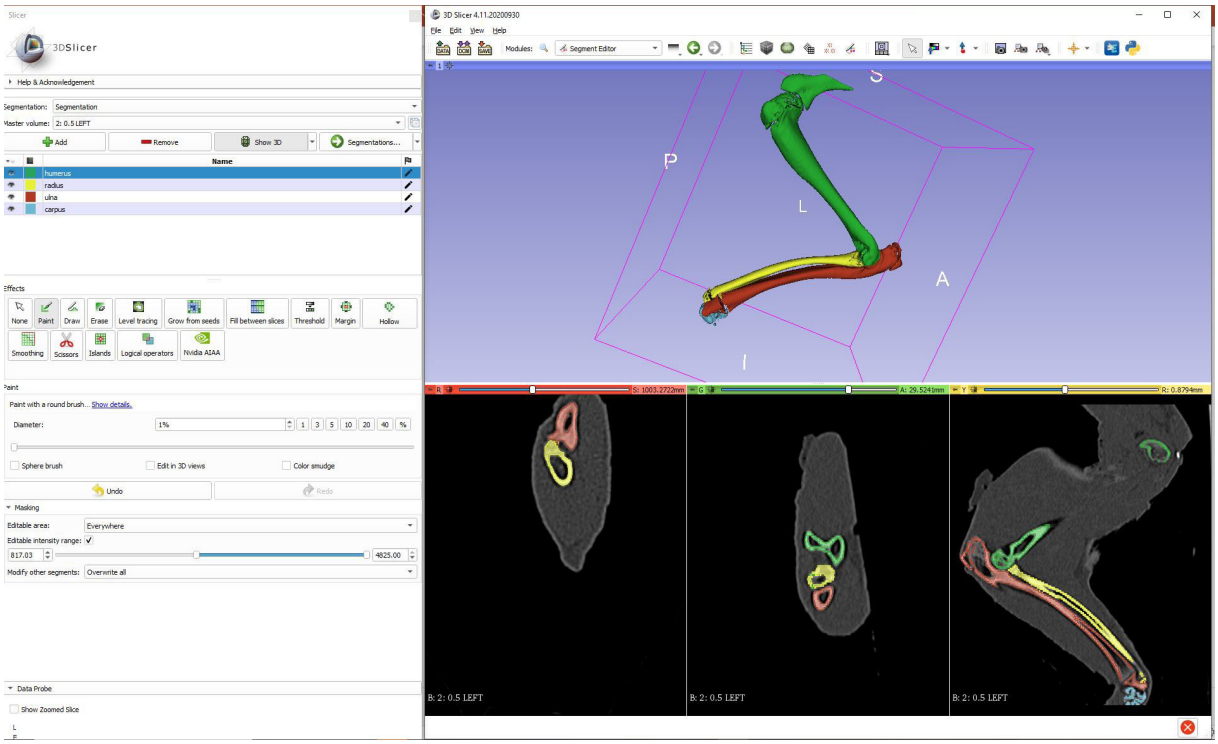


Figure 20: 3D slicer software interface showing the colour coded segmented bone 3D model.

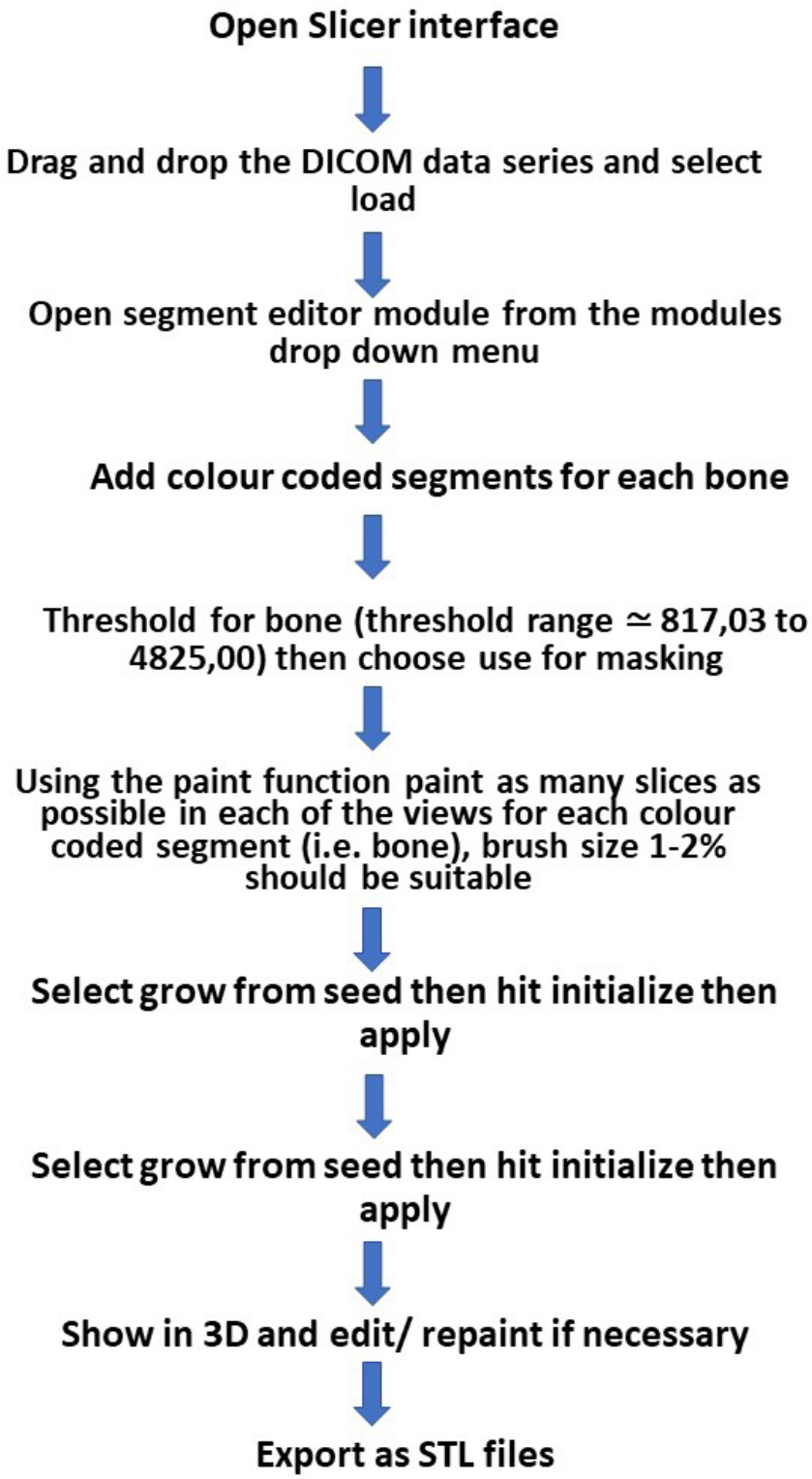


Figure 21: Flow diagram demonstrates the steps for rabbit bone model segmentation out of CT scan.



Figure 22: Autodesk Mesh mixer software interface

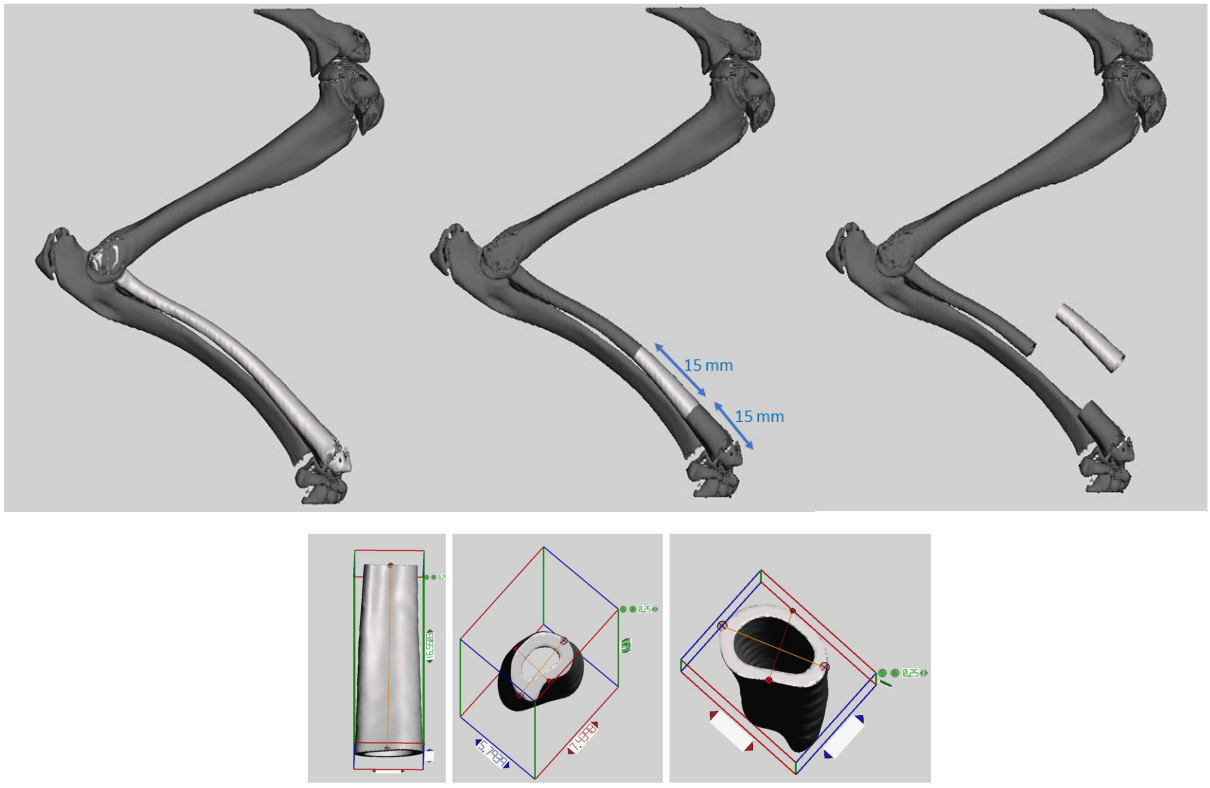


Figure 23: Virtual osteotomy in preparation for implant/scaffold design.

The Osteotomy base starts 15 mm above the radiocarpal joint and the bone defect is 15 mm long.

3.5.2- Ethics approval and experimental design:

3.5.2.a- Ethics approval:

A pilot study of 8 New Zealand white rabbits was conducted at the AO Research Institute (Davos, Switzerland) for the purpose of animal model validation and surgical training (for this study, the animal work was approved by the Ethical Committee of the canton of Grisons in Switzerland (Amt für Lebensmittelsicherheit und Tiergesundheit- Kantonale Tierversuchskommission Graubünden (TVKGR)) approval number GR/15/2021, according to Swiss animal protection laws and regulations. The animal facilities at ARI are accredited by AAALAC International (Association for Assessment and Accreditation of Laboratory Animal Care).

A follow-up (complementary) study of 19 rabbits was then performed at the University of Cambridge, under an approved Home Office license (project licence number PP1153947) as governed by the UK law under the Animals (Scientific Procedures) Act 1986.

3.5.2.b- Sample size calculation:

As part of the experimental design process, a literature review was performed to inform the sample size calculation. We have also used an online sample size calculator (https://www.stat.ubc.ca/~rollin/stats/ssize/n2.html), assuming that mu2 (test=2) has to be double the value of mu1 (control=1)* for the results (bone healing) to be statistically significant in the DCBM and TCP groups in comparison with the control PCL group. We conservatively estimated a high population standard deviation (sigma=0.7) to account for individual variation. The literature review of the rabbit bone defect model indicated that a sample size of N=7 – 9 would be sufficient to show significance, while the online sample size calculation indicated that N=8 would be sufficient to identify a clinically relevant increase in new bone formation with a power of 0.80.

** H0: mu1 – mu2 = 0 Ha: mu1 – mu2 > 0*

3.5.2.c- Experimental design outlines:

Twenty-seven female, 16 - 19 weeks old, average body weight of 3 kg, New Zealand white rabbits were used in total. Eight rabbits (from Charles River, Sulzfeld, Germany) were operated at the AO Research Institute-Davos, Switzerland, to validate the model and for surgical training, followed by 19 rabbits (15 rabbits were purchased from ENVIGO RMS LTD, Loughborough, UK and 4 rabbits from Charles River UK Limited, Kent, UK) that were operated on at the University of Cambridge, UK, Biomedical Services Research Animal Facility. The rabbits were purchased at 12 weeks of age and quarantined for 4 - 6 weeks to

reach skeletal maturity and for health observation purposes. The rabbits were housed on floor pens (enclosures) in pairs during the acclimatisation period, then singly housed (by dividing each pen using see-through wire pen-dividers) for the entire post-operative period until euthanasia at 12 weeks.

Study summary: Rabbits were randomly allocated to each biomaterial group – 10 rabbits received DCBM scaffolds (test group), 9 rabbits received TCP scaffolds (positive control), and 8 rabbits received PCL scaffolds (negative control). The rabbits' left forelimbs were operated on to create a 15 mm segmental bone defect as a critical size bone defect, which was then grafted using one of our 3D printed scaffolds. For the follow-up period, pain scoring was done twice a day for the first 3 post-operative days, then once weekly afterwards; radiographs of the operated limb were taken immediately after surgery and then every second week until euthanasia at 12 weeks. Fluorochrome labels were injected at three different time points after surgery (3 weeks Calcein Green, 6 weeks Xylenol Orange and 9 weeks Oxytetracycline) to evaluate new bone formation over time without the need to sacrifice additional animals. At week 12 post-operatively, rabbits were schedule 1 euthanised using an anaesthetic overdose. The grafted limbs were dissected and submitted for micro-CT scanning and histology processing. See **Figure 24** for a summarised study plan. Appendix 1 is an example coversheet generated for each rabbit to facilitate follow-up.

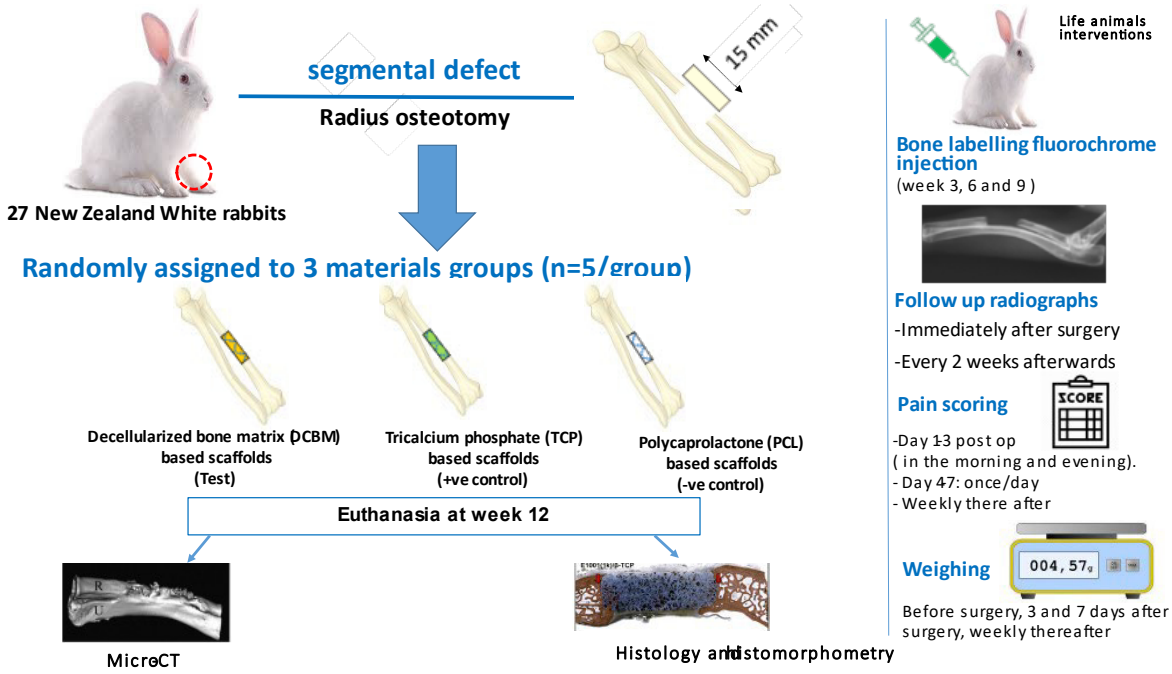


Figure 24: Rabbit study outline.

3.5.3- Anaesthesia and preoperative preparation:

3.5.3.a- In the prep room:

The rabbits were **pre-medicated** with a combination of medetomidine (0.2 mg/kg), midazolam (0.5 mg/kg) and fentanyl (5 µg/kg) intramuscularly in the pre-operative preparation area approximately 20 min before starting the aseptic preparation of the surgical field; continuous oxygen flow was supplied via a face mask. **An intravenous cannula** (22G, 25 mm Blue BD Venflon IV, Winged Cannula with Injection Port, UK MEDI, Cat. No. 39145; Norwich, Norfolk, UK) was then placed in the rabbit's marginal ear vein. For systemic analgesia, all rabbits received carprofen 4 mg/kg IV after premedication. A detailed list of anaesthetic and analgesic drugs used for the rabbit study is listed in **Table 31** below. Anaesthesia was induced using propofol intravenously (0.2 mg/kg IV); then, the rabbits were intubated using a 3.5 mm diameter cuffed endotracheal tube (Medisave, SKU: 01-1130; Weymouth, UK). A supraglottic airway device (v-gel® ADVANCED for rabbits, size R-4; D30004, Docsinnovent Ltd, Hemel Hempstead, UK) was placed if intubation was not possible. A continuous oxygen supply was provided during the pre-operative preparation.

To ensure proper analgesia, either nerve-stimulator guided brachial plexus nerve block using lidocaine 2 % (0.3 ml/kg, equating to a total dose of 6 mg/kg) or lidocaine continuous rate infusion-CRI (a bolus of 2 mg/kg over a 5 min period, followed by a CRI at 100 µg/kg/min for a duration of 90 min) were administered. A parallel study was done by the anaesthesia team using the comparative data from these 2 protocols.

The surgical site (left forelimb) was clipped from the top of the shoulder to below the carpus (medially and laterally), in addition to the fur on the chest underneath the axilla. The rabbit's nails were trimmed, and the surgical site was scrubbed three times with chlorhexidine-based soap (Hibiscrub®; Mölnlycke, Gothenburg, Sweden), three times with 70 % ethanol, then covered with an ethanol-soaked surgical sponge. The foot was wrapped with a cohesive bandage (Vetrap; 3M, Bracknell, UK). Eye lubricant was applied (Lubrithal™ eye gel; Dechra, Hadnall, Shrewsbury, UK) (**Figure 25** summarises the events that took place at the prep room). Then, the **rabbit was transferred to the operation room.**

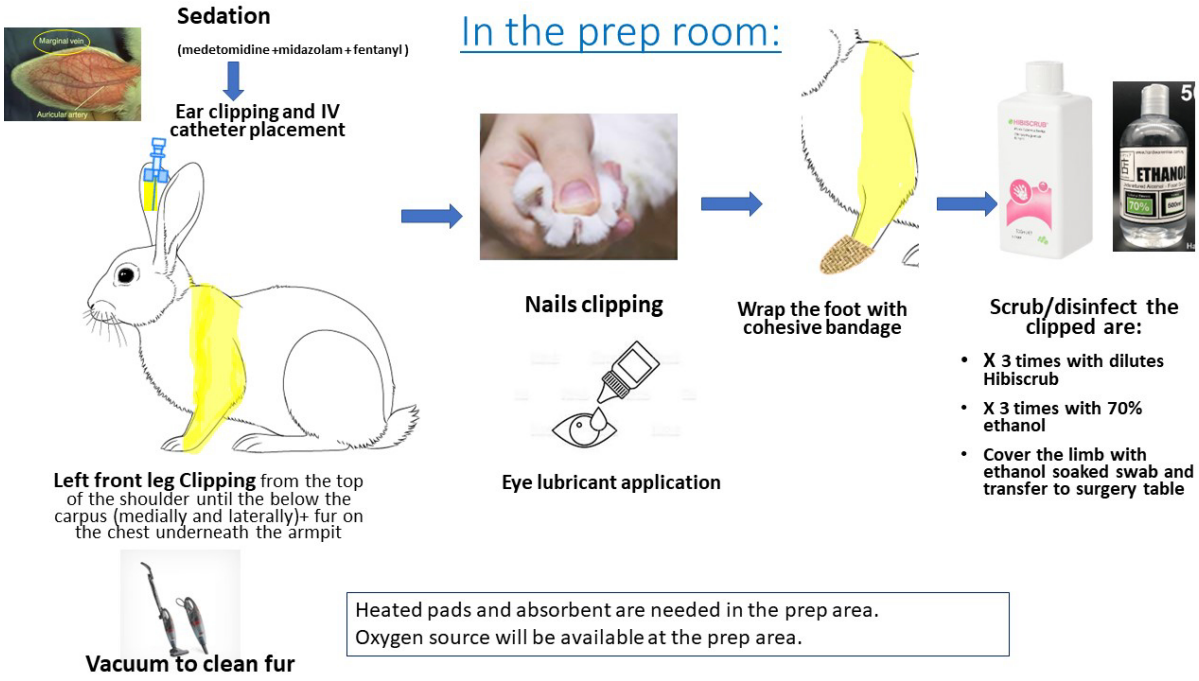


Figure 25: Surgical prep-room procedures.

Table 31: List of anaesthetic and analgesic drugs used for the rabbit study, its doses and commercial brand names.

Use	Drug	Commercial name, supplier and concentration	Dose
Preanesthetic	Medetomidine	Domitor® (1 mg/ml) Vetoquinol UK Ltd; Towcester, UK	0.1 mg/kg IM
	Midazolam	Hypnovel (5 mg/ ml) Neon Healthcare Ltd; Hertford, UK	0.5 mg/kg IM
	Fentanyl	Fentadon 50 µg/ml Injection Dechra; Shrewsbury, UK	0.005 mg/kg IM
Anaesthesia induction	Propofol	PropoFlo Plus 10 mg/ml Emulsion for injection/in fusion Abbott; Chicago, Illinois, USA	0.2 mg/kg IV
Maintenance/ inhalation general anaesthesia	Isoflurane	Isoflurane USP 100% Inhalation Vapour. Piramal Critical Care Ltd; Middlesex, UK	1.5 - 2.0 % in Oxygen
Antagonist	Atipamezole	Antisedan (5 mg/ml) Orion Corporation, Zoetis; NJ, USA	0.5 - 1.0 mg/kg IM
Local anaesthetic	Lidocaine	Lidocaine Hydrochloride 2% Hameln pharmaceuticals Ltd; Gloucester, UK	Brachial plexus nerve block (6 mg/kg) Lidocaine CRI (a bolus of 2 mg/kg over a 5 min period, followed by a CRI at 100 µg/kg/min for a duration of 90 mins)
Fluid therapy	Ringer's lactate solution	Aqupharm® No. 11 Aqupharm, York, UK	10 ml/kg/hr IV infusion
Analgesia	Carprofen	Rimadyl 5% RXV, Zoetis; NJ, USA	4 mg/kg IV or SC (5 doses) Preop then daily for 4 days
	Buprenorphine	Bupaq - 0.3 mg/ml Chanelle Pharma, Hungerford, Berkshire, UK	0.06 mg/kg S/C q 8 h for 3 days
Euthanasia	Pentobarbital	Dolethal 200 mg/ml Vetoquinol UK Ltd; Towcester, UK	200 mg/kg (= 1 ml/kg) IV

3.5.3.b- In the operating room

The anaesthesia was maintained using isoflurane in oxygen and air delivered via a modified T-piece. During general anaesthesia, the rabbits were monitored using pulse oximetry, oesophageal temperature, capnography and inspiratory and expiratory anaesthesia gas analysis. (See Appendix 2 - example anaesthesia monitoring sheets)

A fentanyl bolus (dose 5 μg/kg) was administered as rescue analgesia if the heart rate or respiratory rate increased by 20 % from baseline during the surgery. The baseline values were recorded immediately prior to the surgical start time. Ringer's lactate solution was administered at a rate of 10 ml/kg/hr IV infusion intra-operatively.

The rabbit was positioned in left lateral recumbency on a heating pad set to 38 °C. The surgical draping and aseptic preparation of the left forelimb was performed in the following sequence:

1- The foot was wrapped in an autoclaved cohesive bandage (Vetrap) so the double-gloved surgeon could handle/hold the limb. Intraoperative skin preparation was performed using chlorhexidine gluconate and an isopropyl alcohol antiseptic applicator (ChloraPrep ™ 3 ml clear applicators, BD, Franklin Lakes, NJ, USA).
2- A U-drape / split-sheet (3M™ Steri-Drape™ Surgical Split Sheets, 9043- 152 x 183 cm; 3M, Cat. No. 7000053578, Bracknell, UK) followed by a fenestrated adhesive drape (3M™ Steri-Drape™ Adhesive Aperture Drape, 9028 - 75 x 75 cm (6 x 8 cm aperture; 3M- Cat. No. 7000053569, Bracknell, UK) were placed around the left forelimb to isolate the surgical site. Any exposed part of the surgical table was then covered by a plain rectangular surgical drape (Adhesive Drapes, Bastos Viegas 75 x 90 cm; IMS Euro Ltd, Cat. No. 488-203, Stockport, UK).
3- A second application of skin antiseptic (ChloraPrep ™ 3 ml clear applicators, BD, Franklin Lakes, NJ, USA) was performed, followed by wrapping the prepared limb with a sterile transparent incise through drape (Individually Packed, sterile Incise Drapes 25 x 28 cm; 3 M, Cat. No. 7000053578, Bracknell, UK).

The operation room layout is demonstrated in **Figure 26**. See Appendix 3 for an example surgery report sheet.

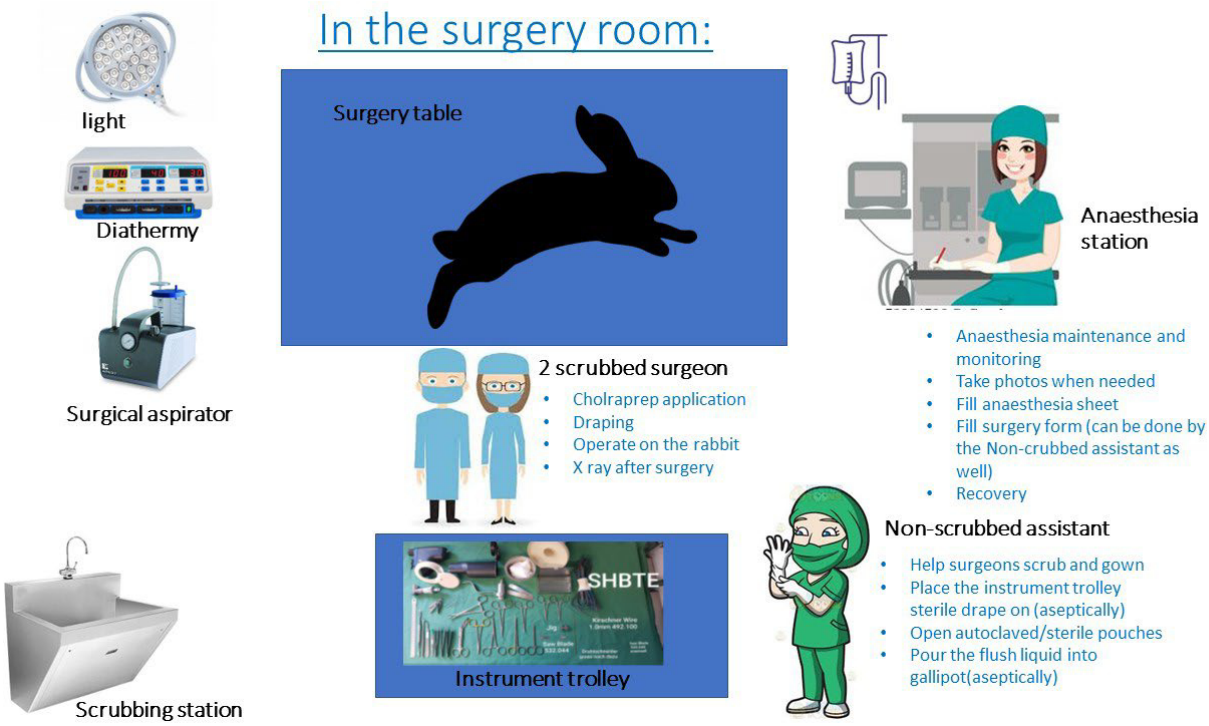


Figure 26: Operating room layout

3.5.4- Surgical procedure and post-operative care.

3.5.4.a-Surgeries:

- Using a No. 15 scalpel blade, a 3.5 cm long incision was made on the medial aspect of the rabbit's antebrachium in order to expose the radial diaphysis starting 1.5 cm above the radiocarpal joint and extending upward, ending 5 cm above the radiocarpal joint. The visible part of the radius lies between the extensor and flexor muscle groups.
- The cephalic vein was identified and freed from the connective tissue to allow mobilisation and protection during the surgery. Any bleeding was stopped using a diathermy unit.
- The mid 1/3 of the radial diaphysis was exposed by blunt dissection, taking care not to damage the periosteum followed by placing specially made small size self-retaining soft tissue retractors (RISystem, Landquart, Switzerland) at the proximal and distal ends of the incision (see #3 in **Figure 27** for surgical instruments).
- A Titanium K Wire 1.0 mm Ø (Freelance surgical, Cat. No. 6.032.10, Bristol, UK) was inserted (using SmartDriver Duo™, wire drive reference 6643-045; MicroAire, Charlottesville, VA, USA) was inserted 5 cm above the radio-carpal joint, centred in the medial radial diaphysis. This K wire was used as an anchor for a specially designed cutting guide to ensure an accurate and reproducible 15 mm osteotomy. The

cutting guide was custom-made at the tools workshop at the AO Research Institute (ARI)-Davos, Switzerland.

- The muscles attached to the caudal aspect of the radius were sharply dissected close to the bone and released in preparation for the osteotomy.
- Malleable Walton Retractors (13 mm x 175 mm) - (Freelance surgical Cat. No. A11-1331-01, Bristol, UK) were placed between the radius and the ulna to protect the underlying ulna and the surrounding tissue during the osteotomy (see item #4 in **Figure 27**). The cephalic vein was displaced cranially and protected by the tissue retractor.
- The custom-made osteotomy jig (cutting guide) with slots designed to be 15 mm apart, was threaded through the inserted k-wire (see **Figure 29** for the positioning of the cut guide/jig in cadaveric training limb), and the proximal and distal osteotomy cuts (15 mm apart) were made using Synthes Sagittal Saw Blades - Fine Teeth (4 mm Width / 15 mm L / 0.4 mm Thickness (DePuySynthes®, Cat. No. 532.044; Warsaw, Indiana, USA) with an oscillating saw (Micro-Aire smart drive Duo sagittal saw, reference 6673, SN 1764; MicroAire, Charlottesville, VA, USA used in Cambridge and Colibri; DePuySynthes, saw attachment Cat. No. 532.021; Warsaw, Indiana, USA was used in Davos).
- The jig only allowed cutting through/marking the cis cortex; hence, the jig was removed, and the osteotomies were completed through the trans cortex freehand using the same saw blade and the oscillating saw while taking care to avoid the ulna, with continuous flushing with saline during cutting.
- When the two osteotomies were completed, the bone segment (ostectomy) was removed from the surgical site by cutting the interosseus ligament between the radius and ulna. A picture of the empty defect was taken. See **Figure 28.**
- The inserted titanium K wire was cut at the level of the cis cortex and left in situ as a reference indicator for post-operative imaging and post-mortem histology evaluation.
- Afterwards, the 3D-printed scaffold allocated to the operated rabbit was implanted into the bone defect as a press-fit implant to span the ostectomy completely. A picture of the filled defect was taken. See **Figure 28.**
- Finally, the muscles and subcutaneous tissue were sutured in cruciate and simple continuous suture patterns respectively using 5/0 Vicryl (Ethicon Vicryl Rapide™ Sutures 5/0 USP Taper point plus needle (17 mm size), IMS Euro Ltd, Cat. No. W9969; Stockport, UK) and the skin was sutured using a buried intradermal suture

pattern with 4/0 Monocryl (Ethicon Monocryl® Plus Antibacterial Sutures 4/0 USP, reverse cut prone multi-pass needle (19 mm needle size), IMS Euro Ltd, Cat. No. MCP496H; Stockport, UK), followed by skin glue application (VETBOND tissue adhesive; Vet Direct, Cat. No. VB3M, Newcastle upon Tyne, UK).

- A layer of spray bandage (Opsite Film Dressing Spray; Smith & Nephew, Cat. No. 66004978, Watford, Hertfordshire, UK) was applied to protect the surgical site. The limb was covered with a sterile surgical sponge, and the rabbit was transferred to the imaging room for post-operative radiographs. Mediolateral (ML) and anterior-posterior (AP) radiographs of the operated limb were taken immediately after surgery (then every 2 weeks afterwards). For the X-ray, the tube was set to be 70 cm distance from the X-ray cassette (and the limb), 45 KV energy, 0.16 MA current and 0.04 seconds exposure time. After the radiographs were captured, the sedation was reversed by injecting atipamezole (Antisedan- 0.5-1.0 mg/kg IM), and the rabbits were monitored until recovery, in sternal recumbency. Closer monitoring was performed by the anaesthesia team for 24 h after surgery for their parallel study mentioned above (Lidocaine nerve-stimulator guided brachial plexus nerve block vs CRI).

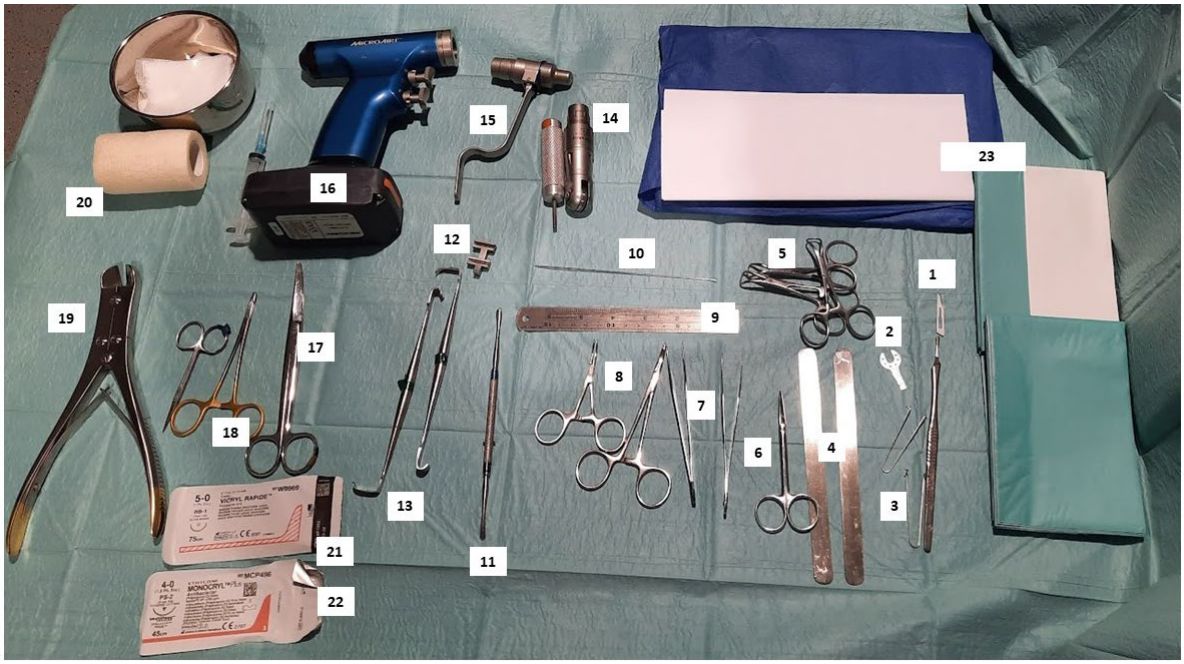


Figure 27: Surgical instruments for the rabbit radial defect surgery.

1- 15 blade scalpel 2- Synthes Sagittal Saw Blades(cat.# 532.044 - Fine Teeth 4mm Width/ 15mm L/0.4mm Thickness). 3- self retaining soft tissue retractors (RISystem). 4- Malleable Walton Retractor (13 mm x 175 mm)- freelance surgical # A11-1331-01. 5- Towel clamps 6 and 17 – different type scissors 7- Adison thumb forceps 8- mosquito haemostats 9- autoclavable ruler 10- 1 mmØ k wire 11-Freer Raspatorium S/B 185mm (OL165R) Aesculap 12- Custom made osteotomy cut guide (Jig) 13- Senn retractors 14-Auscultation saw attachment (Micro-Aire smart drive Duo sagittal saw (REF 6673 -SN 1764) with a key. 15- MicroAire Smart Driver Duo™- wire drive reference 6643-045 16- MicroAire SmartDriver Duo™- 6643 16- MicroAire Smart Driver Duo™ with rechargeable battery. 18- Olsen-Hegar Needle Holder with Suture Scissors (14 cm). 19- Wire Cutters (2.2 mm capacity) freelance surgical- A22-2317-03. 20-Autoclaved cohesive bandage (vetrap). 21- Ethicon Vicryl Rapide™ Sutures 5/0 USP Taper point plus needle (17 mm size). 22- Ethicon Monocryl® Plus Antibacterial Sutures 4/0 USP – reverse cut prone multi pass needle (19 mm needle size). 23- surgical drapes (listed above).

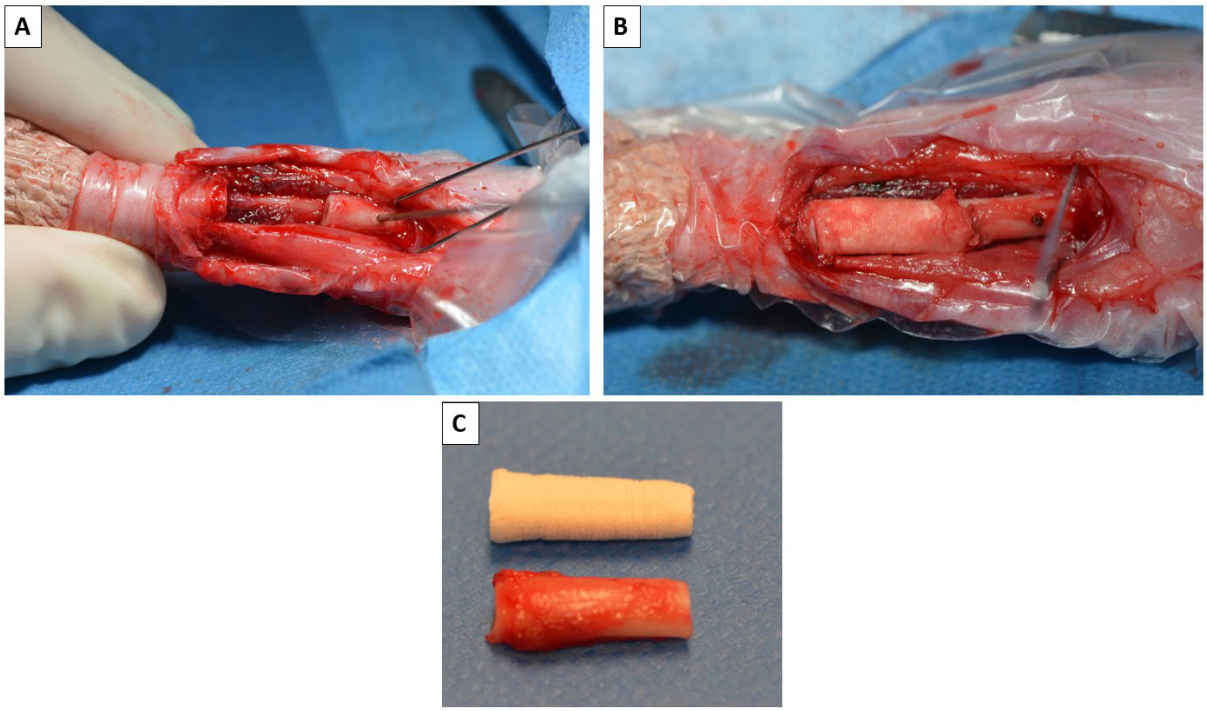


Figure 28: Rabbit radius 15 mm bone defect A) empty defect B) defect after scaffold implantation. C) the osteotomised bone segment side to side to the 3D printed scaffold

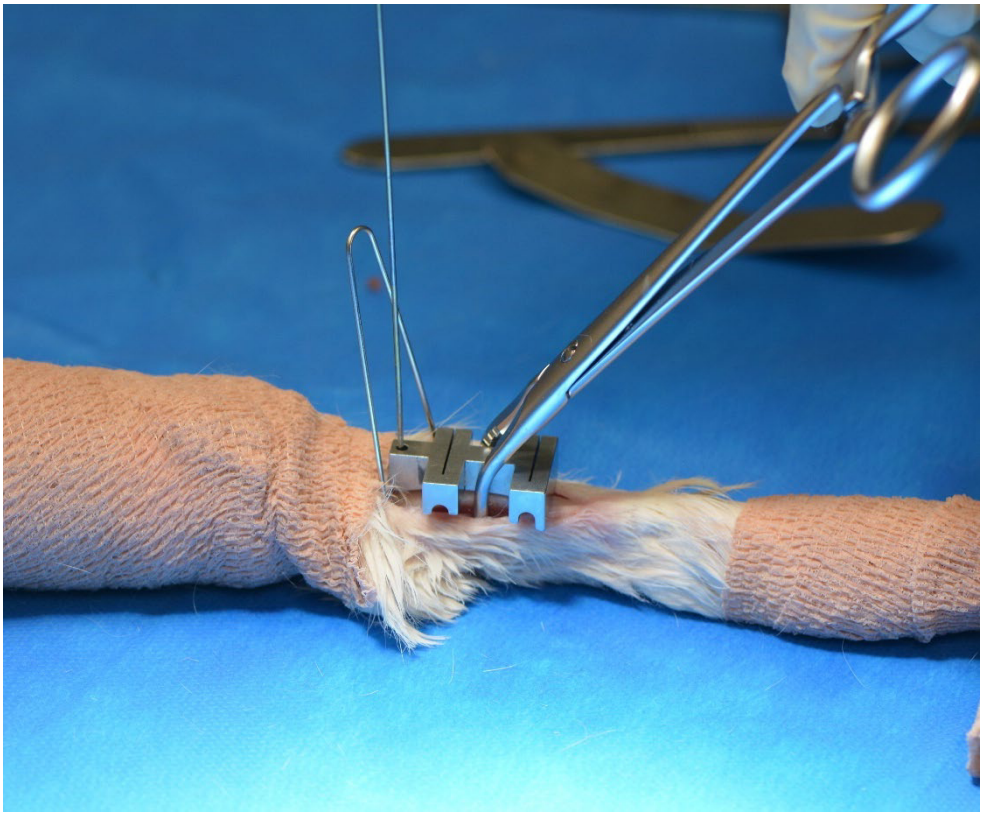


Figure 29: Cadaveric practice surgery demonstrates the osteotomy guide (jig) positioning.

3.5.4.b-Postoperative care:

Pain scoring and pain management:

Rabbits were checked twice a day for the first three days following surgery. They were monitored for their general behaviour, appetite, and degree of weight-bearing on the operated leg. The surgical incision, respiration, eyes, fur, and faeces were also monitored. The results were noted on an objective score sheet (see **Table 32** below and Appendix 1). The scoring was continued once daily for the first seven postoperative days, then once a week afterwards as long as the score stayed within a pre-defined limit; otherwise, the scoring frequency was increased again. Post implantation, rabbits were singly housed on floor pens for the entire postoperative period until euthanasia at 12 weeks.

For pain management, Carprofen 4 mg/kg was injected subcutaneously (S/C) once a day for 4 post-operative days and Buprenorphine 0.06 mg/kg S/C every 8 hours for 3 postoperative days. Frequency was increased as needed. See Appendix 1 for the pain management schedule as mentioned in the animal folder cover sheet, and see **Table 31** above for drugs suppliers, concentration and doses.

Table 32: Rabbits post-operative scoring system.

Scoring criteria	
Behaviour	
Quiet and attentive= 0 Lethargic (reduce reaction to stimuli) = 1 Apathetic (non-reactive) = 4	
Appearance (fur eye & skin)	
Clean =0 Little dirty & sticky = 2 Very dirty & sticky = 3	
Nictating membrane	
Nonvisible = 0 Visible =3	
Food intake	
Normal = 0 Reduced = 1 Not eating = 2	
Water intake	
Normal = 0 Reduced = 1 Not drinking = 2	
Weight bearing	
Normal/ full weight bearing = 0 Reduced weight bearing = 1 Severely reduced weight being =2 Non weight bearing= 3	
Coprophagy	
No = 0 Yes =1	
Body temperature	
Normal (38.5-39.5 °C) In range = 0 Not in range= 1	
Wound healing	
Normal = 0 Inflammation (hot, red, swollen)=2 Infection (oozing secretion) = 4	
Body weight	
Similar to baseline =0 1-10% reduction = 1 11-20% reduction = 2 > 20% reduction =4	
Faeces consistency	
Normal=0 Soft= 2	
Total	Score < 3 mild Score 4-9 Moderate (animal to be checked, additional dosage of pain medication or shorter interval between doses if needed). Score 10 or more (severe) consider euthanasia. Score more than 6 for 3 consecutive days (consider euthanasia).
Signature	

3.5.5- In-Life animal outcomes:

3.5.5.a-Body weight:

The rabbits were weighed on day 3 and day 7 after surgery, then once a week thereafter.

3.5.5.b- Radiographs:

Medio-lateral (ML) and anterior-posterior (AP) radiographs of the operated limb were captured immediately after surgery and then every 2 weeks thereafter. For the X-ray, the tube (Practix 30 Mobile X-Ray; Philips Electronics UK Limited, Farnborough, UK) was set to be 70 cm distance from the x-ray cassette (and the limb), 45 KV energy, 0.16 mA current and

0.04 seconds exposure time. For the fortnightly radiographs, the rabbits were sedated prior to imaging with a combination of medetomidine (0.2 mg/kg), midazolam (0.5 mg/kg) and fentanyl (5 µg/ kg) intramuscularly. The sedation was reversed at the end of the imaging session via injecting Atipamezole (Antisedan - 0.5-1.0 mg/kg IM).

The X-ray cassettes were processed using a (CR-35X Digitizer; Agfa Health Care, Mortsel, Belgium) and SE Media DICOM viewer version 4.0 (Agfa Health Care, Mortsel, Belgium).

3.5.5.c- Fluorochrome labels injection:

Fluorochrome labels were injected at three different time points after surgery (3 weeks Calcein Green, 6 weeks Xylenol Orange and 9 weeks Oxytetracycline) to evaluate new bone formation over time without the need to sacrifice additional animals (**see Table 33**).

Table 33: Fluorochrome labels injection time points and doses.

Fluorochrome label	Brand name	Time point	Dose/ injection route
Calcein Green	Calcein disodium salt (Honeywell Fluka- Cat. No. 21030; Aylesbury, UK)	3 weeks post-surgery	Prepared as 0.5% sterile filtered solution in normal saline, and administered to a final dose of 5mg/kg of animal (therefore, 1 mL/kg) subcutaneously
Xylenol Orange	Xylenol Orange tetrasodium salt (Honeywell Fluka Cat. No. 33825; Aylesbury, UK)	6 weeks post-surgery	Prepared as 9% sterile filtered solution in normal saline, and administered to a final dose of 90 mg/kg of animal (therefore, 1 mL/kg) subcutaneously
Oxytetracycline	Engemycin® 10% DD Solution for injection. MSD Animal Health – Cat. No. G2470; Milton Keynes, UK)	9 weeks post-surgery	Administered at 25 mg/kg of animal (therefore, 0.25 mL/kg) subcutaneously.

3.5.6-Euthanasia and post-mortem outcomes:

3.5.6.a-Euthanasia:

The euthanasia was performed by means of an intravenous overdose of barbiturate (Pentobarbital, Dolethal – dose 200 mg/kg (= 1 ml/kg) IV). Legs that had been operated on

were dissected and fixed in cold 70 % ethanol until further processed for µ-CT scanning and histology.

3.5.6.b-Post-mortem outcomes:

The fixed specimens were submitted for µ-CT scanning and then sent to the histology lab for undecalcified histology processing.

3.5.6.b.I- Micro Computed tomography (µ-CT) scanning:

- Scanning:

The post-mortem leg scanning was performed in collaboration with the biomedical engineering research group at the University of Cambridge Department of Engineering. A microfocus CT Scanner (XT H 225 ST Industrial CT Scanner; Nikon (Nikon Metrology NV); Leuven, Belgium) was used to scan each specimen individually, with scan settings as the following: 19.99 µm pixel size, beam energy 90 KV, beam current 60µ Amp, power 5.4 Watts and exposure of 1 frame per second (FPS).

The region of interest for the µ-CT scanning extended from 15 mm above the implanted scaffold to 15 mm below the scaffold.

- Data processing:

The data was imported to VGSTUDIO MAX 2022.1 software for inspection and 3D model/ mesh reconstruction. The data were exported as STL and DICOM files for further analysis.

- Micro-CT data analysis:

Objective comparison of the scans from animals in 3 materials groups was conducted on the CT scans and reconstructed 3D models from these CT scans to identify areas of new bone formation and any anatomical changes.

3.5.6.b.II- Decalcified bone sections:

Specimens from animals culled from the study due to surgical complications or medical comorbidities were fixed in 70 % ethanol and sent to the histopathology service (Department of Veterinary Medicine, University of Cambridge) for histopathological evaluation.

The bones were decalcified for 15-18 h in hydrochloric acid (10%)/ sodium chloride (20%) based decalcification solution (Decal II- rapid; atom scientific- Cat. No. RRDC1-G, Hyde, Cheshire, UK) at room temperature. Followed by processing, embedding in paraffin, sectioning and H&E staining (as explained in section 3.3.2.1.b).

The specimens were sectioned along the longitudinal axis of the bone (and the implant). During histopathological evaluation, we focused on the following regions: proximal and distal

osteotomy sites, inside the osteotomy/ implant site, anterior to the osteotomy (the periosteum) and posterior to the osteotomy (the interosseous space between radius/ implant and ulna). Evaluation criteria were based on a scoring system developed in collaboration with the AO Research Institute (ARI), Davos, Switzerland and are summarised in **Table 35**.

3.5.6.b.III- Undecalcified histology processing:

- **Specimens' dehydration:**

The bone specimens were dehydrated in a graded series of ethanol (70 % - 80 % - 90 % - 100% "twice") for 72 h each. Followed by air drying in a fume hood for 48 h.

- **Embedding:**

The bone specimens were embedded in polyester clear casting resin mixed with MEKP (Methyl Ethyl Ketone Peroxide) catalyst (ABL STEVENS, product code SCR5 and CAT 100, respectively; Sandbach, UK). The mixture ratio was 40 resin,1 MEKP.

EXAKT embedding moulds (1 compartment, large 16 mm deep mould - JEFF STEVENS Ltd, Cat. No. 41450; Cirencester-UK) were used to pour the resin over the bone specimens. The resin was left to cure for 48 h under a vacuum in a fume hood, with a gradual vacuum increase to avoid air bubble formation.

- **Sectioning, mounting and grinding:**

The embedded blocks were sectioned into a series of 2 mm slices with a cutting plane parallel to the longitudinal axis of the bone, using IsoMet® 5000 linear precision saw (Buehler, Lake Bluff, IL-USA). The sections were visually inspected to select the best representative cutting level that includes adequate implant/bone interface before mounting on transparent plastic microscopic slides (EXAKT 50 x 75 x 2 mm slides- Cat. No. 41540, Oklahoma City, OK-USA), then grinding and polishing to a final 200 µm thick sections using AutoMet™ 300 Pro Grinder-Polisher (Buehler, Lake Bluff, IL, USA).

The processed (unstained) undecalcified bone sections (slides) were submitted for confocal microscopy to image the fluorochrome labels firstly, then stained using Stevenel's blue-Van Gieson Picrofuchsin stains afterwards for histopathological scoring/analysis.

- **Bone labelling fluorochromes imaging:**

A Nikon AxR (iT2 eclipse) inverted confocal microscope and Nikon-NIS element AR 5.41.01 software (Nikon Europe B.V., Amstelveen, NL) were used to acquire the images, using the Nikon long plan field correction, 20x magnification, 0.35 numerical aperture and 24 mm

working distance (super long working distance; Nikon L plan, SLWD, 20x/0.32, WD 24) objective. The filter settings for the three fluorochrome labels are detailed in **Table 34** below.

An objective analysis of the acquired images was performed based on the distribution of the fluorochromes across the bone section, as well as quantitative image analysis using Fiji image J software [721] to quantify the percentage of positively labelled areas for each fluorochrome. For the quantitative image analysis, a Kolmogorov–Smirnov test was used to test for data normality, P value ≥ 0.05 meant the data were considered normally distributed, while P≤ 0.05 meant the data were not normally distributed. Comparisons between parametric data from the three groups were made using an one-way ANOVA (using IBM SPSS Statistics for Windows, Version 28.0) [621] followed by running a Bonferroni post hoc test to determine the significance of differences between the frequencies of categorical variables. For all tests, P values of ≤ 0.05 were considered to be significant.

Table 34: Filters setting for the bone fluorochromes labels imaging.

Fluorochrome	Excitation	Emission	Matching LED Light Source	Assigned colour code
Calcein green	509	541	488 nm	Yellow
Xylenol orange	546	630	550 nm	Magenta
Oxytetracycline	429	477	405 nm	Cyan

❖ **Undecalcified bone sections Staining:**

The undecalcified bone sections were stained following the Stevenel's blue-Van Gieson Picrofuchsin staining protocol.

Materials used:

- Methylene Blue (Fisher Scientific, Fisher BioReagents™, Cat. No. 10307033, Loughborough, UK).
- Potassium Permanganate (Fisher Scientific, Fisher Chemical™, Cat. No.12626757, Loughborough, UK)
- Acid Fuchsin (Thermo Fischer, Thermo Scientific™, Cat. No. 400211000, Loughborough, UK)
- Saturated picric acid (Sigma Aldrich, Cat. No. P6744, Gillingham, Dorset, UK)
- Distilled water
- Ethanol
- Incubator or water bath

Staining solution preparation:

Stevenel's blue:

- 1 g of Methylene Blue was dissolved in 75 ml DW.
- 1.5 g of the potassium permanganate was dissolved in 75 ml of DW.
- The 2 solutions were mixed and heated in a water bath at 100 °C to ensure that any precipitate was dissolved properly.
- Then the solution was cooled down to room temperature until use (it is stable for up to 2 years and can be reused several times).

Van Gieson Picrofuchsin:

- 0.1 g of acid fuchsin was dissolved in 10 ml DW, then 100 ml of saturated picric acid was added, and the mixture was stored at room temperature (it is stable for up to 2 years and can be reused several times).

Bone section (slide) staining procedure:

- Stevenel's blue (SB) staining solution was warmed to 56 °C in a water bath, and then the slides were soaked in the SB solution for 5 min followed by washing in DW and blotted dry.
- The slides were soaked in Van Gieson staining solution for 2 min, followed by rinsing in DW and blotted dry. Finally, the slides were washed in 100 % ethanol and blotted dry. Slides were then stored until they were ready for microscopic evaluation.

❖ **Histopathology scoring system:**

A histopathology scoring system was developed in collaboration with the AO Research Institute (ARI), Davos, Switzerland.

Upon staining the slides, the bone sections were evaluated for the criteria detailed in **Table 35** below focusing on the following regions: proximal and distal osteotomy sites, inside the osteotomy / implant site, anterior to the osteotomy (the periosteum) and posterior to the osteotomy (the interosseous space between radius / implant and ulna).

Table 35: histopathology scoring system for undecalcified bone sections.

Criteria	Score/ interpretation
1-Proliferative changes	0 None
Defect closure inside the osteotomy	1 >20%
Defect bridging anterior to the osteotomy (periosteal ossification)	2 20-39%
Defect bridging posterior to the osteotomy and interosseous space (between radius and Ulna)	3 40-59% 4 60-79%
Osseous integration / bone ingrowth	5 80-100%
2-Degenerative bone changes	
Osteonecrosis	
Sequester	
Osteolysis	
3-Phagocytosis	0 No changes
Macrophages	1 Minimal
Giant cells	2 Slight
4-Inflammatory changes	3 Moderate
Fibrous tissue	4 Severe
Lymphocytic (= non-purulent) inflammation	5 Massive
Granulocytic (= purulent) inflammation	
Necrotizing inflammation	
Osteomyelitis (inflammation near bone marrow)	
5- Infection	0 Absent
Bacteria (cocci or bacilli visible)	1 Present

Chapter 4: Results

4-Results

4.1- Adipose derived mesenchymal stem cells characterisation:

4.1.1- Cell morphology:

4.1.1.a. Inverted light microscopy:

Primary cell cultures established from the 3 species (sheep, rabbit, and rat) were examined under an inverted light microscope. The cells were adherent to the tissue culture plastic, tended to grow in colonies **(Figure 30),** with a fibroblastic morphology ranging from spindle shaped to triangular or flat shaped, with large, round nuclei and prominent nucleoli, which were surrounded by finely dispersed chromatin particles **(Figure 31).**

4.1.1.b. Immunofluorescence:

The images from immunofluorescent staining of the sheep, rabbit, and rat Ad-MSCs confirmed the fibroblast-like morphology where the β-actin appears as numerous, thin, parallel, intersecting fibre bundles extending across the entire cytoplasm (**see Figure 32**) which are characteristic of undifferentiated MSCs.

4.1.1.c. Scanning electron microscope (SEM):

Cells adherent to the surface of glass coverslips had a fibroblastic appearance, with extended filopodia (black arrows) and abundant extra cellular matrix (**see Figure 33).**

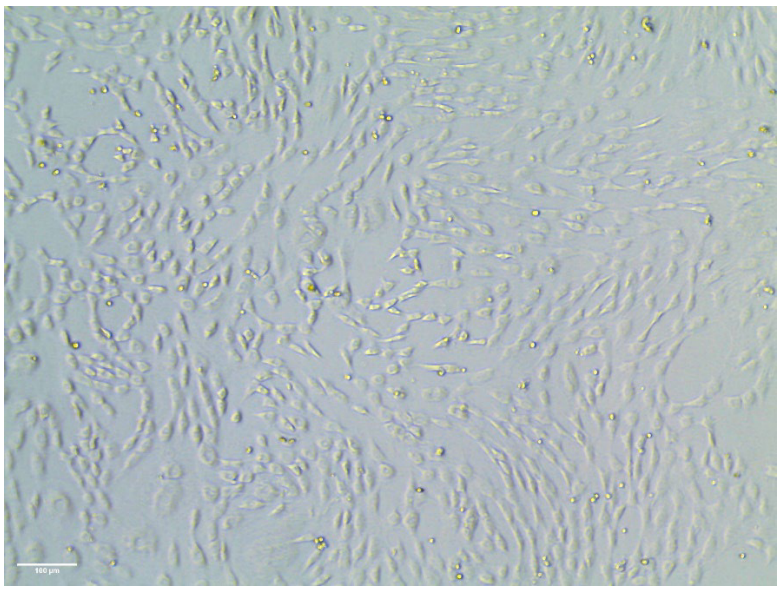


Figure 30: Rat Ad-MSCs growing on tissue culture plastic, imaged using inverted light microscope (4x original magnification; scale as indicated).

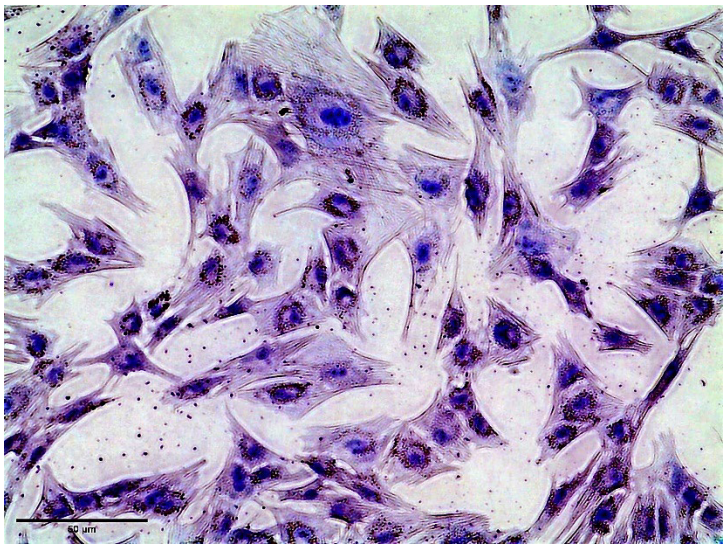


Figure 31: Inverted light microscope image of haematoxylin-stained ovine Ad-MSCs.

Demonstrating the fibroblastic appearance that ranges from spindle shaped to triangular or flat shaped. The nuclei were round, relatively large and had prominent nucleoli, surrounded by finely dispersed chromatin particles (20x original magnification; scale as indicated).

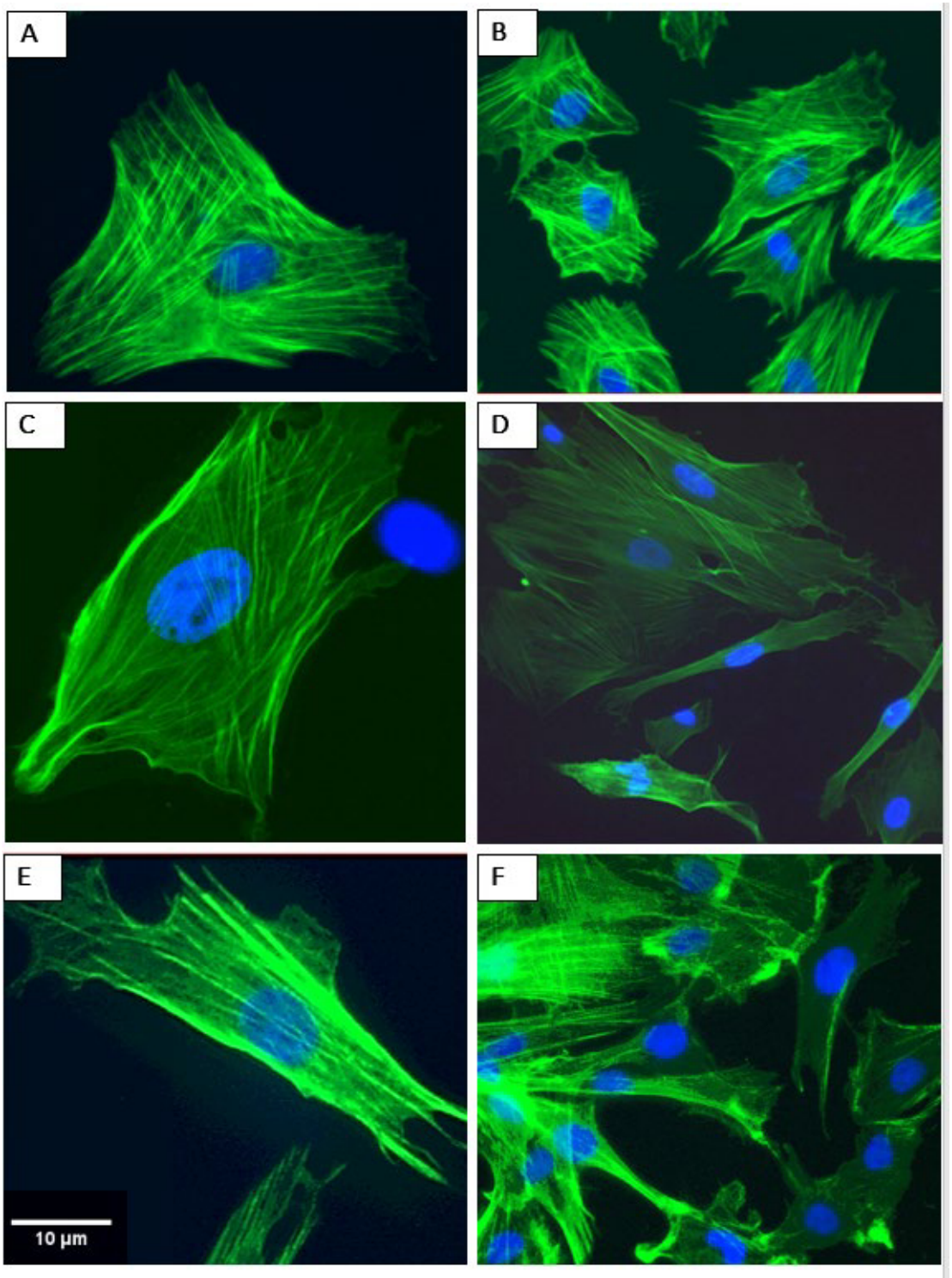


Figure 32: Immunofluorescent staining of Ad-MSCs. Beta-actin in the cytoskeleton was labelled with Alexa Fluor® 488/ FITC (green) and the nucleus counterstained with DAPI (blue).

Ovine (A and B), rabbit (C and D) and rat (E and F) Ad-MSCs. A, C and E 40x; B, D and F 20x original magnification); scale as indicated.

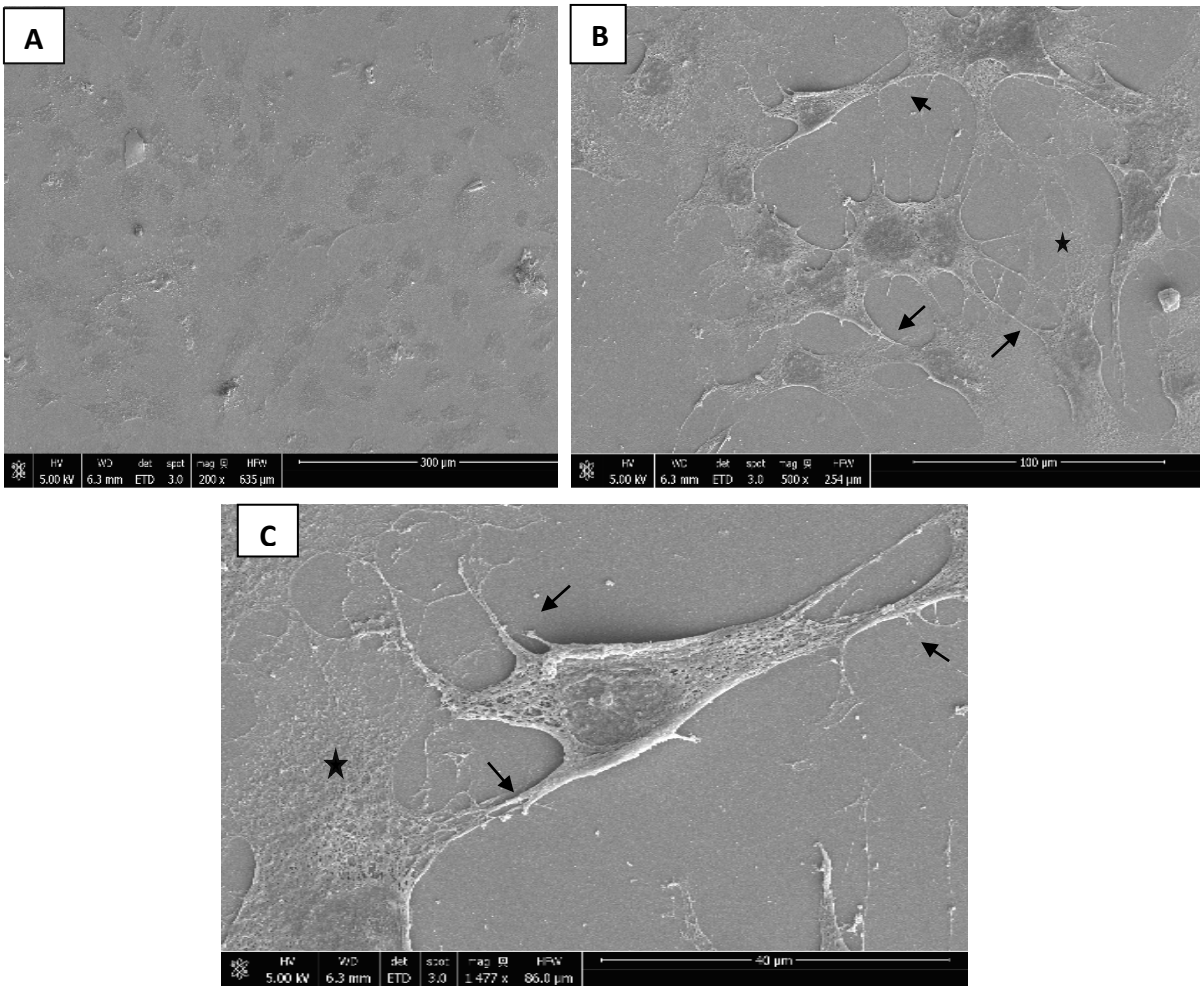


Figure 33: Ad-MSCs populating the surface of glass coverslips and imaged using SEM.

Showing fibroblastic appearance with extended filopodia (black arrows) and abundant extra cellular matrix (*). Original magnifications 200x (A), 500x (B) and 1477x (C).

4.1.2: Behaviour in tissue culture

4.1.2.a- Colony Forming Unit (CFU) assay

The isolated Ad-MSCS from the 3 species grew in colonies 7 - 10 days after low density seeding **(see Figure 34).**

4.1.2.b- Cell proliferation and viability assay (MTT):

Ad-MSCs isolated from the sheep, rabbit and rat showed similar growth patterns over time (**see Figure 35 and Table 36**). The measured absorbance of the MTT formazan product exhibited a 5.09 fold increase from day 1 to day 3 for the ovine Ad-MSCs; 4.822 fold increase for the rabbit Ad-MSCs and 3.163 fold increase for the rat Ad-MSCs. From day 3 to day 7 there were 2.809, 2.103 and 2.179 fold increases for the ovine, rabbit and rat Ad-MSCs respectively. Finally, from day 7 to day 10 there were 1.597, 1.859 and 2.267 fold increases for the ovine, rabbit and rat Ad-MSCs respectively (**Figure 36).**

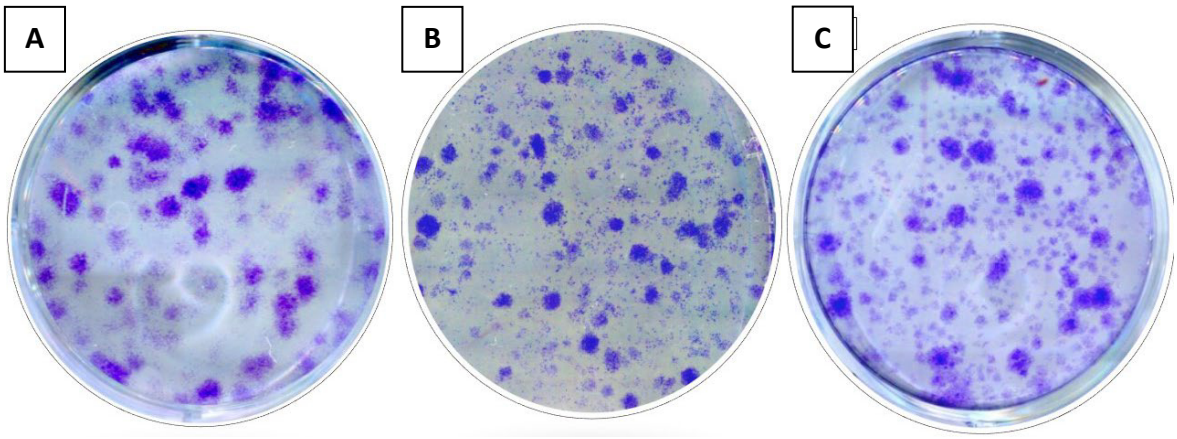


Figure 34: Crystal violet stained Ad-MSCs colonies.

A) Ovine Ad-MSCs B) Rabbit Ad-MSCs C) Rat Ad-MSCs

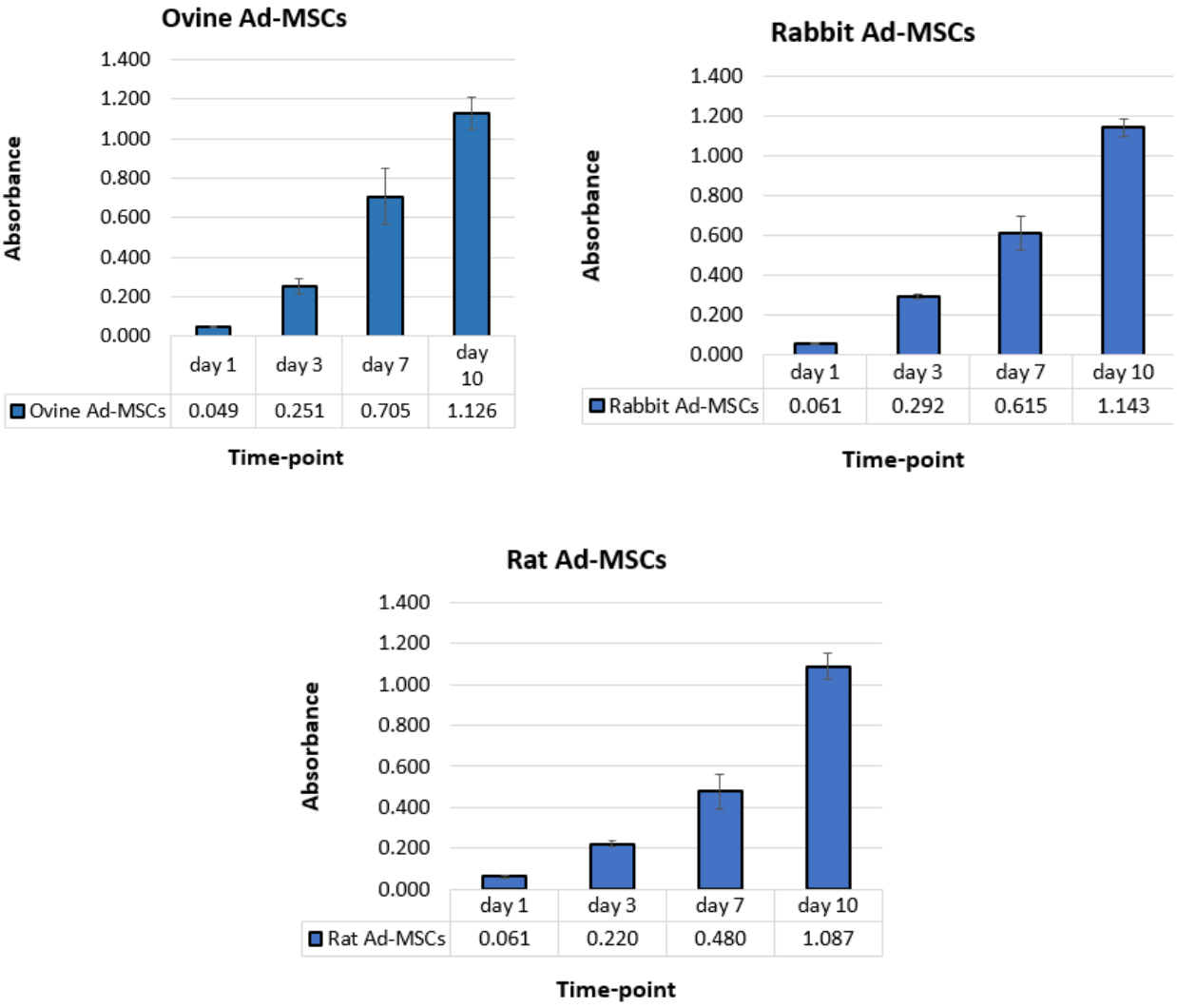


Figure 35: Ad-MSCs proliferation over time as determined by MTT assay.

Data represent mean (±SD) for six measurements at each time point.

Table 36: Ad-MSCs quantified proliferation (absorbance at 570 nm) over time

	Day 1	Day 3	Day 7	Day 10
Ovine MSCs	0.049 ± 0.002	0.251 ± 0.38	0.705 ± 0.141	1.126 ± 0.079
Rabbit MSCs	0.061 ± 0.002	0.292 ± 0.012	0.615 ± 0.086	1.143 ± 0.042
Rat MSCs	0.061 ± 0.005	0.220 ± 0.014	0.480 ± 0.084	1.087 ± 0.064

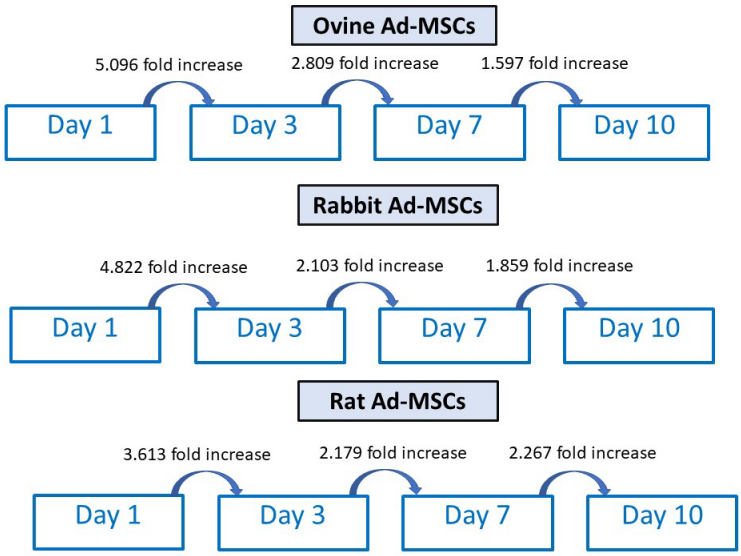


Figure 36: Fold-increase in MTT absorbance over time for ovine, rabbit and rat MSCs.

4.1.2.c- Cell migration assay (scratch wound healing assay):

Ad-MSCs from 3 species demonstrated the ability to migrate into the wound space to fill the created gap **(see Figure 37).** The results from the Kolmogorov Smirnov test of normality indicate that data were normally distributed (P=0.200). The difference in wound closure % values were statistically significant (P<0.001) for MSCs isolated from different species; with rabbit Ad-MSCs having the highest closure % (85.31 %) and ovine Ad-MSCs having the lowest closure % (83.12 %, See **Table 37**).

Table 37: Scratch wound assay area measurements.

Species	**Area measurment (mm)**		**Wound closure%**
	0 hr	**24 hr**	
Ovine MSCs	280.28 ± 2.29	45.61 ± 1.28 ***	83.12 % ±1.09
Rabbit MSCs	285.17 ± 1.32	40.92 ± 0.79 ***	85.31 % ± 0.84
Rat MSCs	299.52`± 2.26	46.79 ± 1.70 ***	84.06 %± 0.87
The data represent mean (±SD) for triplicate measurements at each time point. *** denotes statistically significant differences P ≤ 0.001.			

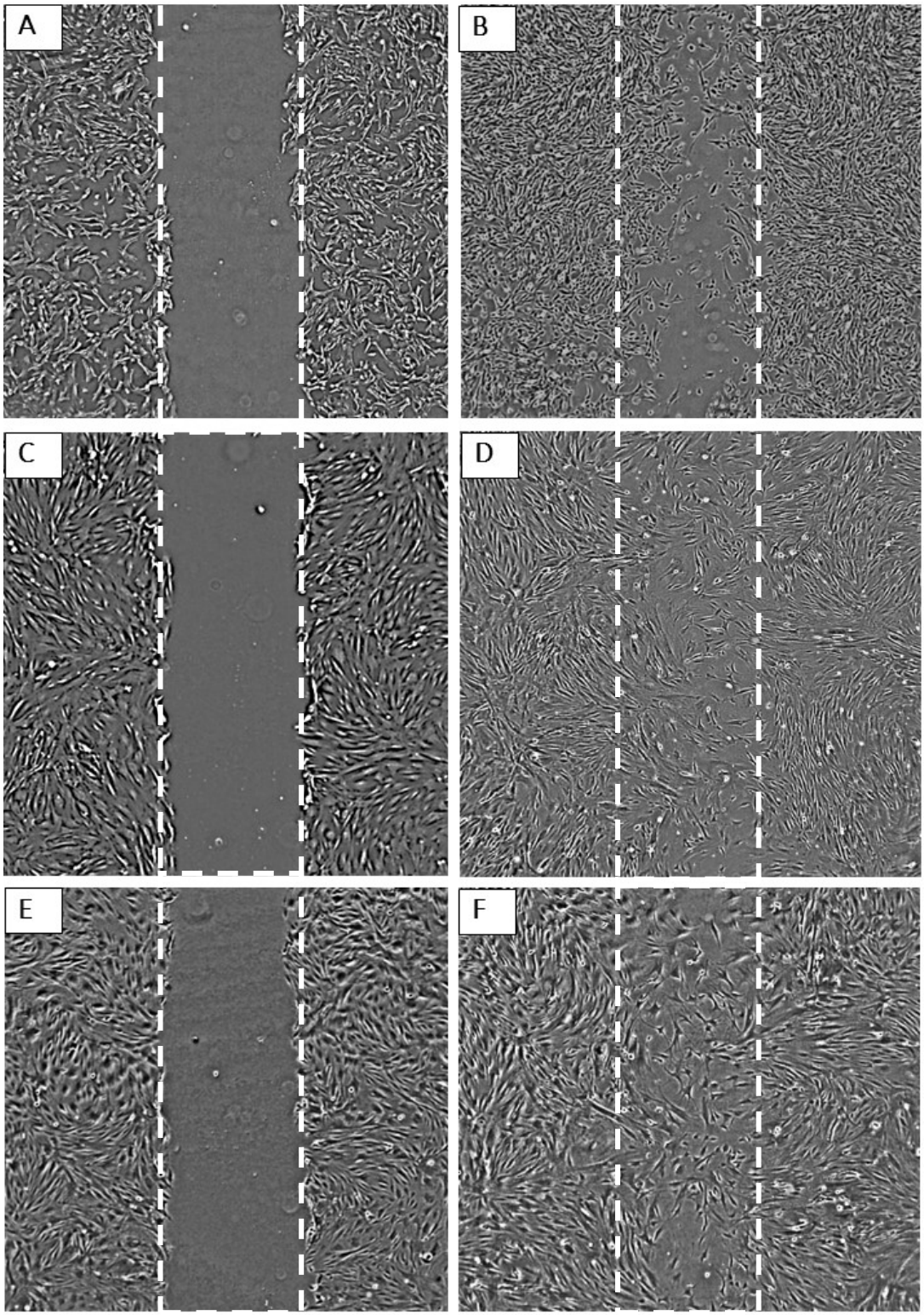


Figure 37: Wound healing assay to evaluate Ad-MSCs migration ability.

Baseline (A, C and E) and 24 hours later (B, D and D). The middle zone (between the dashed lines) indicates the wound gap. Cells from all three species are shown: ovine (A and B), rabbit (C and D) and rat (E and F).

4.1.3: Trilineage differentiation

The isolated Ad-MSCs from the 3 species (sheep, rabbit, and rat) exhibited the ability to differentiate towards osteogenic, chondrogenic and adipogenic lineages when cultured in the corresponding differentiation media (DM). The differentiation was indicated by positive staining and stain quantification for alizarin red S, Alcian blue and Oil red-O stains respectively (see **Figure 38, 39 and 40**). The results from the Kolmogorov Smirnov test of normality indicated that data were normally distributed (p=0.200) for the Alizarin red S, Alcian blue and Oil red-O staining for the ovine, rabbit and rat MSCs grown in DM. Independent T-tests confirmed that there were significant differences ($P \leq 0.05$)* between the stain quantification values from cells cultured in growth media (GM) and differentiation media (DM) for the 3 stains in the 3 species.

* For Ovine and rabbit Ad-MSCs $P<0.001$ for Alizarin red, Alcian blue and Oil red-O. While, for rat Ad-MSCs $P= 0.006$ for Alizarin red, and $P<0.001$ for Alcian blue and Oil red O.

4.1.4: Immunophenotypic characterisation (Flowcytometry):

The key cell surface markers (CD90, CD105, CD44, CD45 and CD73) were expressed differently on the Ad-MSCs isolated from the 3 species (sheep, rabbit and rat) as shown in **Table 38 and Figure 41.**

Table 38: The expression pattern of cell surface markers for Ad-MSCs isolated from sheep (ovine), rabbit and rat.

	CD90	CD105	CD44	CD45	CD73
Ovine Ad-MSCs	Positive (50.80%)	Positive (84.00%)	Positive (98.40%)	Negative	Positive (30.88%)
Rabbit Ad-MSCs	Positive (57.16%)	Negative	Positive (54.38%)	Negative	Negative
Rat Ad-MSCs	Positive (99.60%)	Negative	Positive (6.10%)	Negative	Negative

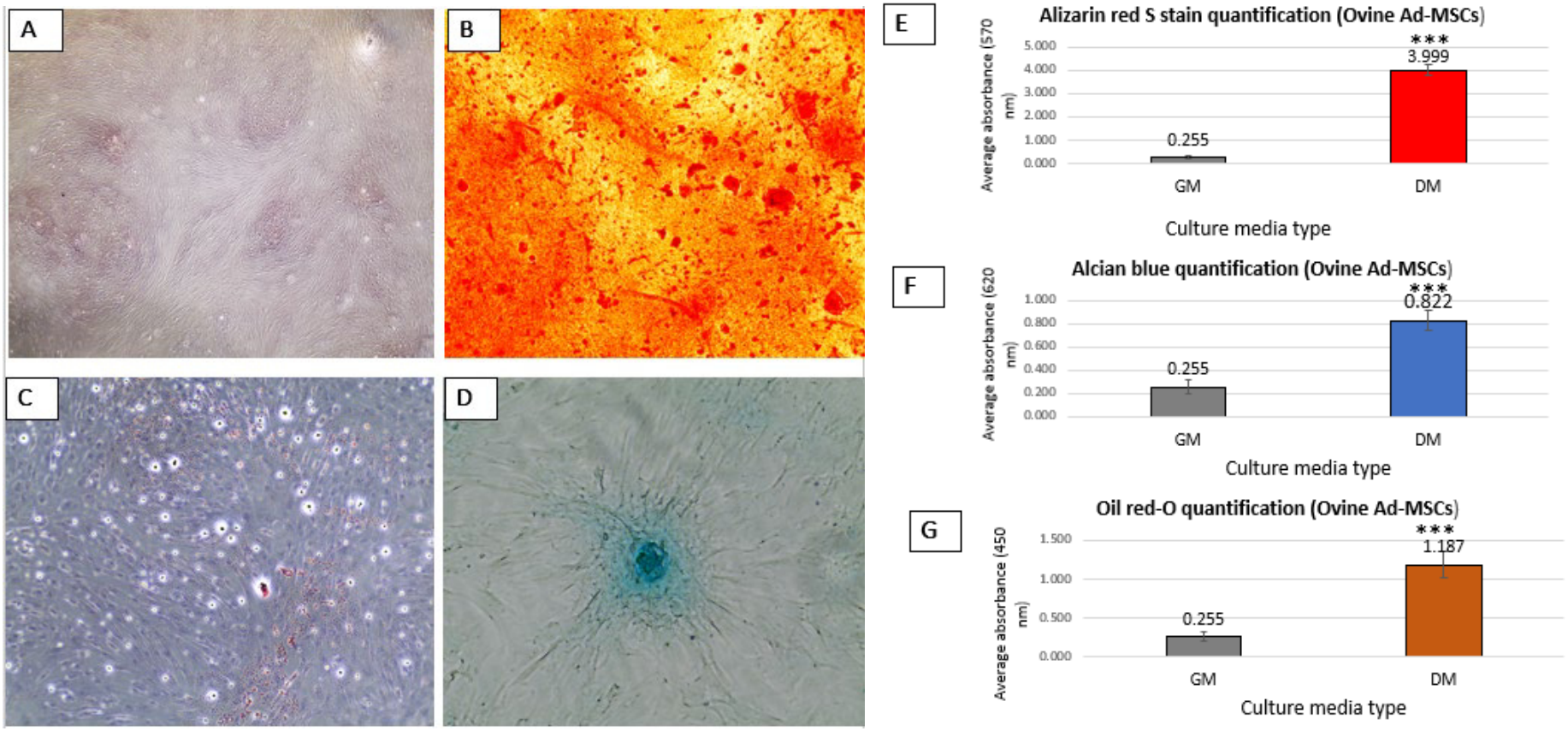


Figure 38: Trilineage differentiation of ovine Ad-MSCs as demonstrated by positive special staining and stains quantification.

A) Undifferentiated ovine Ad-MSCs (4x original magnification).

B) Positive alizarin red staining indicating successful osteogenic differentiation (4x original magnification).

C) Positive Oil red-O staining indicating successful adipogenic differentiation (10x original magnification).

D) Positive Alcian blue staining indicating successful chondrogenic differentiation (20x original magnification).

E) Alizarin red S stain quantification F) Alcian blue stain quantification G) Oil red-O quantification. GM= cell grown in growth media vs. DM= cells grown in differantiation media. Data represent mean (±SD) for 4 measurements at each culture media type. *** denotes statistically significant differences $P \leq 0.001$

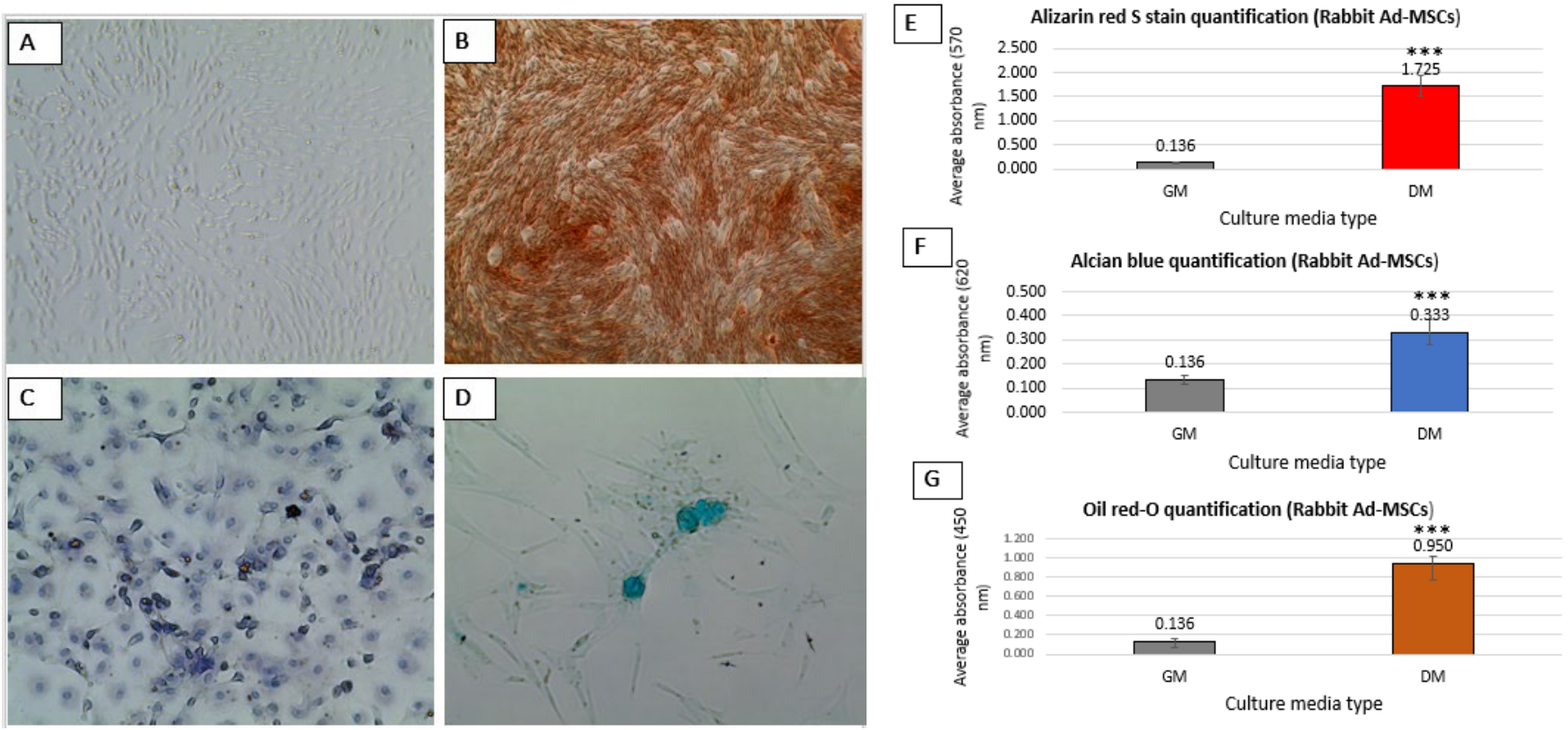


Figure 39: Trilineage differentiation of rabbit Ad-MSCs as demonstrated by positive special staining and stains quantification.

A) Undifferentiated rabbit Ad-MSCs (4x original magnification).

B) Positive alizarin red staining indicating successful osteogenic differentiation (4x original magnification).

C) Positive Oil red-O staining indicating successful adipogenic differentiation (10x original magnification).

D) Positive Alcian blue staining indicating successful chondrogenic differentiation (20x original magnification).

E) Alizarin red S stain quantification F) Alcian blue stain quantification G) Oil red-O quantification. GM= cell grown in growth media Vs. DM= cells grown in differantiation media. Data represent mean (±SD) for 4 measurements at each culture media type. *** denotes statistically significant differences $P \leq 0.001$

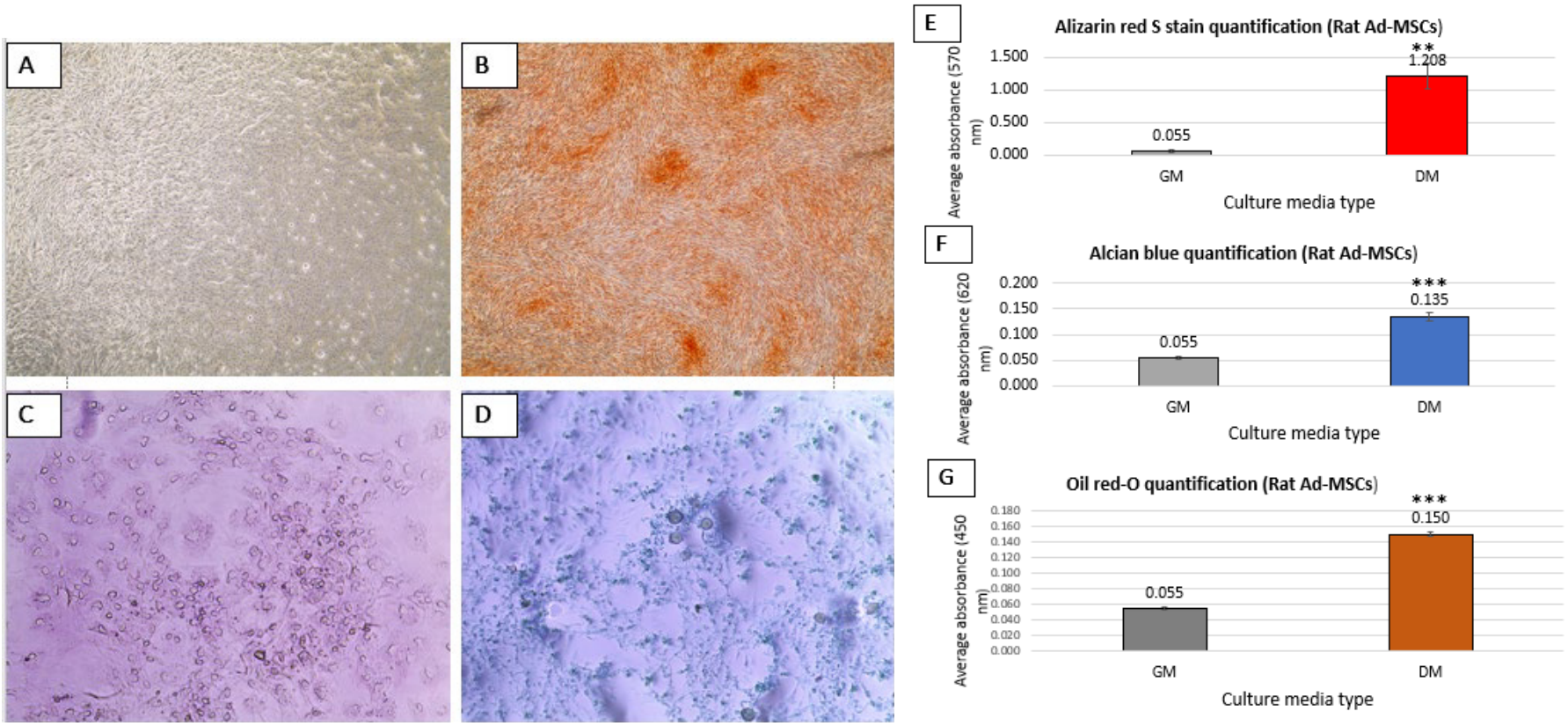


Figure 40: Trilineage differentiation of rat Ad-MSCs as demonstrated by positive special staining and stains quantification.

A) Undifferentiated rat Ad-MSCs (4x original magnification).

B)Positive alizarin red staining indicating successful osteogenic differentiation (4x original magnification).

C) Positive Oil red-O staining indicating successful adipogenic differentiation (10x original magnification).

D) Positive Alcian blue staining indicating successful chondrogenic differentiation (10x original magnification).

E) Alizarin red S stain quantification F) Alcian blue stain quantification G) Oil red-O quantification. GM= cell grown in growth media Vs. DM= cells grown in differantiation media. Data represent mean (±SD) for 4 measurements at each culture media type. *** denotes statistically significant differences $P \leq 0.001$

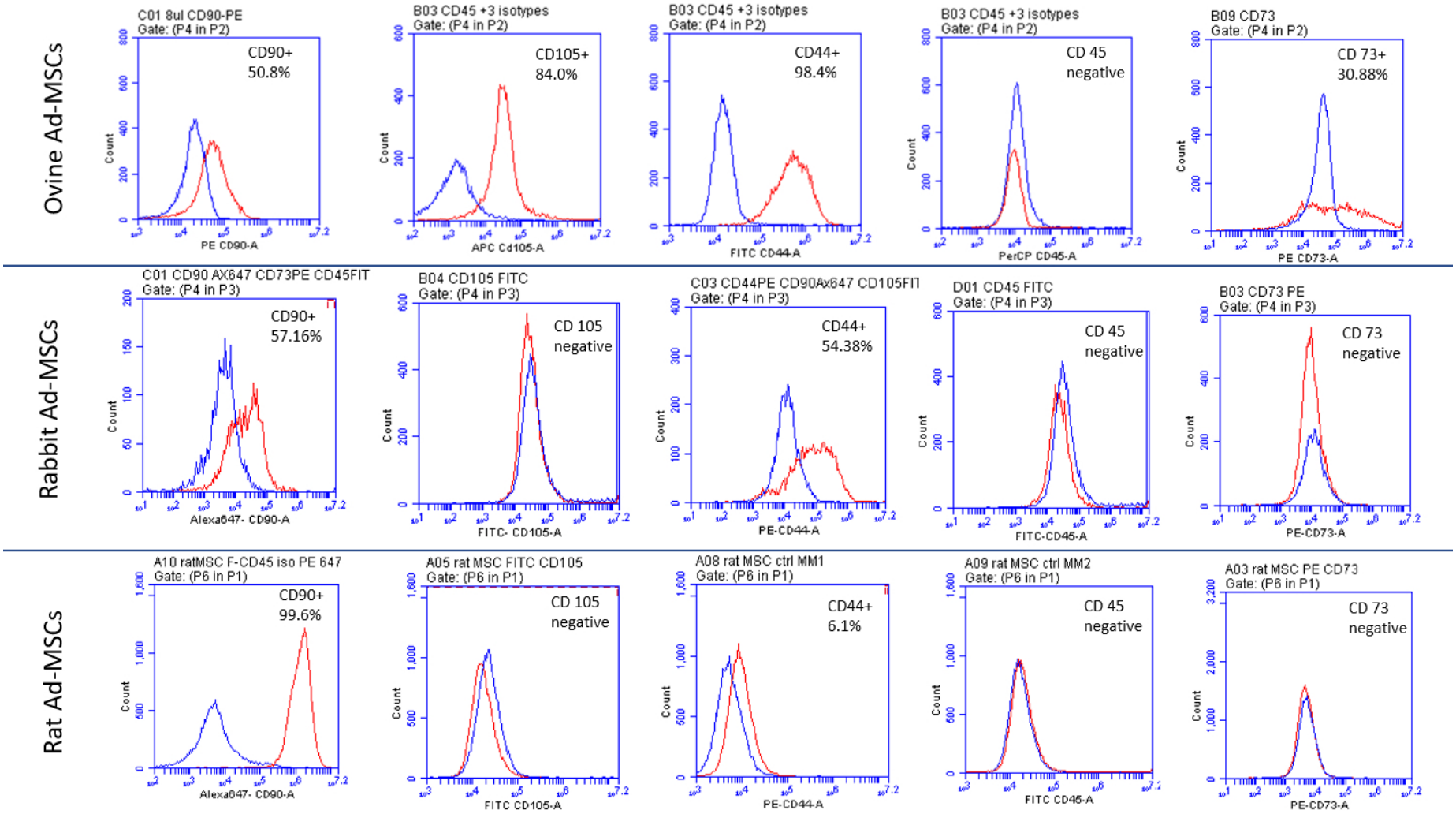


Figure 41: Immunophenotypic characteristics of ovine, rabbit and rat Ad-MSCs comparing the expression of CD90, CD105, CD44, CD45 and CD73 surface markers.

The red curve is the signal from the antibody stained MSCs and the blue curve is the corresponding isotype (negative) control.

4.1.5- Ad-MSCs differentiation towards osteogenic lineage

4.1.5.a- ALP activity

The fluctuation in the level of ALP activity at different time points during osteogenic differentiation followed a similar pattern in Ad-MSCs isolated from the 3 species. At all the time points (except at day 21), the level of ALP activity was significantly different ($p<0.001$) between cells cultured in GM versus those cultured in DM. By day 21, the ALP level had dropped, so there was no significant difference between its level under GM versus DM conditions ($P=0.89$, 0.29 and 0.10 for ovine, rabbit and rat Ad-MSCs respectively). The results from the Kolmogorov Smirnov test of normality indicated that data were normally distributed ($p=0.200$) for the ovine, rabbit and rat MSCs grown in DM at all time points. The ALP activity level (μmol p-NP/μg protein/min) of the cells grown in osteogenic DM increased gradually from day 3 to reach a peak at day 14, then sharply declined by day 21 **(Figure 42).** The increment in the ALP activity level was significant from day 3 to day 7 ($P<0.001$), as well as from day 7 to day 14 ($P= 0.01$ and 0.02 for ovine and rabbit respectively) but, it dropped by day 14 in the case of rat Ad-MSCs ($P= 0.03$). The drop in the level by day 21 was statistically significant compared to the previous time points ($P<0.001$).

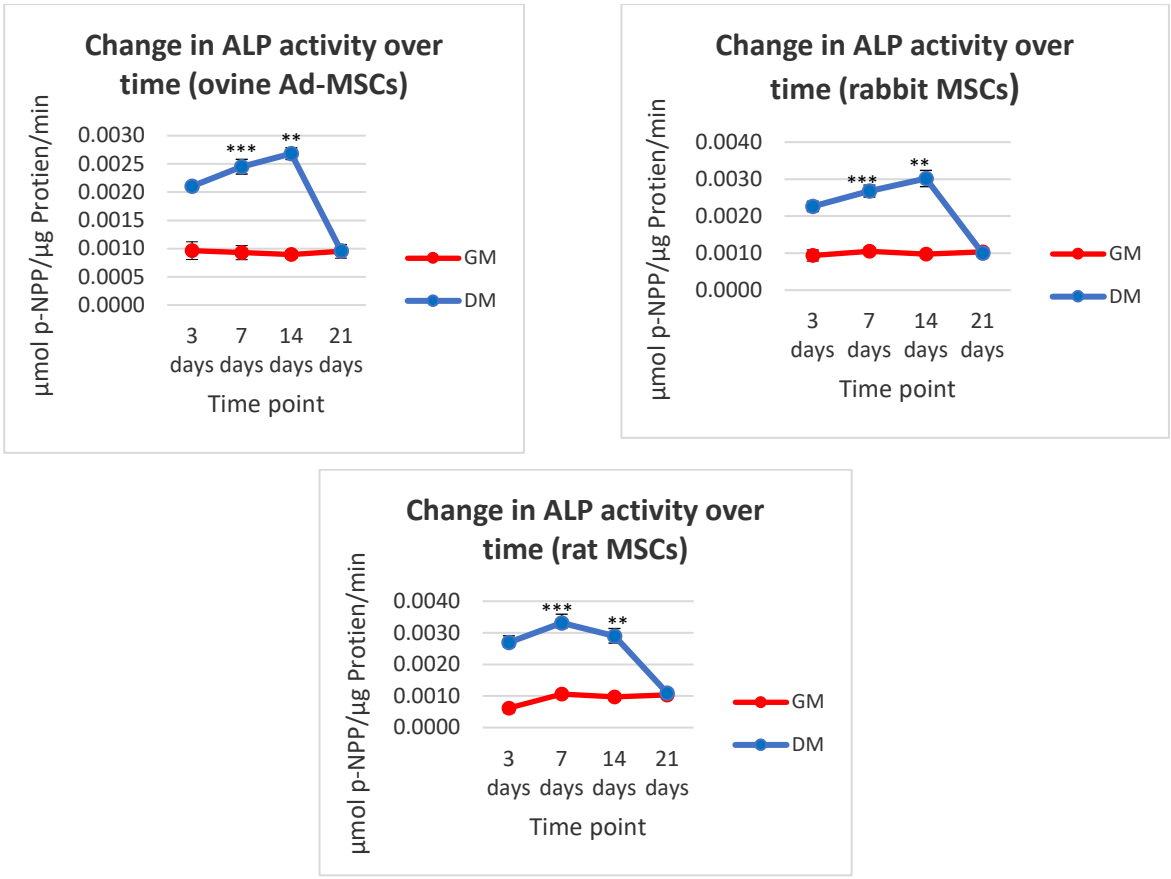


Figure 42: Changes in ALP activity at different time points for (ovine, rabbit and rat) Ad-MSCs grown at growth media (GM-red line) vs osteogenic differentiation media (DM- blue line), at day 3, 7, 14 and day 21.
Data represent mean (±SD) for 6 measurements for each media type at each time point.

** $P \leq 0.01$ *** $P \leq 0.001$ (denotes statistically significant differences).

4.1.5.b-Alizarin red S staining (ARS) and quantification

The matrix mineralisation stage of MSCs differentiating towards the osteogenic lineage was detected through Alizarin red S staining and stain quantification. In the 3 species, alizarin red quantification took an upward trend over time, reaching its peak by day 21 in osteogenic DM. There was a significant difference between the quantified ARS from cells cultured in GM and those cultured in DM at all time points ($P<0.001$). The increment in the quantified ARS level was significant at each of the timepoints ($P<0.001$), with the highest quantifiable amount of of ARS was detectable at day 21 in osteogenic DM (**Figure 43).** The results from the Kolmogorov Smirnov test of normality indicated that the data were normally distributed for the rabbit and rat MSCs grown in DM at all time points ($P=0.200$). This was also true for the ovine MSCs except at week 1 ($P=0.024$).

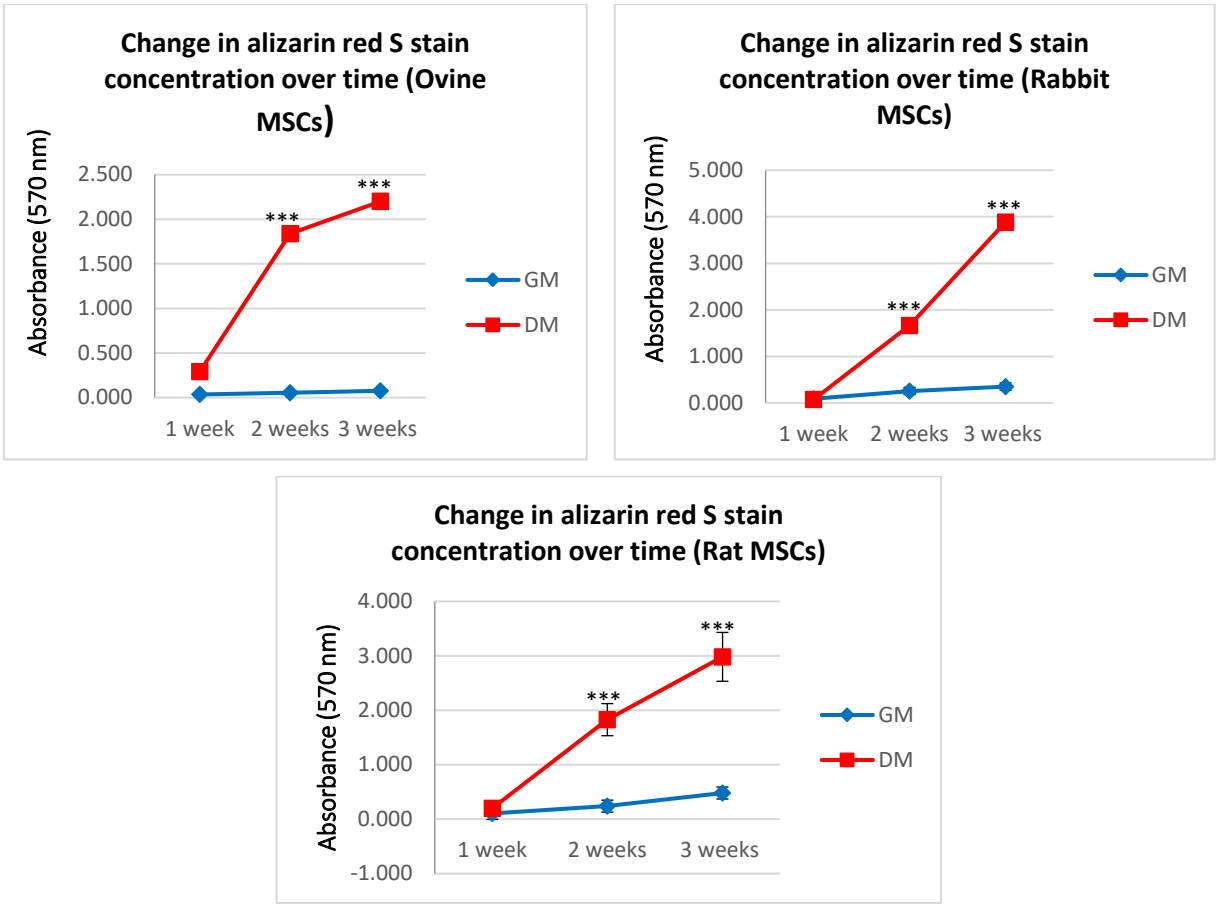


Figure 43: Changes in alizarin red stain concentration at different time points for (ovine, rabbit and rat) Ad-MSCs grown in growth media (GM) vs osteogenic differentiation media (DM), at week 1, 2 and 3.

Data represent mean (±SD) for 6 measurements for each media type at each time point.

*** denotes statistically significant differences $P \leq 0.001$

4.1.5.c- Osteogenesis markers gene panel expression level (via qPCR)

The rat and rabbit Ad-MSCs (respectively) showed stronger expression of the genes of osteogenic marker in general in comparison with ovine Ad-MSCs, as indicated by the level of fold increase (**see Table 39**). Tthe temporal pattern of gene expression **by ovine Ad-MSCs** cultured in osteogenic DM was as the following: at day 7, osteonectin (ON), osteocalcin (OC) and collagen-I (COL-I) started to show increased expression levels with, the peak expression of Runx-2, osteonectin (ON), collagen I(COL-I) and osteopontin (OPN) seen at day 14 (week 2), and that of osteocalcin (OC) at day 21 (week 3), see **Figure 44.**

For **rabbit Ad-MSCs**, COL-I and OPN had peak expression by day 7 and RUNX-2 showed a significant increase at day 14 and continued to increase to reach a peak at day 21. Similar to RUNX-2, OC reached peak expression at day 21, see **Figure 45**.

Finally, in **rat Ad-MSCs**, the RUNX-2 and ON expression peak was seen on day 7, while peak expression of COL-I and OPN was on day 14, and OC was on day 21, see **Figure 46.**

Data represent mean (±SD) for dublicate measurements at each time point.

Table 39: Fold increase in the level of osteogenic markers genes at different time points for Ad-MSCs cultured in osteogenic differentiation media.

	Ovine Ad-MSCs			**Rabbit Ad-MSCs**			**Rat Ad-MSCs**		
	Day 7	Day 14	Day 21	Day 7	Day 14	Day 21	Day 7	Day 14	Day 21
RUNX-2	1.47 ±0.35	3.99 * ±0.20	0.81 ±0.05	0.08 ±0.003	28.74 * ±0.13	32.40 * ±0.14	3174.30 * ±0.27	0.00 ±0.00	5.95 * ±0.09
ON	3.24 * ±0.13	4.03 * ±0.07	0.69 ±0.22	20.39 * ±0.20	82.58 * ±0.06	0.000 ±0.00	1935.02 * ±0.32	0.00 ±0.00	230.52 * ±0.20
OC	2.18* ±0.03	1.72 * ±0.17	11.31* ±0.07	0.00 ±0.00	0.00 ±0.00	67.76 * ±0.13	590.60 * ±0.35	0.00 ±0.00	3187.86 * ±0.52
COL-I	1.47 * ±0.14	3.99 * ±0.07	0.81 ±0.14	58.84 * ±0.14	0.00 ±0.00	0.00 ±0.00	3270.62 * ±0.75	0.00 ±0.00	0.00 ±0.00
OPN	0.00 ±0.00	3.00 * ±0.03	0.00 ±0.02	5.88 * ±0.04	0.00 ±0.00	0.920 ±0.02	1784.30 * ±0.44	0.00 ±0.00	0.00 ±0.00
(*) denotes statistically significant difference $P \leq 0.05$									

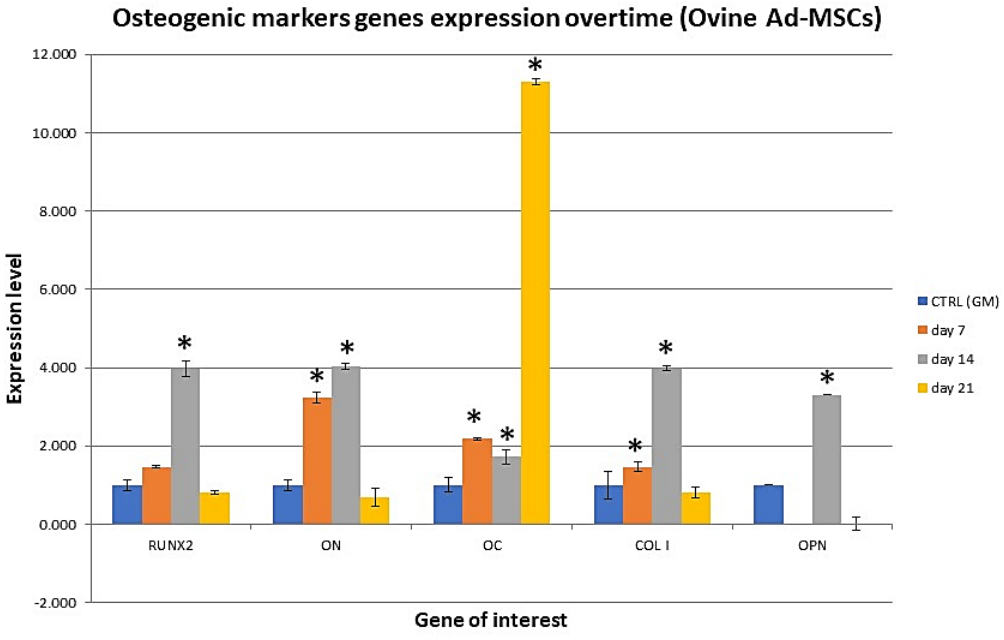


Figure 44: Expression of osteogenesis marker genes in ovine Ad-MSCs cultured for 7, 14 and 21 days in differentiation media (DM).

Asterisk (*) denotes statistically significant differences from controls $P \leq 0.05$.

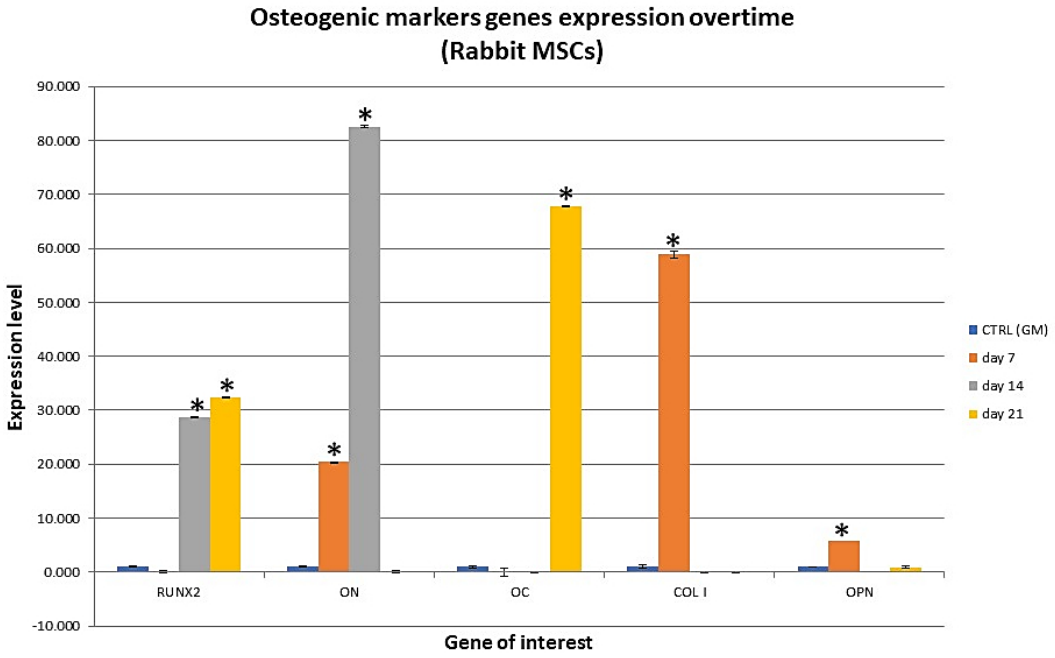


Figure 45: Expression of osteogenesis marker genes in rabbit Ad-MSCs cultured for 7, 14 and 21 days in differentiation media (DM).

Asterisk (*) denotes statistically significant differences from controls $P \leq 0.05$.

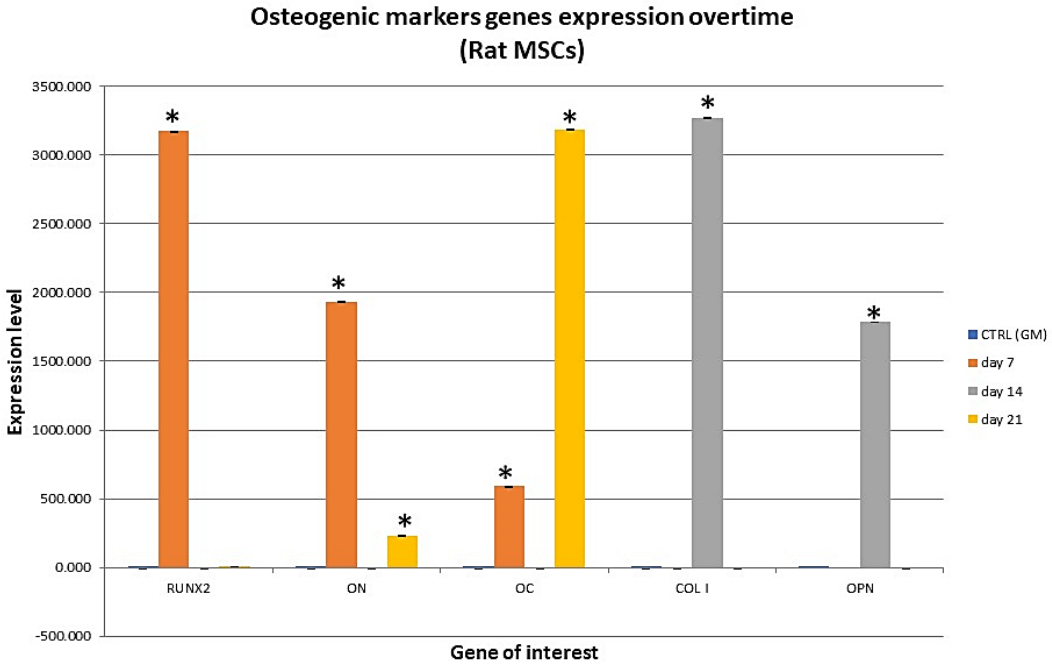


Figure 46: Expression of osteogenesis marker genes in rat Ad-MSCs cultured for 7, 14 and 21 days in differentiation media (DM).

Asterisk (*) denotes statistically significant differences from controls $P \leq 0.05$.

4.1.5.d- Scanning Electron Microscopy (SEM):

After 2 weeks incubation in osteogenic differentiation media, cells exhibited osteoblastic appearance, flattened with a rough surface and surrounded by abandoned extracellular matrix (**Figure 47).**

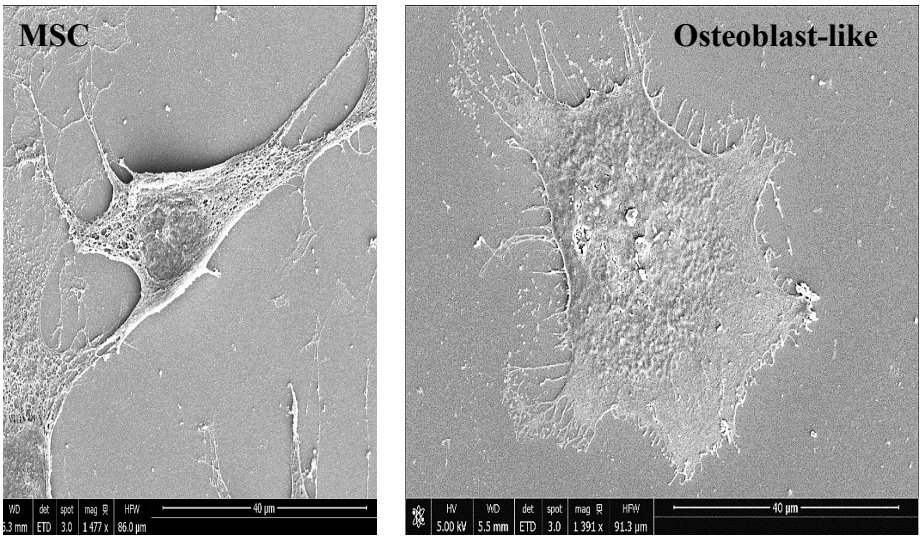


Figure 47: SEM images (x1391), highlighting the morphological difference between undifferentiated MSC Vs MSC differentiating towards osteogenic lineage (osteoblast-like cell).

4.2-The effect of extracorporeal shockwaves (ESW) on MSCs

4.2.1-The effect of focused vs radial ESW on Ad-MSCs (direct application)

4.2.1.a-Effect of Shockwave treatment on Ad-MSCs proliferation:

During the first 24 hours, the 0.05 mJ/mm^2 focused (F) group had the highest proliferation rate (86.36% of control) and the 2.4 bar radial (R) group had the lowest proliferation rate (67.73% of control). By day 3, the pattern had been reversed as the 2.4 bar radial group had the highest proliferation rate (92.42%) and the 0.05 mJ/mm^2 focused group had the lowest proliferation rate (66.99% of control). The 2.4 bar radial group kept the highest proliferation rate by day 7, even higher than the untreated control group (107.46% of control) while the lowest proliferation rate at this point was the 1.2 bar radial group (70.25% of control). At all time points, there was a significant difference between the different treatment groups ($P<0.001$ at 24 h and day 7 and $P=0.017$ at day 3; details in **Figure 48**). The results from the Kolmogorov Smirnov test of normality are summerised in Table 40 below.

4.2.1.b- Effect of Shockwave treatment on Ad-MSCs osteogenic differentiation:

All groups exhibited the ability to differentiate toward the osteogenic lineage as confirmed by positive alizarin red S staining and the significant difference between readings obtained from stain quantification from the GM control groups and osteogenic DM groups ($P<0.001$). The results from the Kolmogorov Smirnov (KS) test of normality indicated that the data were normally distributed for all groups at all time points ($P=0.200$). The one way ANOVA to compare the effect of different ESW treatments on cells grown in osteogenic DM, showed significant differences between treatment groups ($P<0.001$); where the values from the 1.8 bar R treatment group were statistically lower than the values from 0.05 mJ/mm^2 F ($P=0.019$), 0.12 mJ/mm^2 F ($P<0.001$) and the 2.4 bar R ($P= 0.001$) treatment groups. Other than that, there were no statistically significant difference between the remaining treatment groups (P value ranges from 0.09 to 1.00), see **Figure 49.**

Table 40: The results from the Kolmogorov Smirnov test of normality for ESW treated cultures.

ESWT settings	**KS test P value**		
	Day 1	**Day 3**	**Day 7**
0.5 F	0.200	0.186	0.200
0.12 F	0.200	0.009*	0.035*
0.4 F	0.123	0.200	0.095
1.2 R	0.051	0.200	0.200
1.8 R	0.043	0.200	0.200
2.4 R	0.143	0.200	0.200
P value ≥ 0.05 means the data are normally distributed, while P≤ 0.05 means the data are not normally distributed.			

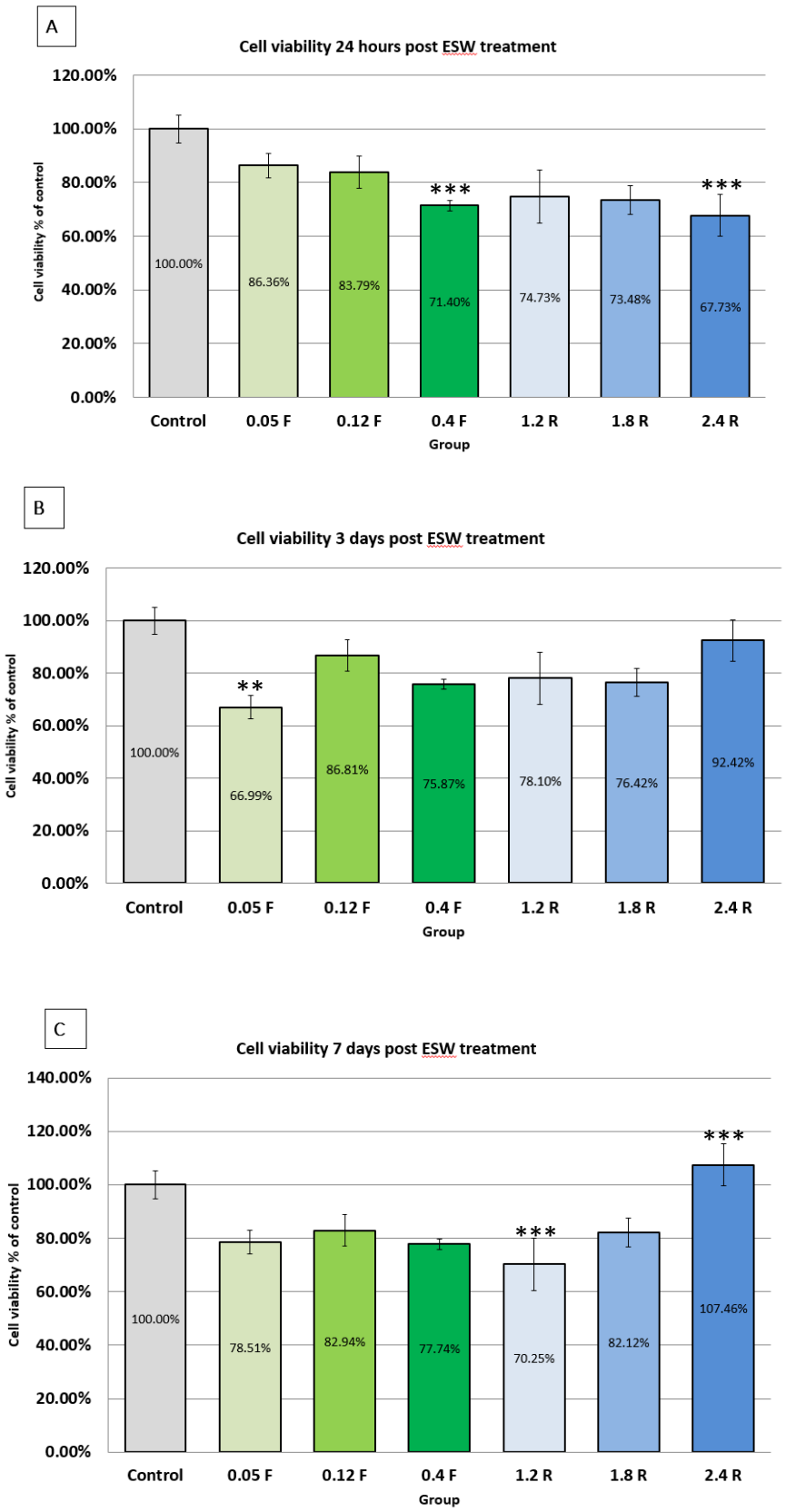


Figure 48: The effect of focused and radial shockwave treatment on ovine Ad-MSCs proliferation at day 1 (A), day 3 (B), day 7 (C) post-treatment

Data represent mean (±SD) for triplicate measurements per treatment group per time point

*** denotes statistically significant differences $P \leq 0.001$

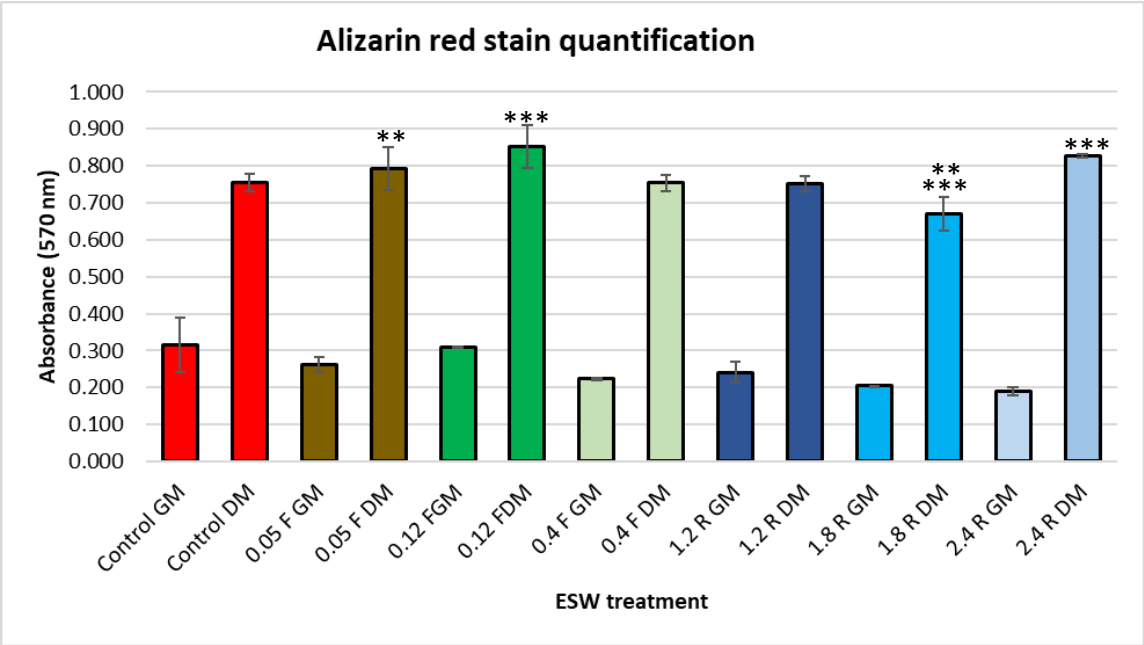


Figure 49: Quantification of Alizarin red stain in control and shock wave treated ovine Ad-MSCs.

Data represent mean (±SD) for triplicate measurements per treatment group per time point

** P ≤ 0.01 *** P ≤ 0.001 denotes statistically significant differences

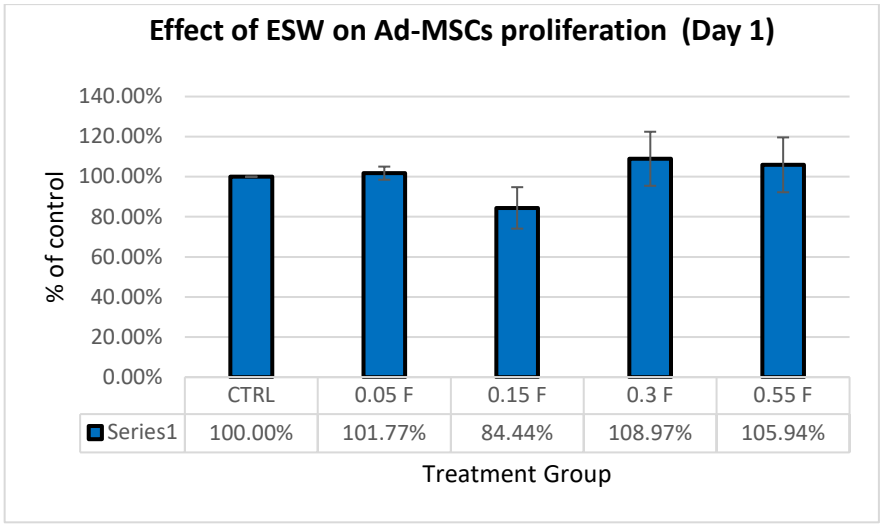
4.2.2- The effect of focused ESW on Ad-MSCs (designed water bath *in vitro* testing apparatus):

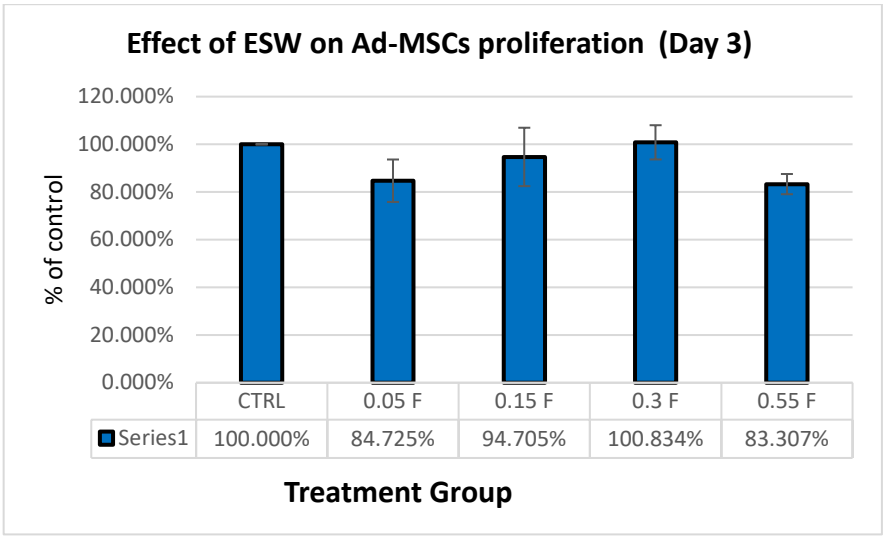
4.2.2.a-Cell Proliferation (MTT assay):

The results from the Kolmogorov Smirnov test of normality indicated that the data were normally distributed for all groups at all time points (P=0.200).

On day 1, the proliferation rate of the cells treated with 0.15 mJ/mm^2 focused (F) ESW was significantly lower than those treated with 0.05 F (P=0.023), 0.3 F (P<0.001) and 0.55 F (P=0.003) mJ/mm^2 ESW frequencies. However, there was no significant difference between the untreated control and all the treatment groups (P≥0.05)*. At day 3, the 0.05 F mJ/mm^2 and the 0.55 F mJ/mm^2 groups had significantly lower proliferation rates than the control and the 0.3 F mJ/mm^2 groups (P=0.004 and 0.002 respectively). By day 7 in cell culture, there was no significant difference between groups (P=1.00), see **Figure 50.**

* P= 1.00, 0.056, 0.97 and 1.00 when comparing the untreated control to 0.05, 0.15, 0.3 and 0.55 mJ/mm^2 Focused ESWT respectively.





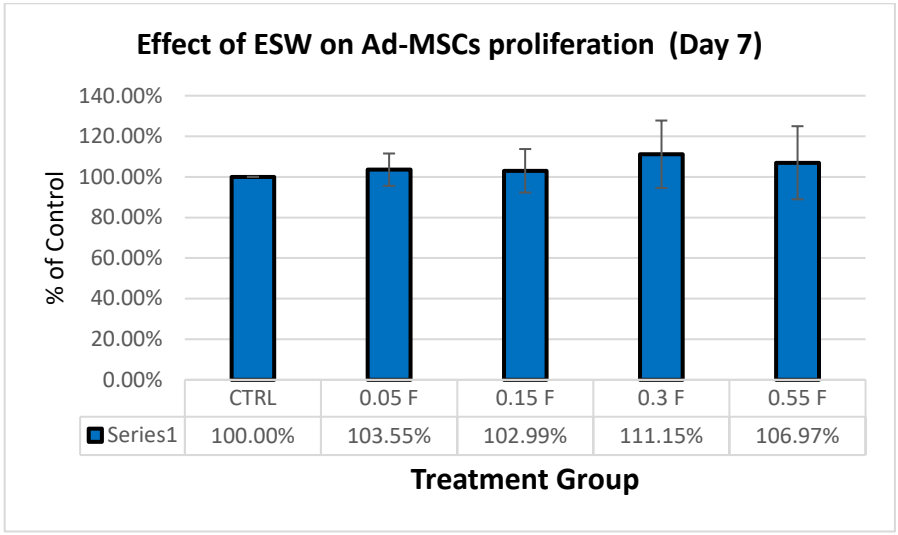


Figure 50: Effect of ESW treatment using in vitro water bath treatment setting on ovine Ad-MSCs proliferation.

Data represent mean (±SD) for 4 measurements per treatment group per time point

4.2.2.b-Osteogenic differentiation:

The cells in all treatment groups were able to demonstrate osteogenic differentiation ability through positive alizarin red staining. The results from the Kolmogorov Smirnov test of normality indicated that the data were normally distributed for all groups at all time points (for the 0.05 F group P= 0.093, for the 0.15 F group P=0.085, for the 0.3 and 0.55 F groups P=0.200).

Ad-MSCs treated with 0.55 mJ/mm2 F ESW had significantly higher quantified alizarin red staining in comparison to all the other treatment groups (P=0.05 in comparison to control, P<0.001in comparison to 0.05 F and 0.15 F and P=0.005 in comparison to 0.3 F group), while the alizarin red stain quantification values of the 0.15 F mJ/mm2 group were significantly lower than the control (P<0.001), 0.3 mJ/mm2 F (P=0.006) and the 0.55 mJ/mm2 F (P<0.001) groups, see **Figure 51**.

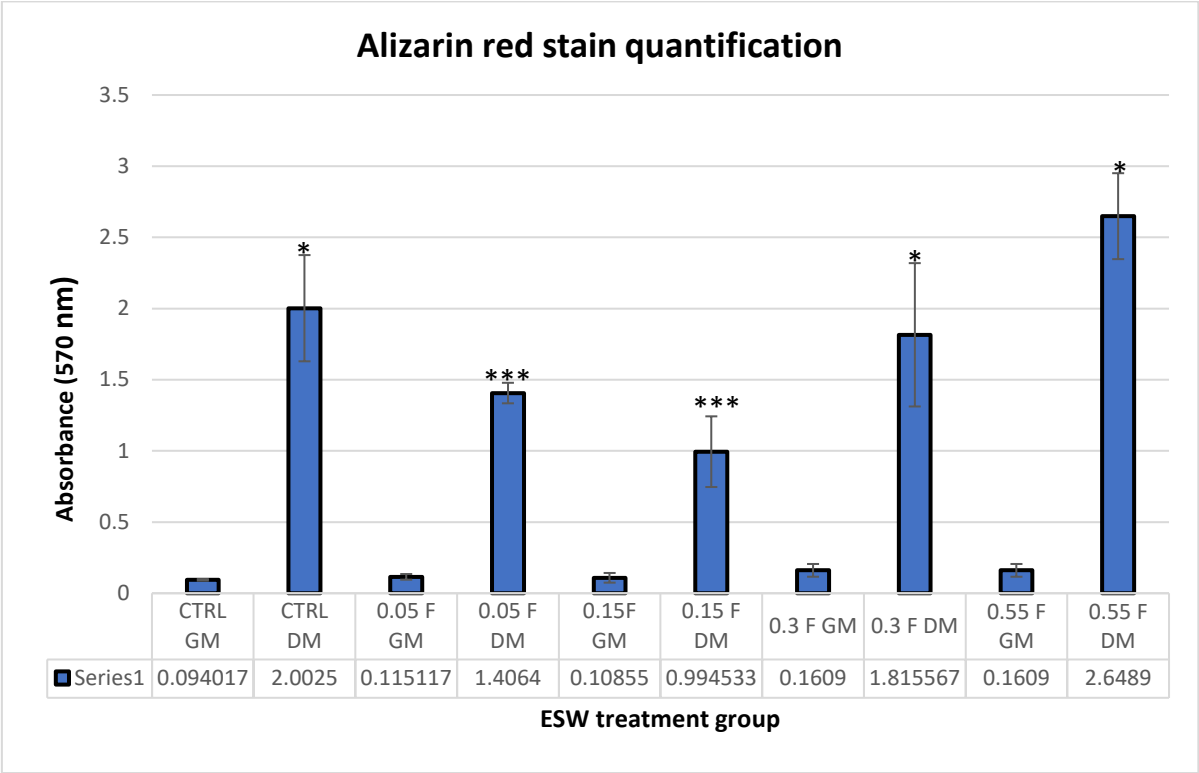


Figure 51: Effect of ESW treatment using *in vitro* water bath treatment setting on ovine Ad-MSCs osteogenic differentiation as indicated by alizarin red stain quantification.

Data represent mean (±SD) for 4 measurements per treatment group per time point.

* P ≤ 0.05 *** P ≤ 0.001 denotes statistically significant differences

4.3- Bone graft substitute biomaterials (scaffolds) fabrication and *in vitro* characterisation:

4.3.1-Confirmation of donor cells elimination in decellularised bone cores:

4.3.1.a- DNA quantification of the DCBM:

The results from the DNA quantification (Picogreen assay) showed a 97.40 % reduction in DNA content in comparison to the unprocessed bovine bones with final DNA concentration of 49.16 ng/ml for the DCBM vs 1891.41 ng/ml for the unprocessed bovine bones (**see Figure 52**).

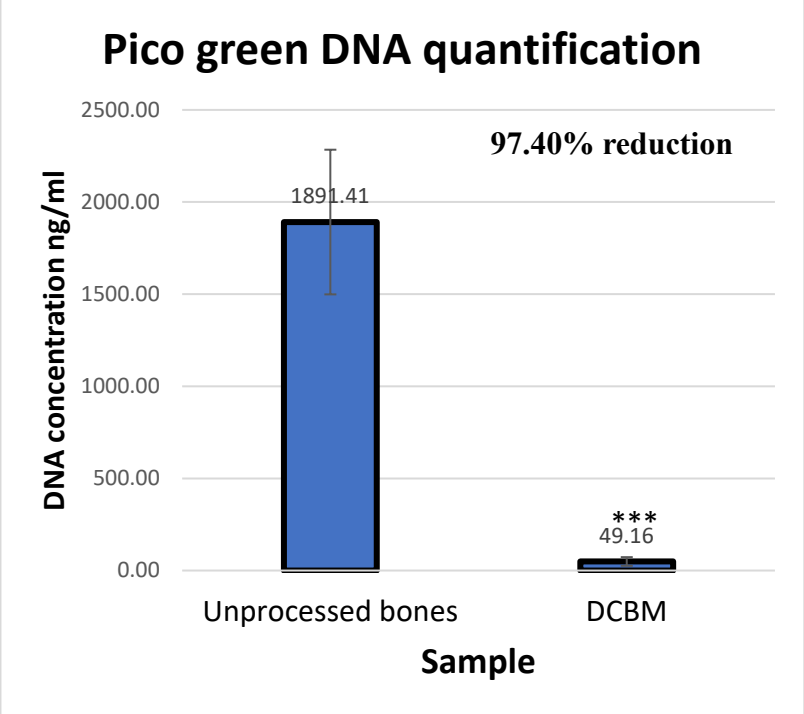


Figure 52: DNA quantification of unprocessed bone vs DCBM using a Pico green assay.

Data represent mean (±SD) for 7 measurements sample type.

*** $P \leq 0.001$ denotes statistically significant differences.

Starting with 20 mg sample weight during the DNA extraction step (as per the manufacturer instructions using DNeasy Blood & Tissue Kit (see methodology section 3.3.2.1.a), that means that the DNA concentration = 49.16 ng/ 20 mg DCBM (hence, **2.46 ng/mg DCBM**) and 1891.41 ng/20 mg unprocessed bone (hence, **99.07 ng/ mg unprocessed bone**).

4.3.1.b- Histological confirmation:

Histological examination of H&E and DAPI stained sections from the unprocessed bone cores and the bone cores that underwent decellularisation (DCBM) confirmed bone marrow clearing and effective elimination of viable osteocytes (see **Figure 53**).

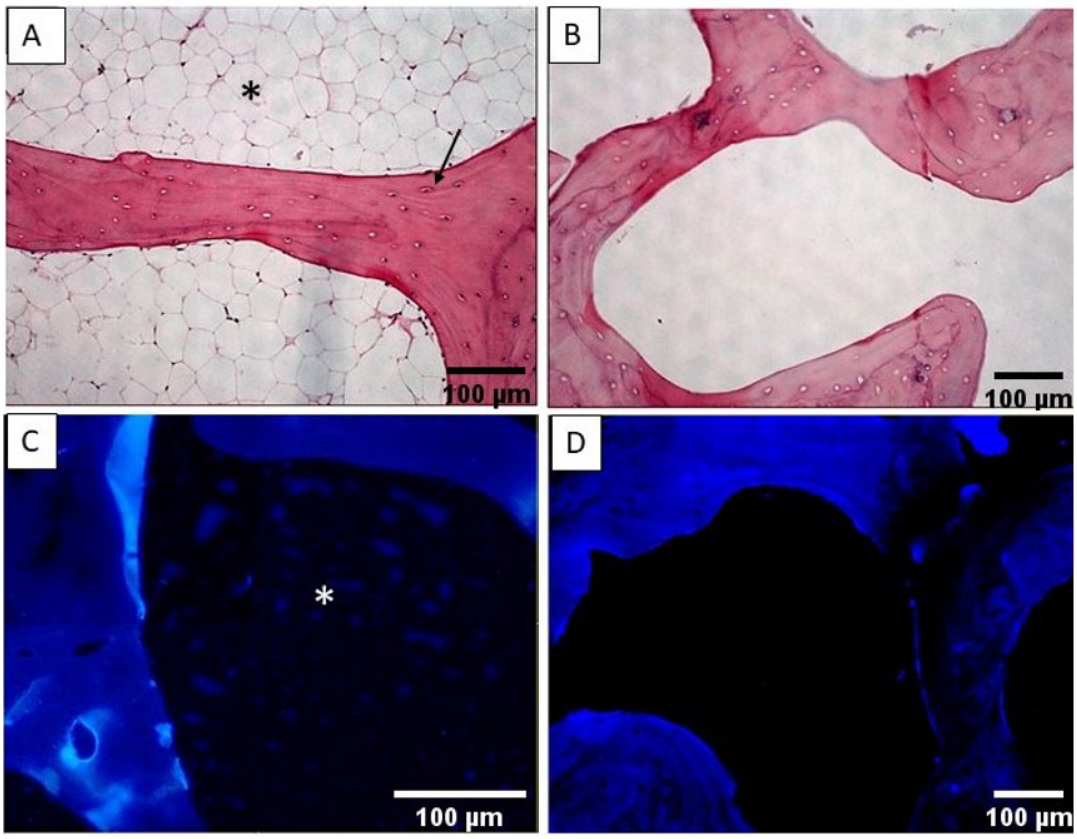


Figure 53: H&E (A,B) and DAPI staining (C,D) of unprocessed bone (A and C) vs Decellularised bone matrix DCBM (B and D) confirming absence of bone marrow (*) and cellular elements (osteocytes-black arrow) following decellularisation.

4.3.2- Mineralisation status in decellularised bone cores:

Calcium content in the DCBM was 17.70 ± 0.05 µg/ml (equivalent to 17.70 µg calcium/50 mg DCBM or 354.048 µg calcium/g DCBM), while the calcium content in unprocessed bone was 36.21 µg/ml ± 0.14 (equivalent to 36.21 µg calcium/50 mg bone or 724.20 µg calcium/g bone), hence **51.11 % reduction in calcium content after decellularisation.**

Phosphate content was 160.92 nmol/ml (equivalent to 160.92 nmol/30 mg DCBM or **5.36 nmol phosphate/ g DCBM**), while the phosphate content in unprocessed bone was 192.07 ± 0.04 nmol/ml (equivalent to 192.07 nmol/30 mg bone or 6.40 nmol phosphate/g bone), hence **16.21 % reduction in phosphate content after decellularisation**.

4.3.3-Cytocompatibility in 3D printing scaffolds:

The results from the Kolmogorov Smirnov test of normality indicate that the data were normally distributed for the three material groups at all time points (P=0.200). The data analysis of the MTT assay results showed no significant negative effect (P=0.056) on Ad-MSCs cell viability across scaffold groups; expressed as percentage of PCL control at 3 time-points (day 3, 5 and 7). At day 5, the DCBM group had a significantly higher proliferation rate in comparison with TCP group (P<0.001), **see Figure 54**.

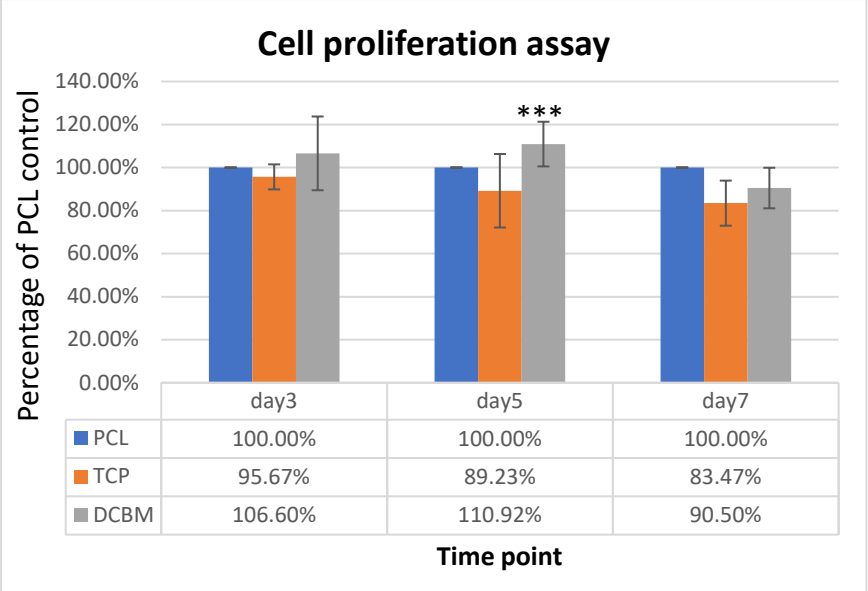


Figure 54: Cytocompatibility of cell seeded scaffolds.

Cell proliferation assay (MTT) results expressed as percentage of control at day 3, 5 and 7 post seeding with rabbit's Ad-MSCs.

Data represent mean (±SD) for 5 measurements for each material group per time point.

*** $P \leq 0.001$ denotes statistically significant differences

4.3.4 – Osteoinductivity in 3D printing scaffolds:

4.3.4.a- qRT-PCR analysis for quantification of the level of expression of osteogenesis markers:

The qRT-PCR data showed that RUNX-2, osteopontin (OPN), Collagen I (COL I) and to a lesser extent alkaline phosphatase (ALP) genes were up-regulated in Ad-MSCs seeded on DCBM scaffolds, while only RUNX-2 and COLI were upregulated in Ad-MSCs seeded on TCP scaffolds, in comparison with those seeded on the PCL scaffold (**see Figure 55**).

4.3.4.b- Alizarin Red staining:

Positive Alizarin-Red staining was achieved in both DCBM and TCP based-scaffolds. Alizarin red stain quantification from TCP and DCBM scaffolds was significantly higher than the PCL scaffolds ($P<0.001$), while there was no significant difference between the DCBM and TCP scaffolds ($P=0.76$), see **Figure 56.**

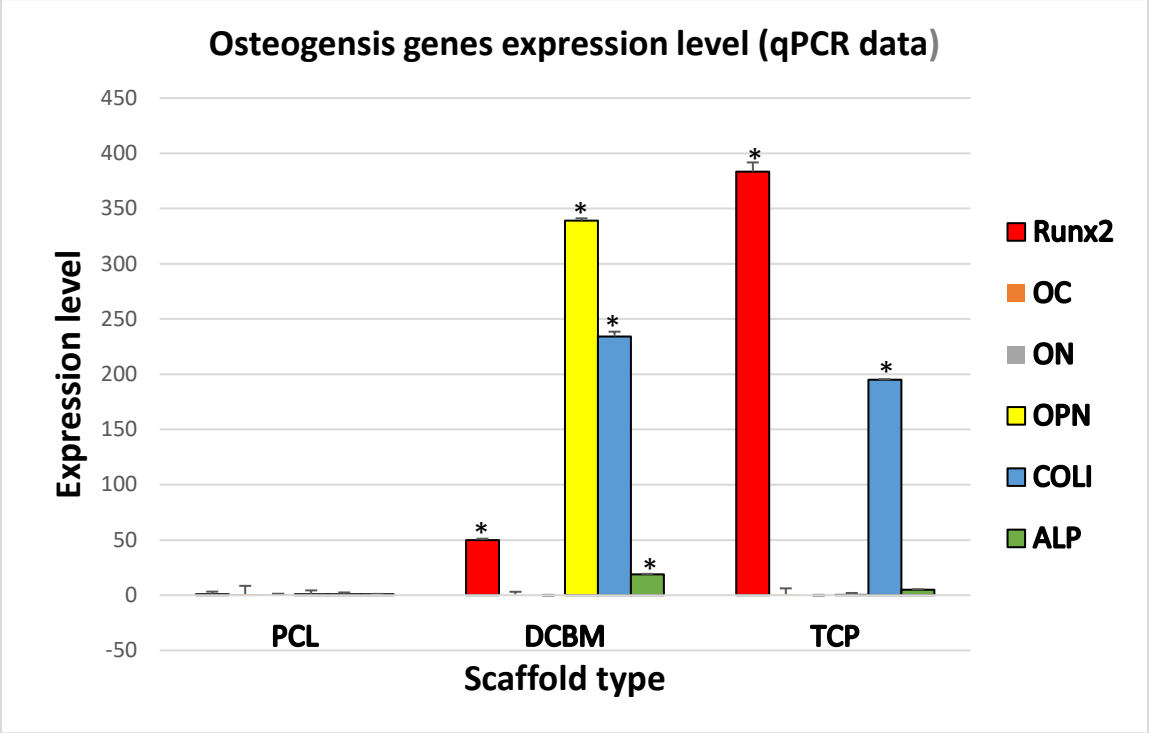


Figure 55: Effects of scaffold material composition on the expression of osteogenic marker genes.

Data represent mean (±SD) for 5 measurements for each material group.
* P ≤ 0.05 denotes statistically significant differences

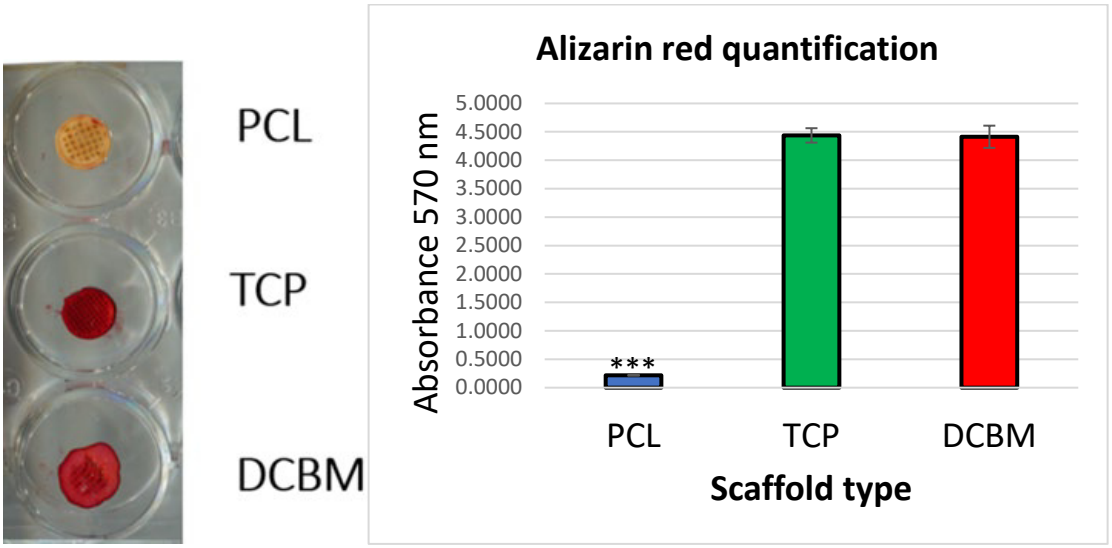


Figure 56: Alizarin red staining and quantification of the 3 scaffolds groups.

Data represent mean (±SD) for 5 measurements for each material group.

*** P ≤ 0.001 denotes statistically significant differences

4.3.5- Microstructure:

4.3.5.a-SEM:

Both the DCBM and TCP demonstrated surface roughness, equally spaced uniform macro-pores resulting from the printed lattice design (average 250 x 230 µm) as well as smaller micro pores upon higher magnification (size ranges from 2 to 20 µm). However, the PCL scaffold lacked these features, it had a much wider macro-pores (average# 720 x740 µm), no micropores and a smoother surface, see **Figure 57.**

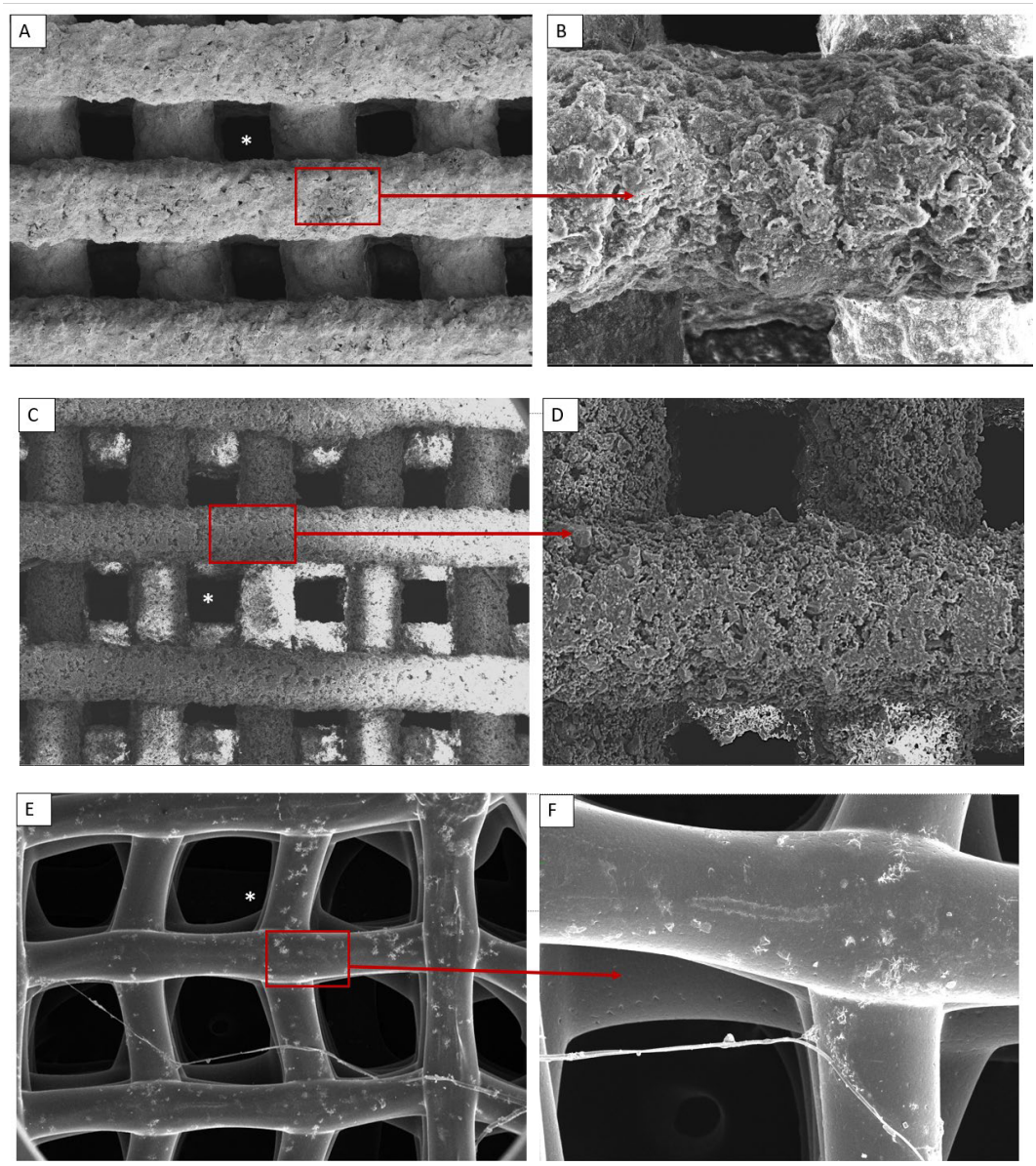


Figure 57: SEM images of the 3 scaffolds groups.

DCBM (A and B) and TCP (C and D) demonstrate surface roughness, and microporosity (*), while PCL lacks these features. A, C and E are at x 50 magnification while B, D and F are at x 150 magnification for the DCBM, TCP and PCL respectively.

4.3.5.b- Micro-Computed Tomography (µ-CT):

The data from µ-CT analysis are summarised in **Table 41** below. In spite of printing all the scaffolds from the same original CAD design and using the same G-code, the final 3D printed products demonstrated intragroup and intergroups microstructural variabilities. The results from the Kolmogorov Smirnov test of normality indicated that the data were normally distributed for all parameters in the 3 material groups (P=0.200), except for the trabecular thickness in the DCM group (P=0.031) and the trabecular separation in the TCP group (P=0.024). Upon running a one-way ANOVA, the differences between the porosity % and trabecular thickness in the 3 material groups were not statistically significantly different (P=0.09 and 0.40 respectively) while the PCL group had the largest pore diameter (trabecular separation) with statistically significant measurements (P =0.003) in comparison with both the DCBM and TCP scaffolds. In all the measured parameters there was no significant difference between the DCBM and the TCP scaffolds (P=0.128, 1.00 and 1.00 for porosity %, trabecular thickness and pore diameter respectively).

Data represent mean (±SD) for triplicate measurements for each material group.

Table 41: Scaffolds microstructure morphometric parameters as indicated by micro-CT analysis.

Scaffold type / **Parameters**	**DCBM**	**TCP**	**PCL**
Total volume (TV) µm^3	5.270 x10^8 ±3.58 x10^8	4.941 x10^8 ±1.15 x10^8	4.409 x10^8 ± 6.35 x10^7
Material volume (MV) µm^3	2.994 x10^8 ± 1.74 x10^8	3.357 x10^8 ±4.28 x10^7	2.554 x10^8 ± 4.64 x10^7
Percent of material volume (MV/TV)%	56.799 % ± 6.077	67.949 % ± 8.995	57.939 % ±5.411
Porosity %	43.201 % ± 6.077	32.051 % ± 8.995	42.061% ± 5.411
Trabecular thickness µm	509.538±70.752	448.914 ±39.021	455.063± 76.535
Trabecular separation (pore diameter) µm	184.378± 47.114	199.519 ± 12.946	368.503 ±4.237**
** P ≤ 0.01 denotes statistically significant differences			

4.3.6- Biomechanical properties:

The biomechanical data demonstrated that 3D printed DCBM scaffolds were able to support loads of up to 80.89 N, having a stiffness of 78.14 N/mm and a Young's modulus of 15.54 MPa. The data from TCP was within the same range (139.25, 639.22 and 127.16

respectively) with no statistical significance between the values from 2 material groups (P=0.45, 0.74 and 0.84 for peak load, stiffness, and Young's modulus respectively). However, the plain PCL scaffolds had significantly higher values for all 3 parameters in comparison to DCBM and TCP based scaffolds (P<0.001), see **Table 42** for detailed results.

Data represent mean (±SD) for 5 measurements for each material group.

The results from the Kolmogorov Smirnov (KS) test of normality indicated that the data were normally distributed for all parameters in the 3 material groups (P value as indicated in **Table 42**).

Table 42: Comparison of the mechanical and material properties of the tested scaffolds.

	DCBM based scaffolds	**TCP based scaffolds**	**Plain PCL scaffolds**
Average Peak load (N)	80.89 ±15.45 KS test P value=0.200	139.36 ± 40.14 KS test P value=0.200	1389.25 ±93.60 *** KS test P value=0.098
Average stiffness (N/mm)	78.14± 11.59 KS test P value=0.200	70.96 ± 14.05 KS test P value=0.176	639.22 ±31.45 *** KS test P value=0.176
Average Young's modulus (Mpa)	15.54±2.30 KS test P value=0.200	14.11 ± 2.79 KS test P value=0.176	127.16 ± 6.25 *** KS test P value=0.200
*** P ≤ 0.001 denotes statistically significant differences. KS test P value ≥ 0.05 means the data are normally distributed, while P≤ 0.05 means the data are not normally distributed.			

4.4- Testing the local biological effect of the selected biomaterials (scaffolds) after implantation (biocompatibility testing): a rat subcutaneous implantation preclinical model:

4.4.1-General health

All rats remained healthy for the duration of the experiment. Slight swelling around the implant site was observed during the early post-operative period, which subsided after one week. Wound dehiscence occurred in one rat 24 hour postoperatively, but upon inspection there were no signs of infection, and the implants were still in place, hence a decision was made to re-suture the wound and keep the rat on the study.

4.4.2-Gross pathology

At necropsy examination, neovascularisation was evident in the peri-implant area of the DCBM and TCP groups, which was absent in the PCL and polyethylene (PE) control groups (**Figure 58**). In 3 rats upon dissection at 8 weeks post-implantation, the implants had moved

from the original implantation site in the subcutaneous space, yet no other observable changes were noticed/reported.

4.4.3-Histopathology

The results from the histopathological scoring to evaluate the local biological effect after implantation as well as material biodegradation for DCBM based scaffolds are summarised in **Table 43,** for TCP are summarised in **Table 44** and for PCL in **Table 45.** The collective scores and conclusion for the 3 material groups are summarised in **Table 46.** Representative microscopic images are shown in **Figures 59, 60, 61 and 62.**

The results from the Kolmogorov Smirnov (KS) test of normality indicate that the data are normally distributed for all parameters in the 3 material groups (P=0.200).

All the 3 materials (DCBM, TCP and PCL) induced slight bio-irritation and exhibited slight signs of biodegradation at 4 weeks and 8 weeks after implantation**.** It worth mentioning that DCBM local biological effect score at 4 weeks' time point is the highest among the 3 materials group (8.55 DCBM vs 6.45 and 4.78 for TCP and PCL respectively), however upon running one way ANOVA there was no significant difference between the groups (P=0.136). By week 8 time point the scores were within the same range (5.09, 5.00 and 5.83 for DCBM, TCP and PCL respectively) with no significant difference between the groups (P=0.640).

Macrophages, giant cells and lymphocytes infiltration, fibrosis, and neovascularisation (Score ranges 1-3 – refer to Table 28 in the methods chapter titled- local biological effect after implantation scoring system for details) were the prominent recorded histological features in the 3 tested materials groups. The DCBM and TCP implants showed more signs of biodegradation (particularly surface erosion and fragmentation) than PCL. However, bearing in mind that DCBM and TCP scaffolds underwent decalcification during histology processing that most likely the reason behind fragmentation is processing related rather than biodegradation.

Table 43: Local biological effect after implantation and biodegradation for DCBM Scaffolds.

Local biological effect after implantation score	4 week time point						8 week time point							
	DCBM 1		DCBM 2		DCBM 3		DCBM 4		DCBM 5		DCBM 6		DCBM 7	
	Test	Control	Test	Control	Test	Control	Test	Control	Test	Control	Test	Control	Test	Control
Average inflammatory cell infiltration score	9.33	3.00	7.67	3.00	11.00	4.00	8.00	4.00	8.00	3.00	6.33	4.00	7.00	2.00
Average fibrosis, neovascularisation, calcification and fatty infiltration score	5.00	2.00	4.67	2.00	5.00	3.00	5.67	4.00	5.67	5.00	5.00	4.00	5.67	5.00
Total score for local biological effect after implantation	14.33	5.00	12.33	5.00	16.00	7.00	13.67	8.00	13.67	8.00	11.33	8.00	12.67	7.00
Test (-) control	9.33		7.33		9.00		5.67		5.67		3.33		5.67	
Average group score	**8.55**						**5.09**							
Conclusion	**Slight**						**Slight**							
Average Biodegradation score	**6.00**	**1.00**	**6.00**	**1.00**	**7.00**	**0.00**	**5.00**	**0.00**	**7.00**	**1.00**	**8.00**	**2.00**	**7.00**	**0.00**
Test (-) control	**5.00**		**5.00**		**7.00**		**5.00**		**6.00**		**6.00**		**7.00**	
Average group score	**5.67**						**6.00**							
Conclusion	**slight**						**slight**							

Conclusion: Under the conditions of this study, the test sample was considered a

– non-irritant (0,0 up to 2,9) – slight irritant (3,0 up to 8,9) – moderate irritant (9,0 up to 15,0) – severe irritant (> 15) to the tissue as compared to the negative control sample.

Table 44: Local biological effect after implantation and biodegradation for TCP scaffolds:.

Local biological effect after implantation score	4 week time point						8 week time point							
	TCP 1		TCP 2		TCP 3		TCP 4		TCP 5		TCP 6		TCP 7	
	Test	Control	Test	Control	Test	Control	Test	Control	Test	Control	Test	Control	Test	Control
Average inflammatory cell infiltration score	6.33	2.00	7.00	2.00	5.33	2.00	8.00	2.00	7.00	5.00	7.33	3.00	8.00	6.00
Average fibrosis, neovascularisation, calcification and fatty infiltration score	3.67	3.00	5.67	2.00	4.67	2.00	5.00	4.00	4.33	3.00	4.33	3.00	4.00	2.00
Total score for local biological effect after implantation	10.00	5.00	12.67	4.00	9.67	4.00	13.00	6.00	11.33	8.00	11.67	6.00	12.00	8.00
Test (-) control	5.00		8.67		5.67		7.00		3.33		5.67		4.00	
Average group score	6.45						5.00							
Conclusion	Slight						Slight							
Average Biodegradation score	6.00		8.00		7.00		9.00		7.00		6.00		7.00	
Test- control	6.00				6.00				5.00				7.00	
Average group score	5.67						5.25							
Conclusion	Slight						Slight							

Conclusion: Under the conditions of this study, the test sample was considered a

– non-irritant (0,0 up to 2,9) – slight irritant (3,0 up to 8,9) – moderate irritant (9,0 up to 15,0) – severe irritant (> 15) to the tissue as compared to the negative control sample.

Table 45: Local biological effect after implantation and biodegradation for PCL Scaffolds.

Local biological effect after implantation score	4 week time point						8 week time point							
	PCL 1		PCL 2		PCL 3		PCL 4		PCL 5		PCL 6		PCL 7	
	Test	Control	Test	Control	Test	Control	Test	Control	Test	Control	Test	Control	Test	Control
Average inflammatory cell infiltration score	5.33	3.00	6.00	3.00	7.67	3.00	6.00	2.00	5.33	2.00	5.67	2.00	6.33	3.00
Average fibrosis, neovascularisation, calcification and fatty infiltration score	2.67	2.00	2.67	2.00	4.00	1.00	3.67	3.00	4.33	2.00	4.00	2.00	5.00	1.00
Total score for local biological effect after implantation	8.00	5.00	8.67	5.00	11.67	4.00	9.66	5.00	9.66	4.00	9.67	4.00	11.33	4.00
Test (-) control	3.00		3.67		7.67		4.66		5.66		5.67		7.33	
Average group score	4.78						5.83							
Conclusion	Slight						Slight							
Average Biodegradation score	3.00	1.00	5.00	2.00	5.00	0.00	4.00	1.00	3.00	1.00	4.00	2.00	5.00	2.00
Test- control	2.00		3.00		5.00		3.00		2.00		2.00		3.00	
Average group score	3.33						2.50							
Conclusion	Slight						Slight							

Conclusion: Under the conditions of this study, the test sample was considered a

– non-irritant (0,0 up to 2,9) – slight irritant (3,0 up to 8,9) – moderate irritant (9,0 up to 15,0) – severe irritant (> 15) to the tissue as compared to the negative control sample.

Table 46: Collective histological scoring of the local biological effect after implantation and biodegradation for the 3 materials.

Bio-material group	Local biological effect after implantation score		Biodegradation score	
	4 weeks	8 weeks	4 weeks	8 weeks
DCBM	8.55 (slight)	5.09 (slight)	5.67 (slight)	6.00 (slight)
TCP	6.45 (slight)	5.00 (slight)	5.67 (slight)	5.25 (slight)
PCL	4.78 (slight)	5.83 (slight)	3.33 (slight)	2.50 (slight)

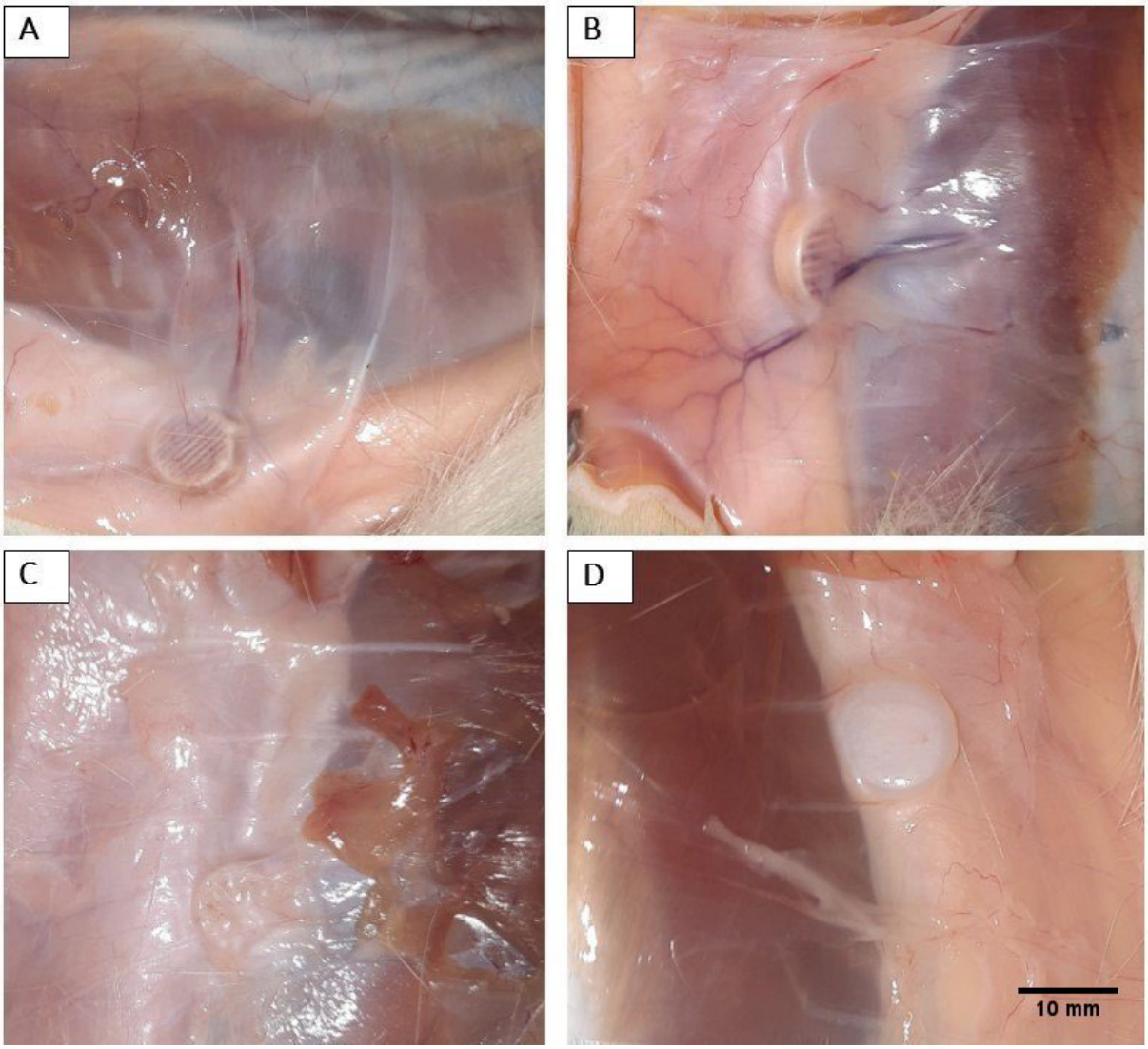


Figure 58: Representative photographs of the gross pathology findings.

There was obvious neovascularisation around sites implanted with DCBM (A) and TCP (B) but not with on PCL (C) or the PE control (D).

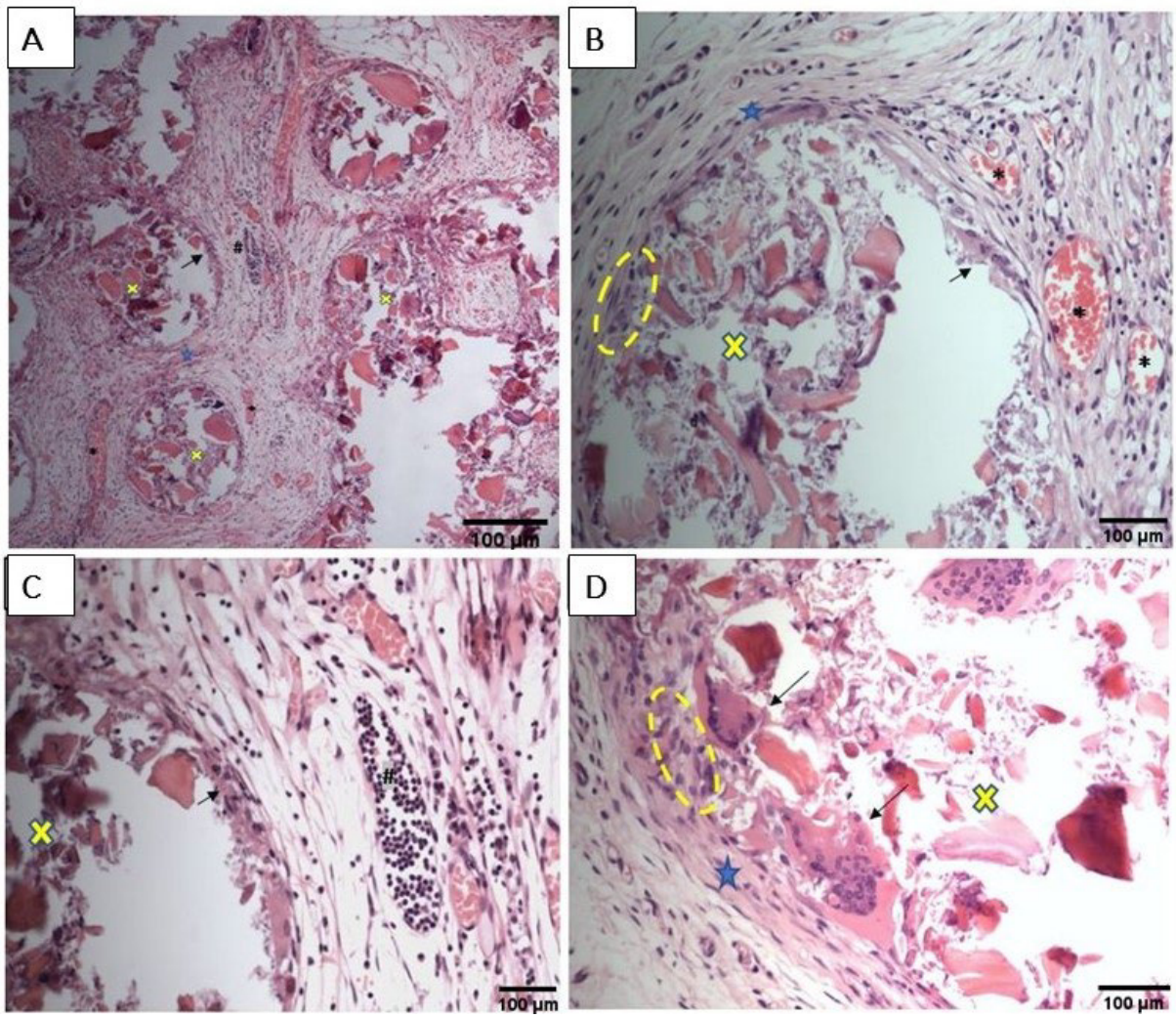


Figure 59: Local biological effect 8 weeks post-implantation of DCBM based scaffolds. Original magnifications x4 (A), x10 (B and C), and x40 (D).

Key:

Black arrow: multinucleated giant cells

Blue star: Fibrous tissue capsule.

Black asterisk * blood vessels (neovascularisation).

lymphocytic infiltration

Dotted circle: macrophages

Yellow cross : scaffold fragmentation

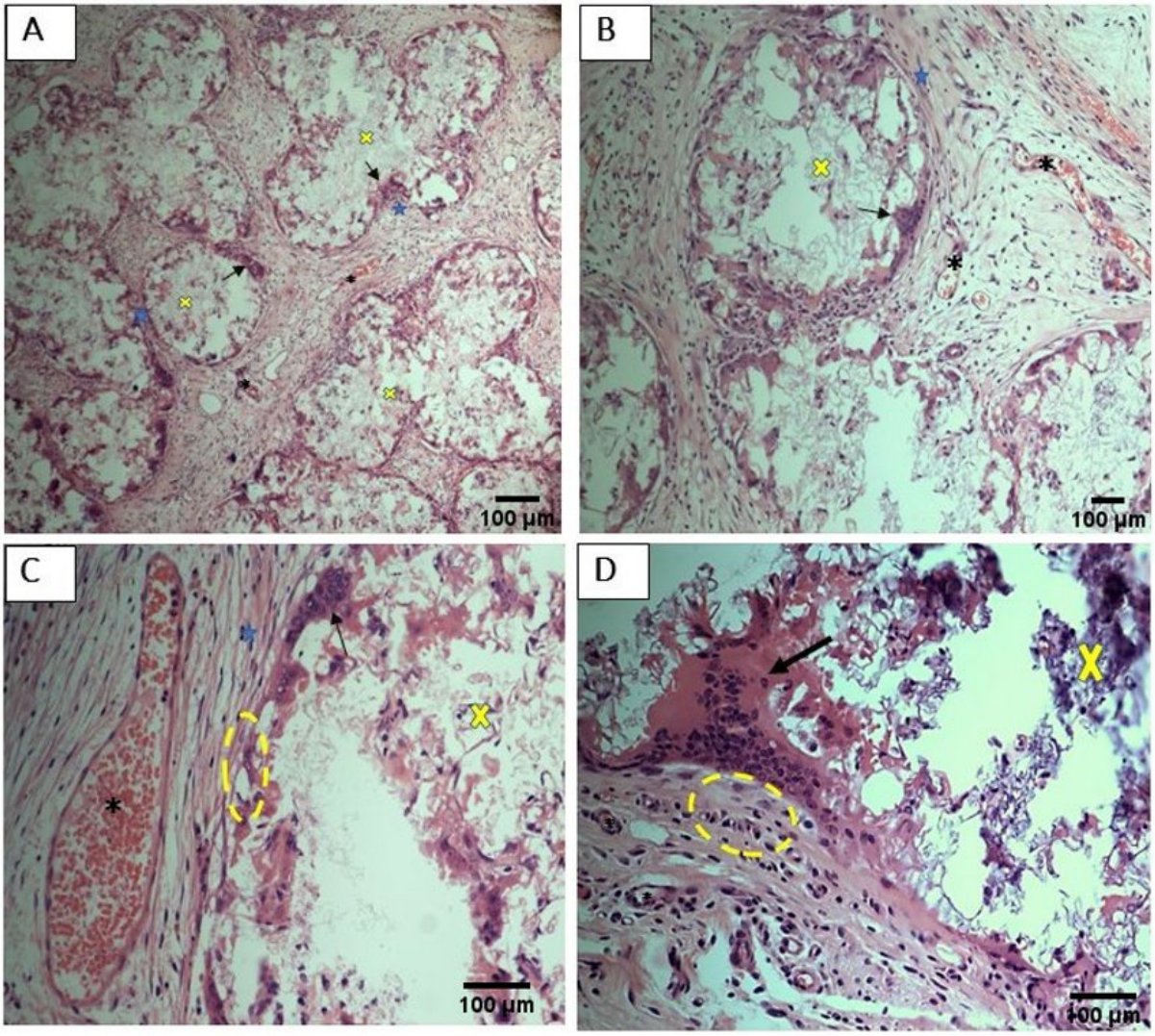


Figure 60: Local biological effect 8 weeks post-implantation of TCP based scaffolds. Original magnifications x4 (A), x10 (B), x20 (C) and x40 (D).

Key:

Black arrow: multinucleated giant cells

Blue star: Fibrous tissue capsule.

Black asterisk * blood vessels (neovascularisation).

lymphocytic infiltration

Dotted circle: macrophages

Yellow cross : scaffold fragmentation

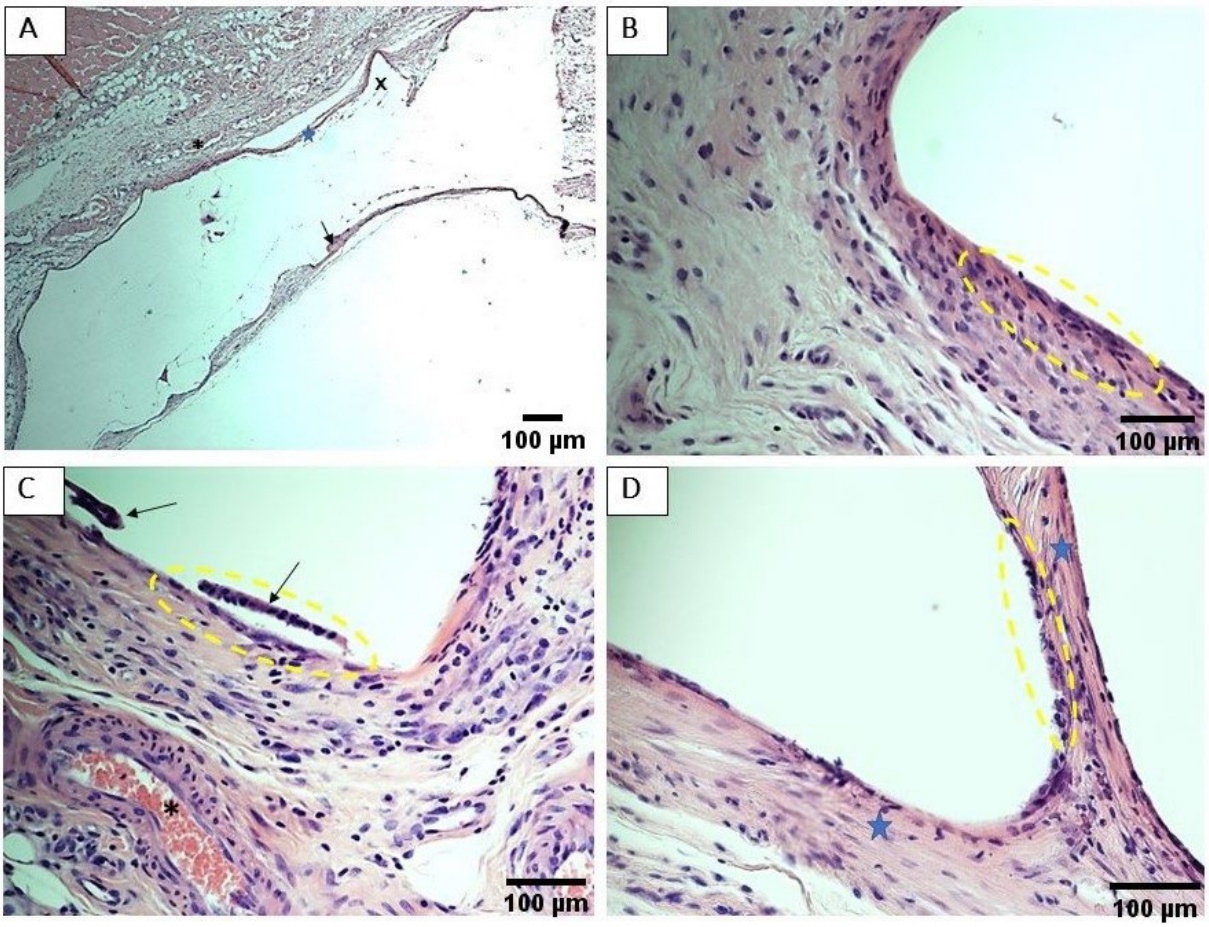


Figure 61: Local biological effect 8 weeks post-implantation of PCL scaffolds.

Original magnifications x4 (A), x10 (B), x20 (C) and x40 (D).

Key:

Black Arrow: multinucleated giant cells

Blue star: Fibrous tissue capsule.

Black asterisk * blood vessels (neovascularisation).

Dotted circle: macrophages

X : scaffold surface erosion

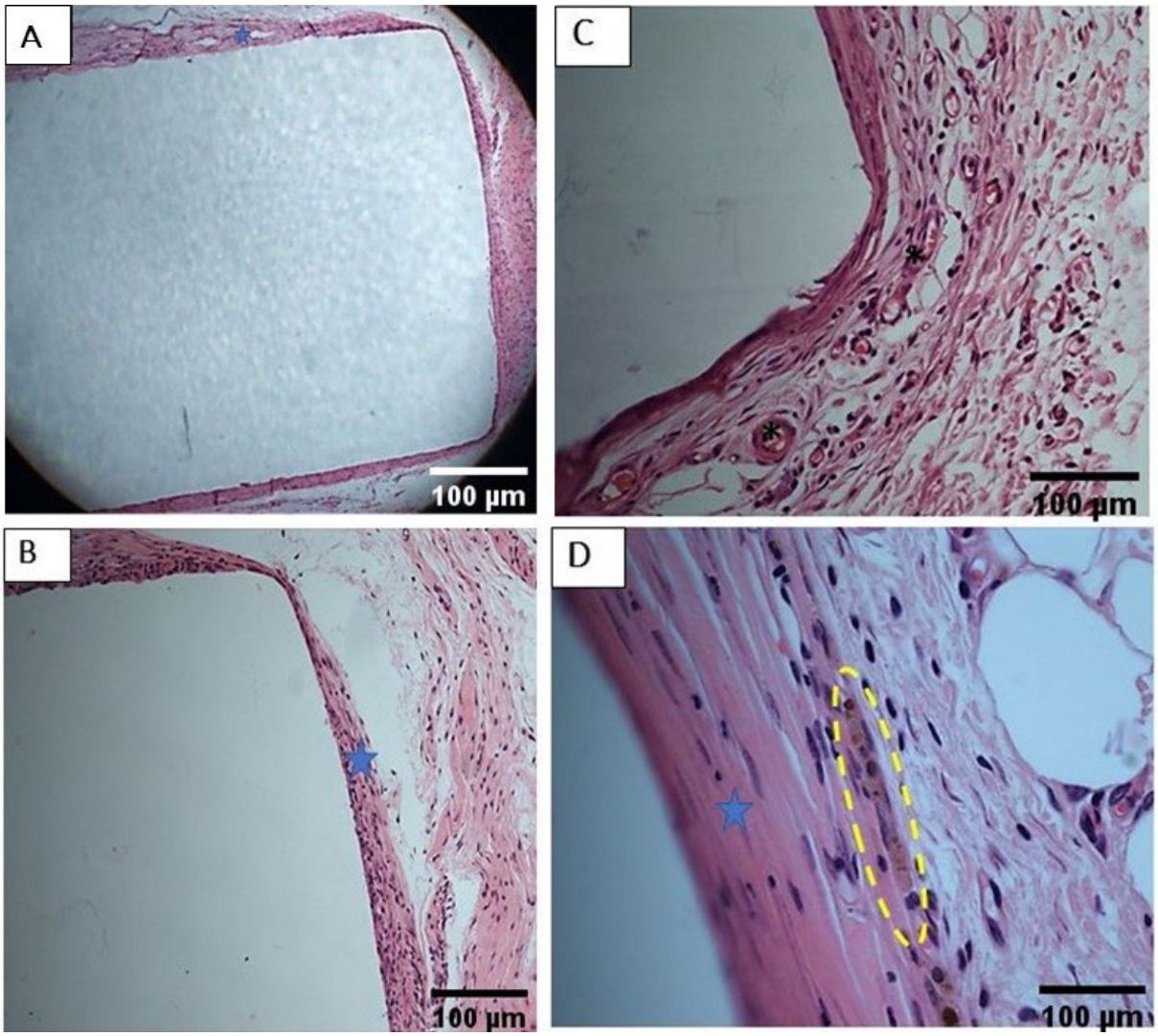


Figure 62: Local biological effect 8 weeks post-implantation of polyethylene (PE) control implants. Original magnifications x4 (A), x10 (B), x20 (C) and x40 (D).

Key:

Blue star: Fibrous tissue capsule.

Black asterisk * blood vessels (neovascularisation).

Dotted circle: macrophages (notice hemosiderosis in the macrophages populated area).

4.5- Evaluation of the ability to support bone healing in a critical size segmental long bone defect.

4.5.1. In-Life animals' outcomes:

4.5.1.a: Intra-operative observations:

The average surgery time (first incision to wound closure) was 53 ±10 minutes.

During surgical implantation of the scaffolds, 4 scaffolds (3 TCP+ 1 DCBM) broke during insertion into the bone defect and had to be replaced by a new sterile one.

Aside from controllable bleeding (particularly upon dissecting the muscles attached to the caudal aspect of the radius and interosseous ligament between radius and ulna), there were no major intraoperative complications to report.

4.5.1.b: General health observation and pain scoring:

Reduced weight bearing on the operated limb (score 2), redness and swelling around the incision (score 2) were recorded in all the rabbits for the first 48 hours after surgery, that gradually returned to normal (score 0) by day 5 post-operatively. Slight weight loss (less than 10 % reduction, score 1) was recorded in 12 rabbits at day 3 post-operatively, yet upon weighing the rabbits at day 7 post-surgery, all the rabbits that had been operated on showed an increase in their body weight in comparison with day 0 (the day of surgery). See **Table 32** (rabbits post-operative scoring system) in the methods section for details of the scoring system.

Seroma around the elbow joint was observed in one rabbit at day 5 post-operatively, that subsided upon extending the carprofen injections for additional 48 hours (dose: 4 mg/kg S/C once a day). Another rabbit showed reduced weight bearing on the operated limb soon after the analgesia ceased (at day 4 post-operatively). In the first instance we decided to extend the analgesia course for an additional 48 hours (buprenorphine 0.06 mg/kg S/C Q 8 h and carprofen 4 mg/kg S/C once a day), and the rabbit did improve; however, it showed reduced weight bearing once again when the analgesia ceased. Upon physical examination of the operated limb, we identified that the cause of lameness was that the indicator pin inserted during surgery was inserted too far across the radius and could be felt underneath the skin from the lateral side of the limb, causing irritation when the rabbit moved. Other than that, there were no signs of inflammation or any wound complications. The pin was removed under sedation through a stap incision followed by applying skin glue to close the pin

extraction puncture wound. Analgesia were administered for an additional 48 h, after which the rabbit was fully weight bearing with no further health concerns for the rest of the study.

Unplanned culling

Five animals (out of the total 27) were removed early from the study as a result of either surgical complications or medical comorbidities. These are summarised in **Table 47.**

Table 47: Unplanned culling in the rabbit bone defect study.

Surgery date	**Culling/euthanasia date**	**Surgery place/animal ID**	**Implant type**	**Reason for culling**
17/8/2021	31/8/2021	ARI-Davos 321075	DCBM	Implant displacement detected at radiographs 2 weeks post operatively (see **Figure 63)**
20/1/2022	28/2/2022	Cambridge-UK M00714530 (3864)	TCP	Wound noticed at one of the digits, that did not respond to treatment and developed infection (see **Figure 64)**
20/1/2022	28/1/2022	Cambridge-UK M00714492 (3870)	PCL	An ulcer was noticed at the sole of the foot of the operated limb that quickly deteriorated into foot gangrene (see **Figure 65**). Bacteriology and histopathology report from the dissected foot post euthanasia -Appendix 4
31/1/2022	26/4/2022	Cambridge-UK M00714493 (3744)	DCBM	Implant displacement detected at week 12 (end of study) radiographers (see **Figure 66)**
2/2/2022	26/4/2022	Cambridge-UK M00714483 (3854)	PCL	As PCL is radiolucent, we could not detect the implant displacement on radiographs- However, during limb dissection post euthanasia (at week 12)- the implant was displaced into soft tissue (**see Figure 67**)



Figure 63: Radiographs showing implant displacement 2 weeks post-operatively (ARI-321075-DCBM) A) Anterio-Posterior (AP) view, and B) Medio-lateral (ML) view.



Figure 64: Skin complication (skin necrosis and sloughing) necessitated culling of one animal (rabbit M00714530 (3864)-DCBM), A) on 15/2/2022, and B) on 28/2/2022 (the date of culling).

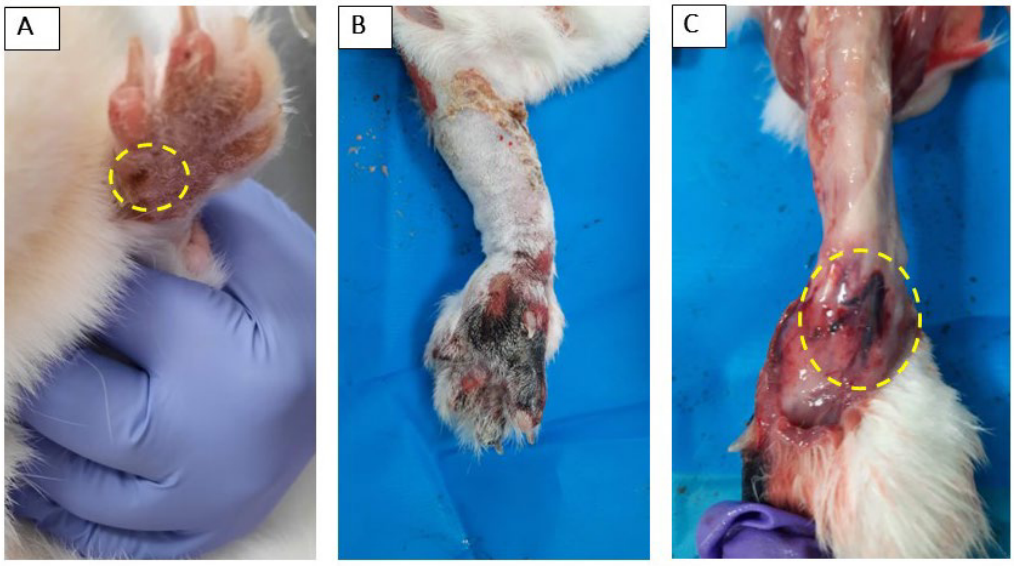


Figure 65: Ulcer on the sole of the foot that quickly complicated into gangrenous lesion (rabbit M00714492 (3870)-PCL).

A) Ulcer noticed on 24/1/2022, B) foot gangrene on 28/1/2022 and C) blocked blood vessels at the level of the carpus anterior aspect-seen upon dissecting the foot. Bacteriology and histopathology report from the dissected foot post euthanasia -Appendix 4.

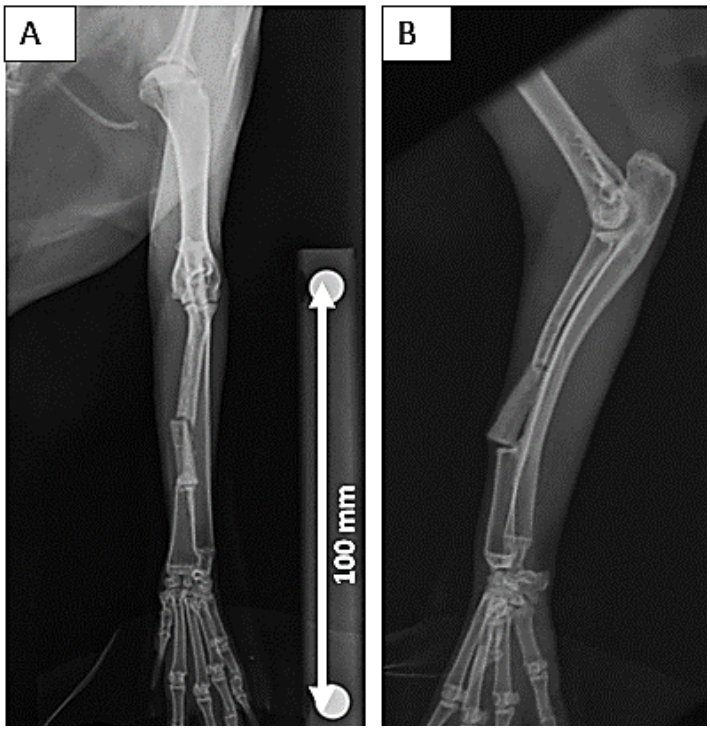


Figure 66: Radiographs showing implant displacement 12 weeks post-operatively (rabbit M00714493 (3744)-DCBM). A) Anterio-Posterior (AP) view, and B) Medio-Lateral (ML) view**.**

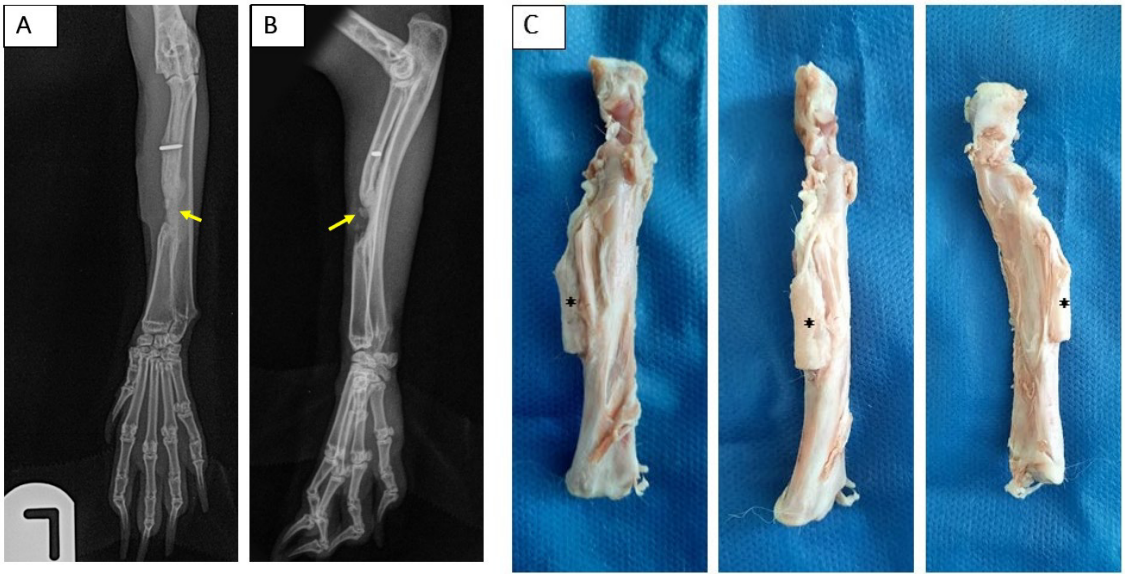


Figure 67: Implant displacement 12 weeks post-operatively (M00714483 (3854)-Cambridge-PCL).

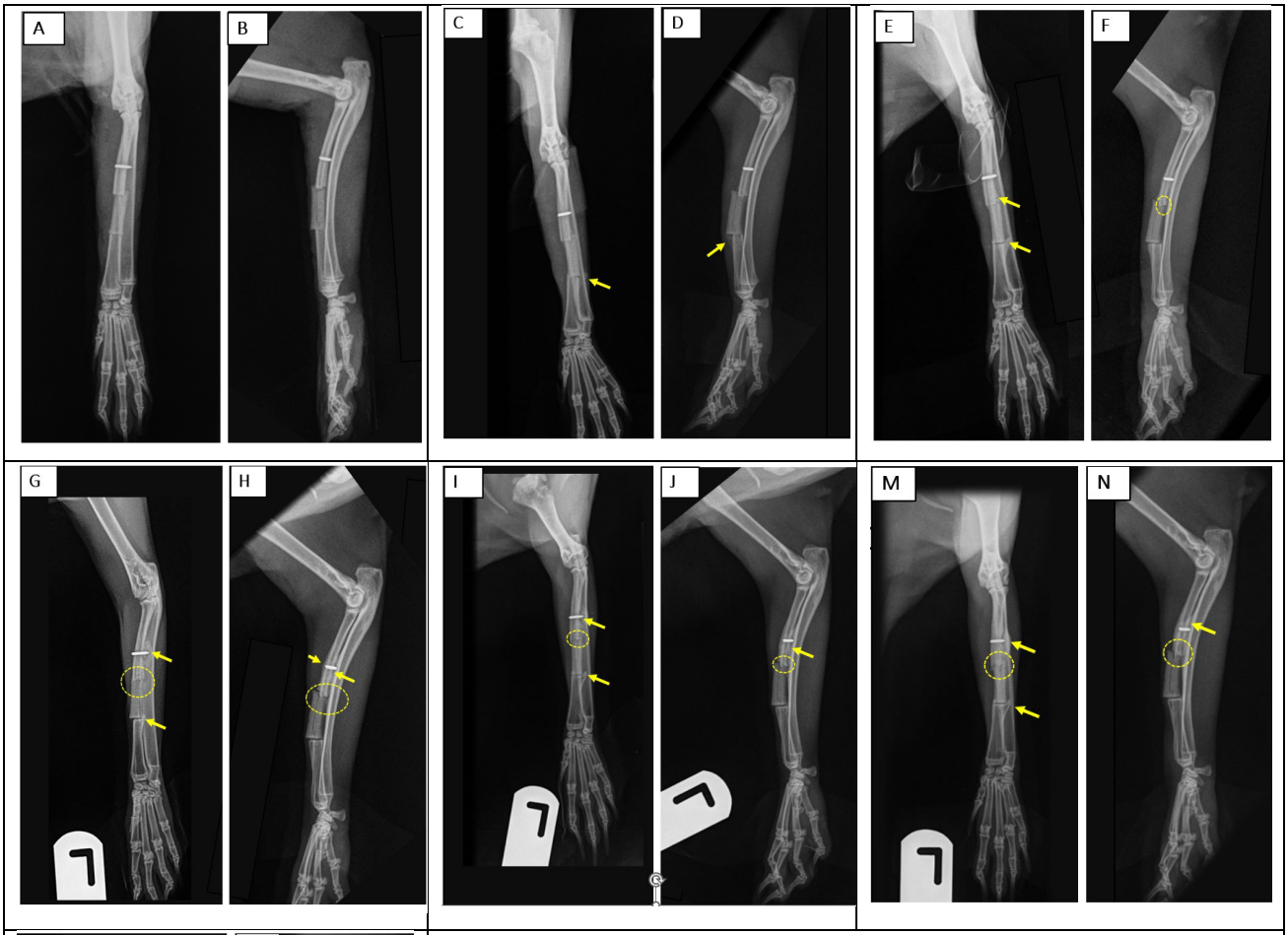
A- Anterio-Posterior (AP) view, B- Medio-lateral (ML) view, while upon dissecting the limb post euthanasia (C), the implant was displaced into the soft tissue *. The radiolucent PCL wasn't detectable in radiographs.

Note: the new bone formation inside the bone defect area (yellow arrow).

4.5.1.c: Radiographs:

- **Decellularised bone matrix (DCBM) group:**

The follow up radiographs showed bony exostoses at the level of the distal osteotomy cut by week 2 post-operatively (see **Figure 68 C and D**). At week 4, partial osteointegration between the scaffold and the bone surface with new bone formation was visible at the level of proximal osteotomy, and the exostoses at the level of the distal osteotomy cut were more prominent (i.e. showing higher radiopacity and growing larger in size), see **Figure 68 E and F**. At week 6, new bone formation in the interosseous space and at the level of the indicator pin was visible on radiographs (see **Figure 68 G and H**). No major changes were observed between week 8 and week 12 and complete osteointegration was not achieved by week 12 (end of the study) (see **Figure 68**).



A and B = Immediately after surgery- day 0(AP and ML respectively)

C and D = 2 weeks after surgery (AP and ML respectively)

E and F = 4 weeks after surgery (AP and ML respectively)

G and H = 6 weeks after surgery (AP and ML respectively)

I and J = 8 weeks after surgery (AP and ML respectively)

K and L = 10 weeks after surgery (AP and ML respectively)

M and N = 12 weeks after surgery (AP and ML respectively)

Figure 68: An example radiographs series taken every 2 weeks from day 0 to week 12 of a rabbit received a DCBM scaffold (rabbit ID: Cambridge M00714484 (3755) DCBM).
At week 2 (C and D): Bony exostoses at the level of the distal osteotomy cut (yellow arrow).
At week 4 (E and F): Partial osteointegration (dotted circle) between the scaffold and the bone surface and new bone formation (yellow arrow) was visible at the level of proximal osteotomy, and the exostoses at the level of the distal osteotomy cut were more prominent (have higher radiopacity and grew larger in size).
At week 6 (G and H): New bone formation in the interosseous space and at the level of indicator.
No major changes observed between week 8 and week 12 (I to N) and no complete osteointegration was achieved by week 12 (end of the study).

Slight implant displacement was detected during week 2 follow up radiographs in two of the animals received DCBM scaffolds as an implant, creating a gap between the implant posterior surface and the ulna. By week 8 new bone formation was noticeable in this gap. We decided to keep these 2 rabbits in the study as they were weight bearing and did not exhibit any health concerns (**see Figure 69).**

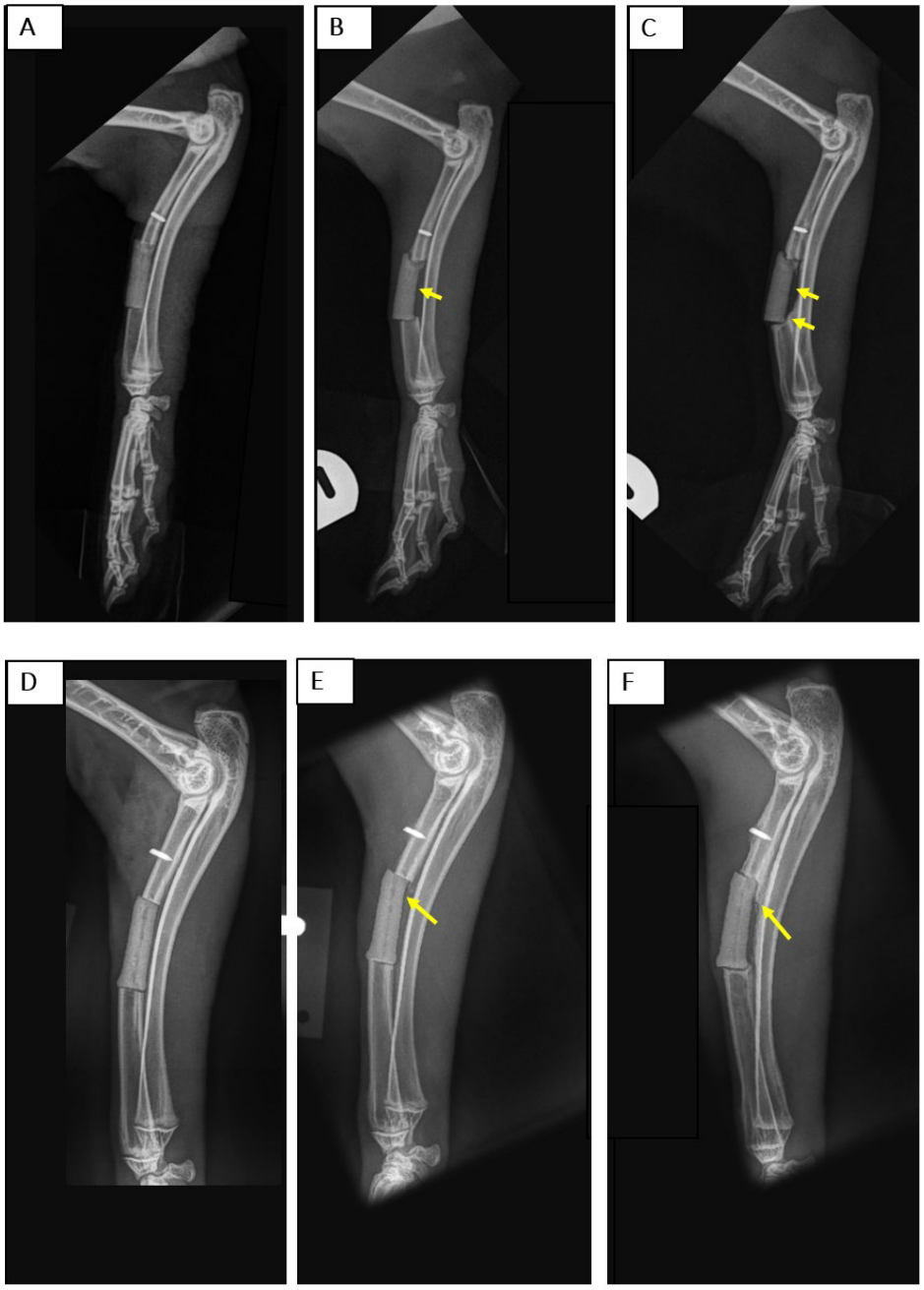


Figure 69: Implant displacement in 2 of the animals received DCBM scaffolds (A to C: Cambridge M00754120 (K47261) and D to F: ARI 321073).
A and D are the day 0 postoperative radiographs.
B and E are the 2 week follow-up radiographs showing implant displacement creating a gap between the implant posterior surface and the ulna.
C and F are the 8 week follow-up radiographs showing new bone formation in the created gap.

- **Tri-Calcium Phosphate (TCP) group:**

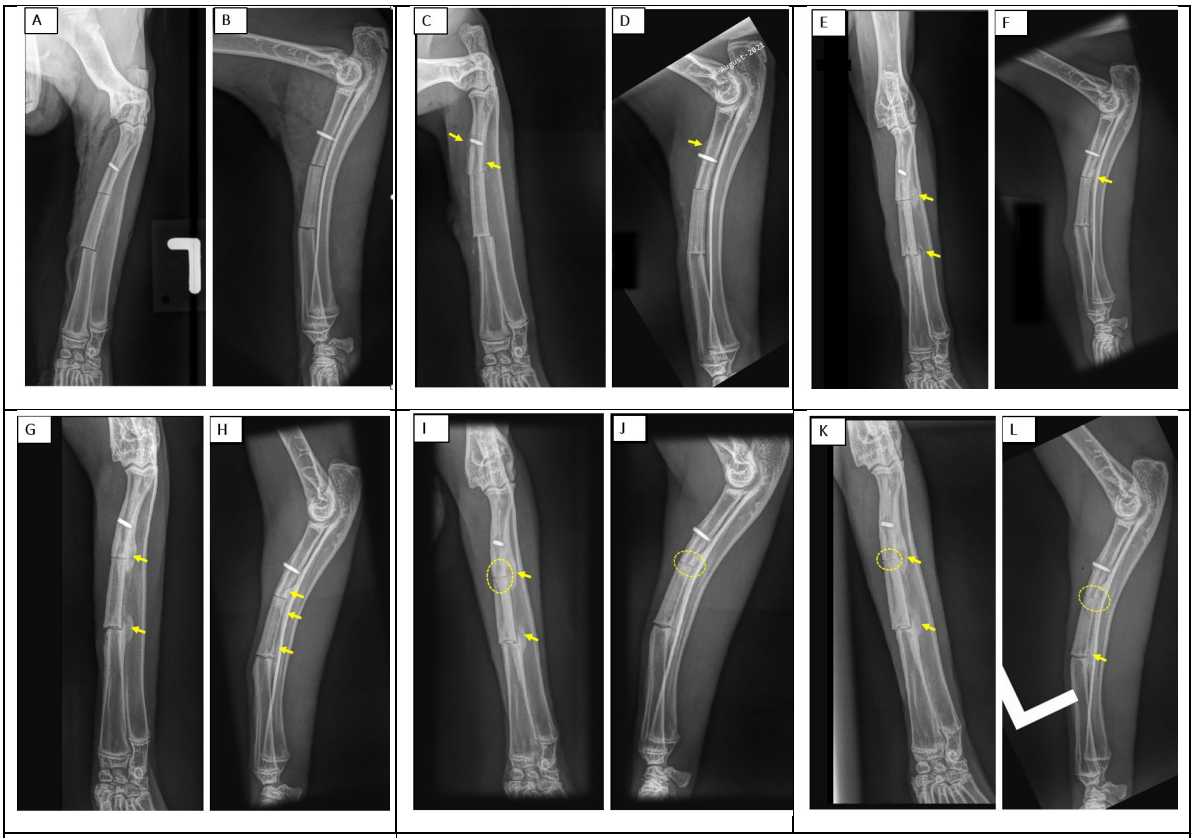
The follow up radiographs showed periosteal ossification, that has a feathery appearance, around the indicator pin and new bone formation in the inter-osseous space between the radius and ulna by week 2 post-operatively. At week 4 and week 6 radiographs, the periosteal ossification around the pin lost its feathery appearance and the new bone formation in the interosseous space became more prominent with higher radiopacity, smoother boundaries, and a larger surface area. By week 8, healing/osteointegration between implant and bone was noticeable at the level of the proximal osteotomy cut yet no healing was detectable at the level of the distal osteotomy cut. Week 10 and week 12 radiographs did not show tangible differences from the week 8 radiographs. **See Figure 70** for a series of radiographs from day 0 to week 12 of one of the rabbits that received a TCP scaffold**.**

Accidental partial osteotomy of the ulna at the level of the distal osteotomy cut was seen in one rabbit upon imaging directly after surgery, that healed by the time of the 2 week follow-up radiographs (**see Figure 71**).

Osteointegration at the level of the proximal and distal osteotomy cuts detected in one rabbit in the TCP group by week 4 post-operative radiograph **(see Figure 72).**

- **Polycaprolactone (PCL) group:**

As PCL is a radiolucent material, new bone formation and bone ingrowth were clearly detectable on radiographs (in comparison to the radiopaque DCBM and TCP). In the follow up radiographs, new bone formation at the level of the osteotomy sites by week 4 post-operatively was seen, however complete defect closure was not seen in any of the animals by the end of the study (at week 12) (**see Figure 73**). In one rabbit the osteointegration within the scaffold followed the scaffold's porosity unique pattern **(see Figure 74).**



A and B = Immediately after surgery- day 0 (AP and ML respectively)
C and D = 2 weeks after surgery (AP and ML respectively)
E and F = 4 weeks after surgery (AP and ML respectively)
G and H = 6 weeks after surgery (AP and ML respectively)
I and J = 8 weeks after surgery (AP and ML respectively)
K and L = 10 weeks after surgery (AP and ML respectively)
M and N = 12 weeks after surgery (AP and ML respectively)

Figure 70: An example radiographs series taken every 2 weeks from day 0 to week 12 of a rabbit received a TCP scaffold (rabbit ID: ARI_ 321074_TCP).
At week 2 (C and D): new bone formation around the indicator pin (feathery-periosteal ossification) as well as in the inter osseous space between radius and Ulna (yellow arrows).
At week 4 (E and F) and week 6 (G and H): the new bone formation around the indicator pin and in the interosseous space became more prominent (more radiopaque, smoother boundaries and larger surface area).
By week 8 (I and J), healing/osteointegration between the scaffold and the level of proximal osteotomy cut was observed (dotted circle), yet no signs of healing at the level of distal osteotomy sites.
No further changes were observed at week 10 (K and L) and week 12 (M and N) radiographs

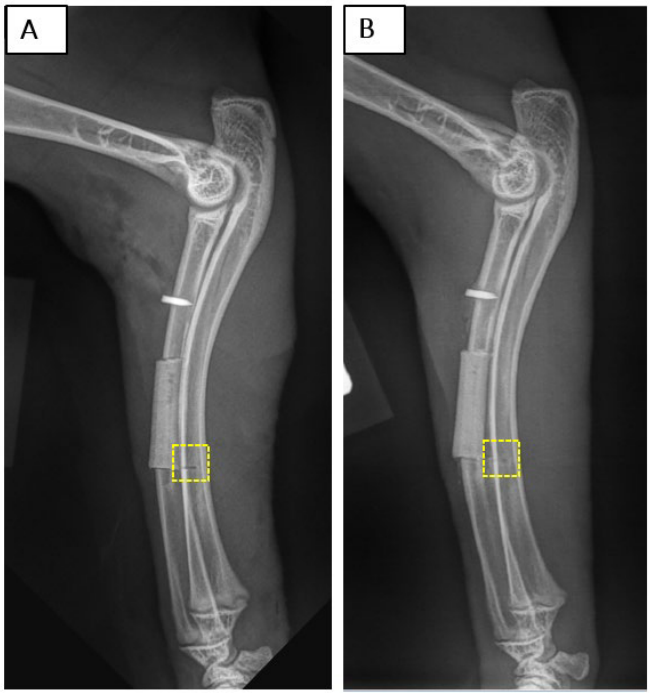


Figure 71: Accidental partial osteotomy of the ulna at the level of the distal osteotomy cut directly after surgery (A) that healed by the time for the 2 weeks follow-up radiographs (B). Rabbit ID (ARI_321072_TCP).

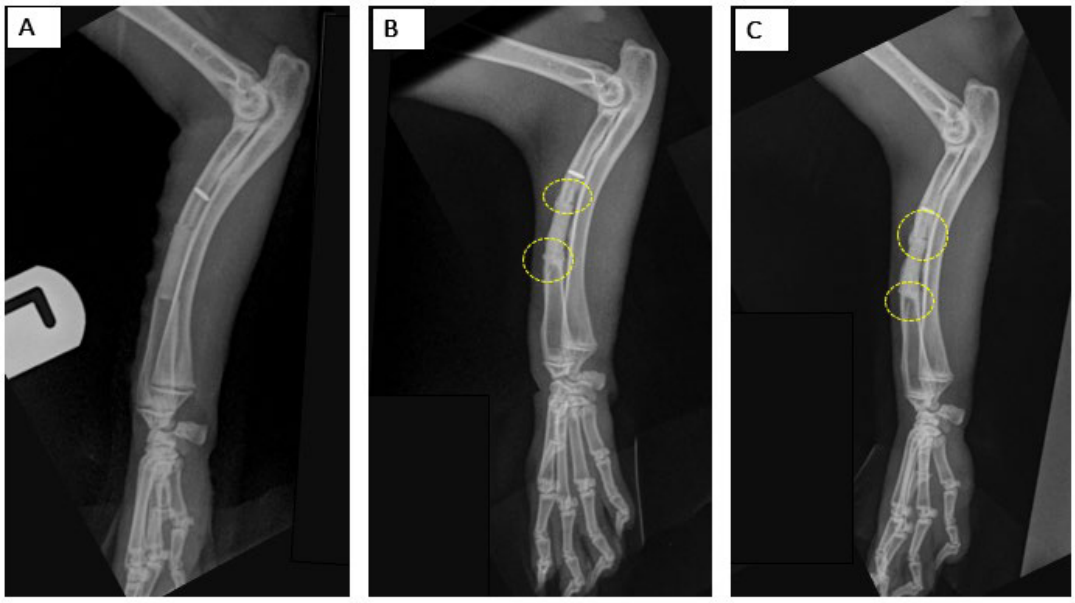
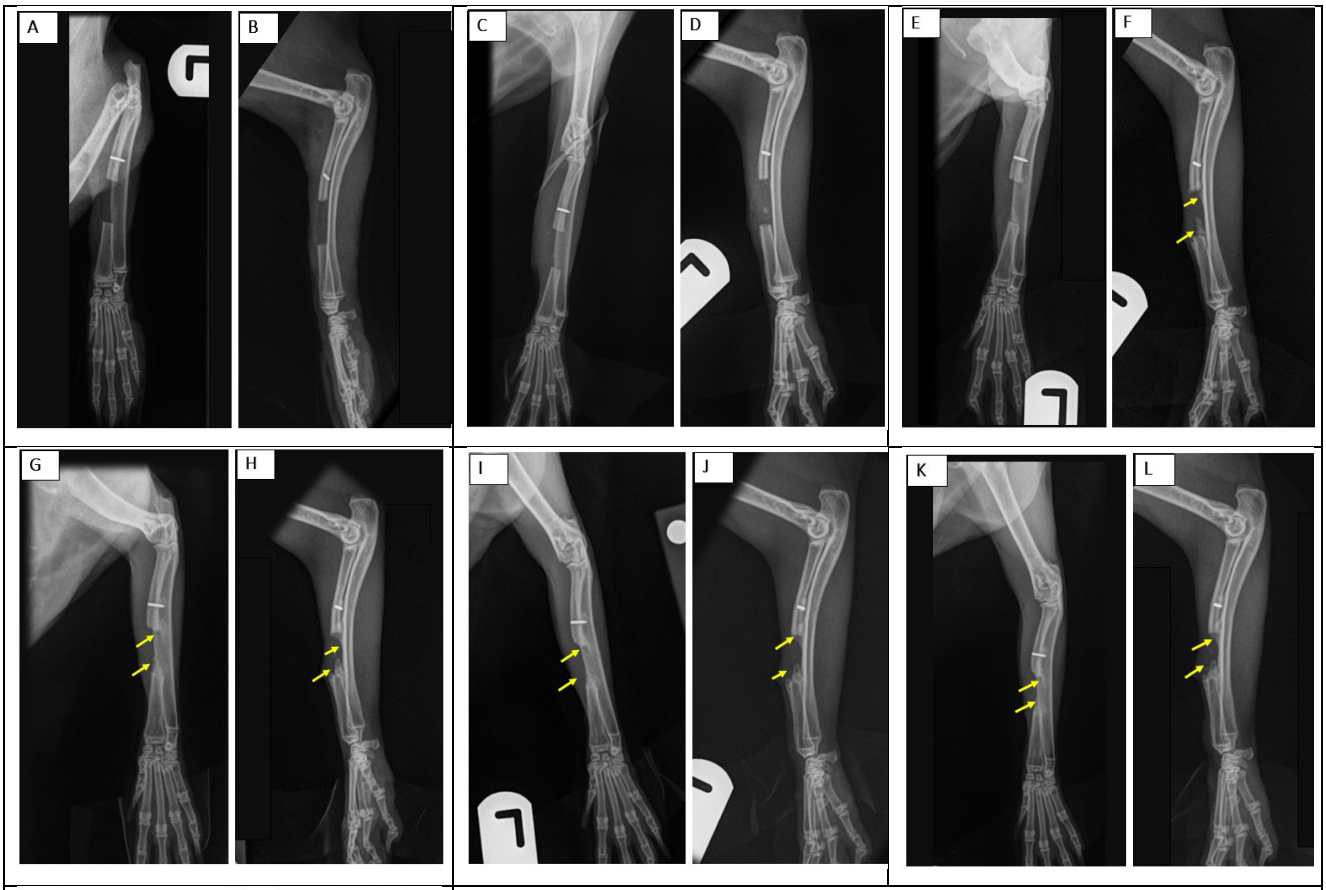


Figure 72: Osteointegration at the level of the proximal and distal osteotomy cuts 4 weeks post-operatively (Cambridge, M00754118 (K67332)-TCP).

A) Day 0 B) week and C) week 6 postoperatively.



A and B = Immediately after surgery-day 0 (AP and ML respectively)
C and D = 2 weeks after surgery (AP and ML respectively)
E and F = 4 weeks after surgery (AP and ML respectively)
G and H = 6 weeks after surgery (AP and ML respectively)
I and J = 8 weeks after surgery (AP and ML respectively)
K and L = 10 weeks after surgery (AP and ML respectively)
M and N = 12 weeks after surgery (AP and ML respectively)

Figure 73: An example radiographs series taken every 2 weeks from day 0 to week 12 of a rabbit received a PCL scaffold (rabbit ID: Cambridge- M00714487 (3877)-PCL).

Showing new bone formation around the osteotomy sites from week 4 (E and F) onwards.

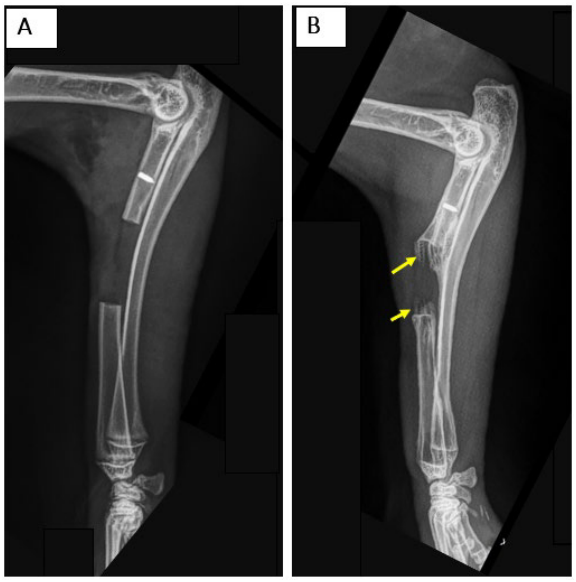


Figure 74: Osteointegration within PCL scaffold following the scaffold's unique porosity pattern. A) day 0 B) week 12 post operatively. (Rabbit ID: ARI-321077-PCL).

4.5.2: Post-mortem evaluation

4.5.2.a: Histopathological evaluation:

This section describes the microscopic morphological changes, with special focus on group-specific differences. The individual animal histopathological scoring data can be found in the Appendix 5.

4.5.2.a.I- Bone fluorochrome labels:

Due to autofluorescence from both the bones and the implants, it was impossible to differentiate newly formed bone labelled with oxytetracycline (cyan colour code, injected 9 weeks post-surgery) and the native tissues. Trying different laser settings did not resolve the issue. Hence, I decided to use it as a background outlining the bone/implant construct section's structure.

Calcein green (colour code yellow, injected at 3 weeks post-surgery) and xylenol orange (colour code Magenta, injected at 6-weeks post-surgery) were clearly distinguishable in all sections.

- **Objective analysis of the fluorochrome images:**

Similar to the undecalcified bone section histological evaluation (explained in section 4.5.2.a.II below), 4 main areas were examined for new bone formation: inside the osteotomy (bone in-growth), anterior to the osteotomy (periosteal ossification), caudal to the osteotomy (interosseous space), and osteointegration at the level of osteotomy cuts.

In all 3 groups there was pronounced fluorescence of both the calcein green and xylenol orange labels at the interosseous space and moderate signalling at the level of the osteotomy sites (**see Figure 75**), yet only one animal (from DCBM group) had xylenol orange signal anterior to the osteotomy (periosteal ossification) and 2 animals (one from the TCP group and one from the PCL group) had minimal xylenol orange signal inside the osteotomy site (bone ingrowth), see **Figure 75 C and D.** Slight scaffold autofluorescence while scanning for xylenol orange was observed in the DCBM and TCP groups; these areas of autofluorescence were excluded during the quantitative analysis.

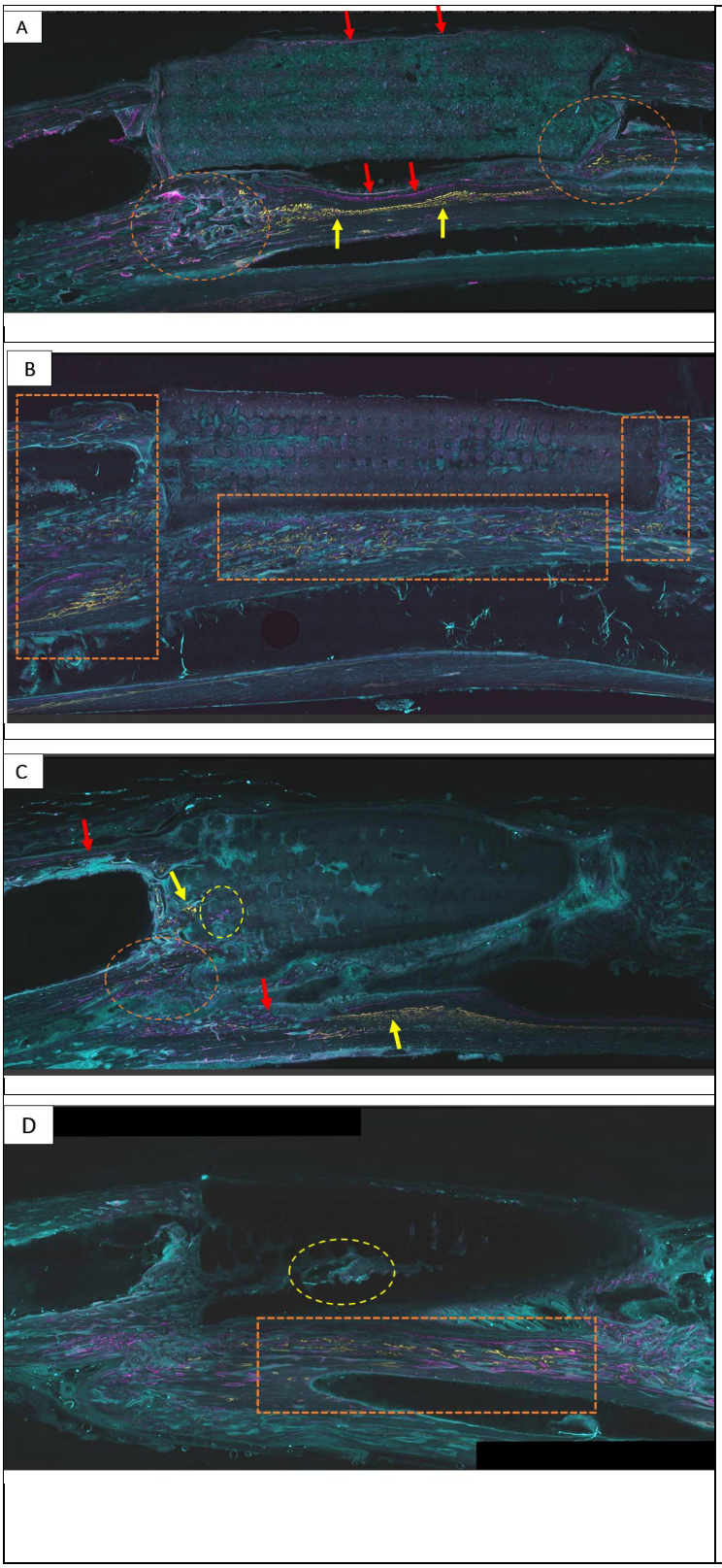


Figure 75: Bone fluorochrome labelling acquired using Nikon AxR (iT2 eclipse) inverted confocal Microscope and processed using Nikon-NIS element AR 5.41.01 software.

- Calcein green injected at week 3 after surgery – colour code yellow
- Xylenol orange injected at week 6 after surgery – colour code magenta.
- Oxytetracycline injected at week 9 after surgery – colour code cyan (due to universal labelling of the section and autofluorescence from the bone and implants – it has been used as background).
- Yellow arrows= calcein green – Red arrows= xylenol orange

A) A representative bone section from the DCBM group (animal ID: Cambridge M00754120 (K47261). Positive labelling for both calcein green and xylenol orange were seen at the interosseous space and around osteotomy sites. In addition to periosteal positive xylenol orange labelling.

B and C) A representative bone section from the TCP group (animal ID: ARI- 321074 and Cambridge M00754118-K67332). Positive labelling for both calcein green and xylenol orange were seen at the interosseous space and around osteotomy sites. In addition to minimal xylenol orange and calcein green signal inside the osteotomy site (C).

D) A representative bone from the PCL group (animal ID: Cambridge- M00714482-3830). Positive labelling for both calcein green and xylenol orange were seen at the interosseous space and around osteotomy sites. In addition to minimal xylenol orange inside the osteotomy site.

- **<u>Quantitative analysis of the fluorochrome images:</u>**

The average area percentage and signal intensity of the calcein green and xylenol orange are demonstrated in **Table 48** below. Upon running a one-way ANOVA there was no significant difference (P=0.136) between the 3 material groups in any of these parameters. However,

comparing the 2 labels within the same material group by running a paired T-test, the % area of xylenol orange was significantly higher than the % area of calcein green in the DCBM (P=0.009) and TCP (P<0.001) groups yet no significant difference between the 2 labels was seen in the PCL group (P=0.054).

Table 48: Fluorochrome labels quantitative analysis.

	Calcein green area %	Calcein green signal intensity	Xylenol orange area %	Xylenol signal intensity
DCBM group	0.33± 0.06	5.61± 0.74	0.65 ± 0.29 ***	7.20 ± 1.03
TCP group	0.40 ± 0.19	6.43 ± 1.32	0.87 ± 0.11**	6.53 ± 1.41
PCL group	0.46 ± 0.08	6.16 ± 0.60	0.66 ± 0.25	7.04 ± 0.34

4.5.2.a.II- Stevenel's blue-Van Gieson Picrofuchsin stained undecalcified bone sections:

After sending the 5 specimens from culled animals (see Table 47 in the unplanned culling section above) for decalcified histology sectioning, these were the remaining specimens that were included in the undecalcified histology evaluation: 8 specimens from the DCBM group, 8 specimens from the TCP group and 6 specimens from the PCL group. For the DCBM group, the new bone formation was stronger around the implant (periosteal and the interosseous space) rather than proper osteointegration and bone in-growth (in other words, the **DCBM scaffold tends to be osteoinductive rather than osteoconductive**). Aside from slight fibrosis (score 1-2; within the layer of periosteal ossification or in the interosseous space) and lymphocytic infiltration, there were no other reported inflammatory changes. There were no degenerative changes, phagocytosis or infections reported either (see **Table 49** and **Figure 76**). The TCP group showed superior osteointegration and bone in-growth to the DCM group, while periosteal ossification was less evident in the **TCP group (moderate osteoinduction** and **slight osteoconduction)**. Fibrosis (score 1-2) was evident, yet no other inflammatory, degenerative changes or infection were present (see **Table 49** and **Figure 77**). Finally, the PCL group had the highest rates (and scores) for bone in-growth among the 3 groups. The periosteal and interosseous space new bone formation was moderate in the **PCL group (superior osteoconduction** and **moderate osteoinduction)**. Similar to DCBM and TCP scaffolds, fibrosis (score 1-2) was evident, yet no other inflammatory, degenerative changes or infections were present (see **Table 49 and Figure 78**).

Table 49: Summary of the microscopic morphological changes in the 3 tested bio-materials groups at week 12 after implantation in rabbits' 15 mm radius defect.

	DCBM group	**TCP group**	**PCL group**
1-Proliferative changes			
Defect closure inside the osteotomy (bone ingrowth)	Bone ingrowth was low (mainly grade 0–1), limited to small sporadic islands of new bone formation inside the implant pores in 2 of the rabbits.	6 out of the 8 animals in this group had a degree of bone ingrowth score range 1-3.	Bone ingrowth was report in all the rabbits in PCL group (particularly at the level of distal osteotomy (score 1-3)
Defect bridging anterior to the osteotomy (periosteal ossification)	Periosteal ossification was prominent in this group, 5 rabbits had score =2-3, while 2 rabbits had score=1 and only one rabbit scored 0	Periosteal ossification was slight in this group in comparison with DCBM. 4 rabbits had score=1, and the other 4 scored 0 for periosteal ossification.	Periosteal ossification was present in all the rabbits in this group (score =1-3)
Defect bridging posterior to the osteotomy and interosseous space (between radius and ulna)	New bone formation in the interosseous space (score 2-3) was evident in all the rabbits in this group.	New bone formation in the interosseous space (score 1-3) was evident in all the rabbits in this group.	New bone formation in the interosseous space (score 1-4) was evident in all the rabbits in this group
Osteointegration (at the level of osteotomies)	Osteointegration was poor in this group, mostly restricted to the proximal osteotomy site with (score range 0-1).	Moderate osteointegration was evident in all the rabbits in the TCP group (score 1-3).	Strong osteointegration was evident in all the rabbits in the PCL group (score 2-3).
2-Degenerative bone changes			
Osteonecrosis sequester osteolysis	No reported degenerative bone changes.	No reported degenerative bone changes.	No reported degenerative bone changes.
3-Phagocytosis			
Macrophages Giant cells	No macrophages were detectable.	No macrophages were detectable.	No macrophages were detectable.

	DCBM group	TCP group	PCL group
4-Inflammatory changes			
Fibrous tissue	Fibrosis (score 1-2) within the layer of periosteal ossification or in the interosseous space was observed in all the rabbits included in this group.	Fibrosis (score 1-2) within the layer of periosteal ossification or in the interosseous space was observed in 6 rabbits and 2 rabbits scored 0 for fibrosis.	Fibrosis (score 1-2) within the layer of periosteal ossification or in the interosseous space was observed in all the rabbits in this group
Lymphocytic (= non-purulent) inflammation	4 rabbits in this group had minimal to slight (score 1-2) lymphocytic infiltration.	No lymphocytic infiltration was detectable	No lymphocytic infiltration was detectable
Granulocytic (= purulent) inflammation	No signs of purulent inflammation were reported	No signs of purulent inflammation were reported	No signs of purulent inflammation were reported
Necrotizing inflammation	No signs of necrotizing inflammation were reported	No signs of necrotizing inflammation were reported	No signs of necrotizing inflammation were reported
Osteomyelitis (inflammation near bone marrow)	No signs of osteomyelitis were reported	No signs of osteomyelitis were reported	No signs of osteomyelitis were reported
5- Infection			
Bacteria (cocci or bacilli visible)	No signs of infection were reported	No signs of infection were reported	No signs of infection were reported
Osteomyelitis (inflammation near bone marrow)			

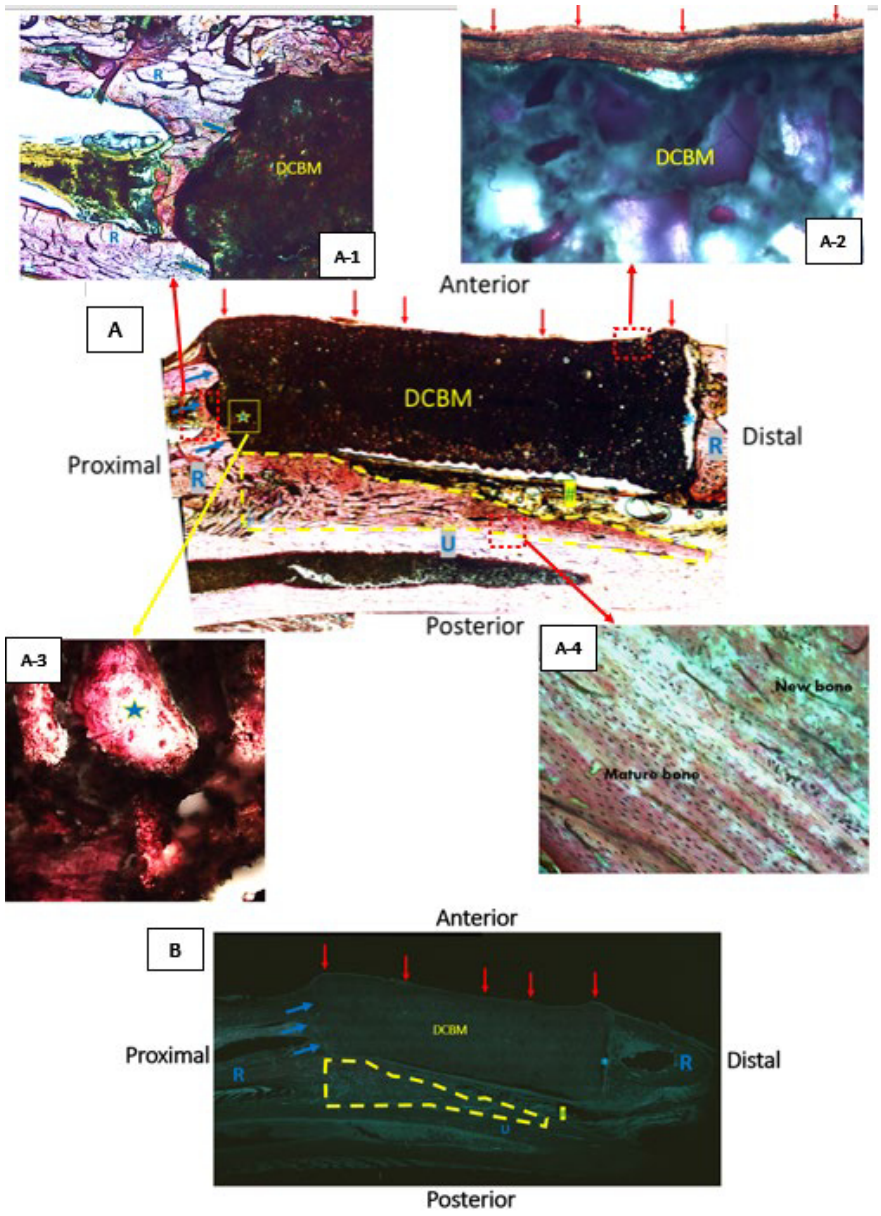


Figure 76: Undecalcified bone section with DCBM implant.

A) Stevenel's blue-Van Gieson Picrofuchsin stained section

B) Confocal microscope scanned slide using with the oxytetracycline adjusted filter

Blue arrows: osteointegration at the level of proximal osteotomy cut. (A-1: x10 magnification of the area of osteointegration).

Red arrows: new bone formation anterior to implant- periosteal ossification (A-2: x20 magnification of the periosteal ossification).

Yellow dotted polygon: new bone formation posterior to implant (in the interosseous space between radius and ulna).

Blue asterisk *: Gap between the scaffold and surrounding bone (lack of osteointegration)

Blue star: island of new bone formation inside the scaffold (bone ingrowth)- (A-3: x20 magnification)

A-4 is a focus on the mature bone (organised)/ newly formed bone interface (less organised) at the interosseous space between radius and ulna. Green #: fibrous tissue R: Radius U: Ulna

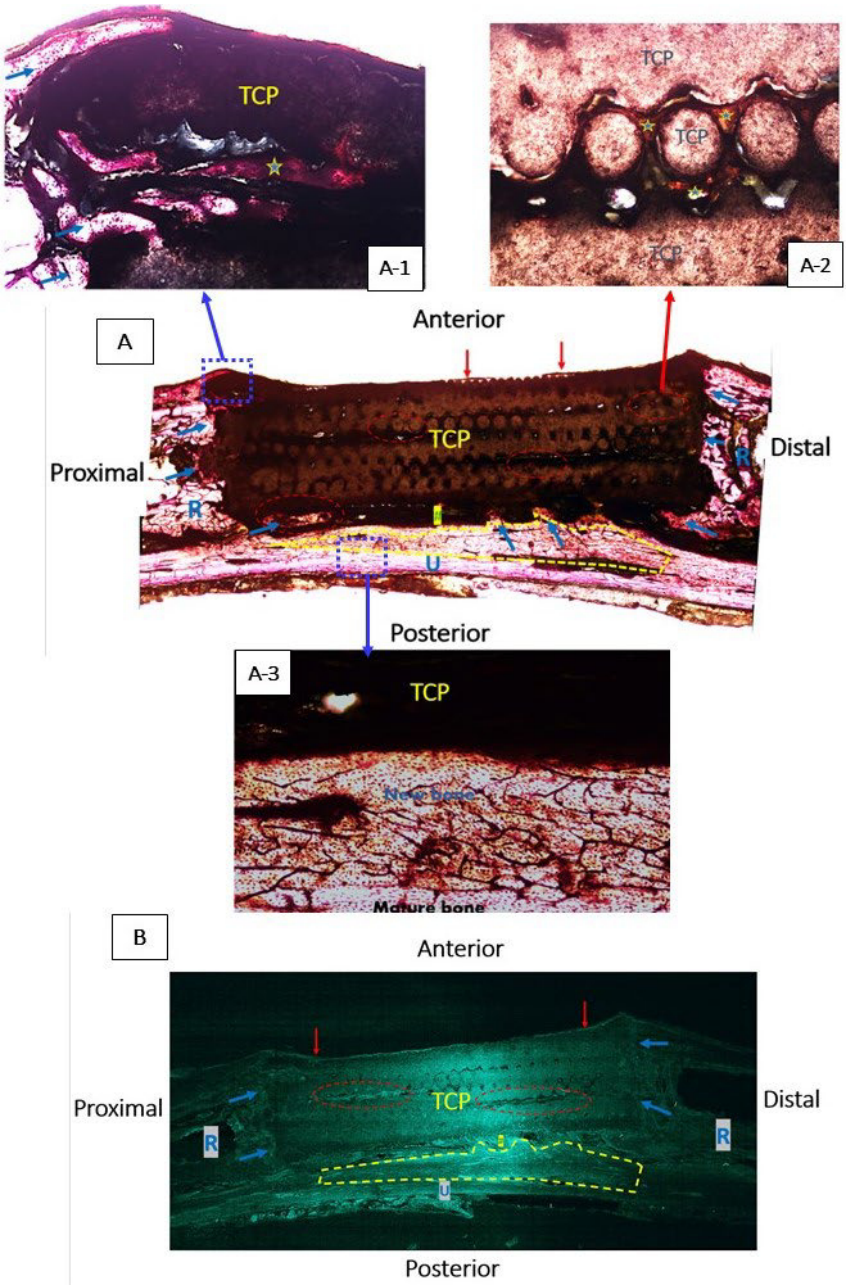


Figure 77: Undecalcified bone section with TCP implant.

A) Stevenel's blue-Van Gieson Picrofuchsin stained section

B) Confocal microscope scanned slide using with the oxytetracycline adjusted filter

Red arrows: new bone formation anterior to implant (periosteal ossification)

Yellow dotted polygon: new bone formation posterior to implant (in the interosseous space between radius and ulna).

Blue arrows: osteointegration at the level of proximal and distal osteotomy cut (A-1: x20 magnification of the area of osteointegration).

Red dotted oval: new bone formation inside the implant (bone ingrowth)- (A-2: is x20 magnification of area of bone ingrowth within the implant pores- blue star).

A-3: The stratification of the structural layers of bone/implant interface (implant-new bone -mature bone).

Green #: fibrous tissue R: Radius U: Ulna

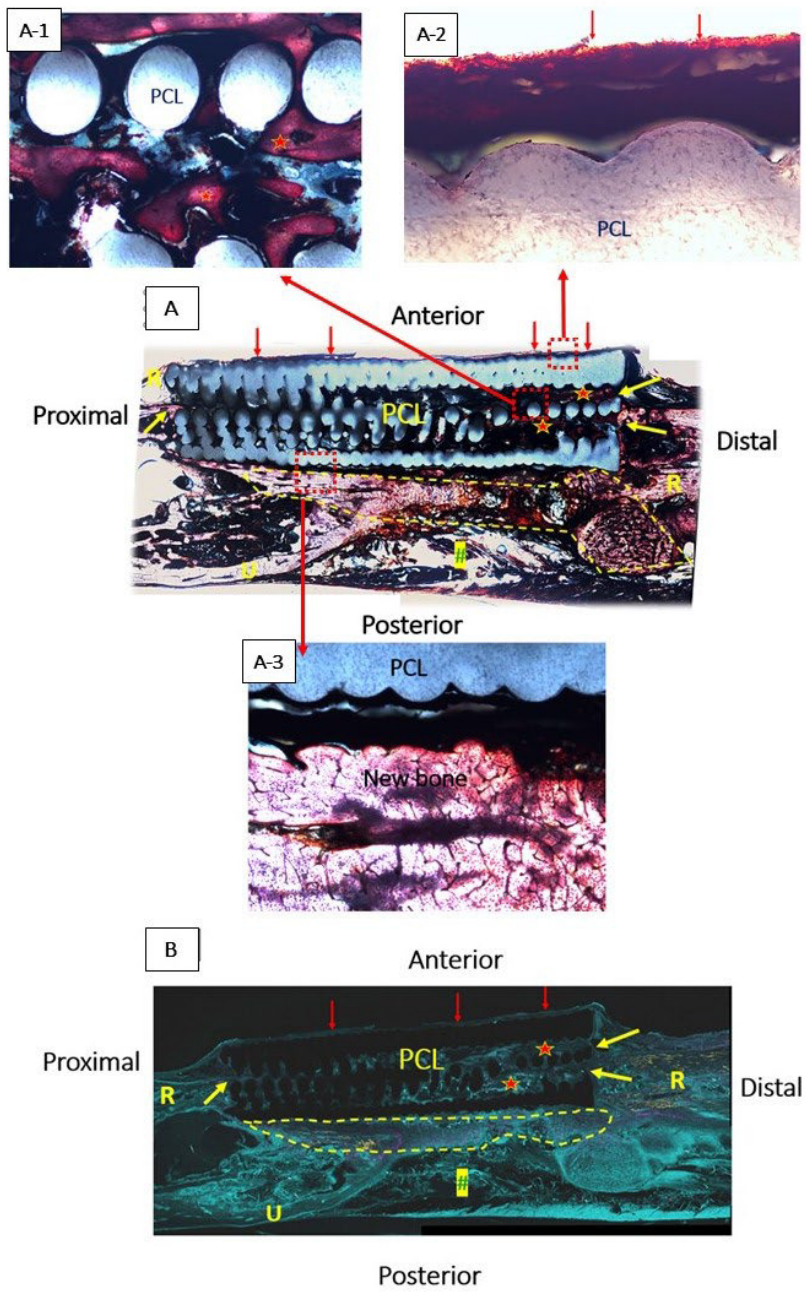


Figure 78: Undecalcified bone section with PCL implant.

A) Stevenel's blue-Van Gieson Picrofuchsin stained section

B) Confocal microscope scanned slide using with the oxytetracycline adjusted filter

Red arrows: new bone formation anterior to implant (periosteal ossification) -(A-1: x20 magnification of area of periosteal ossification).

Yellow dotted polygon: new bone formation posterior to implant (in the interosseous space between radius and ulna).

Red star: new bone formation inside the implant (bone ingrowth)- (A-2: x20 magnification of area of bone ingrowth within the implant pores)

Yellow arrows: osteointegration at the level of proximal and distal osteotomy cut.

A-3: The implant new bone interface. Green #: fibrous tissue R: Radius U: Ulna

4.5.2.a.III- Haematoxylin and Eosin (H&E) stained decalcified bone sections:

The findings from the decalcified bone sections of the 5 animals culled from the study are summarised in **Table 50 and Figures 79 to 82** below.

Table 50: Histological findings from the decalcified bone sections.

Animal ID	Implant type	Findings
Cambridge-UK M00714493 (3744)	**DCBM**	- Bone ingrowth at the proximal osteotomy level with different stages of cell differentiation towards the osteogenic lineage (**Figure 79 A and B**). - Lymphocytic infiltration and fibrosis (**Figure 79 C**). - Mesenchymal cells migration and attachment to a fragment of the DCBM scaffold (**Figure 79 D**) .
ARI-Davos 321075	**DCBM**	- Granulocytes and macrophages infiltration inside the osteotomy site **(Figure 80 A)** **-** Subperiosteal ossification around the osteotomy sites **(Figure 80 B)**
Cambridge-UK M00714530 (3864)	**TCP**	New bone formation in the interosseous space and mesenchymal cells migration towards the TCP particles (**Figure 81**)
Cambridge-UK M00714492 (3870)	**PCL**	Aside from fibrosis no further changes were observed
Cambridge-UK M00714483 (3854)	**PCL**	The most characteristic feature was what we can describe as chondrogenic osteogenesis inside the osteotomy site, where chondrocytes like cells, mesenchymal cells and osteoblast like cells were coexistent (**see Figure 82)**

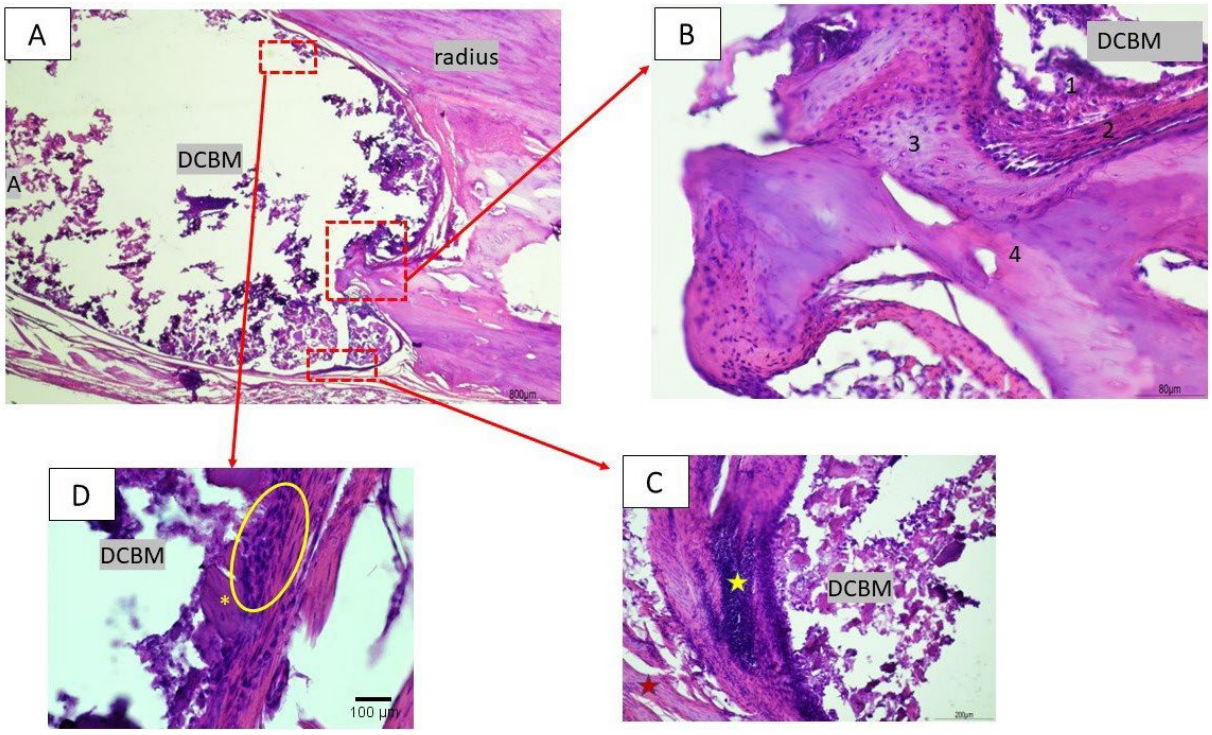


Figure 79: H&E stained decalcified bone section corresponding to specimen ID: Cambridge M00714493 (3744) - DCBM (culled at week 12 postoperatively due to implant displacement).

A- x4 focus at the level of proximal osteotomy

B- x20 focus on the area of bone ingrowth showing layers of cells at different stages of differentiation: Mesenchymal cells (1) osteoblast like cells (2) newly formed bone (less organised) (3) mature bone (more organised) (4).

C- x20 focus on area of lymphocytic infiltration (yellow star)- fibrous layer (red star).

D-Mesenchymal cells (yellow oval) adhered to a fragment from the DCBM scaffold (yellow asterisk).

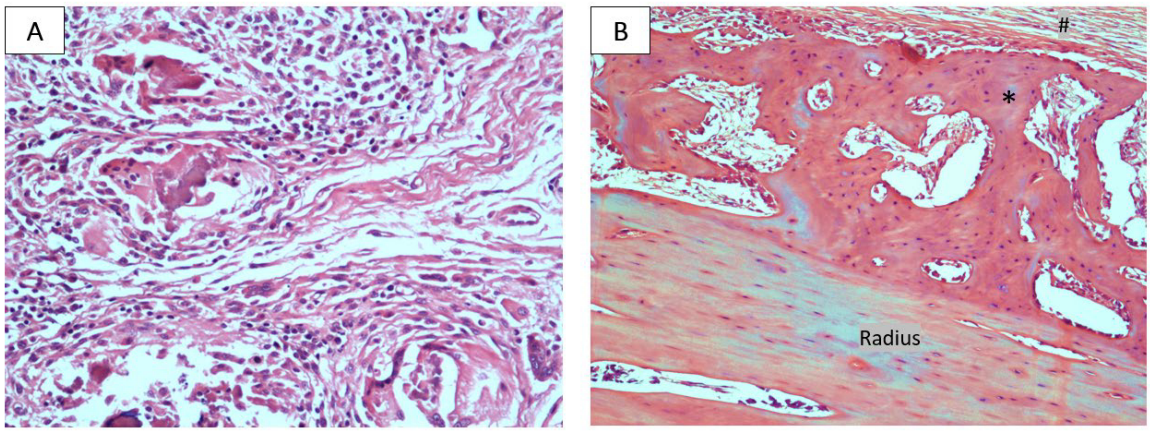


Figure 80: H&E stained decalcified bone section corresponding to specimen ID: ARI-321075 - DCBM (culled at 1 week postoperatively due to implant displacement).

A- granulocytes and macrophages infiltration inside the osteotomy site

B- Subperiosteal ossification around the osteotomy site. Newly formed woven bone (*). Fibrous tissue layer #.

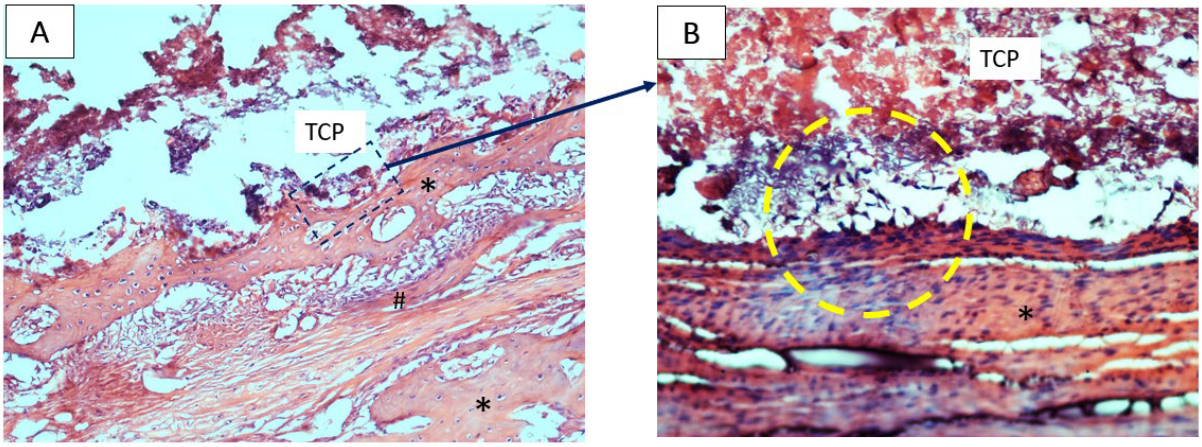


Figure 81: H&E stained decalcified bone section from corresponding to Specimen ID: Cambridge- M00714530 (3864) - TCP (culled at 6 weeks postoperatively due wound complications).

A- New bone formation (*) and fibrosis (#) in the interosseous space posterior to the TCP scaffold.

B- Focus on the material/new bone interface (x20) showing mesenchymal cells migration toward the TCP particles.

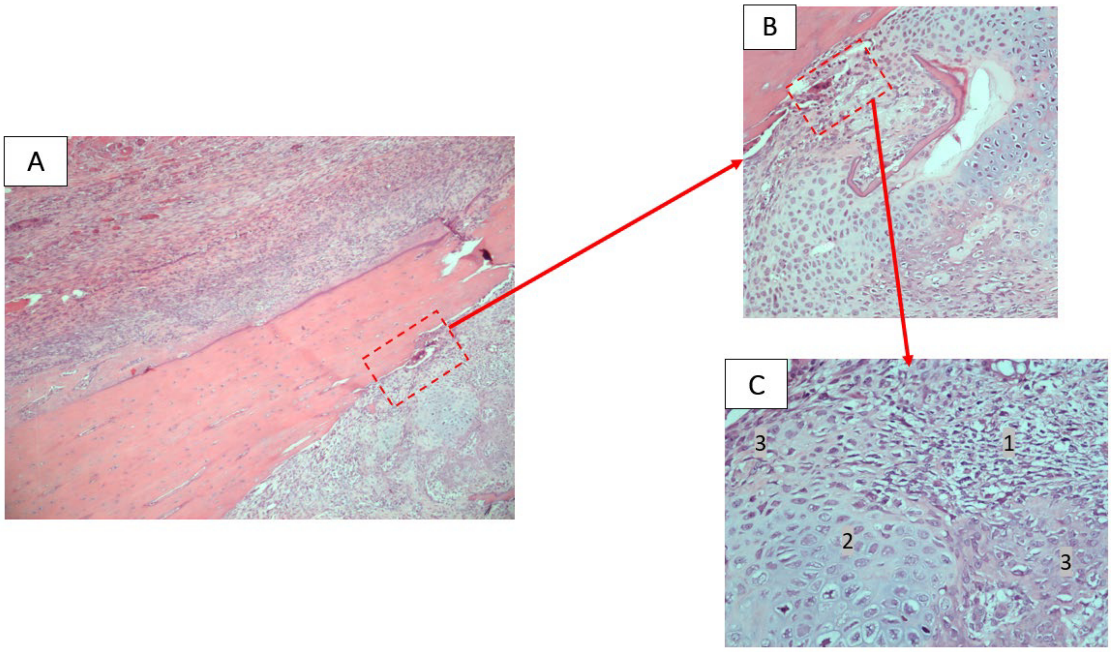


Figure 82: H&E stained decalcified bone section corresponding to specimen ID: Cambridge-M00714483 (3854) -PCL (culled at 12 weeks postoperatively due implant displacement).

A- Bone ingrowth x4

B- Features of chondrogenic osteogenesis x10

C- The 3 distinct cell populations: mesenchymal cells (1), chondrocytes like cells (2), Osteoblast like cells (3)- x20.

4.5.2.b: Micro-CT

Quantifying the volume of newly formed bone was challenging in the post-mortem micro-CT scans due to the absence of reference scans from each animal at the time of surgery and/or of an empty untreated bone defect group. Yet, the CT- images as well as the reconstructed 3D models from each scan/rabbit provided valuable supportive details about the structural changes of the bone/implant construct 12 weeks after surgery.

In both the DCBM and TCP groups, there was newly formed bone around the proximal and distal osteotomy sites. New bone in the interosseous space between radius and ulna was detectable in the scans from the 3 material groups: DCBM (moderate), TCP group (slight) and the PCL group (significant). Due to the radiolucency of PCL, it was feasible to see the changes inside the bone defect area, newly formed bone was evident particularly at the level of distal osteotomy as well as sporadic bone in-growth in the defect area (**see Figures 83, 84 and 85**). Yet no full defect closure (bridging) was achieved in any of the material groups.

Osteointegration at the level of proximal osteotomy and bone in-growth were seen in the axial planes of the CT scans from the 3 material groups. Soft tissue-like in-growth within the scaffold's pores (most likely, fibrous tissue) was seen in the DCBM group, see **Figures 86, 87 and 88**.

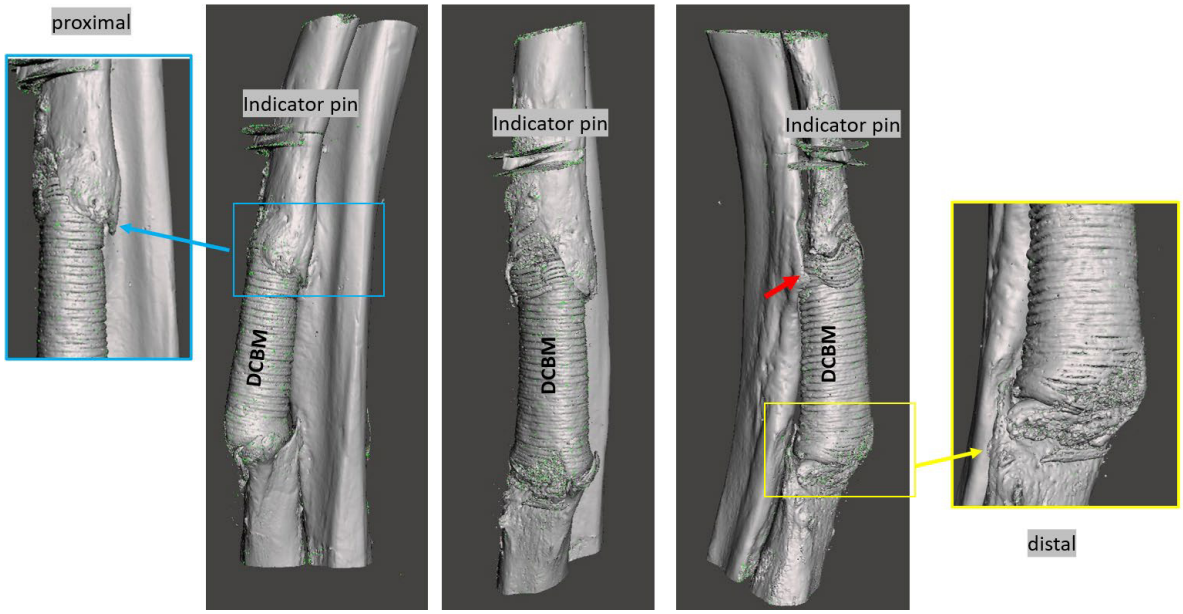


Figure 83: Representative reconstructed 3D models out of µ-CT scans of rabbit's antebrachium from the DCBM group (week 12 after surgery)- rabbit ID Cambridge- M00714491(3703)-DCBM).

Notice the new bone formation around the proximal osteotomy sites (blue rectangle), distal osteotomy site (yellow rectangle) and caudal to the implant (red arrow).

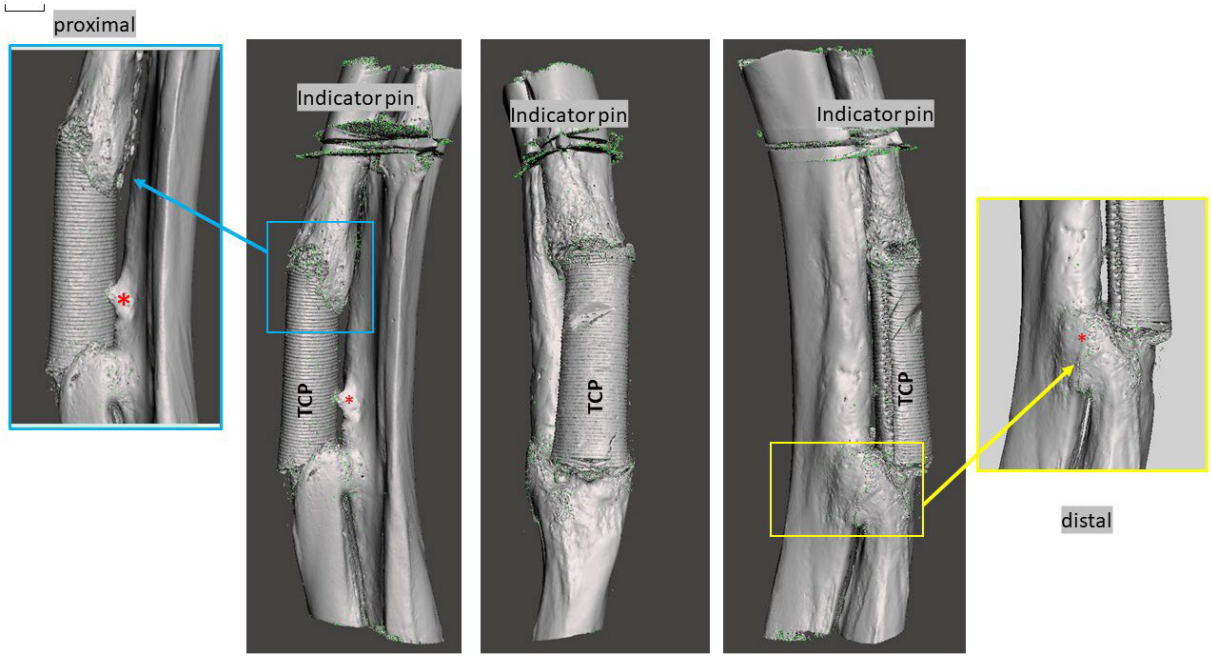


Figure 84: Representative reconstructed 3D models out of µ-CT scans from of rabbit's antebrachia from TCP group (week 12 after surgery)- post-mortem (week 12 after surgery)- rabbit ID (Cambridge – M00714485 (38537)-TCP).

showing:

- New bone formation around the proximal osteotomy sites (blue rectangle) and distal osteotomy site (yellow rectangle).
- New bone in the interosseous space between radius and ulna (red asterisk)

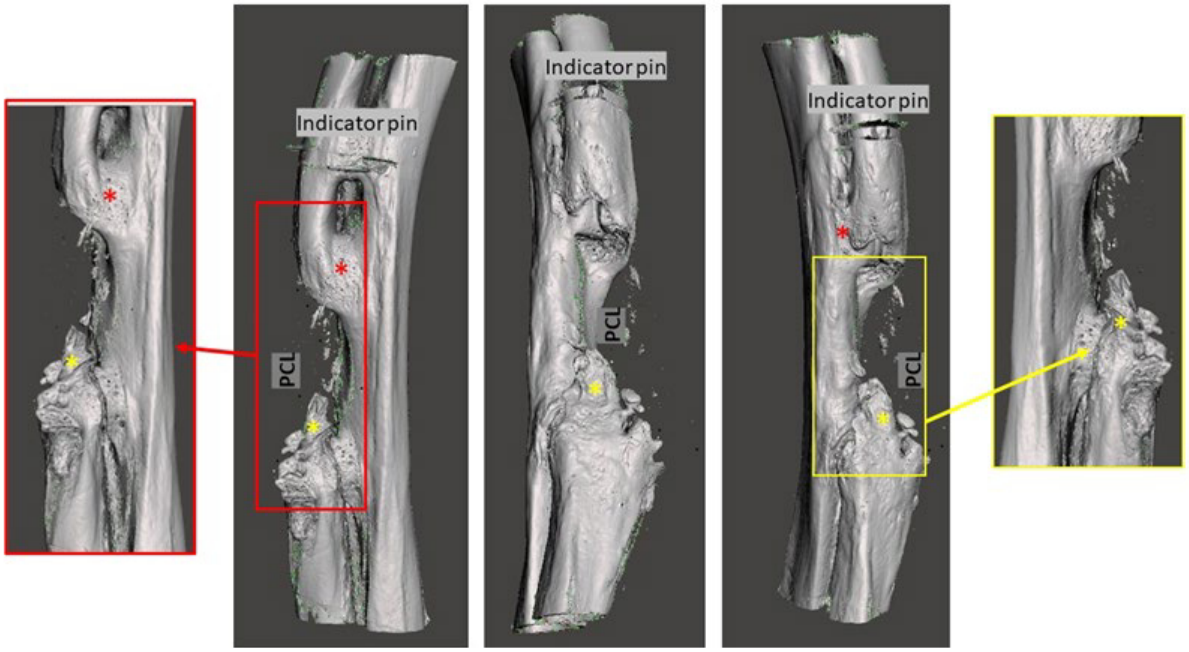


Figure 85: Representative reconstructed 3D models out of µ-CT scans from of rabbit's antebrachia from the PCL group, post-mortem (week 12 after surgery)- rabbit ID (Cambridge-M00714490 (3849)-PCL).

Due to the radiolucency of PCL, it was feasible to see the changes inside the bone defect area. Newly formed bone was evident particularly at the level of the distal osteotomy (yellow asterisk). In addition, there was significant new bone in the interosseous space between the radius and ulna (red asterisk).

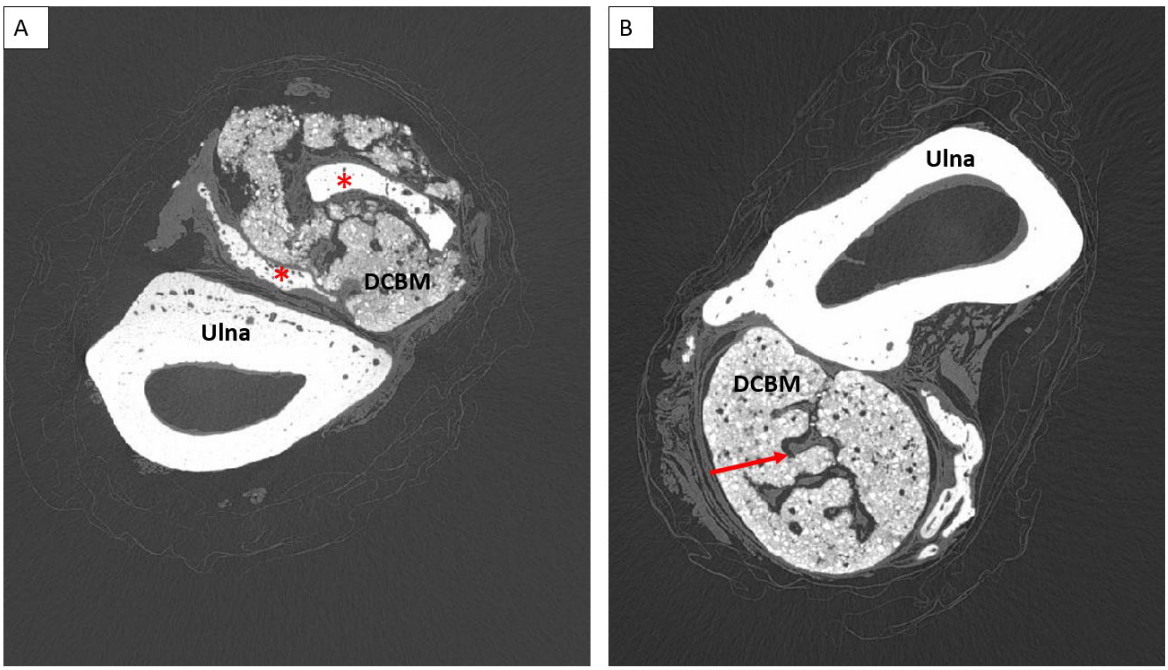


Figure 86: Axial plane micro-CT slices (rabbit ID-Cambridge- M00714531(3833)-DCBM group) showing: A) osteointegration at the level of proximal osteotomy (asterisk). B) soft tissue-like ingrowth within the scaffold's pores (most likely, fibrous tissue).

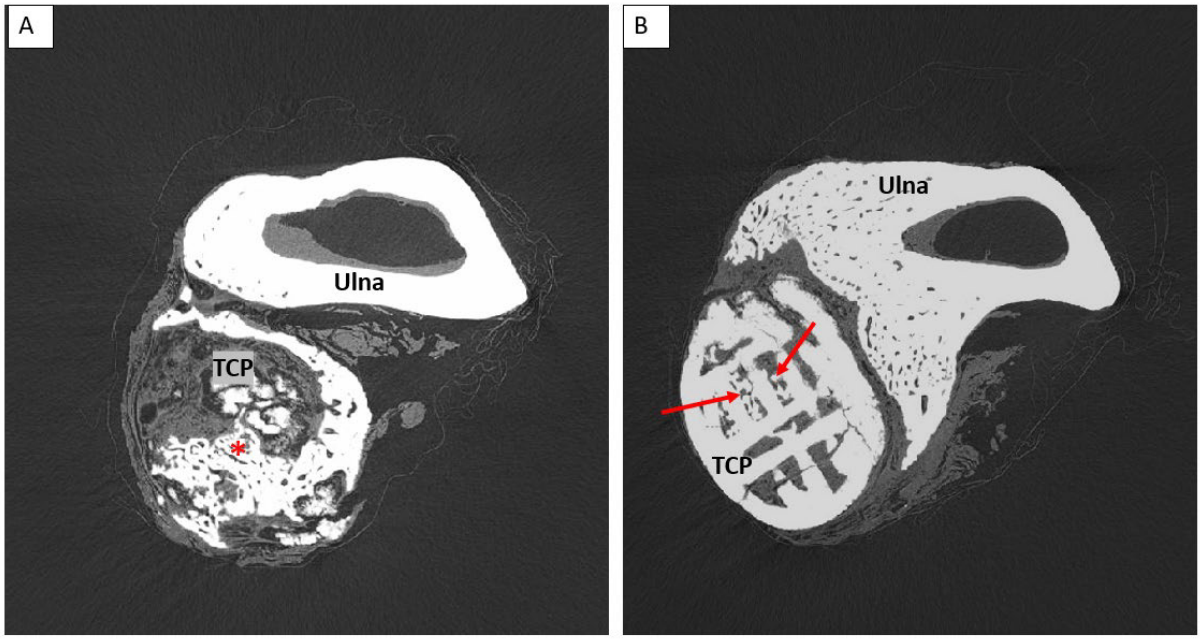


Figure 87: Axial plane micro-CT slices (rabbit ID-Cambridge- M00714532 (3743)-TCP group) showing: A) osteointegration at the level of proximal osteotomy (asterisk). B) bone ingrowth within the scaffold's pores.

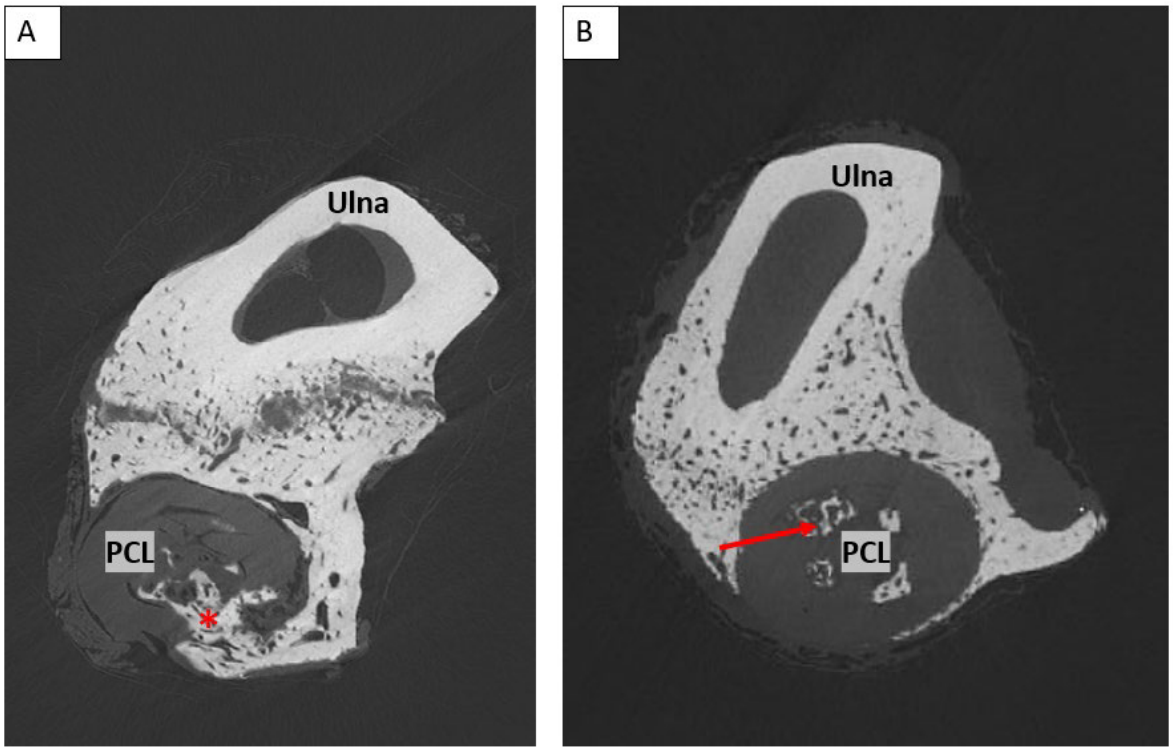


Figure 88: Axial plane micro-CT slices (rabbit ID-Cambridge- M00714490 (3849)-PCL group) showing: A) osteointegration at the level of proximal osteotomy (asterisk). B) bone ingrowth within the scaffold's pores.

Chapter 5: Discussion

5- Discussion

Non-healing and critical size bone defects represent a challenge in the fields of orthopaedics, cranio-maxillofacial and spine surgeries. The tissue engineering-themed approach for repair holds tremendous potential in offering a solution to the millions of patients (human and animals) who struggle with these bone defects secondary to trauma, cancer, infection, or congenital abnormalities; however, there is an undeniable gap between research and the clinic. Thousands of papers are published each year highlighting new perspectives or offering new therapies or implantable devices, yet relatively few new therapies or implants have reached the clinic. Significant cost and regulatory challenges are the main reasons hindering the transition from bench to bed (lab to clinic). The goal of my work was to use tissue engineering as a tool to develop and characterise bone graft substitute biomaterials that can support bone healing for load-bearing critical size bone defects that can be customised to the specific needs of the patient. I am aware that the work in this thesis is nothing but a first step towards the final goal and that further research and regulatory approvals are necessary before moving to clinical application.

The work included in this thesis relies on five main pillars that support the main goal, namely:

1) Cell work: isolation and characterisation of Ad-MSCs.

2) An *in vitro* extracorporeal shockwave therapy (ESWT) preliminary trial: investigating the effect of ESWT on Ad-MSC proliferation and differentiation.

3) Bio-material synthesis: scaffold fabrication, 3D printing and *in vitro* characterisation.

4) *In vivo* biocompatibility testing: rat subcutaneous implantation model

5) *In vivo* bone defect repair evaluation: rabbit radius segmental bone defect study.

In this section, we will discuss the findings from each of these themes.

5.1- Adipose derived mesenchymal stem cells (Ad-MSCs) characterisation:

5.1.I-Ad-MSCs defining criteria:

In the cell characterisation experiments, I aimed to confirm that the cells I isolated from adipose tissue met the defining criteria of mesenchymal stem (stromal) cells (MSCs). My findings were well aligned with the international society for cellular therapy (ISCT) guidelines on the minimal criteria for defining multipotent mesenchymal stromal cells [445], including the fibroblastic morphology with thin parallel beta-actin fibrils extending across the cellular cytoplasm visible after immunofluorescent staining [733], adherence to tissue culture plastic, tendency to grow in colonies, self-renewal (proliferation) and migration abilities. In addition, they showed the ability to differentiate into multiple cell lineages as well as exhibiting specific immunophenotypic characteristics (namely: positive expression of CD105, CD73, CD44 and CD90, and lacked expression of CD45, CD34, CD14 [446, 447, 449]). Bearing in mind that the ISCT guidelines were established to identify human MSCs (particularly bone marrow-derived MSCs), tissue of origin and inter-species differences must be accounted for, particularly when it comes to surface marker expression [734]. The MSCs isolated from ovine, rabbit and rat adipose tissue matched the required criteria in relation to morphology, behaviour in culture and multipotentiality. However, the immunophenotypic characteristics were variable in cells isolated from the different species. For instance, the ovine Ad-MSCs weakly expressed CD90 and CD73. The weak and even lack of CD90 expression in ovine Ad-MSCs has been described previously by Boxall et al. (2012) and Rozemuller et al. (2010) [450, 451] and negative CD73 expression in ovine MSCs was reported by Martınez-Lorenzo et al. (2009) [734]. Khan et al. (2016) reported 96.9 ± 5.9 % cross-reactivity of rat anti-mouse CD73 (TY/23) antibody to ovine CD73, yet there is a possibility that the weak CD73 expression could be attributed to poor cross reactivity to the anti-mouse antibody. The rabbit Ad-MSCs were CD105 and CD73 negative, which is consistent with the findings of Lee et al. (2014) [735] and Martınez-Lorenzo et al. (2009) [734], although Zomer et al. (2018) [736] reported cross reactivity between the mouse anti-human CD73 (AD2) and CD105 (MEM-226) antibodies and rabbit CD73 and CD105, again it is possible that negative expression of these markers was due to the lack of cross-reactivity. Finally, the negative expression of CD44, CD105 and CD73 on rat Ad-MSCs is in line with the findings of Bayati et al. (2013), Ranera et al. (2011), Lee et al. (2017) and Li et al. (2021) [737-740]. However, I believe that testing different antibody panels (and validating inter-

species antibodies reactivity) is something that needs further investigation in future work, not only for rat Ad-MSCs but also for the other species as well, particularly as species specific antibodies are not as widely available for MSCs isolated from animal tissues as they are for human (and to some extent rodent) MSCs.

Other methods that could be used for MSC immunophenotyping based on marker expression and/or to prove that negative marker expression was truly due to lack of cross reactivity, could include RT-PCR analysis or western-blotting to screen for the target surface markers [741, 742].

The results from the MSCs characterisation assays confirm that the cells we isolated from adipose tissue are multipotent mesenchymal stem cells and these cells meet the minimal criteria for defining multipotent mesenchymal stromal cells. Particularly based on the cells' ability to self-renew and to differentiate towards multiple lineages (osteogenic, chondrogenic and adipogenic lineages), which are considered distinctive criteria of MSCs [743].

5.1.II- Ad-MSCs Differentiation towards osteogenic lineage:

In this set of experiments, I was not only aiming to confirm whether Ad-MSCs can differentiate towards the osteogenic lineage (which has already been established as a part of the tri-lineage differentiation assays) but also to investigate the biochemical, molecular, and morphological cues during the different stages of differentiation towards this lineage (given that my work focuses on bone healing). The results from the osteogenic differentiation assays of MSCs isolated from 3 species (ovine, rabbit and rat) reflected a distinguishable pattern (or sequence of events). Alkaline phosphatase (ALP), RUNX-2, Collagen I (Col-I), osteonectin (ON), and, to a lesser extent, osteopontin (OPN) are considered early osteogenesis markers, having a role in the matrix maturation phase. In contrast, osteocalcin (OC), positive calcium binding staining (such as alizarin red stain) are late osteogenesis (matrix mineralisation) markers. To the best of my knowledge, there is very little available literature on the chronology of molecular and cellular events in Ad-MSC differentiation towards the osteogenic lineage; most of the published data are related to identifying the ability of the MSCs to differentiate towards the osteogenic lineage rather than what happens at different stages of MSC osteogenic differentiation. The early (proliferation and matrix maturation) vs. late (matrix maturation) osteogenesis marker-related research is predominantly done using osteoblasts [469, 472, 744, 745]. Regarding the fluctuation of osteogenesis marker gene expression at different time points, I have observed that the onset as well as the amplitude of change in rat and rabbit Ad-MSCs started earlier (at day 7 vs. at day 14) and had much higher

values than in ovine MSCs (as explained in **Figure 44, 45 and 46 and Table 39** in the results section).

Understanding the temporal sequence of the osteogenesis molecular cues and biomarkers can be used as a template to better understand the molecular profile of fracture non-union [746, 747] and other bone diseases such as osteoporosis [748] and osteogenesis imperfecta [749]. This could offer a valuable tool to develop novel gene therapies [750, 751] or genetically engineered animal models for preclinical studies [752].

5.2-The effect of extracorporeal shockwaves (ESW) on MSCs proliferation and differentiation

The choice of the ESWT type and setting in the first set of experiments was based on the lowest and the highest available setting in the DUOLITH® VET shockwave machine (Storz Medical, Tägerwilen, Switzerland). Yet, I elected to proceed with only focused ESWT in the second set of experemints as it was the agreed upon setting for clinical use. Although there available guideline by the National Institute for Health and Care Excellence (NICE) published guidelines on the use of Extracorporeal shockwave therapy for refractory plantar fasciitis, refractory Achilles tendinopathy and refractory tennis elbow [586-588]. However, the published literature on the topic using ESWT to treat musculoskeletal disorders still needs further validation.

5.2.1-The effect of focused vs radial ESW on Ad-MSCs (direct application)

In the first instance, the data from this set of experiments suggest that focused ESW treatment had an initial boosting effect on MSC proliferation, yet at later time points, radial ESW treated MSCs seem to have higher proliferation rates. Neither focused nor radial ESW treatment had a significant effect on MSC osteogenic differentiation ability. Similar findings were reported by Raabe et al. (2013) and Weihs et al. (2014) [539, 753]. However, I cannot eliminate the possibility that these results were inconclusive due to the issue of shockwave phase shifting attributed to the difference in the acoustic impedance between air and culture media (as explained in literature review section 2.4.d). Hence, the second set of ESW related experiments in a water bath were designed.

5.2.2- The effect of focused ESW on Ad-MSCs (designed water bath *in vitro* testing apparatus):

In this set of experiments, I elected to use focused ESWT as it is the most clinically relevant for fracture non-union related applications [568, 570, 754]. Although, ESWT did not

negatively affect the Ad-MSC proliferation, it did not have a positive influence on it either. However, the highest tested frequency (0.55 mJ/mm2) promoted Ad-MSCs osteogenic differentiation as reflected by alizarin red staining quantification.

Either using direct application or in the water bath setting, trying to understand (and test) the effect of ESWT on tissue (such as bone) healing in *in vitro* settings has proven to be very challenging. Cells and cell culture are not reflective of the complexity of tissues where vascularisation, innervation and inter-cellular communication plays a huge role in how tissues (and organs) respond to biomechanical stimuli. Hence *in vivo* testing (either preclinical or clinical studies) will be more realistic and impactful to better understand and apply. Due to budget and time restrictions, I could not include testing the effect of ESW on bone healing in my *in vivo* preclinical study, yet it is something to be considered as future work, particularly as ESWT to promote bone repair is included as a protocol in our Home Office animal (project) licence.

5.3- Bone graft substitute biomaterials (scaffolds) fabrication and *in vitro* characterisation:

5.3.1-Confirmation of donor cells elimination:

In this set of experiments, I was aiming to confirm the effectiveness of the decellularisation protocol I optimised to ensure elimination of the cellular components of the trabecular bone core I harvested from bovine femurs. As a rule of thumb, to indicate effective tissue decellularisation, the residual DNA content should be ≤ 50 ng/mg of decellularised tissue and upon histological examination, the tissue should not contain any visible nuclear material when stained with DAPI or H&E [266, 321, 755]. The results I obtained from DNA quantification and the histological evaluation conform to these pre-set criteria with a final DNA concentration of 2.46 ng/mg DCBM (and a 97.40 % reduction in DNA content in comparison to unprocessed bones) and cellular/nuclear clearing upon gross and histopathological evaluation.

Ensuring donor cell elimination is a crucial first step when working with modified xenografts and decellularised tissue matrices for biological safety and biological compatibility perspectives. No further testing or procedures can be carried out without ensuring proper elimination of the immunogenic donor cells first.

5.3.2- Mineralisation status

The decellularisation protocol I used included weak acid treatment (1.5 % peracetic acid) which was most likely the lead reason for the reduced calcium content in the decellularised bone (354.048 µg calcium/g) in comparison with untreated bone (724.20 µg calcium/g); a 51.11 % reduction. Although the calcium content was reduced, the final product was not completely demineralised. Hence, it iss important not to confuse decellularised bone matrix (DCBM) with demineralised bone matrix (DMBM), which is a different category of bone graft substitute, typically prepared from allogeneic bone rather than xenogeneic bone [756].

5.3.3-Cytocompatibility:

Cytocompatibility (or lack of cytotoxicity) testing is essential in a biomaterial's biosafety evaluation, and so, suitability for implantation [592]. Regarding DCBM (or decellularised tissue matrices in general), cytotoxicity can be induced by the biomaterial and residual chemical reagents and/or enzymes used during tissue decellularisation. For the 3D printed scaffolds, in addition to the biomaterial, the solvents used during bioink formulation can also be a source of cytotoxicity. Hence, the importance of validating the scaffold's cytocompatibility.

PCL is an FDA-approved biodegradable polymer [289] and it represents 15 % of the composition of my positive control (TCP) as well as the test (DCBM) scaffolds, hence I elected to use it as a negative (non-cytotoxic) control. Neither the DCBM nor TCP scaffold had any adverse effect on Ad-MSC proliferation or viability as reflected by the MTT cell viability assay, which was a first step in the pathway of testing/proving the scaffold's biosafety.

5.3.4 - Osteoinductivity:

Given that my application of interest in this study is bone healing, an assessment of the tested scaffold's capability to support MSC differentiation towards the osteogenic lineage was a logical step. Upregulation of osteogenesis marker genes (RUNX-2, osteopontin (OPN), collagen I (COLI), and to a lesser extent alkaline phosphatase (ALP) in Ad-MSCs seeded with DCBM (even in the absence of osteogenic DM) is a strong indicator that DCBM scaffolds have the essential microstructural and molecular cues to induce and support MSC osteogenic differentiation and that is a strong indicator of anticipated *in vivo* osteoinductivity via recruitment, proliferation, and differentiation of host immature stem cells (MSCs) [17]. The fact that the markers above are indicators of early stages of osteogenesis (matrix maturation), in addition to the absence of osteocalcin (OC) upregulation, which is a late

osteogenesis marker (matrix mineralisation) suggested that the DCBM scaffolds did encourage MSC osteogenic differentiation, but this was more or less restricted to the early stages of osteogenesis without further progression to late osteogenesis (during the length of the experiment, 21 days). Trying to link these findings to the findings from the *in vivo* bone defect study might explain why the newly formed bone seen around the DCBM scaffolds in the histology sections and in 3D models from μ-CT scans had a mostly disorganised (woven) appearance. However it may also reflect the length of the *in vivo* experiment (12 weeks); longer time points might produce different findings.

The same observations apply to the TCP scaffolds as the cells within them only induced RUNX-2 and COLI upregulation.

The positive Alizarin red staining that was seen in cdlls is most likely attributed to the native calcium content in the DCBM and TCP scaffolds.

5.3.5- Microstructure:

The images from SEM reflected the unique topography of each group's material. DCBM and TCP scaffolds had more complexity in their topographical (and micro-structural) features compared to PCL scaffolds, particularly the surface roughness macro and micro-porosities, which were lacking in PCL. Pore size (or trabecular spacing) was the most prominent difference between PCL and the other scaffolds (DCBM and TCP), with significantly larger pore size in the case of PCL.

Scaffold porosity and pore size relate to the surface area available for the adhesion and growth of cells both *in vitro* as well as *in vivo* and to the potential for host tissue in-growth [687]. High porosity encourages osteointegration, neovascularisation, better nutrient and oxygen exchange [688, 689]. However, there is a trade-off between porosity and the scaffold's mechanical properties (moduli) [690, 691]. Pores smaller than 100 μm in diameter were found to restrict vascular penetration. Interestingly, these results correlate well with the diameter of the physiological Haversian systems in bone tissue that possess an approximate diameter of more than 100 μm [687, 692]. Pores and pore inter-connections >300 μm in diameter were found to allow sufficient vascularisation [689]; a pore size of around 500 – 600 μm is ideal for osteointegration [693]. In addition to pore size, the shape of those pores also plays a role in determining the scaffold properties; for example research has shown that circular pores of around 500 μm lead to superior cell adhesion [694].

According to the findings of Torres et al. (2014 and 2015), Xiao et al. (2020) and Salehi et al. (2020) [757-760], the scaffold's surface roughness has a strong influence on the osteogenic response; it favours cell attachment, proliferation, and osteogenic differentiation [695, 696]. A rough scaffold surface not only provides a wider growth space to accommodate more cells but also allows the scaffold to absorb more water and expose more protein adsorption sites, thus promoting cell attachment and proliferation [686].

Despite printing all the scaffolds from the same original CAD design using the same G-code and printing parameters, the final 3D printed product of the scaffolds demonstrated variability within the same material group and between the different material groups, which exemplifies on the challenge of reproducibility (and consistency) when using 3D printing as a material/scaffold manufacturing method. Despite the profound advantages of using 3D printing technologies in manufacturing implantable medical devices, particularly with the versatility of biomaterials that can be 3D printed and the customisability of the 3D printed implants to be tailored to each patient's individual needs, the biggest drawback of 3D printable implants is the poor reproducibility between different print batches even when using the exact same print settings/parameters. This is a point of further investigation and a portal to further collaboration with bioengineers and material scientists to understand better why this occurs and predict the deviation of the 3D printed object from the initial design.

5.3.6- Biomechanical properties:

In addition to the limited anatomical customisability, one of the main reasons I elected not to use intact decellularised bone cores without further processing (such as milling then 3D printing) is the significant variability of bone material and mechanical properties based on the anatomical location where the bone is harvested from even within the same bone from the same individual [48, 761] (the microstructure data from intact DCBM bone cores in comparison to unprocessed bone cores demonstrating the high standard deviation values are summarised in appendix 6).

The 3D printed scaffolds showed more uniform bio-mechanical (and material) properties. The plain PCL scaffolds had undeniably superior mechanical properties compared to the DCBM and TCP-based scaffolds. But this has to be balanced with the osteoinductive properties offered by the DCBM and/or bioceramics (such as TCP) with the mechanical robustness provided by the polymeric component without compromising printability. In other words, adding PCL to the DCBM (or TCP) scaffolds improves the scaffold's mechanical properties, while adding bioceramics or DCBM to the PCL scaffolds improves the scaffold's

osteoinductivity. In my study, I used a 15 % PCL:85 % DCBM or TCP composition formula. Nyberg et al. (2017) [12] reported similar findings relating to the mechanical properties in 3D printed 30 % DCBM:70 % PCL scaffolds. Contrary to my (and Nyberg's) findings, Freeman et al. (2019) [20] reported improved mechanical properties by adding DCBM to a PCL scaffold.

5.4- Testing the local biological effect of the selected biomaterials (scaffolds) after implantation (rat subcutaneous implantation preclinical model):

The aim of this study was to evaluate the biomaterial biocompatibility upon *in vivo* implantation as a step prior to implantation into a bone defect. I elected to use a rat preclinical subcutaneous implantation model to evaluate our scaffold's local biological effect after implantation (the material / tissue interaction). This preclinical model is recommended by the ISO 10993-6 and ISO 10993-1 guidelines as well as ASTM F981 guidelines [589, 592, 594], and it has a well-established publication record [762-764].

The histopathological evaluation of the material/tissue interaction (local biological effect) indicated that the materials from the 3 groups (DCBM, TCP and PCL) induced slight bio-irritation at 4 weeks and 8 weeks after implantation which reflects the material's safety for implantation as advised by the ISO 10993- 6 guideline "Biological Evaluation of Medical Devices - Part 6: Tests for local effects after implantation" [589]

In regard to the materials' biodegradation, DCBM and TCP showed more signs of biodegradation (particularly surface erosion and fragmentation) than PCL. However, bear in mind that the DCBM and TCP scaffolds underwent decalcification during histology processing and that is most likely the reason behind fragmentation rather than actual biodegradation (later on, the scaffold intactness seen in the undecalcified bone sections from the rabbit bone defect study also supports this reasoning). Sectioning the wax embedded DCBM and TCP scaffolds was not possible without decalcifying them first as it would have damaged the microtome blades.

Giant cell and macrophage infiltration was more prominent in the DCBM and TCP groups than in the PCL group, which may be the cause of calcium phosphate containing biomaterial surface erosion and remodelling through a combination of surface dissolution, fragmentation as well as cell-mediated phagocytosis, in a process similar to natural bone remodelling [765] while polymers degrade via hydrolysis in the first instance before phagocytosis takes place to remove residual fragments [766].

5.5- Evaluation of the ability to support bone healing in a critical size segmental long bone defect:

The aim of this study was to test the scaffolds' ability to promote bone healing upon implantation in critical size bone defects. The preclinical model of choice was a 15 mm long, segmental defect in rabbit radii.

Rabbit is considered a transitional preclinical model bridging the gap between the small animal models (rodents) and large animal models (small ruminants, pigs, dogs or even primates). The ease of management, the reasonable housing cost in comparison to large animal models and the similarity to veterinary patients (small dogs, cats and pet rabbits) make rabbit an appealing preclinical model particularly in proof-of-concept studies like mine.

I chose a segmental radial defect that is a load-bearing bone defect as the preclinical model to evaluate the performance of my scaffolds (instead of a femoral defect for instance), as it does not necessitate using fixation devices (e.g. pins or plates) due to the support of the adjacent ulna. This makes it relatively simple, less expensive, less risky, more refined from an animal experience perspective, and it has a well-established publication record [599, 612, 613]. In addition, I had previous experience working with a similar animal model with our collaborators at the AO Research Institute (ARI)-Davos, Switzerland.

Choosing a 15 mm long segmental radial defect ensured that the bone defect met the criteria of a critical size bone defect, which is defined in the literature as a bone defect with a length 1–2 cm and greater than 50 % loss of the bone circumference [170, 172, 173], or where the length of the defect is 2 – 3 times the bone diameter [174]. Based on the measurements from the CT scans I obtained from cadaveric rabbits while planning for the study, the mid-diaphyseal diameter of a rabbit's radius ranges from 3.5 - 5 mm, hence a 15 mm long defect meets the criteria above.

The choice of a 12 week experimental timeline was inspired by the FDA definition of a non-healing bone defect as a fracture that has not shown radiographic signs of progression toward healing for three consecutive months and occurred a minimum of nine months previously [88, 89]. Other definitions indicated that the nine months since injury criterion cannot be used for every fracture and recommended that fracture non-union of long bones be recognised after a minimum of six months without any improvement toward union [17, 90]. However, due to budget and timing limitations, I could not extend the experimental duration for 6 - 9 months.

5.5.1-In-Life animal outcomes:

Based on the intraoperative handleability and the follow-up radiographs, we can conclude that TCP scaffolds were the most fragile and required careful handling during implantation, while DCBM scaffolds were more compressive during implantation and more prone to displacement and finally the PCL scaffolds were more rigid and slippery during implantation, and its radiolucency made new bone formation easier to detect on radiographs.

We believe that the foot wounds that led to unexpected animal culling was attributed to the rabbit's housing environment and not related to the surgical procedure itself. The rabbits operated on in Cambridge were individually housed in hay lined, floor pens with wire separators, hence any minor wounds could easily be contaminated by the rabbit's excreta leading to infection and further complications.

5.5.2-Post-mortem outcomes:

The ideal scaffold should achieve osteointegration with the native host bone and have osteoinductive and osteoconductive properties. Based on the findings of the histological evaluation and the micro-CT scans, I can conclude the following: DCBM scaffolds had superior osteoinductive properties (as reflected by new bone formation around the scaffold, i.e. in the interosseous space, plus periosteal ossification); yet it only had limited osteointegration (at the level of proximal osteotomy) and poor osteoconduction as reflected by poor bone in-growth. The TCP scaffolds had moderate osteoinductive properties, moderate osteointegration and limited osteoconduction. Finally, PCL scaffolds had the strongest osteoconduction and moderate osteointegration and osteoinduction. One might conclude that the larger pores of PCL scaffolds (as demonstrated in the microstructure characterisation section 4.3.I.5 and discussed in section 5.3.5) are the reason for superior osteoconduction. The compressive nature of DCBM might lead to structural deformation after implantation, hence pore obliteration, leading to diminished osteoconduction.

Based on the data from fluorochrome quantification, the amount of newly formed bone at week 6 post-implantation (as reflected by the Xylenol orange % area) was significantly higher than the amount of newly formed bone at week 3 post-implantation (as reflected by calcein green % area) in the DCBM and TCP groups but the difference was not significant in the PCL group.

On a different yet related note, the reason I chose yellow, magenta and cyan as colour codes for the fluorochromes instead of green, red and blue is to make my figures accessible to readers with colour blindness.

None of the material groups resulted in complete defect bridging within the 12 week experimental period. In **Figures 76 to 78,** representing the undecalcified bone sections from the 3 material groups, the newly formed bone was predominantly seen at the level of the osteotomy sites and around the implant in the interosseous space (caudal to the implant) and periosteal ossification (cranial to the implant). The characteristic disorganised (woven) appearance of this newly formed bone is indicative of under mineralisation and rapid osteoid (matrix) production by osteoblasts [767, 768] which might be linked to the gene expression pattern of the osteogenic markers (see section 5.3.4 above).

The presence of newly formed bone and mature side by side in the interosseous space suggests bone formation by direct ossification in this area of the implant/bone interface. This is supported by the findings from the decalcified bone histology sections (**Figure 81**) where a layer of MSCs was seen adjacent to the newly formed bone. Bone surface abrasion of the ulna during the surgical procedure and the presence of the osteoinductive/osteoconductive scaffold anterior to it might explain the new bone formation in the interosseous space.

The lymphocytic infiltration seen in 4 of the undecalcified bone sections (and one of the early-culled decalcified sections) of the DCBM group might be an indication of an adaptive immune response, which was believed to be associated with implant failure of metal-on-metal (MoM) joint implants as a result of aseptic loosening [769-771]. One publication supported this by explaining the role of lymphocytes in the pathogenesis of aseptic osteolysis. Activated lymphocytes release powerful cytokines such as IL-2 (interleukin-2), IFN-γ (interferon-gamma), and RANKL (receptor activator of NF-κB ligand), which can, directly and indirectly, promote osteoclast activity and inhibit osteoblast activity leading to peri-implant osteolysis [772]. This is a concerning finding given that it was reported in 50 % of the rabbits in this group and it was concurrent with lack of osteointegration. However, further studies with later timepoints and larger group sizes (n) are needed for a definitive conclusion.

Despite the unplanned culling being considered an unwelcomed complication, sending the specimens from these rabbits for decalcified histology processing and sectioning gave me valuable information about the cellular details of the areas of the newly formed bones. For instance, in the results section **in Figure 79 (B),** I could see cells at different differentiation stages transitioning from mesenchymal cells to osteoblasts and osteocyte-like cells in a process similar to intramembranous (direct) ossification [773, 774]. On the contrary, in **Figure 82** specimen ID (Cambridge- M00714483 (3854) -PCL), culled at 12 weeks post-operatively due to implant displacement, showed features of endochondral (indirect)

ossification. This is consistent with the fact that I did not use rigid internal fixation to stabilise the osteotomy fragments, in addition to the interfragmentary movement, which encourages endochondral ossification pathway [49, 63]. In **Figure 80**, the sub-periosteal ossification can be attributed to a healing process similar to the one that follows a Masquelet induced membrane technique for treating bone defects, where a periosteum-like membrane around the cement spacer is formed [209-212]. However, in the Masquelet technique, the cement spacer has no osteoinductive or osteoconductive properties, and it needs to be removed, followed by filling the bone gap with bone graft. This is not the case for my scaffolds; the newly formed bone (as early as one-week post-implantation) was surrounded by a periosteum-like membrane which is attributed to the osteoinductive properties of the implanted DCBM scaffold. In **Figure 81**, there was new bone formation by direct (intramembranous) ossification in the interosseous space where the new bone formation occurs by direct differentiation of the MSCs to bone forming osteoblasts.

The role of interfragmentary strain (IFS) on bone healing should be taken into consideration. Direct fracture healing requires an inter-fragmentary gap of less than 0.01 mm and inter-fragmentary strain of less than 2 %. If direct healing criteria are not met, indirect fracture healing may occur at an inter-fragmentary strain of less than 10 % [49-54, 775]. Given that indirect (endochondral) healing was seen only in one rabbit that was culled from the study due to implant displacement, it can be assumed that the press-fit scaffold and the support of the adjacent ulna offered enough stability to achieve the biomechanical conditions needed for direct bone healing in the rest of the rabbits.

Future studies with earlier and later evaluation time points are needed for better follow-up and assessment of bone healing. As explained in section 2.1.2 (fracture healing), the endochondral ossification (indirect bone healing) is considered as a series of four sequential yet overlapping stages that involve a response of the periosteum and the surrounding soft tissues at the fracture site. These are inflammation (haematoma formation), soft callus (fibrocartilage) formation, hard callus formation and finally bone remodelling [44, 51]. Having multiple time points would allow me to track the healing progress and to identify the characteristic features of each of these stages. Li et al. [51] suggested that inflammation (peaks within 24 h - 7 days), soft callus (7 - 10 days), hard callus (14 days) and remodelling starts after 3 - 4 weeks and may take years to be completed. However, there are multiple factors (such as animal species, age, fracture type and location) that can influence the onset and duration of each healing stage.

We believe that a design modification of the scaffolds taking into account the antebrachium curvature will enable it to fit more ergonomically and be less likely to be displaced, and a higher porosity (or wider trabecular spacing) will render it more osteoconductive, yet care must be taken that larger pores might negatively affect cell attachment. On the same note, the promise behind 3D printed implants is to produce individually customised implants which are more relevant in a clinical situation; however, scanning each rabbit prior to surgery and designing individually fitted scaffolds/implants was not feasible during our preclinical study because of budget, timing, practical and logistical reasons, hence the standardised design based on scans from cadaveric specimens.

Due to budget and timeline related limitations, I elected to have only 3 experimental groups and one euthanasia time point. However, if these limitations were removed adding an empty defect group as a negative non-treated control would have been valuable in validating the animal model in the context of the critical sized/non-healing bone defect; given that critical size bone defects are defined as a bone defect that will not heal spontaneously (or shows less than 10 % bridging) within the lifetime of the animal (or by the end of the experiment) [33, 169-171]. Besides, an empty defect group would have served as a comparison template to determine the performance of each biomaterial group.

Chapter 6: Conclusion

6- Conclusion:

6.1-Adipose derived Mesenchymal Stem cells (Ad-MSCs) isolation and characterisation.

Based on the results from this section I can conclude the following:

- Adipose tissue is a reliable, easily obtainable source for MSCs isolation.
- Having pre-set guidelines for the minimal identifying criteria for MSCs is useful and essential, yet tissue source and inter-species differences must be taken into consideration.
- Ad-MSCs are capable of differentiation towards the osteogenic lineage with unique molecular markers that can be traced at different stages of differentiation.
- The availability, ease of isolation, the mesodermal origin and ability to differentiate towards osteogenic lineages make Ad-MSCs a good candidate for bone tissue engineering applications.

6.2- The effect of extracorporeal shockwaves (ESW) on MSCs proliferation and differentiation

- *In vitro* testing of the effect of ESW on Ad-MSC proliferation and osteogenic differentiation indicated that focused ESWT has a positive influence on MSC osteogenic differentiation. However *in vitro* tests have a limited ability to mimic natural tissue mechanical and physiological environments.
- Extracorporeal shockwave (ESW) is a promising minimally invasive therapeutic approach for fracture delayed union and non-union, yet more preclinical and clinical studies are needed to better understand the science behind the effect of ESW on tissues and to optimise the treatment dosage (i.e. which setting to be used) and frequency (i.e. number of treatment sessions and timing gap between sessions).

6.3- Scaffolds fabrication (3D printing) and *in vitro* characterisation

- Decellularised bovine bone matrix (DCBM) offers a near limitless supply for a safe, cost-reasonable biomaterial that can be used as a precursor for bone graft substitutes manufacturing.
- DCBM (and TCP) can be successfully formulated into a 3D printable bioink, which renders it a suitable candidate biomaterial for fabricating a customisable patient-specific, bone substitute for complex bone reconstruction surgeries.

- The cytotoxicity screening and osteoinductivity testing suggests that our scaffolds (DCBM, TCP and PCL) are cytocompatible and both DCBM and TCP based scaffolds are osteoinductive and capable of supporting Ad-MSC proliferation and differentiation towards the osteogenic lineage.
- The microstructure evaluation showed unique surface roughness and porosity in the DCBM and TCP groups. Yet, there was an undeniable variability in microstructure within the same material group and between the different groups, necessitating further research to better understand and predict the deviation of the 3D printed object from the initial design.
- The biomechanical testing suggests that both DCBM and TCP have acceptable biomechanical properties, but PCL had superior biomechanics, hence adding PCL to the osteoinductive bioceramics and DCBM may improve the final composite's mechanical properties (on the other side of the coin, adding DCBM and/or TCP to PCL improves the composite's osteoinductivity).

6.4 – *In vivo* biocompatibility testing: rat subcutaneous implantation model

- From the biocompatibility perspective and based on the slight bio-irritation scores from the 3 material groups at week 4 and week 8 post implantation, we concluded that our 3D printed scaffolds are safe for *in vivo* implantation.
- From bio-material behaviour perspective, I am aware that earlier and later time points might be needed to fully understand the materials behaviour in the body.
- Nevertheless, the results from this study were support moving forward to the next stage of *in vivo* testing to evaluate the material's performance in bone defect repair.

6.5- *In vivo* bone defect repair: rabbit radius segmental bone defect study.

- DCBM and TCP scaffolds are mostly osteoinductive, while plain PCL has superior osteoconductivity.
- The difference in scaffold microstructure (particularly pore size) is thought to be the major contributor towards the variable osteoconductivity.
- Newly formed bone was detectable at week 3 and week 6 after surgery as indicated by the bone fluorochrome labels.
- Design modification of the scaffold will render it more ergonomically fitting and less likely to be displaced (particularly the DCBM scaffold) and a higher porosity (or wider trabecular spacing) will render it more osteoconductive, yet care must be taken

that larger pores might negatively affect cell attachment and the scaffold's mechanical stability.

- A non-treated empty defect group or pre-implantation *in vivo* micro-CT scanning are needed as a reference for comparison of the post-mortem changes at week 12. However, that was not feasible due to budget limitations and the inaccessibility of the *in vivo* micro-CT scanner inside the animal facility where the rabbits were housed.
- Further studies with earlier and later time points are needed to better assess the changes of both the bone and the scaffolds over time, particularly as complete healing was not achieved in any of the groups by the end of the study.
- Further studies to evaluate the performance of cell (Ad-MSC) seeded scaffolds *in vivo* from biocompatibility as well as bone healing perspectives.
- A concern has been raised that the DCBM aseptic implant may loosen, based on the undecalcified bone histology finding (specifically lymphocytic infiltration and poor osteointegration).

6.6-Decision on hypotheses testing:

Based on the data from the *in vitro* and *in vivo* characterisation of the 3D printed scaffolds, we reject null hypotheses (H0) 1 and 2:

- *H0 #1*: 3D-printed bovine DCBM-based scaffolds are non-biocompatible and incapable capable of supporting bone repair through enhanced osteoconduction and/or osteoinduction.

Hence, we accept the first alternative hypothesis (Ha #1) "3D-printed bovine DCBM-based scaffolds are biocompatible and capable of supporting bone repair through enhanced osteoconduction and/or osteoinduction".

However, the decision regarding H0 #2 and Ha #2 is slightly more complicated:

- *H0 #2*: The *in vitro* and *in vivo* performance of DCBM-based scaffolds is inferior to that of control material (TCP or PCL).
- *Ha #2*: The *in vitro* and *in vivo* performance of DCBM-based scaffolds is equivalent or superior to that of control material (TCP or PCL)

It is challenging to give a yes or no answer based on the current findings. For instance, we can reject H0 #2 (and accept Ha #2) based on the findings from the *in vitro* testing and *in vivo* biocompatibility studies, but we can neither accept nor reject it for the bone defect healing

rabbit study as each of the materials had its pros and cons. There are also question because of the limitations associated with this study as explained in the discussion section.

Finally, we reject H0 #3 and 4 and accept Ha #3 and #4.

- Ha #3: MSCs isolated from adipose tissue (Ad-MSCs) are capable of differentiating towards osteogenic lineage.
- Ha #4: Extracorporeal shock wave therapy (ESWT) enhances bone healing through encouraging stem cells differentiation to osteoblast like cells.
- H0 #3: MSCs isolated from adipose tissue (Ad-MSCs) are incapable of differentiating towards osteogenic lineage.
- H0 #4: Extracorporeal shock wave therapy (ESWT) does not enhance bone healing.

6.7- Summary Statement:

The work included in my thesis covered a wide range of *in vitro* and *in vivo* experimental work alongside the relevant literature on the topics of bone healing, critical size bone defects and the tissue engineering approach to offer a solution for non-healing (critical size) bone defects.

The ultimate goal of my work is to develop and characterise a biomaterial that can act as a bone graft substitute, aiming to support bone healing for the millions of patients who suffer from extensive bone loss secondary to trauma, cancer resection or infected bone implants. With the uniqueness of each patient's individual needs in mind, the goal is to have an implant that can be tailored accordingly. Through multidisciplinary collaborations, I successfully manufactured porous 3D-printed customisable scaffolds made out of bovine DCBM. The performance of these scaffolds was compared against 3D printed TCP positive control scaffolds and PCL negative control ones.

To characterise the bone implants, I followed a systemic approach to understand the structure, biomechanical properties and osteoinductivity of these novel scaffolds and, above all, to ensure the materials' biosafety by using both *in vitro* and *in vivo* testing. This was done by ensuring cytocompatibility (with Ad-MSCs) and evaluating the scaffolds *in vivo* biocompatibility in a rat preclinical model, before moving forward towards testing these scaffolds as bone graft substitutes in a long bone critical size bone defect preclinical model (in my case, I elected to use a 15 mm segmental defect in rabbit radii).

The results of my work indicated that:

- Ad-MSCs are reliable to use for bone tissue engineering applications due to their self-renewability and ability to differentiate towards osteogenic lineage. However, species variation should be considered when characterising the isolated cells.
- DCBM, TCP and PCL are non-cytotoxic biomaterials while only DCBM and TCP were capable of supporting Ad-MSC osteogenic differentiation
- 3D printing has revolutionised orthopaedic implant manufacturing; however, there are concerns about its reproducibility.
- Adding TCP and DCBM to the printable bioink rendered the scaffolds more osteoinductive; however, adding PCL improved the scaffolds' mechanical properties.
- DCBM, TCP, and PCL scaffolds had slight bio-irritancy and biodegradability scores *in vivo* following the ISO 10993-6 guideline (at week 4 and week 8 post-implantation).
- High scaffold porosity encouraged osteointegration; however, there is a trade-off between porosity and the scaffold's mechanical properties (moduli)
- DCBM and TCP scaffolds are mostly osteoinductive, while plain PCL has superior osteoconductivity.
- Direct (intramembranous) bone healing took place whenever the implant/bone construct was stable. However, indirect (endochondral) healing was reported after implant displacement.
- A concern was raised regarding the possibility that the DCBM aseptic implant may loosen based on the non-decalcified bone histology finding (specifically lymphocytic infiltration and poor osteointegration).

However, given the study limitations (explained in the discussion and conclusion sections), further future studies with:

- Scaffold design modification (accounting for forearm curvature and larger pore size).
- Additional animal groups (such as empty control, autograft and cell seed scaffolds) group.
- Multiple time points (earlier and later than 12 weeks) and larger group size (n).

are needed in order to draw a more informed conclusion.

My study serves as a proof-of-concept (PoC) study, offering a valuable framework for further future research and securing regulatory approvals before proceeding to clinical application.

7-References

1. Andrew H Schmidt, *Autologous bone graft: Is it still the gold standard?* Injury, 2021. **52**: p. S18-S22.
2. Edward M Younger and Michael W Chapman, *Morbidity at bone graft donor sites.* J Orthop Trauma, 1989. **3**(3): p. 192-195.
3. James Wee and Gowreeson Thevendran, *The role of orthobiologics in foot and ankle surgery: allogenic bone grafts and bone graft substitutes.* EFORT open reviews, 2017. **2**(6): p. 272-280.
4. Rozalia Dimitriou, et al., *Complications following autologous bone graft harvesting from the iliac crest and using the RIA: a systematic review.* Injury, 2011. **42**: p. S3-S15.
5. Paul Baldwin, et al., *Autograft, allograft, and bone graft substitutes: clinical evidence and indications for use in the setting of orthopaedic trauma surgery.* Journal of orthopaedic trauma, 2019. **33**(4): p. 203-213.
6. Hoon-Sang Sohn and Jong-Keon Oh, *Review of bone graft and bone substitutes with an emphasis on fracture surgeries.* Biomaterials research, 2019. **23**(1): p. 1-7.
7. Douglas M Ehrler and Alexander R Vaccaro, *The use of allograft bone in lumbar spine surgery.* Clinical Orthopaedics and Related Research®, 2000. **371**: p. 38-45.
8. Ahmad Oryan, et al., *Bone regenerative medicine: classic options, novel strategies, and future directions.* Journal of orthopaedic surgery and research, 2014. **9**(1): p. 1-27.
9. LED Lighting Market Size, *Share & Trends Analysis Report by End-Use (Residential, Commercial), by Product (Lamps, Luminaires), by Application (Indoor, Outdoor), by Region, and Segment Forecasts, 2021–2028.* Fortune Business Insights: Maharashtra, India, 2021.
10. Global Bone Graft, *Substitutes Market Report, 2021–2028*. 2021, GVR-1-68038-154-2. p. 1-145.
11. Market Analysis, *Bone Grafts And Substitutes Market Size, Share & Trends Analysis Report By Material Type (Allograft, Synthetic), By Application (Spinal Fusion, Foot & Ankle, Joint Reconstruction), By Region, And Segment Forecasts, 2022 - 2030.* Grand View research, 2021.
12. Ethan Nyberg, et al., *Comparison of 3D-printed poly-ε-caprolactone scaffolds functionalized with tricalcium phosphate, hydroxyapatite, bio-oss, or decellularized bone matrix.* Tissue Engineering Part A, 2017. **23**(11-12): p. 503-514.

13. Alexandra N Rindone, Ethan Nyberg, and Warren L Grayson, *3D-printing composite polycaprolactone-decellularized bone matrix scaffolds for bone tissue engineering applications*, in *Decellularized Scaffolds and Organogenesis*. 2017, Springer. p. 209-226.
14. Jun-Young Kim, et al., *Synergistic effects of beta tri-calcium phosphate and porcine-derived decellularized bone extracellular matrix in 3D-printed polycaprolactone scaffold on bone regeneration.* Macromolecular Bioscience, 2018. **18**(6): p. 1800025.
15. Ryan Trombetta, et al., *3D printing of calcium phosphate ceramics for bone tissue engineering and drug delivery.* Annals of biomedical engineering, 2017. **45**(1): p. 23-44.
16. G William Jr, et al., *Bone grafts and bone graft substitutes in orthopaedic trauma surgery: a critical analysis.* JBJS, 2007. **89**(3): p. 649-658.
17. Timothy T Roberts and Andrew J Rosenbaum, *Bone grafts, bone substitutes and orthobiologics: the bridge between basic science and clinical advancements in fracture healing.* Organogenesis, 2012. **8**(4): p. 114-124.
18. Safdar N Khan, et al., *The biology of bone grafting.* JAAOS-Journal of the American Academy of Orthopaedic Surgeons, 2005. **13**(1): p. 77-86.
19. Daniel N Bracey, et al., *A decellularized porcine xenograft-derived bone scaffold for clinical use as a bone graft substitute: a critical evaluation of processing and structure.* Journal of functional biomaterials, 2018. **9**(3): p. 45.
20. FE Freeman, et al., *Biofabrication of multiscale bone extracellular matrix scaffolds for bone tissue engineering.* Eur. Cells Mater, 2019. **38**: p. 168-187.
21. Ben P Hung, et al., *Three-dimensional printing of bone extracellular matrix for craniofacial regeneration.* ACS biomaterials science & engineering, 2016. **2**(10): p. 1806-1816.
22. Doaa Adel-Khattab, et al., *Development of a synthetic tissue engineered three-dimensional printed bioceramic-based bone graft with homogenously distributed osteoblasts and mineralizing bone matrix in vitro.* Journal of Tissue Engineering and Regenerative Medicine, 2018. **12**(1): p. 44-58.
23. Marc Bohner, Bastien Le Gars Santoni, and Nicola Döbelin, *β-tricalcium phosphate for bone substitution: Synthesis and properties.* Acta biomaterialia, 2020. **113**: p. 23-41.

24. Hani A Awad, Regis J O'Keefe, and Jeremy J Mao, *Bone tissue engineering*, in *Principles of Tissue Engineering*. 2020, Elsevier. p. 1511-1519.
25. Joseph B Vella, et al., *Three dimensional printed calcium phosphate and poly (caprolactone) composites with improved mechanical properties and preserved microstructure.* Journal of Biomedical Materials Research Part A, 2018. **106**(3): p. 663-672.
26. Jason A Inzana, et al., *3D printed bioceramics for dual antibiotic delivery to treat implant-associated bone infection.* European cells & materials, 2015. **30**: p. 232.
27. Ryan P Trombetta, et al., *Calcium phosphate spacers for the local delivery of sitafloxacin and rifampin to treat orthopedic infections: efficacy and proof of concept in a mouse model of single-stage revision of device-associated osteomyelitis.* Pharmaceutics, 2019. **11**(2): p. 94.
28. Sara Hassouna Elsayed; Matthew Allen, *Decellularized Bovine Bone Extracellular Matrix for Bone Tissue Engineering: Scaffold Preparation And Characterization*, in *ORS annual meeting 2020*. 2020: Phoenix, Arizona, USA.
29. Ming Yan Sara Hassouna Elsayed, Hani Awad, Davide Corbetta, Matthew Allen, *Biocompatibility evaluation of novel 3D printed scaffolds for bone tissue engineering applications*, in *ORS annual meeting 2022*. 2022: Tampa, Florida, USA.
30. Sara Ahmed Hassouna Elsayed and Matthew James Allen. *ADIPOSE-DERIVED MESENCHYMAL STEM CELLS: OSTEOGENIC DIFFERENTIATION CUES AND POTENTIAL BONE TISSUE ENGINEERING APPLICATION*. in *Orthopaedic Proceedings*. 2020. The British Editorial Society of Bone & Joint Surgery.
31. Ming Yang Sara Hassouna Elsayed, Alex Rodriguez, Hani Awad, Matthew Allen *IN VITRO CHARACTERIZATION OF 3D-PRINTED DECELLULARIZED BONE MATRIX BASED SCAFFOLDS FOR BONE TISSUE ENGINEERING APPLICATIONS*, in *EORS annual meeting 2021*. 2021: Rome, Italy.
32. Ming Yan Sara Hassouna Elsayed, Hani Awad, Davide Corbetta, Matthew Allen, *Rat model for in vivo biocompatibility evaluation of novel 3D printed scaffolds for potential bone tissue engineering applications*, in *ICORS 2022 congress* 2022: Edinburgh
33. Jeffrey O Hollinger and James C Kleinschmidt, *The critical size defect as an experimental model to test bone repair materials.* The Journal of craniofacial surgery, 1990. **1**(1): p. 60-68.

34. Maurice LC Anderson, et al., *Critical size defect in the goat's os ilium: A model to evaluate bone grafts and substitutes.* Clinical Orthopaedics and Related Research®, 1999. **364**: p. 231-239.
35. David B Burr and Matthew R Allen, *Basic and applied bone biology*. 2019: Academic Press.
36. Rinaldo Florencio-Silva, et al., *Biology of bone tissue: structure, function, and factors that influence bone cells.* BioMed research international, 2015. **2015**.
37. Feng Xu and Steven L Teitelbaum, *Osteoclasts: new insights.* Bone research, 2013. **1**(1): p. 11-26.
38. Mattia Capulli, Riccardo Paone, and Nadia Rucci, *Osteoblast and osteocyte: games without frontiers.* Archives of biochemistry and biophysics, 2014. **561**: p. 3-12.
39. Teresita Bellido, Lilian I Plotkin, and Angela Bruzzaniti, *Bone cells*, in *Basic and applied bone biology*. 2019, Elsevier. p. 37-55.
40. Oran D Kennedy and Mitchell B Schaffler, *The roles of osteocyte signaling in bone.* The Journal of the American Academy of Orthopaedic Surgeons, 2012. **20**(10): p. 670.
41. Adele L Boskey and Aaron S Posner, *Bone structure, composition, and mineralization.* The Orthopedic clinics of North America, 1984. **15**(4): p. 597-612.
42. Gideon A Rodan, *Introduction to bone biology.* Bone, 1992. **13**: p. S3-S6.
43. Sarah L Dallas, Matthew Prideaux, and Lynda F Bonewald, *The osteocyte: an endocrine cell… and more.* Endocrine reviews, 2013. **34**(5): p. 658-690.
44. Aaron Schindeler, et al. *Bone remodeling during fracture repair: The cellular picture*. in *Seminars in cell & developmental biology*. 2008. Elsevier.
45. Michael Doube, *Closing cones create conical lamellae in secondary osteonal bone.* Royal Society Open Science, 2022. **9**(8): p. 220712.
46. Theo H Smit, Anders Odgaard, and Erich Schneider, *Structure and function of vertebral trabecular bone.* Spine, 1997. **22**(24): p. 2823-2833.
47. Christopher Boyle and Il Yong Kim, *Three-dimensional micro-level computational study of Wolff's law via trabecular bone remodeling in the human proximal femur using design space topology optimization.* Journal of biomechanics, 2011. **44**(5): p. 935-942.
48. Steven A Goldstein, *The mechanical properties of trabecular bone: dependence on anatomic location and function.* Journal of biomechanics, 1987. **20**(11-12): p. 1055-1061.

49. Philip J Wraighte and Brigitte E Scammell, *Principles of fracture healing.* Surgery (Oxford), 2006. **24**(6): p. 198-207.
50. Michael Jagodzinski and Christian Krettek, *Effect of mechanical stability on fracture healing—an update.* Injury, 2007. **38**(1): p. S3-S10.
51. Jiliang Li, Melissa A Kacena, and David L Stocum, *Fracture healing*, in *Basic and applied bone biology*. 2019, Elsevier. p. 235-253.
52. Zhihua Han, et al., *Axial micromotion locking plate construct can promote faster and stronger bone healing in an ovine osteotomy model.* Frontiers in bioengineering and biotechnology, 2021. **8**: p. 593448.
53. Zheng-wei Duan and Hua Lu, *Effect of mechanical strain on cells involved in fracture healing.* Orthopaedic Surgery, 2021. **13**(2): p. 369-375.
54. Jonathon R Sheen and Vishnu V Garla, *Fracture healing overview*, in *StatPearls [Internet]*. 2022, StatPearls Publishing.
55. Amin Bigham-Sadegh and Ahmad Oryan, *Basic concepts regarding fracture healing and the current options and future directions in managing bone fractures.* International wound journal, 2015. **12**(3): p. 238-247.
56. Frederic Shapiro, *Bone development and its relation to fracture repair. The role of mesenchymal osteoblasts and surface osteoblasts.* Eur Cell Mater, 2008. **15**(53): p. e76.
57. George L Barnes, et al., *Growth factor regulation of fracture repair.* Journal of bone and mineral research, 1999. **14**(11): p. 1805-1815.
58. Audrey Remedios, *Bone and bone healing.* Veterinary clinics of North America: small animal practice, 1999. **29**(5): p. 1029-1044.
59. John M Wozney and Vicki Rosen, *Bone morphogenetic protein and bone morphogenetic protein gene family in bone formation and repair.* Clinical orthopaedics and related research, 1998(346): p. 26-37.
60. AM Phillips, *Overview of the fracture healing cascade.* Injury, 2005. **36**(3): p. S5-S7.
61. Thomas A Einhorn, *The science of fracture healing.* Journal of orthopaedic trauma, 2005. **19**(10): p. S4-S6.
62. Lutz Claes, et al., *Influence of size and stability of the osteotomy gap on the success of fracture healing.* Journal of orthopaedic research, 1997. **15**(4): p. 577-584.
63. Richard Marsell and Thomas A Einhorn, *The biology of fracture healing.* Injury, 2011. **42**(6): p. 551-555.

64. Louis C Gerstenfeld, et al., *Fracture healing as a post-natal developmental process: molecular, spatial, and temporal aspects of its regulation.* Journal of cellular biochemistry, 2003. **88**(5): p. 873-884.
65. Steven L Teitelbaum, *Bone resorption by osteoclasts.* Science, 2000. **289**(5484): p. 1504-1508.
66. MTK Mulari, et al., *Osteoblast-like cells complete osteoclastic bone resorption and form new mineralized bone matrix in vitro.* Calcified tissue international, 2004. **75**: p. 253-261.
67. CAL Bassett, *Biophysical principles affecting bone structure.* The biochemistry and physiology of bone, vol. III, 1972: p. 1-76.
68. PI Brånemark, et al., *Osseointegrated titanium fixtures in the treatment of edentulousness.* Biomaterials, 1983. **4**(1): p. 25-28.
69. AF Mavrogenis, et al., *Biology of implant osseointegration.* J Musculoskelet Neuronal Interact, 2009. **9**(2): p. 61-71.
70. K Soballe, et al., *Hydroxyapatite coating converts fibrous tissue to bone around loaded implants.* The Journal of Bone & Joint Surgery British Volume, 1993. **75**(2): p. 270-278.
71. Reinhard Gruber and Dieter D Bosshardt, *Dental implantology and implants-tissue interface*, in *Stem Cell Biology and Tissue Engineering in Dental Sciences*. 2015, Elsevier. p. 735-747.
72. JE9922731 Davies, *Mechanisms of endosseous integration.* International Journal of Prosthodontics, 1998. **11**(5).
73. Scott F Gilbert, *Developmental biology. 6th Editio.* Sunderland (MA): Sinauer Associates.[Google Scholar], 2000.
74. Leslie J Degroot, J Larry Jameson, and David M De Kretser, *Endocrinology: adult and pediatric*. 2016: Elsevier Saunders.
75. Andrew OM Wilkie and Gillian M Morriss-Kay, *Genetics of craniofacial development and malformation.* Nature Reviews Genetics, 2001. **2**(6): p. 458-468.
76. Gillian M Morriss-Kay and Andrew OM Wilkie, *Growth of the normal skull vault and its alteration in craniosynostosis: insights from human genetics and experimental studies.* Journal of anatomy, 2005. **207**(5): p. 637-653.
77. Hanna Isaksson, et al., *Comparison of biophysical stimuli for mechano-regulation of tissue differentiation during fracture healing.* Journal of biomechanics, 2006. **39**(8): p. 1507-1516.

78. LE Claes and CA Heigele, *Magnitudes of local stress and strain along bony surfaces predict the course and type of fracture healing.* Journal of biomechanics, 1999. **32**(3): p. 255-266.
79. L. A. González-Torres, et al., *Influence of the frequency of the external mechanical stimulus on bone healing: a computational study.* Med Eng Phys, 2010. **32**(4): p. 363-71.
80. Smriti Ghimire, et al., *The investigation of bone fracture healing under intramembranous and endochondral ossification.* Bone Reports, 2021. **14**: p. 100740.
81. Leanora Anne Mills and A Hamish RW Simpson, *The relative incidence of fracture non-union in the Scottish population (5.17 million): a 5-year epidemiological study.* BMJ open, 2013. **3**(2): p. e002276.
82. William George Marshall, et al., *Delayed union, non-union and mal-union in 442 dogs.* Veterinary Surgery, 2022. **51**(7): p. 1087-1095.
83. William T McCartney and Bryan J MacDonald, *Incidence of non-union in long bone fractures in 233 cats.* International Journal of Applied Research in Veterinary Medicine, 2006. **4**(3): p. 209.
84. Laura S Phieffer and James A Goulet, *Delayed unions of the tibia.* JBJS, 2006. **88**(1): p. 205-216.
85. Enrique Gómez-Barrena, et al., *Bone fracture healing: cell therapy in delayed unions and nonunions.* Bone, 2015. **70**: p. 93-101.
86. Britt Wildemann, et al., *Non-union bone fractures.* Nature Reviews Disease Primers, 2021. **7**(1): p. 1-21.
87. Hangama C Fayaz, et al., *The role of stem cells in fracture healing and nonunion.* International orthopaedics, 2011. **35**: p. 1587-1597.
88. FDA, *Guidance Document for Industry and CDRH Staff for the Preparation of Investigational Device Exemptions and Premarket Approval Applications for Bone Growth Stimulator Devices; Draft; Availability*, in *United Stated: Office of the Federal Register, National Archives and Records Administration*, F.a.D. Administration, Editor. 1998. p. 36.
89. SK Stewart, *Fracture non-union: a review of clinical challenges and future research needs.* Malaysian orthopaedic journal, 2019. **13**(2): p. 1.
90. Thomas A Russell, *Fractures of the tibia and fibula.* Fractures in adults, 1991. **2**: p. 1915-2039.

91. Christina L Ekegren, et al., *Incidence, costs and predictors of non-union, delayed union and mal-union following long bone fracture.* International journal of environmental research and public health, 2018. **15**(12): p. 2845.
92. David J Hak, et al., *Delayed union and nonunions: epidemiology, clinical issues, and financial aspects.* Injury, 2014. **45**: p. S3-S7.
93. Louise Johnson, et al., *Physical health and psychological outcomes in adult patients with long-bone fracture non-unions: evidence today.* Journal of Clinical Medicine, 2019. **8**(11): p. 1998.
94. Christian Zeckey, et al., *The aseptic femoral and tibial shaft non-union in healthy patients–an analysis of the health-related quality of life and the socioeconomic outcome.* The open orthopaedics journal, 2011. **5**: p. 193.
95. Z Dahabreh, et al., *A cost analysis of treatment of tibial fracture nonunion by bone grafting or bone morphogenetic protein-7.* International orthopaedics, 2009. **33**: p. 1407-1414.
96. Ziad Dahabreh, Rozalia Dimitriou, and Peter V Giannoudis, *Health economics: a cost analysis of treatment of persistent fracture non-unions using bone morphogenetic protein-7.* Injury, 2007. **38**(3): p. 371-377.
97. NK Kanakaris and Peter V Giannoudis, *The health economics of the treatment of long-bone non-unions.* Injury, 2007. **38**: p. S77-S84.
98. Evgeniya Antonova, et al., *Tibia shaft fractures: costly burden of nonunions.* BMC musculoskeletal disorders, 2013. **14**(1): p. 1-10.
99. Tristan E McMillan and Alan J Johnstone, *Technical considerations to avoid delayed and non-union.* Injury, 2017. **48**: p. S64-S68.
100. Kevin O'Halloran, et al., *Will my tibial fracture heal? Predicting nonunion at the time of definitive fixation based on commonly available variables.* Clinical Orthopaedics and Related Research®, 2016. **474**: p. 1385-1395.
101. Britt Wildemann, et al., *Non-union bone fractures.* Nature Reviews Disease Primers, 2021. **7**(1): p. 57.
102. Keir A Ross, et al., *Prediction of tibial nonunion at the 6-week time point.* Injury, 2018. **49**(11): p. 2075-2082.
103. Christopher Tzioupis and Peter V Giannoudis, *Prevalence of long-bone non-unions.* Injury, 2007. **38**: p. S3-S9.

104. AJ Den Outer, et al., *Conservative versus operative treatment of displaced noncomminuted tibial shaft fractures: a retrospective comparative study.* Clinical Orthopaedics and Related Research®, 1990. **252**: p. 231-237.
105. Canadian Orthopaedic Trauma Society, *Nonunion following intramedullary nailing of the femur with and without reaming. Results of a multicenter randomized clinical trial.* The Journal of bone and joint surgery. American volume, 2003. **85**(11): p. 2093-2096.
106. W-J Metsemakers, et al., *Risk factors for nonunion after intramedullary nailing of femoral shaft fractures: remaining controversies.* Injury, 2015. **46**(8): p. 1601-1607.
107. Takashi Noumi, et al., *Intramedullary nailing for open fractures of the femoral shaft: evaluation of contributing factors on deep infection and nonunion using multivariate analysis.* Injury, 2005. **36**(9): p. 1085-1093.
108. Anthony F Farragos, Emil H Schemitsch, and Michael D McKee, *Complications of intramedullary nailing for fractures of the humeral shaft: a review.* Journal of orthopaedic trauma, 1999. **13**(4): p. 258-267.
109. RK Marti, CCPM Verheyen, and PP Besselaar, *Humeral shaft nonunion: evaluation of uniform surgical repair in fifty-one patients.* Journal of orthopaedic trauma, 2002. **16**(2): p. 108-115.
110. Sara Dimartino, et al., *Forearm Fracture Nonunion with and without Bone Loss: An Overview of Adult and Child Populations.* Journal of Clinical Medicine, 2022. **11**(14): p. 4106.
111. Kenji Kawamura and Kevin C Chung, *Treatment of scaphoid fractures and nonunions.* The Journal of hand surgery, 2008. **33**(6): p. 988-997.
112. Jeffrey A Mann and David I Pedowitz, *Evaluation and treatment of navicular stress fractures, including nonunions, revision surgery, and persistent pain after treatment.* Foot and ankle clinics, 2009. **14**(2): p. 187-204.
113. Shuntaro Munakata, et al., *Clinical efficacy of bone reconstruction surgery with frozen cortical bone allografts for nonunion of radial and ulnar fractures in toy breed dogs.* Veterinary and Comparative Orthopaedics and Traumatology, 2018. **31**(03): p. 159-169.
114. Andrea Castilla, et al., *Long-term assessment of bone regeneration in nonunion fractures treated with compression-resistant matrix and recombinant human bone morphogenetic protein-2 in dogs.* Veterinary and Comparative Orthopaedics and Traumatology, 2022. **36**(01): p. 29-38.

115. Bernhard Georg Weber and Oldrich Cech, *Pseudarthrosis: pathophysiology, biomechanics, therapy, results*, in *Pseudarthrosis: pathophysiology, biomechanics, therapy, results*. 1976. p. 323-323.
116. Mehmet Kocaoglu, I Levent Eralp, and F Erkal Bilen, *Nonunion and Osteomyelitis Following Fractures*, in *Orthopedics in Disasters*. 2016, Springer. p. 411-436.
117. Milind Madhav Chaudhary, *Infected nonunion of tibia.* Indian journal of orthopaedics, 2017. **51**(3): p. 256-268.
118. M Depypere, et al., *Pathogenesis and management of fracture-related infection.* Clinical Microbiology and Infection, 2020. **26**(5): p. 572-578.
119. Simon Hackl, et al., *The role of low-grade infection in the pathogenesis of apparently aseptic tibial shaft nonunion.* Injury, 2021. **52**(11): p. 3498-3504.
120. WJ Metsemakers, et al., *Infection after fracture fixation: current surgical and microbiological concepts.* Injury, 2018. **49**(3): p. 511-522.
121. Andrej Trampuz and Werner Zimmerli, *Diagnosis and treatment of infections associated with fracture-fixation devices.* Injury, 2006. **37**(2): p. S59-S66.
122. Werner Zimmerli and Parham Sendi, *Orthopaedic biofilm infections.* Apmis, 2017. **125**(4): p. 353-364.
123. N. Høiby, et al., *ESCMID guideline for the diagnosis and treatment of biofilm infections 2014.* Clin Microbiol Infect, 2015. **21 Suppl 1**: p. S1-25.
124. Elaine M Waters, et al., *Convergence of Staphylococcus aureus persister and biofilm research: can biofilms be defined as communities of adherent persister cells?* PLoS pathogens, 2016. **12**(12): p. e1006012.
125. D López, H Vlamakis, and R Kolter, *Biofilms. Cold Spring Harb Perspect Biol 2: a000398*. 2010, Epub 2010/06/04. cshperspect. a000398 [pii] https://doi. org/10.1101 ….
126. Werner Zimmerli and Claus Moser, *Pathogenesis and treatment concepts of orthopaedic biofilm infections.* FEMS Immunology & Medical Microbiology, 2012. **65**(2): p. 158-168.
127. David R Murdoch, et al., *Infection of orthopedic prostheses after Staphylococcus aureus bacteremia.* Clinical infectious diseases, 2001. **32**(4): p. 647-649.
128. Agnieszka Tomczyk-Warunek, et al., *Retrospective study of nosocomial infections in the orthopaedic and rehabilitation clinic of the medical university of Lublin in the years 2018–2020.* Journal of Clinical Medicine, 2021. **10**(14): p. 3179.

129. AV Tsiskarashvili, et al., *Metabolic bone tissue disorders in patients with long bone fractures complicated by chronic osteomyelitis.* Genij Ortopedii, 2019. **25**(2): p. 149-155.
130. Jérôme Josse, Frédéric Velard, and Sophie C Gangloff, *Staphylococcus aureus vs. osteoblast: relationship and consequences in osteomyelitis.* Frontiers in cellular and infection microbiology, 2015. **5**: p. 85.
131. AG Gristina and Biomaterial-Centered Infection, *Microbial Adhesion Versus Tissue Integration or" The race for the surface.* Science (seen in Manuscript), 1987.
132. Ulrike Dapunt, et al., *Infectious versus non-infectious loosening of implants: activation of T lymphocytes differentiates between the two entities.* International orthopaedics, 2014. **38**: p. 1291-1296.
133. Gerhard Bratschitsch, et al., *Spinal surgery site infection leading to implant loosening is influenced by the number of prior operations.* Global Spine Journal, 2022. **12**(3): p. 458-463.
134. G. M. Calori and P. V. Giannoudis, *Enhancement of fracture healing with the diamond concept: the role of the biological chamber.* Injury, 2011. **42**(11): p. 1191-3.
135. Joshua D Thomas and James L Kehoe, *Bone nonunion*, in *StatPearls [Internet]*. 2022, StatPearls Publishing.
136. Aaron Nauth, et al., *Critical-size bone defects: is there a consensus for diagnosis and treatment?* Journal of orthopaedic trauma, 2018. **32**: p. S7-S11.
137. Alessandro Bistolfi, et al., *Antibiotic-loaded cement in orthopedic surgery: a review.* International Scholarly Research Notices, 2011. **2011**.
138. Michael D McKee, et al., *A prospective, randomized clinical trial comparing an antibiotic-impregnated bioabsorbable bone substitute with standard antibiotic-impregnated cement beads in the treatment of chronic osteomyelitis and infected nonunion.* Journal of orthopaedic trauma, 2010. **24**(8): p. 483-490.
139. Kyriaki Kanellakopoulou and Evangelos J Giamarellos-Bourboulis, *Carrier systems for the local delivery of antibiotics in bone infections.* Drugs, 2000. **59**: p. 1223-1232.
140. RP Howlin, et al., *Antibiotic-loaded synthetic calcium sulfate beads for prevention of bacterial colonization and biofilm formation in periprosthetic infections.* Antimicrobial agents and chemotherapy, 2015. **59**(1): p. 111-120.
141. Zachary C Lum and Gavin C Pereira, *Local bio-absorbable antibiotic delivery in calcium sulfate beads in hip and knee arthroplasty.* Journal of orthopaedics, 2018. **15**(2): p. 676-678.

142. Eleonora Po, et al., *Use of antimicrobial impregnated calcium sulphate beads in the surgical management of mandibular osteomyelitis in an 8-year-old huacaya alpaca.* Veterinary Record Case Reports, 2022. **10**(2): p. e301.
143. F Gouin, et al., *Open wedge high tibial osteotomies: calcium-phosphate ceramic spacer versus autologous bonegraft.* Orthopaedics & Traumatology: Surgery & Research, 2010. **96**(6): p. 637-645.
144. F Biggi, *The biology of fracture healing as related to intramedullary locked nailing*, in *Practice of intramedullary locked nails*. 2002, Springer. p. 5-10.
145. Yong-Gang Ma, et al., *Surgical factors contributing to nonunion in femoral shaft fracture following intramedullary nailing.* Chinese Journal of Traumatology, 2016. **19**(02): p. 109-112.
146. Emmanuele Santolini, et al., *Femoral and tibial blood supply: A trigger for non-union?* Injury, 2014. **45**(11): p. 1665-1673.
147. Robert Zura, et al., *Epidemiology of fracture nonunion in 18 human bones.* JAMA surgery, 2016. **151**(11): p. e162775-e162775.
148. Peter V Giannoudis, Thomas A Einhorn, and David Marsh, *Fracture healing: the diamond concept.* injury, 2007. **38**: p. S3-S6.
149. SM Perren, *Physical and biological aspects of fracture healing with special reference to internal fixation.* Clinical Orthopaedics and Related Research (1976-2007), 1979. **138**: p. 175-196.
150. Megas Panagiotis, *Classification of non-union.* Injury, 2005. **36**(4): p. S30-S37.
151. Muhammad Shahid Khan, et al., *Salvage of infected non-union of the tibia with an Ilizarov ring fixator.* Journal of Orthopaedic Surgery, 2015. **23**(1): p. 52-55.
152. John A Scolaro, et al., *Cigarette smoking increases complications following fracture: a systematic review.* JBJS, 2014. **96**(8): p. 674-681.
153. Jacques Hernigou and Frédéric Schuind, *Smoking as a predictor of negative outcome in diaphyseal fracture healing.* International orthopaedics, 2013. **37**(5): p. 883-887.
154. Dan Clark, et al., *Effects of aging on fracture healing.* Current osteoporosis reports, 2017. **15**(6): p. 601-608.
155. Reinhard Gruber, et al., *Fracture healing in the elderly patient.* Experimental gerontology, 2006. **41**(11): p. 1080-1093.
156. Christopher J Dy, et al., *Sex and gender considerations in male patients with osteoporosis.* Clinical Orthopaedics and Related Research®, 2011. **469**(7): p. 1906-1912.

157. Zhenhan Deng, et al., *Gender differences in tibial fractures healing in normal and muscular dystrophic mice.* American Journal of Translational Research, 2020. **12**(6): p. 2640.
158. Kristen L Lauing, et al., *Acute alcohol exposure impairs fracture healing and deregulates β-catenin signaling in the fracture callus.* Alcoholism: Clinical and Experimental Research, 2012. **36**(12): p. 2095-2103.
159. Dana T Graves, et al., *Impact of diabetes on fracture healing.* Journal of Experimental & Clinical Medicine, 2011. **3**(1): p. 3-8.
160. Hongli Jiao, E Xiao, and Dana T Graves, *Diabetes and its effect on bone and fracture healing.* Current osteoporosis reports, 2015. **13**(5): p. 327-335.
161. LA Boursinos, et al., *Do steroids, conventional non-steroidal anti-inflammatory drugs and selective Cox-2 inhibitors adversely affect fracture healing.* J Musculoskelet Neuronal Interact, 2009. **9**(1): p. 44-52.
162. MPG Bostrom, et al., *Parathyroid hormone-related protein analog RS-66271 is an effective therapy for impaired bone healing in rabbits on corticosteroid therapy.* Bone, 2000. **26**(5): p. 437-442.
163. David R Jeffcoach, et al., *Nonsteroidal anti-inflammatory drugs' impact on nonunion and infection rates in long-bone fractures.* Journal of Trauma and Acute Care Surgery, 2014. **76**(3): p. 779-783.
164. Emily R Dodwell, et al., *NSAID exposure and risk of nonunion: a meta-analysis of case–control and cohort studies.* Calcified tissue international, 2010. **87**(3): p. 193-202.
165. Ersin Kuyucu, Figen Koçyiğit, and Lügen Çiftçi, *The importance of patient compliance in nonunion of forearm fracture.* International journal of surgery case reports, 2014. **5**(9): p. 598-600.
166. M Dvořák, A Nečas, and J Zatloukal, *Complications of long bone fracture healing in dogs: functional and radiological criteria for their assessment.* Acta Veterinaria Brno, 2000. **69**(2): p. 107-114.
167. Mun-Ik Lee, et al., *Surgical Ectrodactyly Repair Using Limb-lengthening and Bone Tissue Engineering Techniques in a Toy Dog Breed.* in vivo, 2020. **34**(2): p. 815-824.
168. Erika Roddy, et al., *Treatment of critical-sized bone defects: clinical and tissue engineering perspectives.* European Journal of Orthopaedic Surgery & Traumatology, 2018. **28**: p. 351-362.

169. John P Schmitz and Jeffrey O Hollinger, *The critical size defect as an experimental model for craniomandibulofacial nonunions.* Clinical Orthopaedics and Related Research (1976-2007), 1986. **205**: p. 299-308.
170. John F Keating, AHRW Simpson, and CM Robinson, *The management of fractures with bone loss.* The Journal of bone and joint surgery. British volume, 2005. **87**(2): p. 142-150.
171. Zbigniew Gugala and Sylwester Gogolewski, *Regeneration of segmental diaphyseal defects in sheep tibiae using resorbable polymeric membranes: a preliminary study.* Journal of orthopaedic trauma, 1999. **13**(3): p. 187-195.
172. Aaron Nauth, et al., *Managing bone defects.* Journal of orthopaedic trauma, 2011. **25**(8): p. 462-466.
173. David W Sanders, et al., *Critical-sized defect in the tibia: is it critical? Results from the SPRINT trial.* Journal of orthopaedic trauma, 2014. **28**(11): p. 632-635.
174. Spyros G Pneumaticos, et al., *Segmental bone defects: from cellular and molecular pathways to the development of novel biological treatments.* Journal of cellular and molecular medicine, 2010. **14**(11): p. 2561-2569.
175. JP Toombs, et al., *Evaluation of Key's hypothesis in the feline tibia: an experimental model for augmented bone healing studies.* American journal of veterinary research, 1985. **46**(2): p. 513-518.
176. SM Fox, et al., *Antebrachial deformities in the dog: treatment with external fixation.* Journal of Small Animal Practice, 1995. **36**(7): p. 315-320.
177. ANN Vandewater, MARVIN L OLMSTEAD, and SHARON STEVENSON, *Partial ulnar osteotomy with free autogenous fat grafting for treatment of radius curvus in the dog.* Veterinary Surgery, 1982. **11**(3): p. 92-99.
178. Patric Garcia, et al., *Development of a reliable non-union model in mice.* Journal of Surgical Research, 2008. **147**(1): p. 84-91.
179. Maximilian M Menger, et al., *Comparison of two non-union models with damaged periosteum in mice: Segmental defect and pin-clip fixation versus transverse fracture and K-wire stabilization.* Bone, 2022. **162**: p. 116475.
180. Carles Bosch, Birte Melsen, and Karin Vargervik, *Importance of the critical-size bone defect in testing bone-regenerating materials.* Journal of Craniofacial Surgery, 1998. **9**(4): p. 310-316.
181. Xue-Qiang Wu, et al., *Development of a tibial experimental non-union model in rats.* Journal of orthopaedic surgery and research, 2021. **16**(1): p. 1-9.

182. Mohamed Mediouni, et al., *An overview of thermal necrosis: present and future.* Current medical research and opinion, 2019.
183. Xin Qi, et al., *Exosomes secreted by human-induced pluripotent stem cell-derived mesenchymal stem cells repair critical-sized bone defects through enhanced angiogenesis and osteogenesis in osteoporotic rats.* International journal of biological sciences, 2016. **12**(7): p. 836.
184. Stuart A Green, *Skeletal defects. A comparison of bone grafting and bone transport for segmental skeletal defects.* Clinical orthopaedics and related research, 1994(301): p. 111-117.
185. Charles A Rockwood, *Rockwood and Wilkins' fractures in children*. Vol. 3. 2010: Lippincott Williams & Wilkins.
186. Mark J Gage, et al., *Management of bone defects in orthopedic trauma.* Bulletin of the NYU Hospital for Joint Diseases, 2018. **76**(1): p. 4-8.
187. Gavriil A Ilizarov, *Clinical application of the tension-stress effect for limb lengthening.* Clinical Orthopaedics and Related Research (1976-2007), 1990. **250**: p. 8-26.
188. Selina Summers and Matija Krkovic, *Bone transport with magnetic intramedullary nails in long bone defects.* European Journal of Orthopaedic Surgery & Traumatology, 2021. **31**: p. 1243-1252.
189. Subodh Shankar Natu, et al., *The biology of distraction osteogenesis for correction of mandibular and craniomaxillofacial defects: A review.* Dental research journal, 2014. **11**(1): p. 16.
190. Joseph G McCarthy, et al., *Distraction osteogenesis of the craniofacial skeleton.* Plastic and reconstructive surgery, 2001. **107**(7): p. 1812-1827.
191. James Aronson, *Current concepts review-limb-lengthening, skeletal reconstruction, and bone transport with the Ilizarov method.* JBJS, 1997. **79**(8): p. 1243-58.
192. Nicola Maffulli, Ubaldo Nele, and Lorenzo Matarazzo, *Changes in knee motion following femoral and tibial lengthening using the Ilizarov apparatus: a cohort study.* Journal of Orthopaedic Science, 2001. **6**(4): p. 333-338.
193. Dror Paley, *Problems, obstacles, and complications of limb lengthening by the Ilizarov technique.* Clin Orthop Relat Res, 1990. **250**(1): p. 81-104.
194. RD Burghardt, et al., *Mechanical failure of the Intramedullary Skeletal Kinetic Distractor in limb lengthening.* The Journal of Bone & Joint Surgery British Volume, 2011. **93**(5): p. 639-643.

195. Peter R Calder, Maritz Laubscher, and W David Goodier, *The role of the intramedullary implant in limb lengthening.* Injury, 2017. **48**: p. S52-S58.
196. Austin T Fragomen and S Robert Rozbruch, *Lengthening of the femur with a remote-controlled magnetic intramedullary nail: retrograde technique.* JBJS Essential Surgical Techniques, 2016. **6**(2).
197. Rainer Baumgart, *The reverse planning method for lengthening of the lower limb using a straight intramedullary nail with or without deformity correction. A new method.* Operative Orthopadie und Traumatologie, 2009. **21**(2): p. 221-233.
198. Stuart A Green, *The evolution of remote-controlled intramedullary lengthening and compression nails.* Journal of orthopaedic trauma, 2017. **31**(6 Suppl): p. S2.
199. Petros Konofaos, et al., *A novel device for long bone osteodistraction: description of device and case series.* Plastic and reconstructive surgery, 2012. **130**(3): p. 418e-422e.
200. Yatin M Kirane, Austin T Fragomen, and S Robert Rozbruch, *Precision of the PRECICE® internal bone lengthening nail.* Clinical Orthopaedics and Related Research®, 2014. **472**: p. 3869-3878.
201. Ahmed I Hammouda, et al., *Treatment of post-traumatic femoral discrepancy with PRECICE magnetic-powered intramedullary lengthening nails.* Journal of Orthopaedic Trauma, 2017. **31**(7): p. 369.
202. Gonzalo Barinaga, Austin M Beason, and Matthew P Gardner, *Novel surgical approach to segmental bone transport using a magnetic intramedullary limb lengthening system.* The Journal of the American Academy of Orthopaedic Surgeons, 2018. **26**(22): p. e477.
203. Ulrik Kähler Olesen, et al., *Plate-assisted bone segment transport with motorized lengthening nails and locking plates: a technique to treat femoral and tibial bone defects.* JAAOS Global Research & Reviews, 2019. **3**(8).
204. G. S. Mundinger, et al., *Distraction Osteogenesis for Surgical Treatment of Craniosynostosis: A Systematic Review.* Plast Reconstr Surg, 2016. **138**(3): p. 657-669.
205. Guilherme Domingos, et al., *Distraction osteogenesis: biological principles and its application in companion animals.* Clinical Implementation of Bone Regeneration and Maintenance, 2019.
206. Yimurang Hamiti, et al., *Reconstruction of massive tibial defect caused by osteomyelitis using induced membrane followed by trifocal bone transport technique: a retrospective study and our experience.* BMC surgery, 2021. **21**: p. 1-10.

207. A. T. C. Ow and L. K. Cheung, *Meta-analysis of mandibular distraction osteogenesis: clinical applications and functional outcomes.* Plast Reconstr Surg, 2008. **121**(3): p. 54e-69e.

208. A. Chugh, D. Mehrotra, and P. K. Yadav, *A systematic review on the outcome of distraction osteogenesis in TMJ ankylosis.* J Oral Biol Craniofac Res, 2021. **11**(4): p. 581-595.

209. Peter V Giannoudis, et al., *Masquelet technique for the treatment of bone defects: tips-tricks and future directions.* Injury, 2011. **42**(6): p. 591-598.

210. Mario Ronga, et al., *Masquelet technique for the treatment of a severe acute tibial bone loss.* Injury, 2014. **45**: p. S111-S115.

211. Andrea I Alford, et al., *Masquelet's induced membrane technique: Review of current concepts and future directions.* Journal of Orthopaedic Research®, 2021. **39**(4): p. 707-718.

212. Alain C Masquelet, *Induced membrane technique: pearls and pitfalls.* Journal of orthopaedic trauma, 2017. **31**: p. S36-S38.

213. H Ahmed, M Shakshak, and A Trompeter, *A review of the Masquelet technique in the treatment of lower limb critical-size bone defects.* The Annals of The Royal College of Surgeons of England, 2023.

214. Satoshi Hatashita, et al., *'Acute Masquelet technique'for reconstructing bone defects of an open lower limb fracture.* European Journal of Trauma and Emergency Surgery, 2021. **47**: p. 1153-1162.

215. Jithendra TB Ratnayake, Michael Mucalo, and George J Dias, *Substituted hydroxyapatites for bone regeneration: A review of current trends.* Journal of Biomedical Materials Research Part B: Applied Biomaterials, 2017. **105**(5): p. 1285-1299.

216. Rusin Zhao, et al., *Bone grafts and substitutes in dentistry: A review of current trends and developments.* Molecules, 2021. **26**(10): p. 3007.

217. GM Calori, et al., *The use of bone-graft substitutes in large bone defects: any specific needs?* Injury, 2011. **42**: p. S56-S63.

218. Suzanne Stewart, et al., *Bone regeneration*, in *Translational regenerative medicine*. 2015, Elsevier. p. 313-333.

219. Sanan Abhay and Stephen J Haines, *Repairing holes in the head: a history of cranioplasty.* Neurosurgery, 1997. **40**(3): p. 588-603.

220. Marc Bohner, *Resorbable biomaterials as bone graft substitutes.* Materials Today, 2010. **13**(1-2): p. 24-30.
221. JM Flynn, *Fracture repair and bone grafting.* OKU, 2011. **10**: p. 11-21.
222. Jeremy A Hall, et al., *Prospective randomized clinical trial investigating the effect of the reamer-irrigator-aspirator on the volume of embolic load and respiratory function during intramedullary nailing of femoral shaft fractures.* Journal of orthopaedic trauma, 2017. **31**(4): p. 200-204.
223. Johanna CE Donders, et al., *Hemorrhagic-Induced Cardiovascular Complications During Reamer–Irrigator–Aspirator-Assisted Femoral Nonunion Treatment.* Journal of Orthopaedic Trauma, 2016. **30**(9): p. e294-e298.
224. Augustus D Mazzocca and Adam Lindsay, *Biologics in orthopaedic surgery*. Chapter 13 Biologics in Hand Surgery. 2018: Elsevier Health Sciences.
225. Nikita Joji and Afshin Mosahebi, *Biomaterials and Structural Fat Grafting*, in *Plastic Surgery-Principles and Practice*. 2022, Elsevier. p. 27-36.
226. George J Martin Jr, et al., *New formulations of demineralized bone matrix as a more effective graft alternative in experimental posterolateral lumbar spine arthrodesis.* Spine, 1999. **24**(7): p. 637-645.
227. Steven Gitelis and Brian J Cole, *The use of allografts in orthopaedic surgery.* Instructional Course Lectures, 2002. **51**: p. 507-520.
228. Hamid Shegarfi and Olav Reikeras, *Bone transplantation and immune response.* Journal of Orthopaedic Surgery, 2009. **17**(2): p. 206-211.
229. Olav Reikerås, et al., *Impact of MHC mismatch and freezing on bone graft incorporation: an experimental study in rats.* Journal of Orthopaedic Research, 2008. **26**(7): p. 925-931.
230. Chad Myeroff and Michael Archdeacon, *Autogenous bone graft: donor sites and techniques.* JBJS, 2011. **93**(23): p. 2227-2236.
231. Mohammed E Elsalanty and David G Genecov, *Bone grafts in craniofacial surgery.* Craniomaxillofacial trauma & reconstruction, 2009. **2**(3-4): p. 125-134.
232. Daniel A Oakes and Miguel E Cabanela, *Impaction bone grafting for revision hip arthroplasty: biology and clinical applications.* JAAOS-Journal of the American Academy of Orthopaedic Surgeons, 2006. **14**(11): p. 620-628.
233. Thomas W Bauer and George F Muschler, *Bone graft materials: an overview of the basic science.* Clinical Orthopaedics and Related Research®, 2000. **371**: p. 10-27.

234. S Kakar, et al., *Bone grafting and enhancement of fracture repair.* Rockwood and Green's Fractures in Adults. 6th ed. Philadelphia, PA: Lippincott Williams & Wilkins, 2006.
235. Robert W Mendicino, Eric Leonheart, and Paul Shromoff, *Techniques for harvesting autogenous bone grafts of the lower extremity.* The Journal of foot and ankle surgery, 1996. **35**(5): p. 428-435.
236. Nabil A Ebraheim, Hossein Elgafy, and Rongming Xu, *Bone-graft harvesting from iliac and fibular donor sites: techniques and complications.* JAAOS-Journal of the American Academy of Orthopaedic Surgeons, 2001. **9**(3): p. 210-218.
237. Thomas J Cypher and Jordan P Grossman, *Biological principles of bone graft healing.* The Journal of foot and ankle surgery, 1996. **35**(5): p. 413-417.
238. André R Gazdag, et al., *Alternatives to autogenous bone graft: efficacy and indications.* JAAOS-Journal of the American Academy of Orthopaedic Surgeons, 1995. **3**(1): p. 1-8.
239. Christopher G Finkemeier, *Bone-grafting and bone-graft substitutes.* JBJS, 2002. **84**(3): p. 454-464.
240. Elke Ahlmann, et al., *Comparison of anterior and posterior iliac crest bone grafts in terms of harvest-site morbidity and functional outcomes.* JBJS, 2002. **84**(5): p. 716-720.
241. Xin Chen, Kai Chen, and Yuxi Su, *Comparison of the inner side and two-sided approaches for iliac crest bone graft harvesting for pediatric pelvic osteotomy.* Journal of Orthopaedic Surgery and Research, 2021. **16**(1): p. 1-7.
242. RW-W Hsu, et al., *Free vascularised fibular grafting for reconstruction after tumour resection.* The Journal of Bone and Joint Surgery. British volume, 1997. **79**(1): p. 36-42.
243. Matthew T Houdek, et al., *Outcomes and complications of reconstruction with use of free vascularized fibular graft for spinal and pelvic defects following resection of a malignant tumor.* JBJS, 2017. **99**(13): p. e69.
244. Arissa M Torrie, et al., *Osteochondral allograft.* Current reviews in musculoskeletal medicine, 2015. **8**(4): p. 413-422.
245. Yasuaki Nakagawa, et al., *Clinical outcomes of donor sites after osteochondral graft harvest from healthy knees.* Orthopaedic Journal of Sports Medicine, 2017. **5**(10): p. 2325967117732525.

246. Ryan Rowland, Michael Colello, and Douglas J Wyland, *Osteochondral autograft transfer procedure: Arthroscopic technique and technical pearls.* Arthroscopy techniques, 2019. **8**(7): p. e713-e719.
247. Nikos Mardas, Vivek Chadha, and Nikolaos Donos, *Alveolar ridge preservation with guided bone regeneration and a synthetic bone substitute or a bovine-derived xenograft: a randomized, controlled clinical trial.* Clinical oral implants research, 2010. **21**(7): p. 688-698.
248. James T MeIIonig, *Human histologic evaluation of a bovine-derived bone xenograft in the treatment of periodontal osseous defects.* International Journal of Periodontics & Restorative Dentistry, 2000. **20**(1).
249. N Tovar, et al., *Evaluation of bone response to various anorganic bovine bone xenografts: an experimental calvaria defect study.* International journal of oral and maxillofacial surgery, 2014. **43**(2): p. 251-260.
250. Jung Heon Lee, et al., *Physicochemical characterization of porcine bone-derived grafting material and comparison with bovine xenografts for dental applications.* Journal of periodontal & implant science, 2017. **47**(6): p. 388-401.
251. Ying-Chen Chen, et al., *Development and characterization of acellular extracellular matrix scaffolds from porcine menisci for use in cartilage tissue engineering.* Tissue Engineering Part C: Methods, 2015. **21**(9): p. 971-986.
252. Eun-Bin Bae, et al., *Comparison of bone regeneration between porcine-derived and bovine-derived xenografts in rat calvarial defects: A non-inferiority study.* Materials, 2019. **12**(20): p. 3412.
253. Jang-Yeol Park, et al., *Socket preservation using deproteinized horse-derived bone mineral.* Journal of periodontal & implant science, 2010. **40**(5): p. 227-231.
254. Kyoung-Je Jang, et al., *Development and characterization of horse bone-derived natural calcium phosphate powders.* Journal of Biosystems Engineering, 2014. **39**(2): p. 122-133.
255. Riccardo Cusinato, et al., *Effectiveness of hydrogen peroxide and electron-beam irradiation treatment for removal and inactivation of viruses in equine-derived xenografts.* Journal of virological methods, 2016. **232**: p. 39-46.
256. Montaser N Alqutub, et al., *Osteogenic Differentiation of Periodontal Ligament Stem Cells Seeded on Equine-Derived Xenograft in Osteogenic Growth Media.* Medicina, 2022. **58**(11): p. 1518.

257. Reza Amid, et al., *Structural and chemical features of xenograft bone substitutes: A systematic review of in vitro studies.* Biotechnology and Applied Biochemistry, 2021. **68**(6): p. 1432-1452.

258. Bi Long, et al., *Evaluation of a novel reconstituted bone xenograft using processed bovine cancellous bone in combination with purified bovine bone morphogenetic protein.* Xenotransplantation, 2012. **19**(2): p. 122-132.

259. Do Kyun Kim, et al., *Comparison of a synthetic bone substitute composed of carbonated apatite with an anorganic bovine xenograft in particulate forms in a canine maxillary augmentation model.* Clinical oral implants research, 2010. **21**(12): p. 1334-1344.

260. Yuan Gao, et al., *Characterization and osteoblast-like cell compatibility of porous scaffolds: bovine hydroxyapatite and novel hydroxyapatite artificial bone.* Journal of Materials Science: Materials in Medicine, 2006. **17**(9): p. 815-823.

261. Hahn Tal, *Autogenous masticatory mucosal grafts in extraction socket seal procedures: a comparison between sockets grafted with demineralized freeze-dried bone and deproteinized bovine bone mineral.* Clinical oral implants research, 1999. **10**(4): p. 289-296.

262. Ferdiansyah Mahyudin, et al., *Comparative effectiveness of bone grafting using xenograft freeze-dried cortical bovine, allograft freeze-dried cortical New Zealand White rabbit, xenograft hydroxyapatite bovine, and xenograft demineralized bone matrix bovine in bone defect of femoral diaphysis of white rabbit: experimental study in vivo.* International Journal of Biomaterials, 2017. **2017**.

263. David Buntoro Kamadjaja, et al., *In vivo analyses of osteogenic activity and bone regeneration capacity of demineralized freeze-dried bovine bone xenograft: a potential candidate for alveolar bone fillers.* International Journal of Dentistry, 2021. **2021**.

264. Gert L de Lange, et al., *A histomorphometric and micro–computed tomography study of bone regeneration in the maxillary sinus comparing biphasic calcium phosphate and deproteinized cancellous bovine bone in a human split-mouth model.* Oral surgery, oral medicine, oral pathology and oral radiology, 2014. **117**(1): p. 8-22.

265. Nina Broggini, et al., *Bone healing around nanocrystalline hydroxyapatite, deproteinized bovine bone mineral, biphasic calcium phosphate, and autogenous bone in mandibular bone defects.* Journal of Biomedical Materials Research Part B: Applied Biomaterials, 2015. **103**(7): p. 1478-1487.

266. Guobao Chen and Yonggang Lv, *Decellularized bone matrix scaffold for bone regeneration*, in *Decellularized Scaffolds and Organogenesis*. 2017, Springer. p. 239-254.
267. T Albrektsson and C Johansson, *Osteoinduction, osteoconduction and osseointegration.* European spine journal, 2001. **10**(2): p. S96-S101.
268. A. H. Schmidt, *Autologous bone graft: Is it still the gold standard?* Injury, 2021. **52 Suppl 2**: p. S18-s22.
269. Solon T Kao and Daniel D Scott, *A review of bone substitutes.* Oral and maxillofacial surgery clinics of North America, 2007. **19**(4): p. 513-521.
270. William R Moore, Stephen E Graves, and Gregory I Bain, *Synthetic bone graft substitutes.* ANZ journal of surgery, 2001. **71**(6): p. 354-361.
271. Reena A Bhatt and Tamara D Rozental, *Bone graft substitutes.* Hand clinics, 2012. **28**(4): p. 457-468.
272. M Navarro, et al., *Biomaterials in orthopaedics.* Journal of the royal society interface, 2008. **5**(27): p. 1137-1158.
273. Larry L Hench and Julia M Polak, *Third-generation biomedical materials.* Science, 2002. **295**(5557): p. 1014-1017.
274. Hockin HK Xu, et al., *Injectable and macroporous calcium phosphate cement scaffold.* Biomaterials, 2006. **27**(24): p. 4279-4287.
275. Elena F Burguera, Hockin HK Xu, and Michael D Weir, *Injectable and rapid-setting calcium phosphate bone cement with dicalcium phosphate dihydrate.* Journal of Biomedical Materials Research Part B: Applied Biomaterials: An Official Journal of The Society for Biomaterials, The Japanese Society for Biomaterials, and The Australian Society for Biomaterials and the Korean Society for Biomaterials, 2006. **77**(1): p. 126-134.
276. Cassidy E Gillman and Ambalangodage C Jayasuriya, *FDA-approved bone grafts and bone graft substitute devices in bone regeneration.* Materials Science and Engineering: C, 2021. **130**: p. 112466.
277. Qingqiang Yao, et al., *Design, construction and mechanical testing of digital 3D anatomical data-based PCL–HA bone tissue engineering scaffold.* Journal of Materials Science: Materials in Medicine, 2015. **26**(1): p. 1-9.
278. RK Kulkarni, et al., *Polylactic acid for surgical implants.* Archives of surgery, 1966. **93**(5): p. 839-843.

279. Ramchandra K Kulkarni, et al., *Biodegradable poly (lactic acid) polymers.* Journal of biomedical materials research, 1971. **5**(3): p. 169-181.

280. JL Dávila, et al., *Fabrication of PCL/β-TCP scaffolds by 3D mini-screw extrusion printing.* Journal of Applied Polymer Science, 2016. **133**(15).

281. William J Ciccone, et al., *Bioabsorbable implants in orthopaedics: new developments and clinical applications.* JAAOS-Journal of the American Academy of Orthopaedic Surgeons, 2001. **9**(5): p. 280-288.

282. AGA Coombes and MC Meikle, *Resorbable synthetic polymers s replacements for bone graft.* Clinical materials, 1994. **17**(1): p. 35-67.

283. Shadi Hassanajili, et al., *Preparation and characterization of PLA/PCL/HA composite scaffolds using indirect 3D printing for bone tissue engineering.* Materials Science and Engineering: C, 2019. **104**: p. 109960.

284. Seyedeh Fatemeh Hashemi, et al., *In-vitro and in-vivo studies of PLA/PCL/gelatin composite scaffold containing ascorbic acid for bone regeneration.* Journal of Drug Delivery Science and Technology, 2021. **61**: p. 102077.

285. Bei Feng, et al., *Engineering cartilage tissue based on cartilage-derived extracellular matrix cECM/PCL hybrid nanofibrous scaffold.* Materials & Design, 2020. **193**: p. 108773.

286. Peiran Wei, et al., *IGF-1-releasing PLGA nanoparticles modified 3D printed PCL scaffolds for cartilage tissue engineering.* Drug Delivery, 2020. **27**(1): p. 1106-1114.

287. Jingqi Ma, et al., *Modification of 3D printed PCL scaffolds by PVAc and HA to enhance cytocompatibility and osteogenesis.* RSC advances, 2019. **9**(10): p. 5338-5346.

288. Thomas Waterkotte, et al., *Long-term Antibody Release Polycaprolactone (PCL) Capsule and the Release Kinetics In Natural and Accelerated Degradation.* bioRxiv, 2022.

289. Michael Argentieri, Christopher N. Schabowsky, and Dheerendra Kommala. *MEDICAL DEVICE MATERIAL PERFORMANCE STUDY- Polycaprolactone (PCL) Safety Profile*. U.S. FDA Center for Devices and Radiological Health 2021; Available from: https://www.fda.gov/media/158492/download.

290. Mark A Birch, et al., *Microporous "honeycomb" films support enhanced bone formation in vitro.* Tissue Engineering Part A, 2013. **19**(17-18): p. 2087-2096.

291. Siyi Wang, et al., *Fabrication and application of a 3D-printed poly-ε-caprolactone cage scaffold for bone tissue engineering.* BioMed Research International, 2020. **2020**.

292. Dinghua Liu, et al., *3D printed PCL/SrHA scaffold for enhanced bone regeneration.* Chemical Engineering Journal, 2019. **362**: p. 269-279.

293. Su A Park, Su Hee Lee, and Wan Doo Kim, *Fabrication of porous polycaprolactone/hydroxyapatite (PCL/HA) blend scaffolds using a 3D plotting system for bone tissue engineering.* Bioprocess and biosystems engineering, 2011. **34**(4): p. 505-513.

294. Ruby Dwivedi, et al., *Polycaprolactone as biomaterial for bone scaffolds: Review of literature.* Journal of oral biology and craniofacial research, 2020. **10**(1): p. 381-388.

295. Israel Engelberg and Joachim Kohn, *Physico-mechanical properties of degradable polymers used in medical applications: a comparative study.* Biomaterials, 1991. **12**(3): p. 292-304.

296. Shaun Eshraghi and Suman Das, *Mechanical and microstructural properties of polycaprolactone scaffolds with one-dimensional, two-dimensional, and three-dimensional orthogonally oriented porous architectures produced by selective laser sintering.* Acta biomaterialia, 2010. **6**(7): p. 2467-2476.

297. Laurence W McKeen, *The effect of heat aging on the properties of sustainable polymers*, in *The effect of long term thermal exposure on plastics and elastomers*

2021, William Andrew. p. 319-320.

298. K De Groot, *Bone induction by allogenous rat dentine implanted subcutaneously.* Archives of Oral Biology, 1974. **19**(6): p. 477-479.

299. M Jarcho and CH Bolen, *MB Thomas, J. Bobick, JF Kay, and RH Doremus,".* J. Mater. Sci, 1976. **11**: p. 2027-2035.

300. RZ LeGeros, et al., *Biphasic calcium phosphate bioceramics: preparation, properties and applications.* Journal of materials science: Materials in Medicine, 2003. **14**(3): p. 201-209.

301. Andreas Kolk, et al., *Current trends and future perspectives of bone substitute materials–from space holders to innovative biomaterials.* Journal of Cranio-Maxillofacial Surgery, 2012. **40**(8): p. 706-718.

302. Laurence E Rustom, Michael J Poellmann, and Amy J Wagoner Johnson, *Mineralization in micropores of calcium phosphate scaffolds.* Acta Biomaterialia, 2019. **83**: p. 435-455.

303. David J Hoelzle, Andrew G Alleyne, and Amy J Wagoner Johnson, *Micro-robotic deposition guidelines by a design of experiments approach to maximize fabrication*

reliability for the bone scaffold application. Acta biomaterialia, 2008. **4**(4): p. 897-912.

304. David J Hoelzle, et al., *Design and manufacture of combinatorial calcium phosphate bone scaffolds.* Journal of biomechanical engineering, 2011. **133**(10).
305. Sarah Michna, Willie Wu, and Jennifer A Lewis, *Concentrated hydroxyapatite inks for direct-write assembly of 3-D periodic scaffolds.* Biomaterials, 2005. **26**(28): p. 5632-5639.
306. P Wongwitwichot, et al., *Comparison of TCP and TCP/HA hybrid scaffolds for osteoconductive activity.* The open biomedical engineering journal, 2010. **4**: p. 279.
307. Yaqin Huang, et al., *Phase Transition from α-TCP into β-TCP in TCP/HA Composites.* International Journal of Applied Ceramic Technology, 2010. **7**(2): p. 184-188.
308. Mehdi Ebrahimi, Michael G Botelho, and Sergey V Dorozhkin, *Biphasic calcium phosphates bioceramics (HA/TCP): Concept, physicochemical properties and the impact of standardization of study protocols in biomaterials research.* Materials Science and Engineering: C, 2017. **71**: p. 1293-1312.
309. Arnaud Bruyas, et al., *Systematic characterization of 3D-printed PCL/β-TCP scaffolds for biomedical devices and bone tissue engineering: Influence of composition and porosity.* Journal of materials research, 2018. **33**(14): p. 1948-1959.
310. Atsuro Yokoyama, et al., *Development of calcium phosphate cement using chitosan and citric acid for bone substitute materials.* Biomaterials, 2002. **23**(4): p. 1091-1101.
311. Jae Hyup Lee, et al., *Fabrication of an rhBMP-2 loaded porous β-TCP microsphere-hyaluronic acid-based powder gel composite and evaluation of implant osseointegration.* Journal of Materials Science: Materials in Medicine, 2014. **25**(9): p. 2141-2151.
312. Wafaa K Abid and Yusra H AL Mukhtar, *Repair of surgical bone defects grafted with hydroxylapatite+ β-TCP combined with hyaluronic acid and collagen membrane in rabbits: A histological study.* Journal of Taibah University medical sciences, 2019. **14**(1): p. 14-24.
313. L Rony, et al., *Hyaluronic acid stimulates osseointegration of β-TCP in young and old ewes.* Calcified Tissue International, 2019. **105**(5): p. 487-496.
314. Christina W Cheng, Loran D Solorio, and Eben Alsberg, *Decellularized tissue and cell-derived extracellular matrices as scaffolds for orthopaedic tissue engineering.* Biotechnology advances, 2014. **32**(2): p. 462-484.

315. Xin-jun Sun, et al., *Heparin-chitosan-coated acellular bone matrix enhances perfusion of blood and vascularization in bone tissue engineering scaffolds.* Tissue Engineering Part A, 2011. **17**(19-20): p. 2369-2378.

316. Yuan-Wu Chen, et al., *Development of a decellularized porcine bone graft by supercritical carbon dioxide extraction technology for bone regeneration.* Journal of Tissue Engineering and Regenerative Medicine, 2021. **15**(4): p. 401-414.

317. Nicola U Zitzmann, et al., *Alveolar ridge augmentation with Bio-Oss: a histologic study in humans.* International Journal of Periodontics & Restorative Dentistry, 2001. **21**(3).

318. Ahmed M Ibrahim, Mervat M Khalil, and Gaafar N El Halawani, *Evaluation Of Anterior Maxillary Horizontal Ridge Augmentation With Simultanous Implant Placement Using Cerabone® Versus Cerabone® Combined With Platelet Rich Plasma (Randomized Clinical Trial).* Alexandria Dental Journal, 2020.

319. Stephen F Badylak, Doris Taylor, and Korkut Uygun, *Whole-organ tissue engineering: decellularization and recellularization of three-dimensional matrix scaffolds.* Annual review of biomedical engineering, 2011. **13**(1): p. 27-53.

320. Guobao Chen, et al., *3D scaffolds with different stiffness but the same microstructure for bone tissue engineering.* ACS applied materials & interfaces, 2015. **7**(29): p. 15790-15802.

321. Peter M Crapo, Thomas W Gilbert, and Stephen F Badylak, *An overview of tissue and whole organ decellularization processes.* Biomaterials, 2011. **32**(12): p. 3233-3243.

322. Yu Seon Kim, et al., *Applications of decellularized extracellular matrix in bone and cartilage tissue engineering.* Bioengineering & translational medicine, 2019. **4**(1): p. 83-95.

323. Thomas W Gilbert, Tiffany L Sellaro, and Stephen F Badylak, *Decellularization of tissues and organs.* Biomaterials, 2006. **27**(19): p. 3675-3683.

324. Yoshihide Hashimoto, et al., *The effect of decellularized bone/bone marrow produced by high-hydrostatic pressurization on the osteogenic differentiation of mesenchymal stem cells.* Biomaterials, 2011. **32**(29): p. 7060-7067.

325. Ana Celeste Oliveira, et al., *Evaluation of small intestine grafts decellularization methods for corneal tissue engineering.* PloS one, 2013. **8**(6): p. e66538.

326. Silke Schwarz, et al., *Decellularized cartilage matrix as a novel biomatrix for cartilage tissue-engineering applications.* Tissue Engineering Part A, 2012. **18**(21-22): p. 2195-2209.

327. Amanda J Sutherland, et al., *Decellularized cartilage may be a chondroinductive material for osteochondral tissue engineering.* PloS one, 2015. **10**(5): p. e0121966.
328. Colin R Butler, et al., *Vacuum-assisted decellularization: an accelerated protocol to generate tissue-engineered human tracheal scaffolds.* Biomaterials, 2017. **124**: p. 95-105.
329. Susan J Ahn, José Costa, and Janet Rettig Emanuel, *PicoGreen quantitation of DNA: effective evaluation of samples pre-or psost-PCR.* Nucleic acids research, 1996. **24**(13): p. 2623-2625.
330. A Costa, et al., *Biologic Scaffolds, Cold Spring Harb.* Perspect. Med, 2017. **7**.
331. Fahimeh Shahabipour, et al., *Scaffolds derived from cancellous bovine bone support mesenchymal stem cells' maintenance and growth.* In Vitro Cellular & Developmental Biology-Animal, 2013. **49**(6): p. 440-448.
332. Christopher A Smith, et al., *Correction: Human decellularized bone scaffolds from aged donors show improved osteoinductive capacity compared to young donor bone.* Plos one, 2017. **12**(11): p. e0187783.
333. Janina Burk, et al., *Freeze-thaw cycles enhance decellularization of large tendons.* Tissue Engineering Part C: Methods, 2014. **20**(4): p. 276-284.
334. Gabriel Fernandez de Grado, et al., *Bone substitutes: a review of their characteristics, clinical use, and perspectives for large bone defects management.* Journal of tissue engineering, 2018. **9**: p. 2041731418776819.
335. Thomas A Russell, Ross K Leighton, and Alpha-BSM Tibial Plateau Fracture Study Group, *Comparison of autogenous bone graft and endothermic calcium phosphate cement for defect augmentation in tibial plateau fractures: a multicenter, prospective, randomized study.* JBJS, 2008. **90**(10): p. 2057-2061.
336. Robert W Bucholz, Ann Carlton, and Ralph Holmes, *Interporous hydroxyapatite as a bone graft substitute in tibial plateau fractures.* Clinical Orthopaedics and Related Research (1976-2007), 1989. **240**: p. 53-62.
337. Chao Shen, et al., *The use of β-TCP in the surgical treatment of tibial plateau fractures.* Knee Surgery, Sports Traumatology, Arthroscopy, 2009. **17**: p. 1406-1411.
338. Michael G Jakubietz, Joerg G Gruenert, and Rafael G Jakubietz, *The use of beta-tricalcium phosphate bone graft substitute in dorsally plated, comminuted distal radius fractures.* Journal of orthopaedic surgery and research, 2011. **6**: p. 1-5.

339. Robert DA Gaasbeek, et al., *Mechanism of bone incorporation of β-TCP bone substitute in open wedge tibial osteotomy in patients.* Biomaterials, 2005. **26**(33): p. 6713-6719.

340. Tomihisa Koshino, et al., *New bone formation around porous hydroxyapatite wedge implanted in opening wedge high tibial osteotomy in patients with osteoarthritis.* Biomaterials, 2001. **22**(12): p. 1579-1582.

341. E. Dehoux, et al., *[High tibial open-wedge osteotomy using a tricalcium phosphate substitute: 70 cases with 18 months mean follow-up].* Rev Chir Orthop Reparatrice Appar Mot, 2005. **91**(2): p. 143-8.

342. Oliver Pieske, et al., *Autologous bone graft versus demineralized bone matrix in internal fixation of ununited long bones.* Journal of trauma management & outcomes, 2009. **3**(1): p. 1-8.

343. Michael G Newman, et al., *Carranza's clinical periodontology*. 2006: Elsevier Brasil.

344. Regina M Benjamin, *Oral health: the silent epidemic.* Public health reports, 2010. **125**(2): p. 158-159.

345. Mark A Reynolds, et al., *The efficacy of bone replacement grafts in the treatment of periodontal osseous defects. A systematic review.* Annals of periodontology, 2003. **8**(1): p. 227-265.

346. Philip J Hanes, *Bone replacement grafts for the treatment of periodontal intrabony defects.* Oral and maxillofacial surgery clinics of North America, 2007. **19**(4): p. 499-512.

347. Emeka Nkenke and Florian Stelzle, *Clinical outcomes of sinus floor augmentation for implant placement using autogenous bone or bone substitutes: a systematic review.* Clinical oral implants research, 2009. **20**: p. 124-133.

348. Lobna Abdel Aziz Aly and Nelly I Hammouda, *Evaluation of implant stability simultaneously placed with sinus lift augmented with putty versus powder form of demineralized bone matrix in atrophied posterior maxilla.* Future Dental Journal, 2017. **3**(1): p. 28-34.

349. Tassos Irinakis, *Efficacy of injectable demineralized bone matrix as graft material during sinus elevation surgery with simultaneous implant placement in the posterior maxilla: clinical evaluation of 49 sinuses.* Journal of Oral and Maxillofacial Surgery, 2011. **69**(1): p. 134-141.

350. Giampiero Cordioli, et al., *Maxillary sinus floor augmentation using bioactive glass granules and autogenous bone with simultaneous implant placement: clinical and histological findings.* Clinical Oral Implants Research, 2001. **12**(3): p. 270-278.
351. Paul S Tiwana, George M Kushner, and Richard H Haug, *Maxillary sinus augmentation.* Dental Clinics, 2006. **50**(3): p. 409-424.
352. Seckin Aydin, et al., *Cranioplasty: review of materials and techniques.* Journal of neurosciences in rural practice, 2011. **2**(02): p. 162-167.
353. Yong Jun Cho and Suk Hyung Kang, *Review of cranioplasty after decompressive craniectomy.* Korean journal of neurotrauma, 2017. **13**(1): p. 9.
354. Hayes B Gladstone, Michael W McDermott, and Darren D Cooke, *Implants for cranioplasty.* Otolaryngologic Clinics of North America, 1995. **28**(2): p. 381-400.
355. Jaakko M Piitulainen, et al., *Outcomes of cranioplasty with synthetic materials and autologous bone grafts.* World neurosurgery, 2015. **83**(5): p. 708-714.
356. Ann W Plum and Sherard A Tatum, *A comparison between autograft alone, bone cement, and demineralized bone matrix in cranioplasty.* The Laryngoscope, 2015. **125**(6): p. 1322-1327.
357. Arun K Gosain, *Hydroxyapatite cement paste cranioplasty for the treatment of temporal hollowing after cranial vault remodeling in a growing child.* Journal of Craniofacial Surgery, 1997. **8**(6): p. 506-511.
358. Hee Tae Koo, Jeongseok Oh, and Chan Yeong Heo, *Cranioplasty Using Three-Dimensional–Printed Polycaprolactone Implant and Free Latissimus Dorsi Musculocutaneous Flap in a Patient with Repeated Wound Problem following Titanium Cranioplasty.* Archives of Plastic Surgery, 2022. **49**(06): p. 740-744.
359. Woo-Shik Jeong, et al., *Clinical application of 3D-printed patient-specific polycaprolactone/beta tricalcium phosphate scaffold for complex zygomatico-maxillary defects.* Polymers, 2022. **14**(4): p. 740.
360. Bo-Yeon Hwang, Kwantae Noh, and Jung-Woo Lee, *Long-Term Follow-Up of a Novel Surgical Option Combining Fibula Free Flap and 3D-Bioprinted, Patient-Specific Polycaprolactone (PCL) Implant for Mandible Reconstruction.* Bioengineering, 2023. **10**(6): p. 684.
361. Ashim Gupta, et al., *Bone graft substitutes for spine fusion: a brief review.* World journal of orthopedics, 2015. **6**(6): p. 449.

362. Alexander R Vaccaro, Harrison A Stubbs, and Jon E Block, *Demineralized bone matrix composite grafting for posterolateral spinal fusion.* Orthopedics, 2007. **30**(7): p. 567.

363. Ho-Jung Chung, et al., *Surgical outcomes of anterior cervical fusion using deminaralized bone matrix as stand-alone graft material: single arm, pilot study.* Korean Journal of Spine, 2016. **13**(3): p. 114.

364. Howard S An, et al., *Comparison between allograft plus demineralized bone matrix versus autograft in anterior cervical fusion| a prospective multicenter study.* Spine, 1995. **20**(20): p. 2211-2216.

365. Panagiotis Korovessis, et al., *Correlative radiological, self-assessment and clinical analysis of evolution in instrumented dorsal and lateral fusion for degenerative lumbar spine disease. Autograft versus coralline hydroxyapatite.* European Spine Journal, 2005. **14**: p. 630-638.

366. Murray JS Beuerlein and Michael D McKee, *Calcium sulfates: what is the evidence?* Journal of orthopaedic trauma, 2010. **24**: p. S46-S51.

367. Isador H Lieberman, Daisuke Togawa, and Mark M Kayanja, *Vertebroplasty and kyphoplasty: filler materials.* The Spine Journal, 2005. **5**(6): p. S305-S316.

368. Afshin Gangi, Bruno A Kastler, and Jean-Louis Dietemann, *Percutaneous vertebroplasty guided by a combination of CT and fluoroscopy.* American Journal of Neuroradiology, 1994. **15**(1): p. 83-86.

369. Zhiwei He, et al., *Bone cements for percutaneous vertebroplasty and balloon kyphoplasty: current status and future developments.* Journal of orthopaedic translation, 2015. **3**(1): p. 1-11.

370. Ibrahim Khairoun, et al., *In vitro characterization and in vivo properties of a carbonated apatite bone cement.* Journal of Biomedical Materials Research: An Official Journal of The Society for Biomaterials, The Japanese Society for Biomaterials, and The Australian Society for Biomaterials and the Korean Society for Biomaterials, 2002. **60**(4): p. 633-642.

371. María Daniela Vlad, et al., *Osteogenic biphasic calcium sulphate dihydrate/iron-modified α-tricalcium phosphate bone cement for spinal applications: In vivo study.* Acta biomaterialia, 2010. **6**(2): p. 607-616.

372. Wanpeng Cao and Larry L Hench, *Bioactive materials.* Ceramics international, 1996. **22**(6): p. 493-507.

373. Dan Lundgren, et al., *Guided bone regeneration of cranial defects, using biodegradable barriers: an experimental pilot study in the rabbit.* Journal of cranio-maxillo-facial surgery, 1992. **20**(6): p. 257-260.
374. Amit S Mistry and Antonios G Mikos, *Tissue engineering strategies for bone regeneration*, in *Regenerative medicine II*. 2005, Springer. p. 1-22.
375. Xiaofeng Shen, et al., *Sequential and sustained release of SDF-1 and BMP-2 from silk fibroin-nanohydroxyapatite scaffold for the enhancement of bone regeneration.* Biomaterials, 2016. **106**: p. 205-216.
376. E Kon, et al., *Autologous bone marrow stromal cells loaded onto porous hydroxyapatite ceramic accelerate bone repair in critical-size defects of sheep long bones.* Journal of Biomedical Materials Research: An Official Journal of The Society for Biomaterials and The Japanese Society for Biomaterials, 2000. **49**(3): p. 328-337.
377. RJ Furlong and JF Osborn, *Fixation of hip prostheses by hydroxyapatite ceramic coatings.* The Journal of bone and joint surgery. British volume, 1991. **73**(5): p. 741-745.
378. Jie Yuan, et al., *Repair of canine mandibular bone defects with bone marrow stromal cells and porous β-tricalcium phosphate.* Biomaterials, 2007. **28**(6): p. 1005-1013.
379. Caixia Xu, et al., *Biocompatibility and osteogenesis of biomimetic Bioglass-Collagen-Phosphatidylserine composite scaffolds for bone tissue engineering.* Biomaterials, 2011. **32**(4): p. 1051-1058.
380. Brian D Holt, et al., *Graphene oxide as a scaffold for bone regeneration.* Wiley Interdisciplinary Reviews: Nanomedicine and Nanobiotechnology, 2017. **9**(3): p. e1437.
381. Hoda Elkhenany, et al., *Graphene supports in vitro proliferation and osteogenic differentiation of goat adult mesenchymal stem cells: potential for bone tissue engineering.* Journal of Applied Toxicology, 2015. **35**(4): p. 367-374.
382. Tapas R Nayak, et al., *Graphene for controlled and accelerated osteogenic differentiation of human mesenchymal stem cells.* ACS nano, 2011. **5**(6): p. 4670-4678.
383. Meena Mahmood, et al., *Role of carbonaceous nanomaterials in stimulating osteogenesis in mammalian bone cells.* Journal of Materials Chemistry B, 2013. **1**(25): p. 3220-3230.
384. Ana Marina Ferreira, et al., *Collagen for bone tissue regeneration.* Acta biomaterialia, 2012. **8**(9): p. 3191-3200.

385. Jayachandran Venkatesan and Se-Kwon Kim, *Chitosan composites for bone tissue engineering—an overview.* Marine drugs, 2010. **8**(8): p. 2252-2266.

386. Jayachandran Venkatesan, et al., *Preparation and characterization of carbon nanotube-grafted-chitosan–natural hydroxyapatite composite for bone tissue engineering.* Carbohydrate Polymers, 2011. **83**(2): p. 569-577.

387. Dawei Zhang, et al., *The development of collagen based composite scaffolds for bone regeneration.* Bioactive materials, 2017.

388. Xiaoyan Ren, et al., *Nanoparticulate mineralized collagen scaffolds induce in vivo bone regeneration independent of progenitor cell loading or exogenous growth factor stimulation.* Biomaterials, 2016. **89**: p. 67-78.

389. C Yashavantha Kumar, et al., *Calcium sulfate as bone graft substitute in the treatment of osseous bone defects, a prospective study.* Journal of clinical and diagnostic research: JCDR, 2013. **7**(12): p. 2926.

390. Uwe Gbureck, et al., *Resorbable dicalcium phosphate bone substitutes prepared by 3D powder printing.* Advanced Functional Materials, 2007. **17**(18): p. 3940-3945.

391. Jian Li, et al., *Visualizing angiogenesis by multiphoton microscopy in vivo in genetically modified 3D-PLGA/nHAp scaffold for calvarial critical bone defect repair.* JoVE (Journal of Visualized Experiments), 2017(127): p. e55381-e55381.

392. Sun-Woong Kang, et al., *Surface modification with fibrin/hyaluronic acid hydrogel on solid-free form-based scaffolds followed by BMP-2 loading to enhance bone regeneration.* Bone, 2011. **48**(2): p. 298-306.

393. Yin-Chih Fu, et al., *Optimized bone regeneration based on sustained release from three-dimensional fibrous PLGA/HAp composite scaffolds loaded with BMP-2.* Biotechnology and bioengineering, 2008. **99**(4): p. 996-1006.

394. Francesco Baino and Chiara Vitale-Brovarone, *Mechanical properties and reliability of glass–ceramic foam scaffolds for bone repair.* Materials Letters, 2014. **118**: p. 27-30.

395. A Nouri, *Titanium foam scaffolds for dental applications*, in *Metallic Foam Bone*. 2017, Elsevier. p. 131-160.

396. Amy Nommeots-Nomm, et al., *Highly degradable porous melt-derived bioactive glass foam scaffolds for bone regeneration.* Acta biomaterialia, 2017. **57**: p. 449-461.

397. Luis Diaz-Gomez, et al., *Biodegradable PCL/fibroin/hydroxyapatite porous scaffolds prepared by supercritical foaming for bone regeneration.* International journal of pharmaceutics, 2017. **527**(1-2): p. 115-125.

398. Jong Eun Lee, et al., *Effects of the controlled-released TGF-β1 from chitosan microspheres on chondrocytes cultured in a collagen/chitosan/glycosaminoglycan scaffold.* Biomaterials, 2004. **25**(18): p. 4163-4173.
399. Anat Perets, et al., *Enhancing the vascularization of three-dimensional porous alginate scaffolds by incorporating controlled release basic fibroblast growth factor microspheres.* Journal of Biomedical Materials Research Part A: An Official Journal of The Society for Biomaterials, The Japanese Society for Biomaterials, and The Australian Society for Biomaterials and the Korean Society for Biomaterials, 2003. **65**(4): p. 489-497.
400. Tiffany N Vo, F Kurtis Kasper, and Antonios G Mikos, *Strategies for controlled delivery of growth factors and cells for bone regeneration.* Advanced drug delivery reviews, 2012. **64**(12): p. 1292-1309.
401. Philipp S Lienemann, Matthias P Lutolf, and Martin Ehrbar, *Biomimetic hydrogels for controlled biomolecule delivery to augment bone regeneration.* Advanced drug delivery reviews, 2012. **64**(12): p. 1078-1089.
402. Otto S Kluin, et al., *Biodegradable vs non-biodegradable antibiotic delivery devices in the treatment of osteomyelitis.* Expert opinion on drug delivery, 2013. **10**(3): p. 341-351.
403. Joaquin García-García, et al., *Modification of the Polymer of a Bone Cement with Biodegradable Microspheres of PLGA and Loading with Daptomycin and Vancomycin Improve the Response to Bone Tissue Infection.* Polymers, 2022. **14**(5): p. 888.
404. Charles N Cornell and Joseph M Lane, *Current understanding of osteoconduction in bone regeneration.* Clinical Orthopaedics and Related Research (1976-2007), 1998. **355**: p. S267-S273.
405. Masahiro Yoneda, et al., *Repair of an intercalated long bone defect with a synthetic biodegradable bone-inducing implant.* Biomaterials, 2005. **26**(25): p. 5145-5152.
406. Naomi Kobayashi, et al., *Brief ultrasonication improves detection of biofilm-formative bacteria around a metal implant.* Clinical Orthopaedics and Related Research®, 2007. **457**: p. 210-213.
407. Kee-Yong Ha, Yang-Guk Chung, and Seung-Joon Ryoo, *Adherence and biofilm formation of Staphylococcus epidermidis and Mycobacterium tuberculosis on various spinal implants.* Spine, 2005. **30**(1): p. 38-43.

408. SJ Piliero, et al., *Histopathology of oral endosteal metallic implants in dogs.* Journal of Dental Research, 1973. **52**(5): p. 1117-1127.
409. Irena Gotman, *Characteristics of metals used in implants.* Journal of endourology, 1997. **11**(6): p. 383-389.
410. Yasumasa Akagawa, et al., *Tissue reaction to implanted biomaterials.* The Journal of Prosthetic Dentistry, 1985. **53**(5): p. 681-686.
411. JH Purk, *Morphologic and structural analysis of material-tissue interfaces relevant to dental reconstruction*, in *Material-Tissue Interfacial Phenomena*. 2017, Elsevier. p. 205-229.
412. Xiaohua Liu and Peter X Ma, *Polymeric scaffolds for bone tissue engineering.* Annals of biomedical engineering, 2004. **32**(3): p. 477-486.
413. Kurosh Rezwan, et al., *Biodegradable and bioactive porous polymer/inorganic composite scaffolds for bone tissue engineering.* Biomaterials, 2006. **27**(18): p. 3413-3431.
414. Masaaki Chazono, et al., *Bone formation and bioresorption after implantation of injectable β-tricalcium phosphate granules–hyaluronate complex in rabbit bone defects.* Journal of Biomedical Materials Research Part A: An Official Journal of The Society for Biomaterials, The Japanese Society for Biomaterials, and The Australian Society for Biomaterials and the Korean Society for Biomaterials, 2004. **70**(4): p. 542-549.
415. M Bohner, *Calcium orthophosphates in medicine: from ceramics to calcium phosphate cements.* Injury, 2000. **31**: p. D37-D47.
416. Jeffrey M Spivak and Amir Hasharoni, *Use of hydroxyapatite in spine surgery.* European Spine Journal, 2001. **10**(2): p. S197-S204.
417. Michiko Sakamoto, *Development and evaluation of superporous hydroxyapatite ceramics with triple pore structure as bone tissue scaffold.* Journal of the Ceramic Society of Japan, 2010. **118**(1380): p. 753-757.
418. Vivekanand Sabanna Kattimani, Sudheer Kondaka, and Krishna Prasad Lingamaneni, *Hydroxyapatite–-Past, present, and future in bone regeneration.* Bone and Tissue Regeneration Insights, 2016. **7**: p. BTRI. S36138.
419. Satyavrata Samavedi, Abby R Whittington, and Aaron S Goldstein, *Calcium phosphate ceramics in bone tissue engineering: a review of properties and their influence on cell behavior.* Acta biomaterialia, 2013. **9**(9): p. 8037-8045.

420. LC Junqueira and J Carneiro, *Basic Histology, text & atlas, MC Graw Hill*. 2003, Medical publishing division, New York, London, Sydney. p. 144.
421. Sonja Ellen Lobo and Treena Livingston Arinzeh, *Biphasic calcium phosphate ceramics for bone regeneration and tissue engineering applications.* Materials, 2010. **3**(2): p. 815-826.
422. Stefan Zwingenberger, et al., *Recommendations and considerations for the use of biologics in orthopedic surgery.* BioDrugs, 2012. **26**(4): p. 245-256.
423. Warren L Grayson, et al., *Engineering anatomically shaped human bone grafts.* Proceedings of the National Academy of Sciences, 2010. **107**(8): p. 3299-3304.
424. Ali Moradi, et al., *Chondrogenic potential of physically treated bovine cartilage matrix derived porous scaffolds on human dermal fibroblast cells.* Journal of biomedical materials research Part A, 2016. **104**(1): p. 245-256.
425. Christopher R Rowland, et al., *The effects of crosslinking of scaffolds engineered from cartilage ECM on the chondrogenic differentiation of MSCs.* Biomaterials, 2013. **34**(23): p. 5802-5812.
426. Michael J Sawkins, et al., *Hydrogels derived from demineralized and decellularized bone extracellular matrix.* Acta biomaterialia, 2013. **9**(8): p. 7865-7873.
427. Noura Alom, et al., *Bone extracellular matrix hydrogel enhances osteogenic differentiation of C2C12 myoblasts and mouse primary calvarial cells.* Journal of Biomedical Materials Research Part B: Applied Biomaterials, 2018. **106**(2): p. 900-908.
428. Francesco Paduano, et al., *Decellularized bone extracellular matrix and human dental pulp stem cells as a construct for bone regeneration.* Journal of Biomaterials science, Polymer edition, 2017. **28**(8): p. 730-748.
429. Fatemeh Kabirian and Masoud Mozafari, *Decellularized ECM-derived bioinks: Prospects for the future.* Methods, 2020. **171**: p. 108-118.
430. Byoung Soo Kim, et al., *Decellularized extracellular matrix: a step towards the next generation source for bioink manufacturing.* Biofabrication, 2017. **9**(3): p. 034104.
431. Alperen Abaci and Murat Guvendiren, *Designing decellularized extracellular matrix-based bioinks for 3D bioprinting.* Advanced Healthcare Materials, 2020. **9**(24): p. 2000734.
432. Richard A Thibault, et al., *Osteogenic differentiation of mesenchymal stem cells on pregenerated extracellular matrix scaffolds in the absence of osteogenic cell culture supplements.* Tissue Engineering Part A, 2010. **16**(2): p. 431-440.

433. Jiehong Liao, et al., *Modulation of osteogenic properties of biodegradable polymer/extracellular matrix scaffolds generated with a flow perfusion bioreactor.* Acta biomaterialia, 2010. **6**(7): p. 2386-2393.
434. Beob Soo Kim, et al., *Recellularization of decellularized human adipose-tissue-derived extracellular matrix sheets with other human cell types.* Cell and tissue research, 2012. **348**(3): p. 559-567.
435. Jianfeng Zhang, et al., *Preparation and evaluation of tibia-and calvarium-derived decellularized periosteum scaffolds.* ACS Biomaterials Science & Engineering, 2017. **3**(12): p. 3503-3514.
436. Cameron RM Black, et al., *Bone tissue engineering.* Current molecular biology reports, 2015. **1**(3): p. 132-140.
437. R. Langer and J. P. Vacanti, *Tissue engineering.* Science, 1993. **260**(5110): p. 920-926.
438. Linda G Griffith and Gail Naughton, *Tissue engineering--current challenges and expanding opportunities.* science, 2002. **295**(5557): p. 1009-1014.
439. María Vallet-Regí, Montserrat Colilla, and Blanca González, *Medical applications of organic–inorganic hybrid materials within the field of silica-based bioceramics.* Chemical Society Reviews, 2011. **40**(2): p. 596-607.
440. Daniel Howard, et al., *Tissue engineering: strategies, stem cells and scaffolds.* Journal of anatomy, 2008. **213**(1): p. 66-72.
441. Robert Bielby, Elena Jones, and Dennis McGonagle, *The role of mesenchymal stem cells in maintenance and repair of bone.* Injury, 2007. **38**(1): p. S26-S32.
442. G Camberlain, et al., *Mesenchymal stem cells: their phenotype, differentiation capacity, immunological features, and potential for homing.* Stem Cells, 2007. **25**(11): p. 2739-2749.
443. Massimo Dominici, et al., *Heterogeneity of multipotent mesenchymal stromal cells: from stromal cells to stem cells and vice versa.* Transplantation, 2009. **87**(9S): p. S36-S42.
444. Mark F Pittenger, et al., *Multilineage potential of adult human mesenchymal stem cells.* science, 1999. **284**(5411): p. 143-147.
445. MLBK Dominici, et al., *Minimal criteria for defining multipotent mesenchymal stromal cells. The International Society for Cellular Therapy position statement.* Cytotherapy, 2006. **8**(4): p. 315-317.

446. David C Colter, Ichiro Sekiya, and Darwin J Prockop, *Identification of a subpopulation of rapidly self-renewing and multipotential adult stem cells in colonies of human marrow stromal cells.* Proceedings of the National Academy of Sciences, 2001. **98**(14): p. 7841-7845.
447. Katia Mareschi, et al., *Multipotent mesenchymal stromal stem cell expansion by plating whole bone marrow at a low cellular density: a more advantageous method for clinical use.* Stem cells international, 2012. **2012**.
448. Michelle Griffin, et al., *Characteristics of human adipose derived stem cells in scleroderma in comparison to sex and age matched normal controls: implications for regenerative medicine.* Stem cell research & therapy, 2017. **8**(1): p. 23.
449. Patrick C Baer and Helmut Geiger, *Adipose-derived mesenchymal stromal/stem cells: tissue localization, characterization, and heterogeneity.* Stem cells international, 2012. **2012**.
450. Henk Rozemuller, et al., *Prospective isolation of mesenchymal stem cells from multiple mammalian species using cross-reacting anti-human monoclonal antibodies.* Stem cells and development, 2010. **19**(12): p. 1911-1921.
451. Sally A Boxall and Elena Jones, *Markers for characterization of bone marrow multipotential stromal cells.* Stem cells international, 2012. **2012**.
452. Mihaela Crisan, et al., *A perivascular origin for mesenchymal stem cells in multiple human organs.* Cell stem cell, 2008. **3**(3): p. 301-313.
453. Arnold I Caplan, *All MSCs are pericytes?* Cell stem cell, 2008. **3**(3): p. 229-230.
454. AJ Frieedenstein, et al., *Hetrotopic of bone marrow. Analysis of precursor cells for osteogenic and hematopoetic tissue.* Transplantacion., 1968. **6**(2): p. 230.
455. AIa Fridenshteĭn, II Piatetskiĭ-Shapiro, and KV Petrakova, *Osteogenesis in transplants of bone marrow cells.* Arkhiv anatomii, gistologii i embriologii, 1969. **56**(3): p. 3.
456. Susanne Kern, et al., *Comparative analysis of mesenchymal stem cells from bone marrow, umbilical cord blood, or adipose tissue.* Stem cells, 2006. **24**(5): p. 1294-1301.
457. Dolores Baksh, Raphael Yao, and Rocky S Tuan, *Comparison of proliferative and multilineage differentiation potential of human mesenchymal stem cells derived from umbilical cord and bone marrow.* Stem cells, 2007. **25**(6): p. 1384-1392.
458. Yumi Fukuchi, et al., *Human placenta-derived cells have mesenchymal stem/progenitor cell potential.* Stem cells, 2004. **22**(5): p. 649-658.

459. GT-J Huang, S Gronthos, and S Shi, *Mesenchymal stem cells derived from dental tissues vs. those from other sources: their biology and role in regenerative medicine.* Journal of dental research, 2009. **88**(9): p. 792-806.

460. Martin Körbling and Paolo Anderlini, *Peripheral blood stem cell versus bone marrow allotransplantation: does the source of hematopoietic stem cells matter?* Blood, 2001. **98**(10): p. 2900-2908.

461. John K Fraser, et al., *Fat tissue: an underappreciated source of stem cells for biotechnology.* Trends in biotechnology, 2006. **24**(4): p. 150-154.

462. Yanxia Zhu, et al., *Adipose-derived stem cell: a better stem cell than BMSC.* Cell biochemistry and function, 2008. **26**(6): p. 664-675.

463. Daniel A De Ugarte, et al., *Comparison of multi-lineage cells from human adipose tissue and bone marrow.* Cells tissues organs, 2003. **174**(3): p. 101-109.

464. John K Fraser, et al., *Adipose-derived stem cells*, in *Mesenchymal Stem Cells*. 2008, Springer. p. 59-67.

465. Sofia Bougioukli, et al., *Gene Therapy for Bone Repair Using Human Cells: Superior Osteogenic Potential of Bone Morphogenetic Protein 2–Transduced Mesenchymal Stem Cells Derived from Adipose Tissue Compared to Bone Marrow.* Human gene therapy, 2018. **29**(4): p. 507-519.

466. Krisztina Szöke, et al., *The effect of medium composition on deposition of collagen type 1 and expression of osteogenic genes in mesenchymal stem cells derived from human adipose tissue and bone marrow.* Process Biochemistry, 2017. **59**: p. 321-328.

467. Fabian Langenbach and Jörg Handschel, *Effects of dexamethasone, ascorbic acid and β-glycerophosphate on the osteogenic differentiation of stem cells in vitro.* Stem cell research & therapy, 2013. **4**(5): p. 117.

468. MJ Coelho and MH Fernandes, *Human bone cell cultures in biocompatibility testing. Part II: effect of ascorbic acid, β-glycerophosphate and dexamethasone on osteoblastic differentiation.* Biomaterials, 2000. **21**(11): p. 1095-1102.

469. GARY S STEIN and JANE B LIAN, *Molecular mechanisms mediating developmental and hormone-regulated expression of genes in osteoblasts: an integrated relationship of cell growth and differentiation*, in *Cellular and molecular biology of bone*. 1993, Elsevier. p. 47-95.

470. Ego Seeman, *Bone quality: the material and structural basis of bone strength.* Journal of bone and mineral metabolism, 2008. **26**(1): p. 1-8.

471. Shirwin M Pockwinse, et al., *Expression of cell growth and bone specific genes at single cell resolution during development of bone tissue-like organization in primary osteoblast cultures.* Journal of cellular biochemistry, 1992. **49**(3): p. 310-323.
472. Thomas A Owen, et al., *Progressive development of the rat osteoblast phenotype in vitro: reciprocal relationships in expression of genes associated with osteoblast proliferation and differentiation during formation of the bone extracellular matrix.* Journal of cellular physiology, 1990. **143**(3): p. 420-430.
473. Gary S Stein, Jane B Lian, and Thomas A Owen, *Relationship of cell growth to the regulation of tissue-specific gene expression during osteoblast differentiation.* The FASEB journal, 1990. **4**(13): p. 3111-3123.
474. Toshihisa Komori, *Regulation of osteoblast differentiation by Runx2*, in *Osteoimmunology*. 2009, Springer. p. 43-49.
475. John D Termine, et al., *Osteonectin, a bone-specific protein linking mineral to collagen.* Cell, 1981. **26**(1): p. 99-105.
476. Mark E Bolander, *Regulation of fracture repair by growth factors.* Proceedings of the Society for Experimental Biology and Medicine, 1992. **200**(2): p. 165-170.
477. Thomas A Linkhart, Subburaman Mohan, and David J Baylink, *Growth factors for bone growth and repair: IGF, TGFβ and BMP.* Bone, 1996. **19**(1): p. S1-S12.
478. Thomas A Einhorn, *The cell and molecular biology of fracture healing.* Clinical Orthopaedics and Related Research®, 1998. **355**: p. S7-S21.
479. Xiaolan Du, et al., *Role of FGFs/FGFRs in skeletal development and bone regeneration.* Journal of cellular physiology, 2012. **227**(12): p. 3731-3743.
480. Diederik HR Kempen, et al., *Growth factor interactions in bone regeneration.* Tissue Engineering Part B: Reviews, 2010. **16**(6): p. 551-566.
481. Arnold I Caplan and Diego Correa, *PDGF in bone formation and regeneration: new insights into a novel mechanism involving MSCs.* Journal of Orthopaedic Research, 2011. **29**(12): p. 1795-1803.
482. Tae-Hyun Kim, et al., *Efficacy of mesoporous silica nanoparticles in delivering BMP-2 plasmid DNA for in vitro osteogenic stimulation of mesenchymal stem cells.* Journal of Biomedical Materials Research Part A, 2013. **101**(6): p. 1651-1660.
483. Janette N Zara, et al., *High doses of bone morphogenetic protein 2 induce structurally abnormal bone and inflammation in vivo.* Tissue Engineering Part A, 2011. **17**(9-10): p. 1389-1399.

484. G Zellin and A Linde, *Effects of recombinant human fibroblast growth factor-2 on osteogenic cell populations during orthopic osteogenesis in vivo.* Bone, 2000. **26**(2): p. 161-168.
485. Nancy E Epstein, *Complications due to the use of BMP/INFUSE in spine surgery: the evidence continues to mount.* Surgical neurology international, 2013. **4**(Suppl 5): p. S343.
486. Emily Jane Woo, *Recombinant human bone morphogenetic protein-2: adverse events reported to the Manufacturer and User Facility Device Experience database.* The Spine Journal, 2012. **12**(10): p. 894-899.
487. A Sethi, et al. *interbody Fusion With Allograft And Rhbmp-2 Leads To Consistent Fusion But Early Subsidence*. in *Orthopaedic Proceedings*. 2009. The British Editorial Society of Bone & Joint Surgery.
488. Rahul Vaidya, et al., *Complications in the use of rhBMP-2 in PEEK cages for interbody spinal fusions.* Clinical Spine Surgery, 2008. **21**(8): p. 557-562.
489. Mario Ronga, et al., *Clinical applications of growth factors in bone injuries: experience with BMPs.* Injury, 2013. **44**: p. S34-S39.
490. Eugene J Carragee, et al., *Cancer risk after use of recombinant bone morphogenetic protein-2 for spinal arthrodesis.* JBJS, 2013. **95**(17): p. 1537-1545.
491. Natalia A Kokorina, et al., *rhBMP-2 has adverse effects on human oral carcinoma cell lines in vivo.* The Laryngoscope, 2012. **122**(1): p. 95-102.
492. Dingding Wang, et al., *Induction of estrogen receptor α-36 expression by bone morphogenetic protein 2 in breast cancer cell lines.* Molecular medicine reports, 2012. **6**(3): p. 591-596.
493. Steven M Koehler, et al., *Does BMP-2 Really Cause Cancer? A Systematic Review of the Literature.* The Spine Journal, 2012. **12**(9): p. S90.
494. Jayesh P Thawani, et al., *Bone morphogenetic proteins and cancer: review of the literature.* Neurosurgery, 2010. **66**(2): p. 233-246.
495. Ahmad Oryan, Soodeh Alidadi, and Ali Moshiri, *Platelet-rich plasma for bone healing and regeneration.* Expert opinion on biological therapy, 2016. **16**(2): p. 213-232.
496. Lucía Gato-Calvo, et al., *Platelet-rich plasma in osteoarthritis treatment: review of current evidence.* Therapeutic advances in chronic disease, 2019. **10**: p. 2040622319825567.

497. Robert E Marx, *Platelet-rich plasma (PRP): what is PRP and what is not PRP?* Implant dentistry, 2001. **10**(4): p. 225-228.

498. J Xu, et al., *Platelet-rich plasma and regenerative dentistry.* Australian dental journal, 2020. **65**(2): p. 131-142.

499. Carola Cavallo, et al., *Platelet-rich plasma: the choice of activation method affects the release of bioactive molecules.* BioMed Research International, 2016. **2016**.

500. B Di Matteo, et al., *Platelet-rich plasma: evidence for the treatment of patellar and Achilles tendinopathy—a systematic review.* Musculoskeletal surgery, 2015. **99**(1): p. 1-9.

501. Daniel Steller, et al., *Impact of incubation method on the release of growth factors in non-Ca2+-activated PRP, Ca2+-activated PRP, PRF and A-PRF.* Journal of Cranio-Maxillofacial Surgery, 2019. **47**(2): p. 365-372.

502. Eduardo Anitua, Mikel Sánchez, and Gorka Orive, *The importance of understanding what is platelet-rich growth factor (PRGF) and what is not.* Journal of Shoulder and Elbow Surgery, 2011. **20**(1): p. e23-e24.

503. A Suchetha, et al., *Platelet concentration in platelet concentrates and periodontal regeneration-unscrambling the ambiguity.* Contemporary clinical dentistry, 2015. **6**(4): p. 510.

504. Robinder S Dhillon, Edward M Schwarz, and Michael D Maloney, *Platelet-rich plasma therapy-future or trend?* Arthritis research & therapy, 2012. **14**(4): p. 1-10.

505. Alberto Hernandez-Fernandez, et al., *Effect of administration of platelet-rich plasma in early phases of distraction osteogenesis: an experimental study in an ovine femur model.* Injury, 2013. **44**(7): p. 901-907.

506. Akishige Hokugo, et al., *Augmented bone regeneration activity of platelet-rich plasma by biodegradable gelatin hydrogel.* Tissue engineering, 2005. **11**(7-8): p. 1224-1233.

507. Behnam Bakhtiarimoghadam, et al., *Comparison capacity of collagen hydrogel, mix-powder and in situ hydroxyapatite/collagen hydrogelscaffolds with and without mesenchymal stem cells and platelet-rich plasma in regeneration of critical sized bone defect in a rabbit animal model.* Journal of Biomedical Materials Research Part B: Applied Biomaterials, 2021. **109**(12): p. 2199-2212.

508. Yang-Hee Kim, Hiroyuki Furuya, and Yasuhiko Tabata, *Enhancement of bone regeneration by dual release of a macrophage recruitment agent and platelet-rich plasma from gelatin hydrogels.* Biomaterials, 2014. **35**(1): p. 214-224.

509. So-Ra Son, et al., *Platelet-rich plasma encapsulation in hyaluronic acid/gelatin-BCP hydrogel for growth factor delivery in BCP sponge scaffold for bone regeneration.* Journal of Biomaterials Applications, 2015. **29**(7): p. 988-1002.

510. Maria Nagata, et al., *Influence of the proportion of particulate autogenous bone graft/platelet-rich plasma on bone healing in critical-size defects: an immunohistochemical analysis in rat calvaria.* Bone, 2009. **45**(2): p. 339-345.

511. Maria J Nagata, et al., *Influence of the ratio of particulate autogenous bone graft/platelet-rich plasma on bone healing in critical-size defects: A histologic and histometric study in rat calvaria.* Journal of Orthopaedic Research, 2010. **28**(4): p. 468-473.

512. RECM Mooren, et al., *The effect of platelet-rich plasma on early and late bone healing: an experimental study in goats.* International journal of oral and maxillofacial surgery, 2007. **36**(7): p. 626-631.

513. Francisco Forriol, et al., *Platelet-rich plasma, rhOP-1®(rhBMP-7) and frozen rib allograft for the reconstruction of bony mandibular defects in sheep. A pilot experimental study.* Injury, 2009. **40**: p. S44-S49.

514. Christiaan JA van Bergen, et al., *Demineralized bone matrix and platelet-rich plasma do not improve healing of osteochondral defects of the talus: an experimental goat study.* Osteoarthritis and Cartilage, 2013. **21**(11): p. 1746-1754.

515. Minas D Leventis, et al., *Experimental study of the effect of autologous platelet-rich plasma on the early phases of osteoinduction by allogenic demineralized bone matrix.* Implant dentistry, 2012. **21**(5): p. 399-405.

516. Fupo He, et al., *Improving bone repair of femoral and radial defects in rabbit by incorporating PRP into PLGA/CPC composite scaffold with unidirectional pore structure.* Journal of Biomedical Materials Research Part A, 2015. **103**(4): p. 1312-1324.

517. Michael R Sarkar, et al., *Bone formation in a long bone defect model using a platelet-rich plasma-loaded collagen scaffold.* Biomaterials, 2006. **27**(9): p. 1817-1823.

518. KM Sajesh, et al., *Sequential layer-by-layer electrospinning of nano SrCO3/PRP loaded PHBV fibrous scaffold for bone tissue engineering.* Composites Part B: Engineering, 2016. **99**: p. 445-452.

519. Kenji Ito, et al., *Osteogenic potential of injectable tissue-engineered bone: a comparison among autogenous bone, bone substitute (Bio-Oss®), platelet-rich plasma, and tissue-engineered bone with respect to their mechanical properties and*

histological findings. Journal of Biomedical Materials Research Part A: An Official Journal of The Society for Biomaterials, The Japanese Society for Biomaterials, and The Australian Society for Biomaterials and the Korean Society for Biomaterials, 2005. **73**(1): p. 63-72.

520. SR Kanthan, et al., *Platelet-rich plasma (PRP) enhances bone healing in non-united critical-sized defects: a preliminary study involving rabbit models.* Injury, 2011. **42**(8): p. 782-789.
521. Gregory Faratzis, et al., *Effect of autologous platelet-rich plasma in combination with a biphasic synthetic graft material on bone healing in critical-size cranial defects.* Journal of Craniofacial Surgery, 2012. **23**(5): p. 1318-1323.
522. Alice Roffi, et al., *Platelet-rich plasma for the treatment of bone defects: from pre-clinical rational to evidence in the clinical practice. A systematic review.* International orthopaedics, 2017. **41**(2): p. 221-237.
523. Allan Fernando Giovanini, et al., *Platelet-rich plasma (PRP) impairs the craniofacial bone repair associated with its elevated TGF-β levels and modulates the co-expression between collagen III and α-smooth muscle actin.* Journal of Orthopaedic Research, 2011. **29**(3): p. 457-463.
524. Aaron S Goldstein, et al., *Effect of convection on osteoblastic cell growth and function in biodegradable polymer foam scaffolds.* Biomaterials, 2001. **22**(11): p. 1279-1288.
525. J Klein-Nulend, RG Bacabac, and MG Mullender, *Mechanobiology of bone tissue.* Pathologie biologie, 2005. **53**(10): p. 576-580.
526. Chenyu Huang and Rei Ogawa, *Mechanotransduction in bone repair and regeneration.* The FASEB Journal, 2010. **24**(10): p. 3625-3632.
527. Ivan Martin, David Wendt, and Michael Heberer, *The role of bioreactors in tissue engineering.* Trends in biotechnology, 2004. **22**(2): p. 80-86.
528. Erin Salter, et al., *Bone tissue engineering bioreactors: a role in the clinic?* Tissue Engineering Part B: Reviews, 2011. **18**(1): p. 62-75.
529. Martina Sladkova and Giuseppe Maria de Peppo, *Bioreactor systems for human bone tissue engineering.* Processes, 2014. **2**(2): p. 494-525.
530. Peter Reher, et al., *The stimulation of bone formation in vitro by therapeutic ultrasound.* Ultrasound in Medicine and Biology, 1997. **23**(8): p. 1251-1258.
531. Thomas K Kristiansen, et al., *Accelerated healing of distal radial fractures with the use of specific, low-intensity ultrasound. A multicenter, prospective, randomized, double-blind, placebo-controlled study.* JBJS, 1997. **79**(7): p. 961-973.

532. Shyu-Jye Wang, et al., *Low intensity ultrasound treatment increases strength in a rat femoral fracture model.* Journal of Orthopaedic Research, 1994. **12**(1): p. 40-47.

533. Kyung Shin Kang, et al., *Osteogenic Differentiation of Human Adipose-Derived Stem Cells Can Be Accelerated by Controlling the Frequency of Continuous Ultrasound.* Journal of Ultrasound in Medicine, 2013. **32**(8): p. 1461-1470.

534. Zhen Li, et al., *Chondrogenesis of human bone marrow mesenchymal stem cells in fibrin–polyurethane composites is modulated by frequency and amplitude of dynamic compression and shear stress.* Tissue Engineering Part A, 2009. **16**(2): p. 575-584.

535. O Schätti, et al., *A combination of shear and dynamic compression leads to mechanically induced chondrogenesis of human mesenchymal stem cells.* Eur Cell Mater, 2011. **22**: p. 214-225.

536. Aurore Van de Walle, Claire Wilhelm, and Nathalie Luciani, *3D magnetic stem cell aggregation and bioreactor maturation for cartilage regeneration.* Journal of visualized experiments: JoVE, 2017.

537. Ming-Tzu Tsai, et al., *Modulation of osteogenesis in human mesenchymal stem cells by specific pulsed electromagnetic field stimulation.* Journal of Orthopaedic Research, 2009. **27**(9): p. 1169-1174.

538. Jon Dobson, et al., *Principles and design of a novel magnetic force mechanical conditioning bioreactor for tissue engineering, stem cell conditioning, and dynamic in vitro screening.* IEEE transactions on nanobioscience, 2006. **5**(3): p. 173-177.

539. O Raabe, et al., *Effect of extracorporeal shock wave on proliferation and differentiation of equine adipose tissue-derived mesenchymal stem cells in vitro.* American journal of stem cells, 2013. **2**(1): p. 62.

540. Dahui Sun, et al., *Shockwaves induce osteogenic differentiation of human mesenchymal stem cells through ATP release and activation of P2X7 receptors.* Stem Cells, 2013. **31**(6): p. 1170-1180.

541. Christina Maria Anna Pia Schuh, et al., *In vitro extracorporeal shock wave treatment enhances stemness and preserves multipotency of rat and human adipose-derived stem cells.* Cytotherapy, 2014. **16**(12): p. 1666-1678.

542. Lisa E Freed and Gordana Vunjak-Novakovic, *Spaceflight bioreactor studies of cells and tissues*, in *Advances in space biology and medicine*. 2002, Elsevier. p. 177-195.

543. G Vunjak-Novakovic, et al., *Bioreactor cultivation conditions modulate the composition and mechanical properties of tissue-engineered cartilage.* Journal of Orthopaedic Research, 1999. **17**(1): p. 130-138.

544. Philippe Sucosky, et al., *Fluid mechanics of a spinner-flask bioreactor.* Biotechnology and bioengineering, 2004. **85**(1): p. 34-46.

545. Yves Martin and Patrick Vermette, *Bioreactors for tissue mass culture: design, characterization, and recent advances.* Biomaterials, 2005. **26**(35): p. 7481-7503.

546. A Hofmann, et al., *Bioengineered human bone tissue using autogenous osteoblasts cultured on different biomatrices.* Journal of Biomedical Materials Research Part A: An Official Journal of The Society for Biomaterials, The Japanese Society for Biomaterials, and The Australian Society for Biomaterials and the Korean Society for Biomaterials, 2003. **67**(1): p. 191-199.

547. Anne Bernhardt, et al., *Optimization of culture conditions for osteogenically-induced mesenchymal stem cells in β-tricalcium phosphate ceramics with large interconnected channels.* Journal of tissue engineering and regenerative medicine, 2011. **5**(6): p. 444-453.

548. Doerte Matziolis, et al., *Osteogenic predifferentiation of human bone marrow-derived stem cells by short-term mechanical stimulation.* The open orthopaedics journal, 2011. **5**: p. 1.

549. M Jagodzinski, et al., *Influence of perfusion and cyclic compression on proliferation and differentiation of bone marrow stromal cells in 3-dimensional culture.* Journal of biomechanics, 2008. **41**(9): p. 1885-1891.

550. John A Ogden, Anna Tóth-Kischkat, and Reiner Schultheiss, *Principles of shock wave therapy.* Clinical Orthopaedics and Related Research (1976-2007), 2001. **387**: p. 8-17.

551. Jun V Kaude, et al., *Renal morphology and function immediately after extracorporeal shock-wave lithotripsy.* American journal of roentgenology, 1985. **145**(2): p. 305-313.

552. Anna M Weihs, et al., *Shockwave treatment enhances cell proliferation and improves wound healing by ATP release coupled extracellular signal-regulated kinase (ERK) activation.* Journal of Biological Chemistry, 2014: p. jbc. M114. 580936.

553. Kristin Dietz-Laursonn, et al., *In-vitro cell treatment with focused shockwaves—influence of the experimental setup on the sound field and biological reaction.* Journal of therapeutic ultrasound, 2016. **4**(1): p. 1-14.

554. Feng-Sheng Wang, et al., *Physical shock wave mediates membrane hyperpolarization and Ras activation for osteogenesis in human bone marrow stromal cells.* Biochemical and biophysical research communications, 2001. **287**(3): p. 648-655.

555. Alexander Hofmann, et al., *Extracorporeal shock wave-mediated changes in proliferation, differentiation, and gene expression of human osteoblasts.* Journal of Trauma and Acute Care Surgery, 2008. **65**(6): p. 1402-1410.
556. Xiongliang Zhang, et al., *The dose–effect relationship in extracorporeal shock wave therapy: the optimal parameter for extracorporeal shock wave therapy.* journal of surgical research, 2014. **186**(1): p. 484-492.
557. Kerstin Neumann, *Untersuchung der Wirkung Extrakorporaler Stoßwellentherapie auf die Haut-Effekte der Mechanotransduktion auf Fibroblasten in-vitro und Analyse von Hautveränderungen in-vivo*. 2012, Staats-und Universitätsbibliothek Hamburg Carl von Ossietzky.
558. P Steinbach, et al., *In vitro investigations on cellular damage induced by high energy shock waves.* Ultrasound in medicine & biology, 1992. **18**(8): p. 691-699.
559. Roberto Frairia, et al., *High energy shock waves (HESW) enhance paclitaxel cytotoxicity in MCF-7 cells.* Breast cancer research and treatment, 2003. **81**(1): p. 11-19.
560. Johannes Holfeld, et al., *Shock wave application to cell cultures.* JoVE (Journal of Visualized Experiments), 2014(86): p. e51076.
561. Jan Willem Van Dongen, et al., *The cytocidal effect of high energy shock waves on human prostatic tumour cell lines.* European Journal of Cancer and Clinical Oncology, 1989. **25**(8): p. 1173-1179.
562. Dah-Shyong Yu, et al., *Effects of high-energy shock waves onmurine renal cell carcinoma.* Urology, 1991. **38**(6): p. 571-576.
563. WL Strohmaier, et al., *Damaging effects of high energy shock waves on cultured Madin Darby canine kidney (MDCK) cells.* Urological Research, 1990. **18**(4): p. 255-258.
564. Vincent P Laudone, et al., *Cytotoxicity of high energy shock waves: methodologic considerations.* The Journal of urology, 1989. **141**(4): p. 965-968.
565. Henrike Renz and Stefan Rupp, *Effects of shock waves on chondrocytes and their relevance in clinical practice.* Archives of orthopaedic and trauma surgery, 2009. **129**(5): p. 641-647.
566. Frank Suhr, et al., *Cell biological effects of mechanical stimulations generated by focused extracorporeal shock wave applications on cultured human bone marrow stromal cells.* Stem cell research, 2013. **11**(2): p. 951-964.

567. Ching-Jen Wang, et al., *The effects of shockwave on bone healing and systemic concentrations of nitric oxide (NO), TGF-β1, VEGF and BMP-2 in long bone non-unions.* Nitric oxide, 2009. **20**(4): p. 298-303.
568. Eric A Elster, et al., *Extracorporeal shock wave therapy for nonunion of the tibia.* Journal of orthopaedic trauma, 2010. **24**(3): p. 133-141.
569. W Schaden, A Fischer, and A Sailler, *Extracorporeal shock wave therapy of nonunion or delayed osseous union.* Clinical Orthopaedics and Related Research (1976-2007), 2001. **387**: p. 90-94.
570. Olivia J Oginska, et al., *Extracorporeal Shock Wave Therapy for the Treatment of Non-Union of a Canine Mandibular Fracture.* VCOT Open, 2019. **2**(02): p. e56-e59.
571. Gerald Haupt, *Use of extracorporeal shock waves in the treatment of pseudarthrosis, tendinopathy and other orthopedic diseases.* The Journal of urology, 1997. **158**(1): p. 4-11.
572. Marije T van Leeuwen, Johannes Zwerver, and Inge van den Akker-Scheek, *Extracorporeal shockwave therapy for patellar tendinopathy: a review of the literature.* British journal of sports medicine, 2009. **43**(3): p. 163-168.
573. John P Furia, *High-energy extracorporeal shock wave therapy as a treatment for chronic noninsertional Achilles tendinopathy.* The American journal of sports medicine, 2008. **36**(3): p. 502-508.
574. Thomas Hausner, et al., *Improved rate of peripheral nerve regeneration induced by extracorporeal shock wave treatment in the rat.* Experimental neurology, 2012. **236**(2): p. 363-370.
575. Rainer Mittermayr, et al., *Extracorporeal shock wave therapy (ESWT) minimizes ischemic tissue necrosis irrespective of application time and promotes tissue revascularization by stimulating angiogenesis.* Annals of surgery, 2011. **253**(5): p. 1024-1032.
576. Alexandra Aicher, et al., *Low-energy shock wave for enhancing recruitment of endothelial progenitor cells: a new modality to increase efficacy of cell therapy in chronic hind limb ischemia.* Circulation, 2006. **114**(25): p. 2823-2830.
577. Wolfgang Schaden, et al., *Shock wave therapy for acute and chronic soft tissue wounds: a feasibility study.* Journal of Surgical Research, 2007. **143**(1): p. 1-12.
578. Ching-Jen Wang, et al., *Long-term outcomes of extracorporeal shockwave therapy for chronic foot ulcers.* journal of surgical research, 2014. **189**(2): p. 366-372.

579. Ching-Jen Wang, et al., *Extracorporeal shockwave therapy in diabetic foot ulcers.* International Journal of Surgery, 2015. **24**: p. 207-209.

580. Ching-Jen Wang, et al., *Extracorporeal shockwave treatment for chronic diabetic foot ulcers.* Journal of surgical research, 2009. **152**(1): p. 96-103.

581. Yeung-Jen Chen, et al., *Recruitment of mesenchymal stem cells and expression of TGF-β1 and VEGF in the early stage of shock wave-promoted bone regeneration of segmental defect in rats.* Journal of orthopaedic research, 2004. **22**(3): p. 526-534.

582. Ching-Jen Wang, Ya-Ju Yang, and Chung-Cheng Huang, *The effects of shockwave on systemic concentrations of nitric oxide level, angiogenesis and osteogenesis factors in hip necrosis.* Rheumatology international, 2011. **31**(7): p. 871-877.

583. F-S Wang, et al., *Temporal and spatial expression of bone morphogenetic proteins in extracorporeal shock wave-promoted healing of segmental defect.* Bone, 2003. **32**(4): p. 387-396.

584. Yeung-Jen Chen, et al., *Activation of extracellular signal-regulated kinase (ERK) and p38 kinase in shock wave-promoted bone formation of segmental defect in rats.* Bone, 2004. **34**(3): p. 466-477.

585. Jai-Hong Cheng and Ching-Jen Wang, *Biological mechanism of shockwave in bone.* International Journal of Surgery, 2015. **24**: p. 143-146.

586. National Institute for Health and Care Excellence (NICE). *Extracorporeal shockwave therapy for refractory plantar fasciitis*. 2009; Available from: https://www.nice.org.uk/guidance/ipg311.

587. National Institute fot Health and Care Excellence (NICE). *Extracorporeal shockwave therapy for Achilles tendinopathy*. 2009; Available from: https://www.nice.org.uk/guidance/ipg571.

588. National Institute for Health and Care Excellence (NICE). *Extracorporeal shockwave therapy for refractory tennis elbow*. 2009; Available from: https://www.nice.org.uk/guidance/ipg313.

589. *ISO 10993-6 Biological evaluation of medical devices-part 6: tests for local effects after implantation*, in *International Organization for Standardization*. 2016. p. 1-21.

590. Pugazhenthan Thangaraju and Shoban Babu Varthya, *ISO 10993- 6: Biological Evaluation of Medical Devices - Part 6: Tests for local effects after implantation*, in *Medical Device Guidelines and Regulations Handbook*. 2022, Springer. p. 163-187.

591. Seeram Ramakrishna, et al., *Safety testing of a new medical device.* Med. Devices, 2015: p. 137-153.

592. *ISO 10993-1 Biological evaluation of medical devices- Part 1: Evaluation and testing within a risk management process*. 2018.

593. Serge D Rousselle, et al., *Pathology of bioabsorbable implants in preclinical studies.* Toxicologic Pathology, 2019. **47**(3): p. 358-378.

594. *ASTM F981 − 04 Standard Practice for Assessment of Compatibility of Biomaterials for Surgical Implants with Respect to Effect of Materials on Muscle and Insertion into Bone*. 2016.

595. VR Sastri, *Material requirements for plastics used in medical devices.* Plastics in medical devices (2nd ed., pp. 33-54). New York, USA: William Andrew Publishing. https://doi. org/10.1016/B978-1-4557-3201-2.00004-5, 2014.

596. Aylin M Deliormanlı, et al., *In vivo evaluation of cerium, gallium and vanadium-doped borate-based bioactive glass scaffolds using rat subcutaneous implantation model.* Ceramics International, 2016. **42**(10): p. 11574-11583.

597. Johannes C Reichert, et al., *A tissue engineering solution for segmental defect regeneration in load-bearing long bones.* Science translational medicine, 2012. **4**(141): p. 141ra93-141ra93.

598. David S Sparks, et al., *A preclinical large-animal model for the assessment of critical-size load-bearing bone defect reconstruction.* Nature Protocols, 2020. **15**(3): p. 877-924.

599. Mengying Liu and Yonggang Lv, *Reconstructing bone with natural bone graft: a review of in vivo studies in bone defect animal model.* Nanomaterials, 2018. **8**(12): p. 999.

600. Padhraig F O'loughlin, et al., *Selection and development of preclinical models in fracture-healing research.* JBJS, 2008. **90**: p. 79-84.

601. Catherine M Cowan, et al., *Adipose-derived adult stromal cells heal critical-size mouse calvarial defects.* Nature biotechnology, 2004. **22**(5): p. 560.

602. Patrick P Spicer, et al., *Evaluation of bone regeneration using the rat critical size calvarial defect.* Nature protocols, 2012. **7**(10): p. 1918.

603. Songfeng Xu, et al., *Reconstruction of calvarial defect of rabbits using porous calcium silicate bioactive ceramics.* Biomaterials, 2008. **29**(17): p. 2588-2596.

604. Hoda Elkhenany, et al., *Graphene based scaffold for stem cell delivery in cortical bone defect.* Conference poster, 2014.

605. Satoshi Kokubo, et al., *Bone regeneration by recombinant human bone morphogenetic protein-2 and a novel biodegradable carrier in a rabbit ulnar defect model.* Biomaterials, 2003. **24**(9): p. 1643-1651.

606. Michael AK Liebschner, *Biomechanical considerations of animal models used in tissue engineering of bone.* Biomaterials, 2004. **25**(9): p. 1697-1714.

607. T Berglundh and J Lindhe, *Healing around implants placed in bone defects treated with Bio-Oss®. An experimental study in the dog.* Clinical Oral Implants Research, 1997. **8**(2): p. 117-124.

608. Antonio A Antunes, et al., *Comparisons between B io-O ss® and Straumann® Bone Ceramic in immediate and staged implant placement in dogs mandible bone defects.* Clinical Oral Implants Research, 2013. **24**(2): p. 135-142.

609. A Ravaglioli, et al., *Mineral evolution of bone.* Biomaterials, 1996. **17**(6): p. 617-622.

610. E Newman, AS Turner, and JD Wark, *The potential of sheep for the study of osteopenia: current status and comparison with other animal models.* Bone, 1995. **16**(4): p. S277-S284.

611. Johannes C Reichert, et al., *Custom-made composite scaffolds for segmental defect repair in long bones.* International orthopaedics, 2011. **35**(8): p. 1229-1236.

612. Lin Zhao, et al., *Comparative study between tissue-engineered periosteum and structural allograft in rabbit critical-sized radial defect model.* Journal of Biomedical Materials Research Part B: Applied Biomaterials, 2011. **97**(1): p. 1-9.

613. Soo-Hwan Kang, et al., *Bone regeneration potential of allogeneic or autogeneic mesenchymal stem cells loaded onto cancellous bone granules in a rabbit radial defect model.* Cell and tissue research, 2014. **355**(1): p. 81-88.

614. William R Walsh, et al., *β-TCP bone graft substitutes in a bilateral rabbit tibial defect model.* Biomaterials, 2008. **29**(3): p. 266-271.

615. Rafael Arcesio Delgado-Ruiz, et al., *Porous titanium granules in critical size defects of rabbit tibia with or without membranes.* International Journal of Oral Science, 2014. **6**(2): p. 105-110.

616. Hirokazu Komaki, et al., *Repair of segmental bone defects in rabbit tibiae using a complex of β-tricalcium phosphate, type I collagen, and fibroblast growth factor-2.* Biomaterials, 2006. **27**(29): p. 5118-5126.

617. Olivier Gauthier, et al., *In vivo bone regeneration with injectable calcium phosphate biomaterial: a three-dimensional micro-computed tomographic, biomechanical and SEM study.* Biomaterials, 2005. **26**(27): p. 5444-5453.

618. Jie Wei, et al., *Hierarchically microporous/macroporous scaffold of magnesium–calcium phosphate for bone tissue regeneration.* Biomaterials, 2010. **31**(6): p. 1260-1269.
619. YJ Liu, et al., *An animal experimental study of porous magnesium scaffold degradation and osteogenesis.* Brazilian Journal of Medical and Biological Research, 2014. **47**: p. 715-720.
620. Hadi Eftekhari, et al., *Assessment of polycaprolacton (PCL) nanocomposite scaffold compared with hydroxyapatite (HA) on healing of segmental femur bone defect in rabbits.* Artificial Cells, Nanomedicine, and Biotechnology, 2017. **45**(5): p. 961-968.
621. Govindaraj Perumal, et al., *Bilayer nanostructure coated AZ31 magnesium alloy implants: In vivo reconstruction of critical-sized rabbit femoral segmental bone defect.* Nanomedicine: Nanotechnology, Biology and Medicine, 2020. **29**: p. 102232.
622. J Yang, et al., *Enhanced repair of a critical-sized segmental bone defect in rabbit femur by surface microstructured porous titanium.* Journal of Materials Science: Materials in Medicine, 2014. **25**(7): p. 1747-1756.
623. Jin-Hyung Shim, et al., *Stimulation of healing within a rabbit calvarial defect by a PCL/PLGA scaffold blended with TCP using solid freeform fabrication technology.* Journal of Materials Science: Materials in Medicine, 2012. **23**(12): p. 2993-3002.
624. Se-Hwan Lee, et al., *Evaluation of mechanical strength and bone regeneration ability of 3D printed kagome-structure scaffold using rabbit calvarial defect model.* Materials Science and Engineering: C, 2019. **98**: p. 949-959.
625. Johannes C Reichert, et al., *The challenge of establishing preclinical models for segmental bone defect research.* Biomaterials, 2009. **30**(12): p. 2149-2163.
626. George F Muschler, et al., *The design and use of animal models for translational research in bone tissue engineering and regenerative medicine.* Tissue Engineering Part B: Reviews, 2010. **16**(1): p. 123-145.
627. Jeremiah Easley, et al., *Biomechanical and histologic assessment of a novel screw retention technology in an ovine lumbar fusion model.* The Spine Journal, 2018.
628. Katsuhisa Yamada, et al., *A preclinical large animal study on a novel intervertebral fusion cage covered with high porosity titanium sheets with a triple pore structure used for spinal fusion.* European Spine Journal, 2015. **24**(11): p. 2530-2537.
629. P Seebeck, et al., *Gait evaluation: a tool to monitor bone healing?* Clinical Biomechanics, 2005. **20**(9): p. 883-891.

630. Stephanie Valentin, et al., *Kinematic parameters of sheep walking on a treadmill.* The Veterinary Journal, 2014. **202**(3): p. 657-658.
631. Jose M Vilar, et al., *Effect of intraarticular inoculation of mesenchymal stem cells in dogs with hip osteoarthritis by means of objective force platform gait analysis: concordance with numeric subjective scoring scales.* BMC veterinary research, 2016. **12**(1): p. 223.
632. Xiaodu Wang, Jay D Mabrey, and C Agrawal, *An interspecies comparison of bone fracture properties.* Bio-medical materials and engineering, 1998. **8**(1): p. 1-9.
633. Pavlos P Lelovas, et al., *The laboratory rat as an animal model for osteoporosis research.* Comparative medicine, 2008. **58**(5): p. 424-430.
634. Ye Li, et al., *Bone defect animal models for testing efficacy of bone substitute biomaterials.* Journal of orthopaedic translation, 2015. **3**(3): p. 95-104.
635. S Castaneda, et al., *Bone mineral measurements of subchondral and trabecular bone in healthy and osteoporotic rabbits.* Skeletal radiology, 2006. **35**(1): p. 34-41.
636. Claire N Thomas, et al., *An overview of 3D printing and the orthopaedic application of patient-specific models in malunion surgery.* Injury, 2021.
637. Yousef AbouHashem, et al., *The application of 3D printing in anatomy education.* Medical education online, 2015. **20**(1): p. 29847.
638. Ellen K O'Brien, et al., *Use of 3D printing for medical education models in transplantation medicine: a critical review.* Current Transplantation Reports, 2016. **3**(1): p. 109-119.
639. Jonathan Minto, et al., *Three-dimensional printing: A catalyst for a changing orthopaedic landscape.* JBJS reviews, 2020. **8**(2): p. e0076.
640. Anurup Ganguli, et al., *3D printing for preoperative planning and surgical training: a review.* Biomedical microdevices, 2018. **20**(3): p. 1-24.
641. Aitor Tejo-Otero, Irene Buj-Corral, and F Fenollosa-Artés, *3D printing in medicine for preoperative surgical planning: a review.* Annals of biomedical engineering, 2020. **48**(2): p. 536-555.
642. Alperen Yilmaz, et al., *3D-printed surgical guides.* Ann Joint, 2019. **4**: p. 16.
643. Francesco Longo, et al., *Three-dimensional computer-assisted corrective osteotomy with a patient-specific surgical guide for an antebrachial limb deformity in two dogs.* Schweizer Archiv für Tierheilkunde, 2019. **161**(7/8): p. 473-479.
644. Andrew J Worth, Katherine R Crosse, and Andrew Kersley, *Computer-assisted surgery using 3D printed saw guides for acute correction of antebrachial angular*

limb deformities in dogs. Veterinary and Comparative Orthopaedics and Traumatology, 2019. **32**(03): p. 241-249.

645. David H Ballard, et al., *Medical 3D printing cost-savings in orthopedic and maxillofacial surgery: cost analysis of operating room time saved with 3D printed anatomic models and surgical guides.* Academic radiology, 2020. **27**(8): p. 1103-1113.
646. KC Wong, et al., *One-step reconstruction with a 3D-printed, biomechanically evaluated custom implant after complex pelvic tumor resection.* Computer Aided Surgery, 2015. **20**(1): p. 14-23.
647. Ethan L Nyberg, et al., *3D-printing technologies for craniofacial rehabilitation, reconstruction, and regeneration.* Annals of biomedical engineering, 2017. **45**(1): p. 45-57.
648. Kevin Tetsworth, Steve Block, and Vaida Glatt, *Putting 3D modelling and 3D printing into practice: virtual surgery and preoperative planning to reconstruct complex post-traumatic skeletal deformities and defects.* SICOT-J, 2017. **3**.
649. Stefano Grossi, et al., *One-Step Reconstruction with Custom-made 3D-printed Scapular Prosthesis After Partial or Total Scapulectomy.* Surgical Technology International, 2020. **36**: p. 341-346.
650. Jack M Haglin, et al., *Patient-Specific Orthopaedic Implants.* Orthopaedic surgery, 2016. **8**(4): p. 417-424.
651. Abid Haleem, Mohd Javaid, and Raju Vaishya, *4D printing and its applications in orthopaedics.* Journal of Clinical Orthopaedics & Trauma, 2018. **9**(3): p. 275-276.
652. Dimitris Mitsouras, et al., *Medical 3D printing for the radiologist.* Radiographics, 2015. **35**(7): p. 1965.
653. Carlo Mangano, et al., *Custom-made 3D printed subperiosteal titanium implants for the prosthetic restoration of the atrophic posterior mandible of elderly patients: a case series.* 3D Printing in Medicine, 2020. **6**(1): p. 1-14.
654. American Medical Association, *American Medical Association Category III codes*. October 19, 2020.
655. Mohd Javaid and Abid Haleem, *Current status and challenges of Additive manufacturing in orthopaedics: an overview.* Journal of clinical orthopaedics and trauma, 2019. **10**(2): p. 380-386.
656. Maika G Mitchell, *Bioprinting: Techniques and Risks for Regenerative Medicine*. 2017: Academic Press.

657. Fabien Guillemot, et al., *Laser-assisted bioprinting to deal with tissue complexity in regenerative medicine.* Mrs Bulletin, 2011. **36**(12): p. 1015-1019.
658. Gregory Gillispie, et al., *Assessment methodologies for extrusion-based bioink printability.* Biofabrication, 2020. **12**(2): p. 022003.
659. Suhun Chae and Dong-Woo Cho, *Biomaterial-based 3D bioprinting strategy for orthopedic tissue engineering.* Acta biomaterialia, 2023. **156**: p. 4-20.
660. Bin Duan, et al., *3D bioprinting of heterogeneous aortic valve conduits with alginate/gelatin hydrogels.* Journal of biomedical materials research Part A, 2013. **101**(5): p. 1255-1264.
661. Hyun-Wook Kang, et al., *A 3D bioprinting system to produce human-scale tissue constructs with structural integrity.* Nature biotechnology, 2016. **34**(3): p. 312-319.
662. Tyler Potyondy, et al., *Recent advances in 3D bioprinting of musculoskeletal tissues.* Biofabrication, 2021. **13**(2): p. 022001.
663. Katja Hölzl, et al., *Bioink properties before, during and after 3D bioprinting.* Biofabrication, 2016. **8**(3): p. 032002.
664. Soroosh Derakhshanfar, et al., *3D bioprinting for biomedical devices and tissue engineering: A review of recent trends and advances.* Bioactive materials, 2018. **3**(2): p. 144-156.
665. Roghayeh Khoeini, et al., *Natural and synthetic bioinks for 3D bioprinting.* Advanced NanoBiomed Research, 2021. **1**(8): p. 2000097.
666. Juergen Groll, et al., *A definition of bioinks and their distinction from biomaterial inks.* Biofabrication, 2018. **11**(1): p. 013001.
667. Lorenzo Moroni, et al., *Biofabrication: a guide to technology and terminology.* Trends in biotechnology, 2018. **36**(4): p. 384-402.
668. Amit Panwar and Lay Poh Tan, *Current status of bioinks for micro-extrusion-based 3D bioprinting.* Molecules, 2016. **21**(6): p. 685.
669. Cesar R Alcala-Orozco, et al., *Converging functionality: Strategies for 3D hybrid-construct biofabrication and the role of composite biomaterials for skeletal regeneration.* Acta Biomaterialia, 2021. **132**: p. 188-216.
670. Lokesh Karthik Narayanan, et al., *3D-bioprinting of polylactic acid (PLA) nanofiber–alginate hydrogel bioink containing human adipose-derived stem cells.* ACS biomaterials science & engineering, 2016. **2**(10): p. 1732-1742.

671. Haitao Cui, et al., *Hierarchical fabrication of engineered vascularized bone biphasic constructs via dual 3D bioprinting: integrating regional bioactive factors into architectural design.* Advanced healthcare materials, 2016. **5**(17): p. 2174-2181.
672. F. Pati, et al., *Printing three-dimensional tissue analogues with decellularized extracellular matrix bioink.* Nat Commun, 2014. **5**: p. 3935.
673. D. Choudhury, et al., *Organ-Derived Decellularized Extracellular Matrix: A Game Changer for Bioink Manufacturing?* Trends Biotechnol, 2018. **36**(8): p. 787-805.
674. C. Y. Zhang, et al., *Three-Dimensional Bioprinting of Decellularized Extracellular Matrix-Based Bioinks for Tissue Engineering.* Molecules, 2022. **27**(11).
675. B. S. Kim, et al., *Decellularized Extracellular Matrix-based Bioinks for Engineering Tissue- and Organ-specific Microenvironments.* Chem Rev, 2020. **120**(19): p. 10608-10661.
676. Ju Young Park, et al., *3D printing technology to control BMP-2 and VEGF delivery spatially and temporally to promote large-volume bone regeneration.* Journal of Materials Chemistry B, 2015. **3**(27): p. 5415-5425.
677. Nureddin Ashammakhi, et al., *Advancing frontiers in bone bioprinting.* Advanced healthcare materials, 2019. **8**(7): p. 1801048.
678. Guifang Gao, et al., *Bioprinting cartilage tissue from mesenchymal stem cells and PEG hydrogel.* 3D Cell Culture: Methods and Protocols, 2017: p. 391-398.
679. Yang Wu, et al., *Three-dimensional bioprinting of articular cartilage: a systematic review.* Cartilage, 2021. **12**(1): p. 76-92.
680. Burak Toprakhisar, et al., *Development of bioink from decellularized tendon extracellular matrix for 3D bioprinting.* Macromolecular bioscience, 2018. **18**(10): p. 1800024.
681. Dong-Hee Kang, et al., *Engineered whole cut meat-like tissue by the assembly of cell fibers using tendon-gel integrated bioprinting.* Nature Communications, 2021. **12**(1): p. 5059.
682. Xiping Jiang, et al., *3D bioprinting of multilayered scaffolds with spatially differentiated ADMSCs for rotator cuff tendon-to-bone interface regeneration.* Applied Materials Today, 2022. **27**: p. 101510.
683. Tyler K Merceron, et al., *A 3D bioprinted complex structure for engineering the muscle–tendon unit.* Biofabrication, 2015. **7**(3): p. 035003.
684. Mine Altunbek, et al., *Design and bioprinting for tissue interfaces.* Biofabrication, 2023.

685. Susheem Kanwar and Sanjairaj Vijayavenkataraman, *Design of 3D printed scaffolds for bone tissue engineering: A review.* Bioprinting, 2021. **24**: p. e00167.

686. Jian Han, et al., *Surface Roughness and Biocompatibility of Polycaprolactone Bone Scaffolds: An Energy-Density-Guided Parameter Optimization for Selective Laser Sintering.* Frontiers in Bioengineering and Biotechnology, 2022. **10**: p. 888267.

687. Jan Henkel, et al., *Bone regeneration based on tissue engineering conceptions—a 21st century perspective.* Bone research, 2013. **1**(1): p. 216-248.

688. N. E. Fedorovich, et al., *Scaffold porosity and oxygenation of printed hydrogel constructs affect functionality of embedded osteogenic progenitors.* Tissue Eng Part A, 2011. **17**(19-20): p. 2473-86.

689. Vassilis Karageorgiou and David Kaplan, *Porosity of 3D biomaterial scaffolds and osteogenesis.* Biomaterials, 2005. **26**(27): p. 5474-5491.

690. Ker Chin Ang, et al., *Investigation of the mechanical properties and porosity relationships in fused deposition modelling-fabricated porous structures.* Rapid Prototyping Journal, 2006. **12**(2): p. 100-105.

691. Joseph R Woodard, et al., *The mechanical properties and osteoconductivity of hydroxyapatite bone scaffolds with multi-scale porosity.* Biomaterials, 2007. **28**(1): p. 45-54.

692. Dietmar W Hutmacher, *Scaffolds in tissue engineering bone and cartilage.* Biomaterials, 2000. **21**(24): p. 2529-2543.

693. A Fukuda, et al., *Osteoinduction of porous Ti implants with a channel structure fabricated by selective laser melting.* Acta Biomaterialia, 2011. **7**(5): p. 2327-2336.

694. Simon Van Bael, et al., *The effect of pore geometry on the in vitro biological behavior of human periosteum-derived cells seeded on selective laser-melted Ti6Al4V bone scaffolds.* Acta biomaterialia, 2012. **8**(7): p. 2824-2834.

695. H. Yuan, et al., *A preliminary study on osteoinduction of two kinds of calcium phosphate ceramics.* Biomaterials, 1999. **20**(19): p. 1799-806.

696. Veronica Borsari, et al., *Physical characterization of different-roughness titanium surfaces, with and without hydroxyapatite coating, and their effect on human osteoblast-like cells.* Journal of Biomedical Materials Research Part B: Applied Biomaterials: An Official Journal of The Society for Biomaterials, The Japanese Society for Biomaterials, and The Australian Society for Biomaterials and the Korean Society for Biomaterials, 2005. **75**(2): p. 359-368.

697. Erin Yiling Teo, et al., *Polycaprolactone-based fused deposition modeled mesh for delivery of antibacterial agents to infected wounds.* Biomaterials, 2011. **32**(1): p. 279-287.

698. Ning Xu, et al., *3D artificial bones for bone repair prepared by computed tomography-guided fused deposition modeling for bone repair.* ACS applied materials & interfaces, 2014. **6**(17): p. 14952-14963.

699. Antonio Armillotta, et al., *Edge quality in fused deposition modeling: II. experimental verification.* Rapid Prototyping Journal, 2017.

700. Fu You, et al., *3D printing of porous cell-laden hydrogel constructs for potential applications in cartilage tissue engineering.* ACS biomaterials science & engineering, 2016. **2**(7): p. 1200-1210.

701. Cristina Colosi, et al., *Microfluidic bioprinting of heterogeneous 3D tissue constructs using low-viscosity bioink.* Advanced materials, 2016. **28**(4): p. 677-684.

702. Sean V Murphy and Anthony Atala, *3D bioprinting of tissues and organs.* Nature biotechnology, 2014. **32**(8): p. 773-785.

703. P Selcan Gungor-Ozkerim, et al., *Bioinks for 3D bioprinting: an overview.* Biomaterials science, 2018. **6**(5): p. 915-946.

704. Hee-Gyeong Yi, Hyungseok Lee, and Dong-Woo Cho, *3D printing of organs-on-chips.* Bioengineering, 2017. **4**(1): p. 10.

705. Carl Schubert, Mark C Van Langeveld, and Larry A Donoso, *Innovations in 3D printing: a 3D overview from optics to organs.* British Journal of Ophthalmology, 2014. **98**(2): p. 159-161.

706. Srikanthan Ramesh, et al., *Extrusion bioprinting: Recent progress, challenges, and future opportunities.* Bioprinting, 2021. **21**: p. e00116.

707. Arthur Bens, et al., *Non-toxic flexible photopolymers for medical stereolithography technology.* Rapid Prototyping Journal, 2007.

708. Chi Zhou, et al., *Digital material fabrication using mask-image-projection-based stereolithography.* Rapid Prototyping Journal, 2013.

709. A Ping Zhang, et al., *Rapid fabrication of complex 3D extracellular microenvironments by dynamic optical projection stereolithography.* Advanced materials, 2012. **24**(31): p. 4266-4270.

710. Mark Frame. *DIY 3D printing of custom orthopaedic implants: a proof of concept study*. in *Orthopaedic Proceedings*. 2014. The British Editorial Society of Bone & Joint Surgery.

711. M Tyndyk, et al., *Assessment of SLS fabricated scaffolds for skeletal reconstruction in the spine.* Journal of Biomechanics, 2006. **39**(1): p. S216.
712. Hesam Shahali, Alka Jaggessar, and Prasad KDV Yarlagadda, *Recent advances in manufacturing and surface modification of titanium orthopaedic applications.* Procedia engineering, 2017. **174**: p. 1067-1076.
713. Leonardo Ciocca, et al., *Direct metal laser sintering (DMLS) of a customized titanium mesh for prosthetically guided bone regeneration of atrophic maxillary arches.* Medical & Biological Engineering & Computing, 2011. **49**(11): p. 1347-1352.
714. Swee Leong Sing, et al., *Direct selective laser sintering and melting of ceramics: a review.* Rapid Prototyping Journal, 2017.
715. Jan Patrick Deckers, et al., *Shaping ceramics through indirect selective laser sintering.* Rapid Prototyping Journal, 2016. **22**(3): p. 544-558.
716. Minxuan Kuang, Libin Wang, and Yanlin Song, *Controllable printing droplets for high-resolution patterns.* Advanced materials, 2014. **26**(40): p. 6950-6958.
717. Anke Teichler, et al., *Inkjet printing of chemically tailored light-emitting polymers.* European polymer journal, 2013. **49**(8): p. 2186-2195.
718. Aman Dhawan, et al., *Three-dimensional bioprinting for bone and cartilage restoration in orthopaedic surgery.* JAAOS-Journal of the American Academy of Orthopaedic Surgeons, 2019. **27**(5): p. e215-e226.
719. Yexin Gu, et al., *Inkjet printed antibiotic-and calcium-eluting bioresorbable nanocomposite micropatterns for orthopedic implants.* Acta biomaterialia, 2012. **8**(1): p. 424-431.
720. Xinda Li, et al., *Inkjet bioprinting of biomaterials.* Chemical Reviews, 2020. **120**(19): p. 10793-10833.
721. Johannes Schindelin, et al., *Fiji: an open-source platform for biological-image analysis.* Nature methods, 2012. **9**(7): p. 676-682.
722. NIH National Liberary of Medcine. *The National Center for Biotechnology Information*. Gene database; Available from: https://www.ncbi.nlm.nih.gov/.
723. *Primer3Plus*. Available from: https://www.bioinformatics.nl/cgi-bin/primer3plus/primer3plus.cgi.
724. Sigma Aldrich Merck. *DNA Oligos and qPCR Probes online ordering system* Available from: https://www.sigmaaldrich.com/GB/en/configurators/tube?product=standard.
725. *IBM SPSS Statistics for Windows*. 2021, IBM Corp. in Armonk, NY.

726. ISO 10993-6, *Biological evaluation of medical devices-part 6: tests for local effects after implantation.* International Organization for Standardization, 2007: p. 1-21.
727. International Organization for Standardization, *ISO 10993-6 Biological evaluation of medical devices. Part 6: Tests for local effects after implantation*. 2016.
728. E. J. Vereyken, et al., *Classically and alternatively activated bone marrow derived macrophages differ in cytoskeletal functions and migration towards specific CNS cell types.* J Neuroinflammation, 2011. **8**: p. 58.
729. F. A. Verreck, et al., *Phenotypic and functional profiling of human proinflammatory type-1 and anti-inflammatory type-2 macrophages in response to microbial antigens and IFN-gamma- and CD40L-mediated costimulation.* J Leukoc Biol, 2006. **79**(2): p. 285-93.
730. *3D Slicer image computing platform*. Available from: https://www.slicer.org/.
731. Andriy Fedorov, et al., *3D Slicer as an image computing platform for the Quantitative Imaging Network.* Magnetic resonance imaging, 2012. **30**(9): p. 1323-1341.
732. Ron Kikinis, Steve D Pieper, and Kirby G Vosburgh, *3D Slicer: a platform for subject-specific image analysis, visualization, and clinical support*, in *Intraoperative imaging and image-guided therapy*. 2014, Springer. p. 277-289.
733. J Pablo Rodríguez, et al., *Cytoskeletal organization of human mesenchymal stem cells (MSC) changes during their osteogenic differentiation.* Journal of cellular biochemistry, 2004. **93**(4): p. 721-731.
734. María José Martínez-Lorenzo, et al., *Phenotype and chondrogenic differentiation of mesenchymal cells from adipose tissue of different species.* Journal of Orthopaedic Research, 2009. **27**(11): p. 1499-1507.
735. Tao-Chen Lee, et al., *Comparison of surface markers between human and rabbit mesenchymal stem cells.* PloS one, 2014. **9**(11): p. e111390.
736. Helena Debiazi Zomer, et al., *Distinct features of rabbit and human adipose-derived mesenchymal stem cells: implications for biotechnology and translational research.* Stem Cells and Cloning: Advances and Applications, 2018. **11**: p. 43.
737. Vahid Bayati, et al., *Expression of surface markers and myogenic potential of rat bone marrow-and adipose-derived stem cells: a comparative study.* Anatomy & cell biology, 2013. **46**(2): p. 113-121.
738. Qiong Li, et al., *CD73+ Mesenchymal stem cells ameliorate myocardial infarction by promoting angiogenesis.* Frontiers in cell and developmental biology, 2021. **9**: p. 637239.

739. Jienny Lee, et al., *Effect of donor age on the proliferation and multipotency of canine adipose-derived mesenchymal stem cells.* Journal of Veterinary Science, 2017. **18**(2): p. 141-148.
740. Beatriz Ranera, et al., *Immunophenotype and gene expression profiles of cell surface markers of mesenchymal stem cells derived from equine bone marrow and adipose tissue.* Veterinary immunology and immunopathology, 2011. **144**(1-2): p. 147-154.
741. H. Pham, et al., *CD73, CD90, CD105 and Cadherin-11 RT-PCR Screening for Mesenchymal Stem Cells from Cryopreserved Human Cord Tissue.* Int J Stem Cells, 2018. **11**(1): p. 26-38.
742. Mária Tirpáková, et al., *Phenotypical characterization and neurogenic differentiation of rabbit adipose tissue-derived mesenchymal stem cells.* Genes, 2021. **12**(3): p. 431.
743. M. Visweswaran, et al., *Multi-lineage differentiation of mesenchymal stem cells - To Wnt, or not Wnt.* Int J Biochem Cell Biol, 2015. **68**: p. 139-47.
744. Masaki Noda, *Cellular and molecular biology of bone*. 2014: Academic Press.
745. A Owen Thomas, et al., *Progressive development of the rat osteoblast phenotype in vitro: Reciprocal relationships in expression of genes associated with osteoblast proliferation and differentiation during formation of the bone extracellular matrix.* Journal of Cellular Physiology, 1990. **143**(3): p. 420-430.
746. Michalis Panteli, et al., *Biological and molecular profile of fracture non-union tissue: current insights.* Journal of cellular and molecular medicine, 2015. **19**(4): p. 685-713.
747. D. M. Lawton, et al., *Expression of the gene encoding the matrix gla protein by mature osteoblasts in human fracture non-unions.* Mol Pathol, 1999. **52**(2): p. 92-6.
748. Tsung-Rong Kuo and Chih-Hwa Chen, *Bone biomarker for the clinical assessment of osteoporosis: recent developments and future perspectives.* Biomarker research, 2017. **5**(1): p. 1-9.
749. L. Nicol, et al., *Alterations in non-type I collagen biomarkers in osteogenesis imperfecta.* Bone, 2019. **120**: p. 70-74.
750. Xi Sun, et al., *Current progress on microRNA-based gene delivery in the treatment of osteoporosis and osteoporotic fracture.* International journal of endocrinology, 2019. **2019**.
751. Christopher H Evans, *Gene therapy for bone healing.* Expert reviews in molecular medicine, 2010. **12**: p. e18.

752. Melanie Haffner-Luntzer, et al., *Review of animal models of comorbidities in fracture-healing research.* Journal of Orthopaedic Research®, 2019. **37**(12): p. 2491-2498.

753. Anna M Weihs, et al., *Shock wave treatment enhances cell proliferation and improves wound healing by ATP release-coupled extracellular signal-regulated kinase (ERK) activation.* Journal of Biological Chemistry, 2014. **289**(39): p. 27090-27104.

754. W Schaden, A Fischer, and A Sailler, *Extracorporeal shock wave therapy of nonunion or delayed osseous union.* Clinical Orthopaedics and Related Research®, 2001. **387**: p. 90-94.

755. Alessandra Costa, et al., *Biologic scaffolds.* Cold Spring Harbor perspectives in medicine, 2017. **7**(9): p. a025676.

756. Elliott Gruskin, et al., *Demineralized bone matrix in bone repair: history and use.* Advanced drug delivery reviews, 2012. **64**(12): p. 1063-1077.

757. Ana B Faia-Torres, et al., *Differential regulation of osteogenic differentiation of stem cells on surface roughness gradients.* Biomaterials, 2014. **35**(33): p. 9023-9032.

758. Ana B Faia-Torres, et al., *Osteogenic differentiation of human mesenchymal stem cells in the absence of osteogenic supplements: A surface-roughness gradient study.* Acta biomaterialia, 2015. **28**: p. 64-75.

759. Ali Salehi, et al., *Efficient mineralization and osteogenic gene overexpression of mesenchymal stem cells on decellularized spinach leaf scaffold.* Gene, 2020. **757**: p. 144852.

760. Dongqin Xiao, et al., *The role of calcium phosphate surface structure in osteogenesis and the mechanisms involved.* Acta Biomaterialia, 2020. **106**: p. 22-33.

761. Benedikt Helgason, et al., *Mathematical relationships between bone density and mechanical properties: a literature review.* Clinical biomechanics, 2008. **23**(2): p. 135-146.

762. Reza Khorramirouz, et al., *A novel surgical technique for a rat subcutaneous implantation of a tissue engineered scaffold.* Acta histochemica, 2018. **120**(3): p. 282-291.

763. Steve WFR Waqanivavalagi, et al., *Subcutaneous Surgical Rat Models for the Evaluation of Decellularised Heart Valve Immunogenicity: A Systematic Review.* Materialia, 2021: p. 101298.

764. Nicholas Bryan, et al., *Characterisation and comparison of the host response of 6 tissue-based surgical implants in a subcutaneous in vivo rat model.* Journal of applied biomaterials & functional materials, 2015. **13**(1): p. 35-42.
765. FCJ Van de Watering, et al., *Biodegradation of calcium phosphate cement composites*, in *Degradation of Implant materials*. 2012, Springer. p. 139-172.
766. AR Boccaccini, et al., *Degradable and bioactive synthetic composite scaffolds for bone tissue engineering*, in *Degradation of Implant Materials*. 2012, Springer. p. 111-137.
767. Omar Hameed, Shi Wei, and Gene P Siegal, *Bone/Osteoid Producing Lesions*, in *Frozen Section Library: Bone*. 2011, Springer. p. 5-23.
768. Rosy Setiawati and Paulus Rahardjo, *Bone development and growth.* Osteogenesis and bone regeneration, 2019. **10**.
769. J. J. Jacobs and N. J. Hallab, *Loosening and osteolysis associated with metal-on-metal bearings: A local effect of metal hypersensitivity?* J Bone Joint Surg Am, 2006. **88**(6): p. 1171-2.
770. V. Y. Ng, et al., *Perivascular lymphocytic infiltration is not limited to metal-on-metal bearings.* Clin Orthop Relat Res, 2011. **469**(2): p. 523-9.
771. A. P. Davies, et al., *An unusual lymphocytic perivascular infiltration in tissues around contemporary metal-on-metal joint replacements.* J Bone Joint Surg Am, 2005. **87**(1): p. 18-27.
772. N. J. Hallab, et al., *Concentration- and composition-dependent effects of metal ions on human MG-63 osteoblasts.* J Biomed Mater Res, 2002. **60**(3): p. 420-33.
773. Takeshi Takarada, et al., *Genetic analysis of Runx2 function during intramembranous ossification.* Development, 2016. **143**(2): p. 211-218.
774. Scott F Gilbert and MJF Barresi, *Developmental biology, ed*. Osteogenesis: The Development of Bones. 2000, Sunderland (MA): Sinauer Associates.
775. A. J. Rechenmacher, et al., *Interfragmentary strain measurement post-fixation to guide intraoperative decision making: a narrative review.* Eur J Orthop Surg Traumatol, 2023.

Acknowledgment

I would like to express my deepest gratitude to my supervisor Professor Matthew Allen, for his support throughout my PhD journey, and a major thanks to:

- The examiner committee Mr Matija Krkovic and Professor Richard Meeson for dedicating the time to read my thesis and giving me the opportunity to present my work during my viva and above all for their constructive feedback.
- My college mentor Dr Barbara Blacklaws, for her guidance, academic and pastoral support throughout my PhD journey.
- The director of graduate education at the department of veterinary medicine, University of Cambridge, Dr David Sargan and Mrs Fiona Roby the research and graduate education administrator for the administrative support related to the PhD course and for being super-efficient, responsive and helpful whenever needed.
- My college tutor Dr Christina Angelopoulos for her academic and pastoral support.
- My several funding bodies:
    - Newton Mosharafa Fund team (a collaboration between the Egyptian Ministry of higher Education and The British council Egypt).
    - The Cambridge Commonwealth, European & International Trust
    - AO VET/ARI Collaborative Research Grant
    - Cambridge University PGR Covid-19 Assistance Scheme
    - School of biological scienced University of Cambridge COVID impact scheme
    - Newnham College completion fund
    - Cambridge Philosophical Society

A huge thanks to:

- Professor Hani Awad (Professor of Biomedical Engineering (BME) and Orthopaedic Surgery) and Mr Ming Yan (Biomedical Engineering- PhD candidate) at the University of Rochester-New York -USA for their help with optimising the 3D printing parameters and bio-ink synthesis for the scaffolds testedd in my study.
- Dr Stephan Zeiter (Manager of the Preclinical Services program at the AO Research Institute Davos (ARI)) anf his team particularly Dr Daniel Arens, Dr Caroline Constant, Mr James Tapia-Dean, Ms Maria Hildebrand, Dr Dominic Gehweiler and

Dr Nora Goudsouzian. For their help with organizing the pilot rabbit study and for hosting me for 3 weeks at ARI for surgical training.

- Dr Claudia Gittel and Ms Sophie Mead from Queen's Veterinary Hospital anaesthesia team for their help with the rabbit study conducted in Cambridge.
- To Professor Michael Sutcliffe (Professor of Biomedical Engineering-University of Cambridge-UK) and his team particularly Mr Alex Casabuena Rodriguez, Mr Graham Smith, Mr Simon Marshall and Mr Tobia Nava for their help with the mechanical testing and the micro-CT scanning.
- Dr Davide Corbetta (Clinical Assistant Professor of veterinary anatomic pathology)-University of Nottingham-UK for his help with the training me on evaluating the material tissue interaction in the rat model. And Ms Debbie Sabin (senior histopathology technician, Department of Veterinary Medicine-University of Cambridge-UK) for her help with processing the tissue from the rat study.
- Dr Fernando Constantino Casas, Specialist in Veterinary Anatomic Pathology, Department of Veterinary Medicine, University of Cambridge for his help with the rabbit study histopathology
- Dr Nicola Lawrence and Dr Rachel Hewitt for their help with the fluorochrome labels confocal microscopy/imaging
- Mr Chris Brown the Named Animal Care & Welfare Officer at MIRA research animal facility – Cambridge and his team, particularly Miss Eleanor Speak (animal care taker) and Miss Jenny Bartley (Deputy facility manager) for supporting procedure room preparation, animal housing and day to day care of the rats and rabbits included in our study.
- Dr. Milorad Radakovic and Mr Frank Gorman for facilitating sourcing the ovine adipose tissue and bovine bone samples.
- Dr. Ronan Daly (Associate Professor in the Institute For Manufacturing-IFM-Department of Engineering, University of Cambridge-UK) for his advice and help in accessing several resources/equipment at the IFM- Cambridge.
- Dr Roger Brooks (Senior Research Associate, Division of Trauma and Orthopaedic Surgery- Addenbrooke's hospital Cambridge) For his advice and help in accessing equipment at the orthopaedic research laboratory- Addenbrooke's hospital Cambridge.

Acknowledgement

- Mr Simon Griggs (senior technician, Department of Materials Science and Metallurgy, University of Cambridge-UK) for his help with the scanning electron Microscopy.

Additional thanks:

- To the awesome colleagues I met throughout the years I spent at the Surgical Discovery Centre-Department of Veterinary Medicine, University of Cambridge, to name a few: Dr Charlotte Palmer, Dr Louisa Deragon Garcia, Mr Jose Franco, Ms Amy Stelman and Ms Nicola St-Onge.
- To the Egyptian Cultural and Educational Bureau-London team.
- To the stores and purchase department of Veterinary Medicine-University of Cambridge team Mr. Joe (Francis) Hart, Mr. Gavin Murphy and Mrs. Janice East.

Finally, and most importantly I want to express my deepest and most sincere gratitude to my parents, brother, and friends for their invaluable support.

Appendices

Appendix 1

Animal folder coversheet

PPL: Allen PP1153947 Project: Sara rabbits radial defect

Animal ID: Animal tattoo: Baseline weight:

Date	time	Task	Signature + time	comment
31/1/2022	Morning	**Surgery day**		Surgery day
		Post-OP x ray		
	Night	Buprenorphine (0.7 ml S/C)		
		Scoring (see attached scoring sheet)		
1/2/2022	Morning	Buprenorphine 0.7 ml s/c		
		Rimadyl (Carprofen) 0.4 ml s/c		
		Scoring(see attached scoring sheet)		
	night	Buprenorphine 0.7 ml s/c		
		Scoring		
2/2/2022	Morning	Buprenorphine 0.7 ml s/c		
		Rimadyl (Carprofen) 0.4 ml s/c		
		Scoring(see attached scoring sheet)		
	night	Buprenorphine 0.7 ml s/c		
		Scoring		
3/2/2022	Morning	Buprenorphine 0.7 ml s/c		3 days after surgery
		Rimadyl (Carprofen) 0.4 ml s/c		
		Scoring(see attached scoring sheet)		
		Weighing (embedded at scoring sheet)		
	night	Buprenorphine 0.7 ml s/c		
		Scoring		
4/2/2022	Morning	Rimadyl (Carprofen) 0.4 ml s/c		
		Scoring(see attached scoring sheet)		
5/2/2022	Morning	Scoring		
6/2/2022	Morning	Scoring		
7/2/2022	Morning	Scoring		1 week after surgery
		Weighing		
14/2/2022		X ray		2 weeks after surgery
21/2/2022		Calcine green 0.5% injection (1ml/kg - s/c)		3 weeks after surgery
28/2//2022		X ray		4 weeks after surgery
14/3/2022		X ray		6 weeks after surgery
		Xylenol Orange 9% injection (1ml/kg-s/c)		
28/3/2022		X ray		8 weeks after surgery
4/4/2022		Oxytetracyclin 10% injection (0.25 ml/ kg/ s/c)		9 weeks after surgery
11/4/2022		X ray		10 weeks after surgery
25/4/2022		**Euthanasia**		**12 week after surgery**
		X rays		

PPL: Allen PP1153947 **Project: Sara rabbits radial defect**

Animal ID: **Baseline weight:**

Time point	Surgery day	Surgery day+1		Surgery day+2		Surgery day+3		Sx day+4	Sx day+5	Sx day+6	Sx day +7
	night	morning	night	morning	night	morning	night	morning	morning	morning	morning
Behaviour											
Quite and attentive= 0 Lethargic (reduce reaction to stimuli)= 1 Apathetic (non-reactive) = 4											
Appearance (fur eye & skin)											
Clean =0 Little dirty & sticky = 2 Very dirty & sticky = 3											
Nictating membrane											
Non visible = 0 Visible =3											
Food intake											
Normal = 0 Reduced = 1 Not eating = 2											
Water intake											
Normal = 0 Reduced = 1 Not drinking = 2											
Weight bearing											
Normal/ full weight bearing = 0 Reduced weight bearing = 1 Severely reduced weight being =2 Non weight bearing= 3											
Caprophagy											
No = 0 Yes =1											
Body temperature											
Normal (38.5-39.5 °C) In range = 0 Not in range= 1	[redacted]	°C	°C	°C	°C	°C	°C	°C	°C	[redacted]	
Wound healing											
Normal = 0 Inflammation (hot, red, swollen)=2 Infection (oozing secretion)= 4											
Body weight											
Similar to baseline =0 1-10% reduction = 1 11-20% reduction = 2 > 20% reduction =4	[redacted]					kg	[redacted]				kg
Faeces consistency											
Normal=0 Soft= 2											
Total											
Signature											

PPL: Allen PP1153947 **Project: Sara rabbits radial defect**

Animal ID: **Baseline weight:**

Time point	Week 2	Week 3	Week 4	Week 5	Week 6	Week 7	Week 8	Week 9	Week 10	Week 11	Week 12
Behaviour											
Quite and attentive= 0 Lethargic (reduce reaction to stimuli)= 1 Apathetic (non-reactive) = 4											
Appearance (fur eye & skin)											
Clean =0 Little dirty & sticky = 2 Very dirty & sticky = 3											
Nictating membrane											
Non visible = 0 Visible =3											
Food intake											
Normal = 0 Reduced = 1 Not eating = 2											
Water intake											
Normal = 0 Reduced = 1 Not drinking = 2											
Weight bearing											
Normal/ full weight bearing = 0 Reduced weight bearing = 1 Severely reduced weight being =2 Non weight bearing= 3											
Caprophagy											
No = 0 Yes =1											
Body temperature											
Normal (38.5-39.5 °C) In range = 0 Not in range= 1	°C	°C	°C	°C	°C	°C	°C	°C	°C	°C	°C
Wound healing											
Normal = 0 Inflammation (hot, red, swollen)=2 Infection (oozing secretion)= 4											
Body weight											
Similar to baseline =0 1-10% reduction = 1 11-20% reduction = 2 > 20% reduction =4	Kg	Kg	Kg	Kg	Kg	Kg	Kg	Kg	Kg	Kg	Kg
Faeces consistency											
Normal=0 Soft= 2											
Total											
Signature											

Score < 3 mild - Score 4-9 Moderate (animal to be checked, additional dosage of pain medication or shorter interval between doses if needed)

Score 10 or more (sever) consider euthanasia - Score more than 6 for 3 consecutive days (consider euthanasia).

Appendix 2

Anaesthesia monitoring form

Animal ID:	**PPL:** Allen PP1153947	**Study:** Rabbit radial defect
Surgery: 15mm radial defect ☐ Left ☐ Right		**Ear Tattoo:**
Surgeon:	**Assistant:** / **Anaesthetist:**	**Bodyweight:** kg
Species: New Zealand White Rabbit	**Age:**	**Date:**

Premedication	**Route**	**Time**
Medetomidine 100mcg/kg.....		
Midazolam 0.5mg/kg.....	IM	.....
Fentanyl 5mcg/kg.....		

Lidocaine Study Group: Brachial Plexus Block (BPB) ☐ CRI ☐

Induction/Intubation Comments.....
.....

Venous Cannula Position
.....
.....

Induction	**Dose (mg)**	**Time**
Propofol		

ETT Size.....mm
Number of Attempts to Intubate.....

Notes / **Drugs / Time**		**Unit/ Route**
Carprofen		5% 4mg/kg IV
Fentanyl		50mcg/ml 5mcg/kg IV
Atipamezole		0.35mg/kg IM
Lactated Ringer's		10ml/kg/hr
Lidocaine 2% – Bolus *Group 1*		2mg/kg IV over 5 min
Lidocaine 2% – CRI *Group 1*		100mcg/kg/min
Lidocaine 2% – BPB *Group 2*		0.3ml/kg *Record time block completed*

		Notes
Recumbency		
Temperature		
SpO_2 (%)		**Prep. Start Time:**
$EtCO_2$ (mmHg)		
FGF O_2 (L/min)		**Surgery Start Time:**
N_2O/Air (L/min)		
Iso vaporizer (%)		**Baseline Values** *(immediately prior to starting surgery)*
$Et_{inhalant}$ (%)		**HR:**
IPPV Pmax (cmH_2O)		**RR::**
Heart Rate		**SAP:** **mmHg**
Respiratory Rate		**MAP:** **mmHg**
SAP (mmHg)		**DAP:** **mmHg**
MAP (mmHg)		**Surgery End Time:**
DAP (mmHg)		**Extubation time:**
Palpebral reflex		
Pupil Size		

Time First Head Lift:	**Time Returned to Cage:**

Appendix 2

Anaesthesia monitoring form

Time Sternal:	*Return when able to maintain sternal position and lift head*

Recovery Notes..……

Post-operative Recording

Micro SD card number:	**Camera Number:**	**Cage Number:**	**Animal ID:**
Video Start Time:		**Video End time:**	

Notes……

……

Pain Scores

Timepoint	**Time**	**RGS /10** *Rescue analgesia if score >5/10*	**BRPS /21**	**Lameness /5**	**Rescue Analgesia** Buprenorphine 50mcg/kg SC
On return to cage					
30 min					
60 min					
90 min					
120 min					☐
+1 hour					☐
10 hours					☐
+1 hour					☐
18 hours					☐
+1 hour					☐

Notes……

……

Faecal Output and Food Intake

Timepoint	**Time**	**Weight of Faecal Pellets in Cage (g)** *Collect manually and weigh, then dispose*	**Description**	
			Normal	**Abnormal** *Describe: small, irregular, dry, wet etc*
On return to cage				
30 min				
60 min				
90 min				
120 min				
10 hours				
18 hours				

Notes……

……

Timepoint	**Time**	**Weight of water bottle** *Empty weight =*	**Weight of Food Pellets in bowl** *Empty weight =*	**Weight of Hay Remaining**
On return to cage				
30 min				
60 min				
90 min				
120 min				
10 hours				

Appendix 2

Anaesthesia monitoring form

18 hours				

Record weight of pellets and water bottle on return to cage – this will be the baseline. Do not replenish pellets, hay or water unless empty/soiled. Record if replaced and record new weight as well so that we can subtract to calculate the weight of pellets consumed.

Notes……
……
……

Legend:

Palpebral Reflex:

- no reaction
(+) hard to elicit but present
+ spontaneous blinking, reflex readily elicited

Pupil:

-- max. Dilation, mydriasis
- Dilation
+ constriction
++ max. constriction, miosis

IV = intravenous

IM = intramuscular

SC = subcutaneous

HR = heart rate (beats per minute)

RR = respiratory rate (breaths per minute)

CRI = continuous rate infusion

SpO_2 = oxygen saturation (%)

EtO_2 = end-tidal carbon dioxide (mm Hg)

FGF = fresh gas flow

IPPV = intermittent positive pressure ventilation

Pmax = maximum inspiratory pressure

SAP = systolic arterial pressure

DAP = diastolic arterial pressure

MAP = mean arterial pressure

ETT = endotracheal tube

NIBP = non-invasive blood pressure

Appendix 3

Surgery report

Study plan code: SP126114 (Rabbit radial defect)

PIL holders: Matthew Allen / Sara Hassouna

Study code: NA

Model: Rabbit 15mm radial defect, left

Date:

Team in the OR:

Surgeon: Assistant:

Anesthetist: Technician:

Animal:

Animal ID / tattoo:

Implant type:

Remarks, discrepancies from standard protocol and undesired events:

Picture of empty defect was taken □
Picture of the filled defect was taken □

Number of scaffold form pre OP µCT scan:

Comments:

Start surgery: _____ End surgery: _____ Total surgery time: ___

Appendix 4

UNIVERSITY OF CAMBRIDGE

Central Diagnostic Services

TEL: +44 (0)1223 337625 FAX: +44 (0)1223 339090 E-mail: clinpath@vet.cam.ac.uk

U B S S
Greenwich House
Madingley Rise
Cambridge
Cambs
CB3 0TX

Queen's Vet School Hospital
Madingley Rd,
Cambridge
CB3 0ES

Sample Details

Submission	157324
Sample Number	**15732401**
Hospital Number	QVH22/1832
Sample Type	Tissue
Request Date	28/02/2022
Report Date	04/03/2022
Report Number	157324-R01

Patient Details

Animal ID	**JK-Mira/Allen,M00714530,C3864 UBSS**
Species	Rabbit
Breed	
Gender	Female
D o B	
Sample Site	**Leg**
Hospital Vet	Jo Keeley

Microbiology

Culture	Sparse mixed growth
Sample site	Leg

# denotes un-validated tests

Report Type : **FINAL**

UNIVERSITY OF CAMBRIDGE

Central Diagnostic Services

TEL: +44 (0)1223 337625 FAX: +44 (0)1223 339090 E-mail: clinpath@vet.cam.ac.uk

U B S S
Greenwich House
Madingley Rise
Cambridge
Cambs
CB3 0TX

Queen's Vet School Hospital
Madingley Rd,
Cambridge
CB3 0ES

Sample Details

Submission	157324
Sample Number	**15732401**
Hospital Number	QVH22/1832
Sample Type	Tissue
Request Date	28/02/2022
Report Date	04/03/2022
Report Number	157324-R01

Patient Details

Animal ID	**JK-Mira/Allen,M00714530,C3864 U B S S**
Species	Rabbit
Breed	
Gender	Female
D o B	
Sample Site	**Leg**
Hospital Vet	Jo Keeley

STAAU : Staphylococcus aureus

STAAU : Staphylococcus aureus

	STAAU	STAAU
Amoxicillin/Clavulanic aci	S	S
Oxacillin	S	S
Cefalotin	S	S
Cefovecin	S	S
Ceftiofur	S	S
Gentamicin	S	S
Kanamycin	S	S
Neomycin	S	S
Enrofloxacin	S	S
Marbofloxacin	S	S
Pradofloxacin	S	S
Erythromycin	S	S
Clindamycin	S	S
Doxycycline	S	S
Tetracycline	S	S
Nitrofurantoin	S	S
Chloramphenicol	S	S
Trimethoprim/Sulphamethoxa	S	S
Benzylpenicillin	R	R
Cefoxitin Screen	NEG	NEG
Inducible Clindamycin Resi	NEG	NEG

J Lundsgaard under the supervision of Dr J Archer VMD PhD FRCPath DipECVCP F
Senior Clinical Training Scholar in Clinical Pathology

# denotes un-validated tests

Report Type : **FINAL**

UNIVERSITY OF CAMBRIDGE

Central Diagnostic Services

TEL: +44 (0)1223 337625 FAX: +44 (0)1223 339090 E-mail: clinpath@vet.cam.ac.uk

U B S S
Greenwich House
Madingley Rise
Cambridge
Cambs
CB3 0TX

Queen's Vet School Hospital
Madingley Rd,
Cambridge
CB3 0ES

Sample Details

Submission	157324
Sample Number	**15732401**
Hospital Number	QVH22/1832
Sample Type	Tissue
Request Date	28/02/2022
Report Date	04/03/2022
Report Number	157324-R01

Patient Details

Animal ID	**JK-Mira/Allen,M00714530,C3864 U B S S**
Species	Rabbit
Breed	
Gender	Female
D o B	
Sample Site	**Leg**
Hospital Vet	Jo Keeley

Incomplete Tests NONE

# denotes un-validated tests

Report Type : **FINAL**

UNIVERSITY OF CAMBRIDGE

Central Diagnostic Services

TEL: +44 (0)1223 337625 FAX: +44 (0)1223 339090 E-mail: clinpath@vet.cam.ac.uk

U B S S
Greenwich House
Madingley Rise
Cambridge
Cambs
CB3 0TX

Queen's Vet School Hospital
Madingley Rd,
Cambridge
CB3 0ES

Sample Details

Submission	157324
Sample Number	**15732402**
Hospital Number	QVH22/1832
Sample Type	Tissue
Request Date	28/02/2022
Report Date	15/03/2022
Report Number	157324-R01

Patient Details

Animal ID	**JK-Mira/Allen,M00714530,C3864 U B S S**
Species	Rabbit
Breed	
Gender	Female
D o B	
Sample Site	**Leg**
Hospital Vet	Jo Keeley

Histopathology

Description

rabbit foot in formalin Skin soft tissue removed before decal of bone.

Sections of skin soft tissue muscle and bone were examined. There was a thick layer of hyperkeratosis above a mildly thickened epidermis with areas of spongiosis close to the central area with loss of the epidermis and replacement by eosinophilic material (coagulation necrosis). In all areas the underlying dermis was broad, cellular and contained in some areas active fibrocytes as well as macrophages and lymphocytes in between collagen fibers. Closer to and underneath the lesion area there were also infiltrates of heterophils both perivascular and in between collagen fibers. In deeper areas there was separation of collagen fibers (oedema). Deep to this area and extending to the muscle borders there were increased numbers of cells. In focal areas there were dense perivascular collections of these cells in the fibrous connective tissue above and below the muscle layers. In some areas hair follicles and glandular structures were intact. In others there were heterophils within the hair follicle epithelium and most follicles contained hair shafts with eosinophilic material (keratinization) surrounding them. In focal areas mixed inflammatory cells were also seen in glandular structures and surrounding them. Focally in deeper fibrovascular tissue extending to the tendon and bone margins there were large dense collections of mostly heterophils disrupting tissue and forming dense eosinophilic granular areas.

Deep bone had areas that were unaffected with a clear distinct surface to cartilage and partially mineralized bone and mature bone. In these areas the bones contained marrow cavities filled with hematopoietic cells.

In deep areas where the inflammatory cells extended these extended into cartilage and bone disrupting the surface and surrounding fragmented mature bone. In the center of this areas bone was fragmented and granular and several large colonies of bacteria (cocci) were found. In these areas of fragmented bone, intact bone

UNIVERSITY OF CAMBRIDGE

Central Diagnostic Services

TEL: +44 (0)1223 337625 FAX: +44 (0)1223 339090 E-mail: clinpath@vet.cam.ac.uk

U B S S
Greenwich House
Madingley Rise
Cambridge
Cambs
CB3 0TX

Queen's Vet School Hospital
Madingley Rd,
Cambridge
CB3 0ES

Sample Details

Submission	157324
Sample Number	**15732402**
Hospital Number	QVH22/1832
Sample Type	Tissue
Request Date	28/02/2022
Report Date	15/03/2022
Report Number	157324-R01

Patient Details

Animal ID	**JK-Mira/Allen,M00714530,C3864 U B S S**
Species	Rabbit
Breed	
Gender	Female
D o B	
Sample Site	**Leg**
Hospital Vet	Jo Keeley

marrow cavities were empty or contained fat and occasionally inflammatory cells. The bone itself had lost normal structure and shape and was thin with loss of mineralization and contained foci of inflammatory cells. The inflammation extended down into at least one toe with disruption of the soft tissue bones and claws.

S aureus was cultured from the skin lesion.

Diagnosis **marked superficial and deep granulomatous dermatitis with deep bone osteomalacia and osteomylitis with bacterial colonies.**

Comment it is possible that the trauma of the surgery and manipulations caused opportunist bacteria to seed into the deep tissues (bone) and continued to expand into pyogranulomatous inflammation with bone damage osteomyelitis / malacia which were not responsive to antibiotics.

Dr J Archer VMD PhD FRCPath DECVCP FRCVS

Incomplete Tests NONE

# denotes un-validated tests

Report Type : **FINAL**

Appendix 5

Individual animal scores from the Stevenel's blue-Van Gieson picro-fuchsin stained non-decalcified histology sections:

A) Decellularised bone matrix (DBM) group:

	C 3	C7	C8	C11	C13	C16	ARI 73	ARI 78
1-Proliferative changes								
Defect closure inside the osteotomy (bone ingrowth)	0	0	0	0	1	0	0	1
Defect bridging anterior to the osteotomy (periosteal ossification)	0	1	2	3	2	3	1	2
Defect bridging posterior to the osteotomy and interosseous space (between radius and ulna)	2	3	3	1	2	2	2	3
Osseous integration	0	0	0	1	1	1	1	1
2-Degenerative bone changes								
Osteonecrosis	0	0	0	0	0	0	0	0
sequester	0	0	0	0	0	0	0	0
osteolysis	0	0	0	0	0	0	0	0
3-Phagocytosis								
Macrophages	0	0	0	0	0	0	2	0
Giant cells	0	0	0	0	0	0	0	0
4-Inflammatory changes								
Fibrous tissue	2	1	1	1	2	2	1	2
Lymphocytic (= non-purulent) inflammation	0	0	1	0	1	2	0	2
Granulocytic (= purulent) inflammation	0	0	0	0	0	0	0	0
Necrotizing inflammation	0	0	0	0	0	0	0	0
Osteomylitis (inflammation near bone marrow)	0	0	0	0	0	0	0	0
5- Infection								
Bacteria (cocci or bacilli visible)	0	0	0	0	0	0	0	0
Osteomyelitis (inflammation near bone marrow)	0	0	0	0	0	0	0	0

B) Tricalcium Phosphate group:

	C2	C9	C12	C17	C18	ARI 72	ARI 74	ARI 76
1-Proliferative changes								
Defect closure inside the osteotomy (bone ingrowth)	0	2	1	0	1	2	3	1
Defect bridging anterior to the osteotomy (periosteal ossification)	1	1	0	1	1	1	0	0
Defect bridging posterior to the osteotomy and interosseous space (between radius and ulna)	1	2	1	1	2	2	2	3
Osseous integration	1	2	3	2	2	3	2	3
2-Degenerative bone changes								
Osteonecrosis	0	0	0	0	0	0	0	0
sequester	0	0	0	0	0	0	0	0
osteolysis	0	0	0	0	0	0	0	0
3- Phagocytosis								
Macrophages	0	0	0	0	0	0	2	0
Giant cells	0	0	0	0	0	0	0	0
4- Inflammatory changes								
Fibrous tissue	1	2	2	0	0	1	2	1
lymphocytic (= non-purulent) inflammation	0	0	1	0	1	2	0	2
granulocytic (= purulent) inflammation	0	0	0	0	0	0	0	0
necrotizing inflammation	0	0	0	0	0	0	0	0
Osteomylitis (inflammation near bone marrow)	0	0	0	0	0	0	0	0
5- Infection								
Bacteria (cocci or bacilli visible)	0	0	0	0	0	0	0	0
Osteomyelitis (inflammation near bone marrow)	0	0	0	0	0	0	0	0

3-Polycaprolactone (PCL) group:

	C6	C10	C14	C19	ARI 71	ARI 77
1-Proliferative changes						
Defect closure inside the osteotomy (bone ingrowth)	2	1	2	2	3	2
Defect bridging anterior to the osteotomy (periosteal ossification)	1	3	2	3	2	1
Defect bridging posterior to the osteotomy and interosseous space (between radius and ulna)	3	2	1	4	3	1
Osseous integration	2	2	2	2	2	3
2-Degenerative bone changes						
Osteonecrosis	0	0	0	0	0	0
sequester	0	0	0	0	0	0
osteolysis	0	0	0	0	0	0
3- Phagocytosis						
Macrophages	0	0	0	0	0	0
Giant cells	0	0	0	0	0	0
4- Inflammatory changes						
Fibrous tissue	2	1	1	1	2	1
lymphocytic (= non-purulent) inflammation	0	0	0	0	0	0
Granulocytic (= purulent) inflammation	0	0	0	0	0	0
necrotizing inflammation	0	0	0	0	0	0
Osteomylitis (inflammation near bone marrow)	0	0	0	0	0	0
5- Infection						
Bacteria (cocci or bacilli visible)	0	0	0	0	0	0
Osteomyelitis (inflammation near bone marrow)	0	0	0	0	0	0

Fluorochrome bone labels individual animal's scores

A) Decellularised bone matrix (DBM) group:

	C 3	C7	C8	C11	C13	C16	ARI 73	ARI 78
Calcein green area%	0.31		0.28	0.31	0.26	0.42	0.30	0.41
Calcein green intensity	5.01		4.84	6.42	5.79	6.84	4.76	5.61
Xylenol orange area %	0.52		0.66	0.41	0.47	0.83	0.41	1.28
Xylenol orange intensity	7.26		6.94	5.96	7.00	8.94	5.96	8.32

B) Tricalcium Phosphate group:

	C2	C9	C12	C17	C18	ARI 72	ARI 74	ARI 76
Calcein green area%		0.48	0.21	0.76	0.44	0.26	0.26	0.48
Calcein green intensity		5.67	5.14	6.37	5.78	6.42	9.22	5.67
Xylenol orange area %		0.96	0.78	0.85	0.70	1.02	0.89	0.96
Xylenol orange intensity		9.00	5.29	5.29	5.29	7.66	6.63	9.00

3-Polycaprolactone (PCL) group:

	C6	C10	C14	C19	ARI 71	ARI 77
Calcein green area%	0.60	0.39		0.35	0.47	0.47
Calcein green intensity	7.30	6.18		5.89	5.64	5.78
Xylenol orange area %	0.68	0.53		1.12	0.36	0.60
Xylenol orange intensity	7.54	7.22		7.07	6.52	6.85

Appendix 6

Microstructure and mechanical properties of decellularised bone matrix bone cores

- **Microstructure:**

SEM:

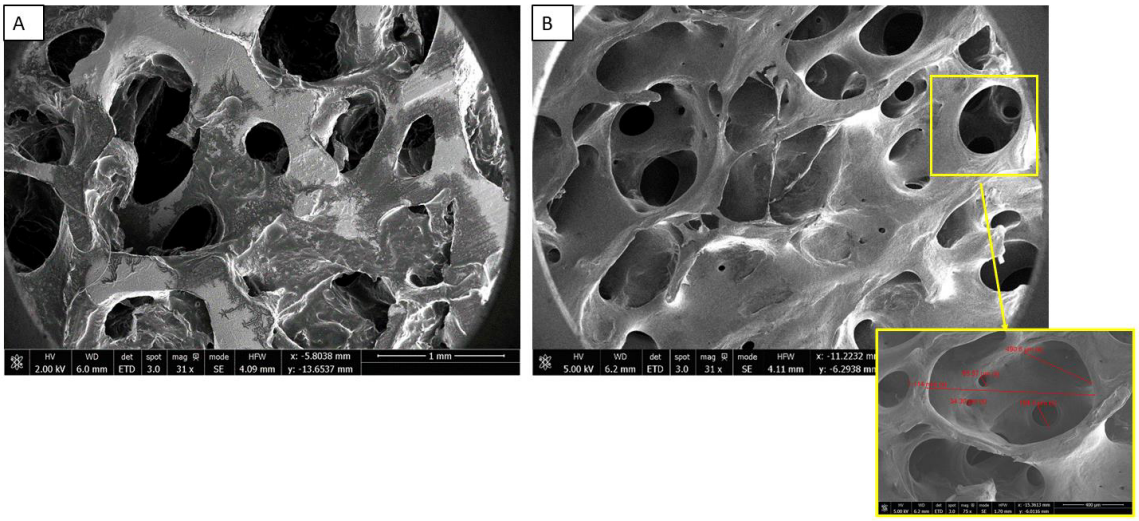


Figure 1: SEM images comparing unprocessed trabecular bone cores (A) to the decellularised bone matrix/ cores (DCBM) (B). Showing the preserved unique trabecular pattern, trabeculation and porosity

Micro CT:

Table.1. Micro-CT data analysis

	Unprocessed bone cores	DCBM
Average total porosity %	33.02% ± 8.66	40.66% ± 4.30
Average trabecular thickness (µm)	288.42 ± 65.90	263.20 ± 52.91

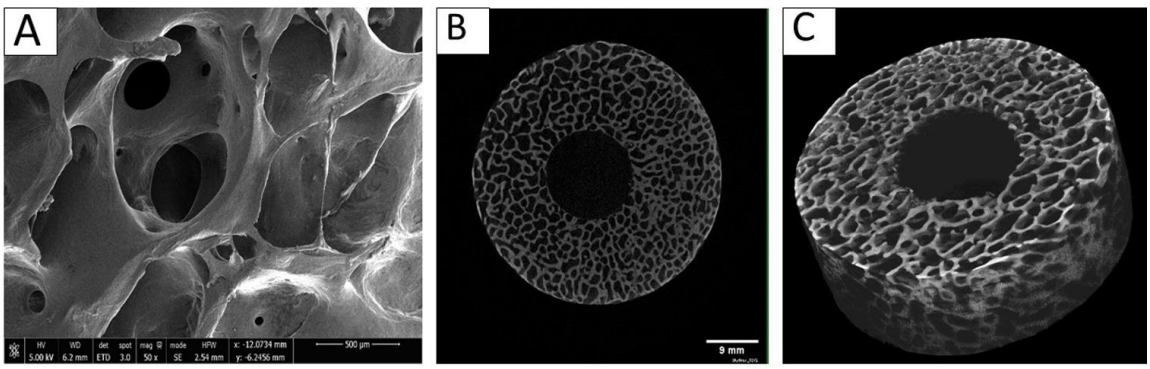


Figure .2: Porosity, interconnectivity, and trabecular pattern of the DCBM using SEM (A) and Micro CT Axial plane (B) and 3 D projection (C).

- **Biomechanical properties:**

	Unprocessed bone cores	DCBM
Average peak load to failure (N)	736.46 ± 326.84	863.351 ± 427.2
Average stiffness (N/mm)	1232.79 ± 279.06	1267.97 ± 535.65
Average Young's modulus MPa	78.09 ± 19.19	83.61 ± 33.38